AD-A229 904

DTIC FILE COPY

The Structure and Dynamics of Tropical-Midlatitude Interactions

DTIC
S ELECTE
DEC 10 1990
E
D

R. Gelaro
R&D Prediction Systems Division
Atmospheric Directorate
Monterey, California 93943-5006

90 12 7 068

Foreword

The Navy is interested in many aspects of atmospheric and oceanic variability that can no longer be treated as mutually exclusive phenomena. For example, it has become clear that seasonal predictions of oceanic storm activity and cloudiness, as well as seasonal variations in most oceanic circulations, are evolving phenomena that are continually modified by feedbacks between the atmosphere and the ocean. At shorter time scales, the prospect for developing coupled whole-earth prediction systems to provide better real-time fleet support depends critically on our ability to identify and understand the processes that link the atmosphere and oceans.

An understanding of the interactions between the tropical oceans and the atmosphere, developed within the context of the Navy's environmental prediction systems, is therefore essential for achieving naval environmental research goals regarding coupled air-sea model development and increased understanding of the role of oceanic processes in the global environment. The objective of the study described in this report is to investigate the influence of tropical ocean thermal anomalies on the general circulation of the atmosphere, placing particular emphasis on the impact of these anomalies on the near-term variability of midlatitude flow.

W. B. Moseley
Technical Director

J. B. Tupaz, Captain, USN
Commanding Officer

Executive Summary

The structure and dynamics of tropical-midlatitude interactions are investigated using the Navy Operational Global Atmospheric Prediction System (NOGAPS). The global response to sea surface temperature anomalies in the tropical Pacific Ocean is analyzed in terms of the normal modes of the NOGAPS model, with an emphasis on investigating the impact of tropical ocean thermal forcing on the dynamics of midlatitude flow. Expressing the results in normal mode form makes it possible to interpret the model response in terms of fundamental structures, such as Rossby modes, Kelvin modes, and inertia-gravity modes. Because the dynamics of the problem are analyzed within the framework of the complete baroclinic forecast model, rather than in a greatly simplified version of the model, the present work represents a direct and important extension of the analyses performed in many idealized modeling studies.

A new diagnostic technique is developed whereby the normal modes are partitioned according to their latitudinal variances in order to obtain estimates of the tropical and extratropical contributions to the anomalous response energy. The analysis reveals that the extratropical response has a significant baroclinic component, in addition to the well-known equivalent barotropic component. Accordingly, it is shown that the anomalous wave pattern in the extratropics is actually composed of two distinct types of horizontal wave motion superimposed on one another. The first type is associated with meridionally propagating large-scale waves that originate in the tropics and have equivalent barotropic structure. The second type is associated with zonally propagating waves that originate in midlatitudes, and whose structures are consistent with synoptic-scale baroclinic disturbances. The synoptic-scale anomalies appear to originate in regions where the meridionally propagating waves intersect the midlatitude westerlies, suggesting that they may be excited by the meridionally propagating waves. These results indicate that tropical ocean thermal forcing may substantially influence midlatitude synoptic-scale weather patterns at preferred locations on time scales of 1 to 2 weeks. Thus, the degree to which sea surface temperature variability can be accurately treated in coupled air-sea models appears to be a crucial limiting factor in their success.

Acknowledgments

---

*Previously the Naval Environmental Prediction Research Facility (NEPRF).

Contents

Accession For	
NTIS GRA&I	☒
DTIC TAB	☐
Unannounced	☐
Justification	
By	
Distribution/	
Availability Codes	
Dist	Avail and/or Special
A-1	

The Structure and Dynamics of Tropical-Midlatitude Interactions

Synopsis

As global models have become the primary tools for atmospheric prediction, it has become increasingly evident that local atmospheric variability (and predictability) is often significantly influenced by events occurring at remote locations. For example, it is now well known that variations in tropical sea surface temperatures (SST) and associated convective heating anomalies, such as those that occur in conjunction with the El Niño/Southern Oscillation (ENSO) phenomenon, can influence the atmospheric general circulation over the entire globe (Wallace and Gutzler, 1981; Horel and Wallace, 1981; Lim and Chang, 1983; Tiedtke, 1984; Mechoso et al., 1987). The overall implication of these facts is that atmospheric and oceanic variability are intimately linked, so that the prospect for extended range prediction of either medium is greatly diminished unless we consider the problem from a whole-earth perspective. Motivated, in part, by this growing body of evidence and by the necessity of providing unsurpassed environmental guidance for fleet support, the United States Navy is actively pursuing a broad research and development effort in coupled air-sea modeling (cf., Air Ocean Prediction (AOP) Plan [63207N], July 1988).

Preliminary tests show that coupled air-sea models are highly sensitive to atmospheric systematic errors. Therefore, before the Navy makes the commitment to develop coupled operational systems, it will be necessary to gain a firm understanding of the complex forcing and feedback mechanisms that link the atmosphere and the oceans. In particular, identifying critical ocean parameters that force the lower atmospheric boundary, understanding the mechanisms that enable these parameters to drive the atmosphere, and understanding the natural buffering mechanisms between the two media which keep the climate system in balance, are essential for driving coupled air-sea prediction models. Substantial progress toward these goals can be made using current operational systems

by assessing their sensitivity to key parameters in the air-sea problem. The appendix of this report details one particular effort in which a version of NOGAPS (Navy Operational Global Atmospheric Prediction System) is used to assess the impact of variations in tropical SST (which is one of the primary drivers of air-sea exchange) on the short-term atmospheric general circulation. From an air-sea modeling perspective, this research provides insight into the magnitude, scale, and dynamic structure of atmospheric response phenomena that may result from systematic errors in model-predicted SST.

Summary

In this study, global-scale interactions between the tropics and the midlatitudes were investigated by analyzing the response of NOGAPS to localized SST anomalies in the tropical Pacific. The primary focus was on improving our understanding of how changes in tropical ocean thermal forcing act to influence the general circulation and, in particular, the dynamics of midlatitude flow. The present analysis differs from those in previous studies of ocean thermal forcing of tropical-midlatitude interactions in two important respects. The first, and most important difference, is that in this study the dynamics of the problem were analyzed within the framework of the complete baroclinic model, instead of a greatly simplified version of the model. This was accomplished, in part, by analyzing the response in terms of the normal modes of the forecast model. This permitted the model response to be interpreted in terms of a spectrum of vertical modes, whose structures can be related to various types of atmospheric motions. Second, rather than focusing on changes that occur on seasonal or annual time scales, such as those associated with the El Niño/Southern Oscillation phenomenon, emphasis was placed on investigating the near-term impact of tropical ocean forcing on the evolution of the global flow. In the present context, this refers to changes

that occur on time scales ranging from 1 week to 1 or 2 months. Toward this end, a series of 50-day simulations was run with and without SST anomalies.

The time-mean anomalous response between days 21 and 50 of the simulations exhibited many of the well-known characteristics associated with tropical forcing anomalies that occur over much longer time scales, as established in previous studies with idealized and general circulation models. However, by using a new technique whereby the normal modes of the NOGAPS model were partitioned according to their latitudinal variances in order to define the tropical and extratropical contributions to the response energy, we showed that the structure and dynamics of the response, especially in the midlatitudes, is considerably more complicated than previously thought. Generally speaking, this added complexity, combined with the relatively rapid growth rates of the midlatitude responses, are indicative of the significant controlling influence of the tropical SST on the short-term midlatitude climate. Moreover, they demonstrate the potential impact of temporally varying SST values, produced, say, as a prognostic variable in a coupled air-sea model, on the atmospheric model climate. Any such impact is, in turn, likely to feed back to the ocean model climate, owing to its sensitivity to atmospheric systematic tendencies.

More specifically, the normal mode analysis revealed that, after several days, the anomalous response in the tropics was dominated by external rotational modes. These modes were shown to be associated with equivalent barotropic waves that propagated to high latitudes. After several days there was also a strong baroclinic response in the rotational modes at vertical mode 4, which appeared to be driven by the convection associated with the increased SST. This was consistent with a strong gravitational response at this vertical mode early in the simulations. It was shown that the prominence of vertical mode 4 (among the internal modes) is noteworthy because it implies that the vertical structure of the local (i.e., tropical) response is determined by the geopotential response to the heating, rather than by the heating itself.

In the midlatitudes, the response was dominated by the external rotational modes, in agreement with the conceptual framework obtained from earlier studies, which showed that equivalent barotropic modes may propagate to high latitudes. However, in addition to the external mode response, the analysis revealed a strong baroclinic response in the rotational modes corresponding to vertical mode 5. The evolution of the baroclinic response roughly followed that of the equivalent barotropic response, with the former growing at a somewhat slower rate. The maximum period of growth for both responses occurred between days 5 and 15, and then reached a state of approximate equilibrium after 20 days. Accordingly, a zonal wave number decomposition showed that the anomalous standing wave pattern in the midlatitudes was actually a superpositioning of two distinct types of horizontal wave motion.

The first type is associated with large-scale, zonally elongated waves that often form distinct meridional wave trains emanating from the tropics toward high latitudes. The equivalent barotropic structure of these waves was confirmed by the fact that they projected very strongly onto the external rotational modes. Remarkably, the emanation points for these wave trains were not necessarily collocated with the tropical SST anomalies. This is consistent with the existence of preferred regions of energy accumulation and subsequent meridional propagation in the tropics, as proposed by Webster and Chang (1988). The second type of wave motion is associated with synoptic-scale, meridionally elongated anomalies that propagated more or less zonally at midlatitudes. These waves clearly exhibited the tilted trough structure associated with synoptic-scale baroclinic waves. It was observed that the synoptic-scale anomalies obtained their maximum amplitudes downstream from where the meridionally propagating wave trains intersected the midlatitude westerlies. These and other results suggest the existence of a cause-and-effect relationship between the meridionally propagating long waves and the synoptic-scale baroclinic waves. Moreover, these anomalies appeared between days 5 and 10 of the simulation, suggesting that anomalous tropical forcing may substantially influence the midlatitude synoptic-scale flow at preferred locations on time-scales less than two weeks.

Recommendations

The results of this study clearly indicate that tropical ocean thermal forcing has a substantial impact on atmospheric variability both locally and at remote locations. Moreover, this impact is likely to be manifested on a wide range of spatial and temporal scales. By combining the results of this study with those of other investigators, we have established a general scenario whereby ocean thermal forcing can excite a hierarchy of responses, culminating in modifications to synoptic-scale weather events in 6-10 days; a steady state response is established within 2-3 weeks. Based on this hierarchy of responses, a series of cause-effect relationships has been proposed but little is understood about the processes that link these responses, the parameters that govern their interactions,

2

or the robustness of these relationships in the real air-sea system. Future research is needed to understand as completely as possible the key links in this response hierarchy. In particular, we need to focus attention on (1) extending our knowledge of tropical dynamics and physics to develop qualitative and quantitative relationships between relevant parameters including the wind, temperature, and sea surface topography; (2) understanding the mechanisms through which energy from tropical forcing anomalies tends to travel longitudinally for great distances before emanating toward higher latitudes from selected locations; and (3) determining the mechanisms through which this meridionally propagating energy interacts with midlatitude westerlies to influence atmospheric phenomena there.

Finally, with regard to the development of coupled air-sea models in which SST is a prognostic quantity, these results demonstrate the enormous potential impact on the quality of even short-range forecasts due to systematic errors, or biases, in model-predicted SSTs. In turn, given the sensitivity of coupled air-sea models to atmospheric biases, the extent to which we can control or eliminate systematic errors in model-predicted SST may be a dominant limiting factor in our ability to predict the general circulation in either medium for any extended length of time. It is thus recommended that a considerable research effort be put forth aimed at understanding the mechanisms through which the atmosphere and the oceans interact in order to regulate SST evolution.

References

Horel, J. D. and J. M. Wallace (1981). Planetary-scale atmospheric phenomena associated with the Southern Oscillation. *Mon. Wea. Rev.*, 109, 813-829.

Lim, H. and C.-P. Chang (1983). Dynamics of teleconnections and Walker circulations forced by equatorial heating. *J. Atmos. Sci.*, 40, 1897-1915.

Mechoso, C. R., A. Kitoh, S. Moorthi, and A. Arakawa (1987). Numerical simulations of the atmospheric response to a sea surface temperature anomaly over the equatorial eastern Pacific Ocean. *Mon. Wea. Rev.*, 115, 2936-2956.

Tiedtke, M. (1984). The effect of penetrative cumulus convection on the large-scale flow in a general circulation model. *Beitr. Phys. Atmosph.*, 57, 216-239.

Wallace, J. M. and D. S. Gutzler (1981). Teleconnections in the geopotential height field during the Northern Hemisphere winter. *Mon. Wea. Rev.*, 109, 785-812.

Webster, P. J. and H.-R. Chang (1988). Energy accumulation and emanation regions at low latitudes: Impacts of a zonally varying basic state. *J. Atmos. Sci.*, 45, 803-829.

Appendix

The Structure and Dynamics of Tropical-Midlatitude Interactions

Ronald Gelaro

1. INTRODUCTION

Ever since the first successful numerical weather forecasts were produced by Charney, Fjørtoft and von Neumann (1950) with an equivalent-barotropic model, atmospheric scientists have striven to increase the skill and range of useful predictability of models used in numerical weather prediction (NWP). The difficulties of this challenge are well known and can be attributed to several factors such as the complexity of the governing equations, the errors that result from trying to represent an infinite-dimensional system such as the atmosphere with finite-dimensional models, and the apparent existence of a theoretical limit of approximately two weeks for predicting the details of the atmospheric flow. Nonetheless, substantial progress has been made in this area, especially during the past decade or so, due in large part to our increased understanding of hydrodynamic processes in the atmosphere and due to the availability of vastly improved computational resources. In particular, these advances have made possible the development of sophisticated global atmospheric prediction models that incorporate realistic representations of most of the important dynamic and physical (*i.e.*, radiative, precipitative and orographic) processes in the atmosphere, along with the spherical geometry of the global earth-atmosphere system.

In spite of the progress that has been made, there remains much uncertainty regarding the ways in which physical forcing in the atmosphere alters the general circulation. Moreover, given the fact that there is a certain degree of regularity associated with many atmospheric phenomena (*e.g.*, the

existence of preferred scales at which unstable waves grow), there can be little doubt that this forcing may focus energy at discrete temporal and spatial scales. In the same way, our lack of understanding regarding the effects of physical forcing, and our subsequent inability to simulate these effects accurately, may explain, at least partially, the fact that systematic errors remain an inherent feature of all atmospheric models. These errors describe the tendency for model simulations to evolve away from the true atmospheric state in some consistent manner. An example of a systematic error is the tendency for some forecast models to weaken the major standing wave pattern in the middle and upper troposphere (Hollingsworth *et al.*, 1980). In the short term, these errors may degrade the forecast before the limit of useful predictability of a model has been reached, and on longer time-scales may influence its seasonal climate.

It is not difficult to imagine the many potential sources of these errors, such as the representation of topography, the characteristics of the difference scheme used to integrate the model equations or the parameterization of subgrid-scale physical processes. Of all these possibilities, perhaps the greatest potential source of systematic error derives from the way in which we simulate the effects of diabatic forcing on the general circulation, especially by cumulus convection. The main reason for this is the lack of understanding of how diabatic heating influences the general circulation. Indeed, the results of studies aimed at assessing the impact of cumulus convection on the general circulation have shown that convective heating can substantially modify the large-scale flow (*e.g.*, Donner *et al.*, 1982; Tiedtke, 1984). Furthermore, Tiedtke concludes that the prospect for useful long-range forecasts is greatly diminished by the uncertainties that exist regarding the effects of cumulus convection and

cloud-radiation interactions in current forecast models.

Recently, the impact of diabatic forcing on the general circulation has gained further attention in light of a growing body of evidence from both observational and simple modeling studies that regions of anomalous forcing in the tropics may exert a marked influence on the circulation patterns at higher latitudes (*e.g.*, Bjerknes, 1969; Horel and Wallace, 1981; Wallace and Gutzler, 1981; Webster, 1981; Hoskins and Karoly, 1981; Lim and Chang, 1983, 1986). The term *teleconnections* has been coined to describe these interactions between the tropics and midlatitudes. The most well-known form of teleconnection is manifested by a series of meridionally propagating anomalies in the stream function or geopotential height field that originates in the tropics and arcs poleward and eastward into the midlatitudes (Figure 1.1). There is substantial observational evidence that these teleconnections are strongly correlated with episodes of anomalous increases in the tropical sea surface temperature (SST), which are known to occur in conjunction with the El Niño-Southern Oscillation (ENSO) phenomenon (Julian and Chervin, 1978). Accordingly, teleconnection patterns are typically observed to occur on monthly to annual time-scales, although as will be discussed shortly, there are strong indications that they occur on shorter time-scales as well. The SST anomalies can alter the intensity and geographical distribution of the major centers of convective forcing in the tropics, which in turn can act as anomalous sources of wave energy. The resulting anomalies appear to have recurrent spatial patterns and are well documented in the observational studies of Horel and Wallace (1981), Wallace and Gutzler (1981) and others. One of the most recognizable anomalous standing wave patterns takes a form known as the *Pacific-North American*
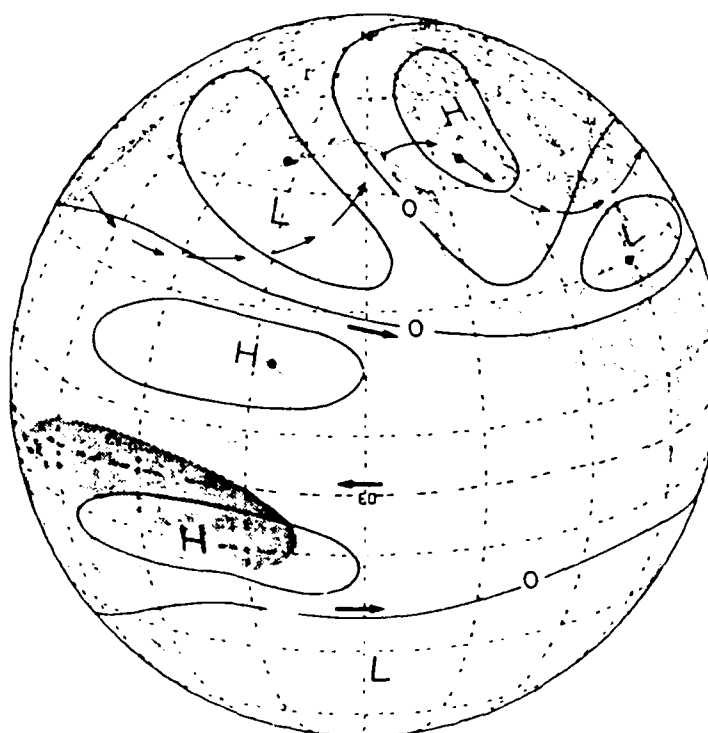
Figure 1.1   Schematic representation of upper tropospheric geopotential
                height anomalies during an episode of warm SST (shaded area) in
                the equatorial Pacific. The darker arrows denote strengthening
                -jets. The lighter arrows denote an anomalous stream line (from
                Horel and Wallace, 1981).

(PNA) pattern (Wallace and Gutzler, 1981) in which the geopotential heights
are relatively low over the Aleutian Islands and off the coast of California, high
over central and western Canada and low again off the east coast of the United
States. This is the pattern depicted in Figure 1.1, which first appeared in Horel
and Wallace (1981). Some of the other recurrent standing wave patterns
discussed by Wallace and Gutzler are the Eastern Atlantic and Eurasian
patterns. The results of numerous simple modeling studies (some of which will
be reviewed shortly) indicate that the anomalies shown schematically in
Figure 1.1 may be interpreted in terms of Rossby wave dispersion on a sphere
from a localized vorticity source near the equator (Hoskins and Karoly, 1981;
Opsteegh and van den Dool, 1980; Horel and Wallace, 1981; Webster, 1981).

It is reasonable to assume that teleconnections such as the one depicted in
Figure 1.1 can influence the standing wave pattern, and thus the seasonal
climate, in the midlatitudes. Where numerical models are concerned, these
results imply that certain systematic forecast errors in the midlatitudes may be
linked directly to errors in the model-predicted tropical diabatic forcing.
However, before the effects of diabatic forcing in numerical models can be
understood completely, it will be necessary to learn more about its interaction
with different scales of the model flow. The problem is complicated by the fact
that, even with the latest increases in model resolution, convective forcing
generally remains a subgrid-scale phenomenon whose effects on the large-scale
flow must be parameterized. Consequently, the parameterization scheme itself is
often a "black box," whose impact on the model flow is manifested at scales
other than those at which the forcing occurs, and therefore, is difficult to assess.
For now, it is important to note simply that teleconnections have been observed

in response to SST anomalies in numerical modeling simulations by several investigators such as Rowntree (1972), Keshavamurty (1982), Shukla and Wallace (1983), Blackmon *et al.* (1983) and Pitcher *et al.* (1988). Tiedtke (1984) observed teleconnections in a series of experiments using the European Centre for Medium-range Weather Forecasts (ECMWF) spectral model (Baede *et al.*, 1979) to examine the effects on the general circulation of various cumulus cloud-radiation interaction schemes. Tiedtke observed that minor changes in cloud-radiation interactions produced significant changes in the position and intensity of the Icelandic Low. The perturbation stream function in his experiment showed a wave train emanating from the quasi-permanent convection over equatorial South America. It is not surprising that the general position of the Icelandic Low coincides with one of the centers of action in the Eastern Atlantic teleconnection pattern described by Wallace and Gutzler (1981). These and other results suggest that exceptionally strong tropical forcing is not always necessary to produce a remote (*i.e.*, midlatitude) response, but rather that such teleconnections occur frequently and are a regular means of interaction between the tropics and extratropics. If this is the case, then we can assume that this interaction plays a vital role in determining the nature of the global circulation, and, that it is essential we model its behavior accurately.

The purpose of this study is to examine the dynamic structure and behavior of teleconnections in a sophisticated global model in order to gain a better understanding of how tropical diabatic forcing influences the general circulation, and in particular, the flow in the midlatitudes. This will be accomplished, in part, by developing and applying new diagnostic tools based on the model normal modes in order to examine explicitly the impact of anomalous

tropical forcing on selected scales of the model flow. The philosophy and approach that will be used will be explained in Section 1.2. However, before proceeding with an explanation of the details of the study. it will be useful to review some of the work upon which our current knowledge of tropical-midlatitude interactions is based. This background will help demonstrate the relevance of the present study and how specifically it might extend our understanding of interactions between the tropics and midlatitudes. Naturally, it is hoped that any insight gained from this study will be applicable to the atmosphere to some degree. However, it should be noted that an understanding of the model response is important in its own right if we hope to improve our ability to simulate the atmosphere.

1.1 Background and Literature Review

As pointed out by Lim and Chang (1983) and others, the response of the tropical atmosphere to diabatic forcing can be separated into two basic types of motions based on their vertical structures. The first type is characterized by cellular motions whose vertical structure reverses sign somewhere in the middle troposphere. The associated circulation is that of "convective overturning" with low-level inflow and upper-level outflow, typical of the Hadley or Walker circulations. The second type has vertical structure that remains relatively constant throughout the troposphere and takes the form of the meridionally propagating response associated with the teleconnection patterns described earlier. Each of these response types can be explained in terms of the vertical modes that describe tropical motions (Matsuno, 1966). The horizontal structure of each response is described by a set of shallow-water equations that has the

equivalent depth of the corresponding vertical mode as its scale height. Generally speaking, we can classify these vertical modes as either baroclinic, in which case their structure varies substantially in the vertical, or equivalent barotropic, in which case their structure varies only slightly in the vertical.[1] The baroclinic modes have relatively slow phase speeds and thus tend to be equatorially trapped by the Coriolis force (Webster, 1972; Gill, 1980; Webster and Chang, 1987). Accordingly, these modes tend to be associated with the cellular (or first) type of response described above, which are generally confined to low latitudes. In contrast, the barotropic modes have relatively rapid phase speeds, and thus are not equatorially trapped. These modes tend to be associated with the propagating (or second) type of response described above. During the last few years, several investigators have exploited this separability by using simple models to gain a qualitative understanding of the atmospheric response to tropical diabatic forcing. In many cases, these studies involve using a form of the linearized shallow water equations on an equatorial beta-plane with some simple forcing. In these models it is necessary to specify an appropriate value for the equivalent depth (*i.e.*, vertical mode) that describes the type of motion one wishes to study. The results from various types of simple modeling studies comprise a considerable amount of the present theoretical knowledge of tropical motions. Some of these are described below.

Using a two-level linear model, Webster (1972) was able to simulate a Walker-type response to the east of an equatorial heat source. He interpreted

---

[1]Actually, only the gravest, or external, mode is equivalent barotropic. However, in systems with finer vertical resolution, the vertical structures of the first few internal modes also remain relatively constant throughout the troposphere, varying only at extremely high levels. See Appendix for details.

this response in terms of Kelvin waves, which are nondispersive eastward propagating gravity modes with zero meridional velocity component. Gill (1980) and Silva Dias *et al.* (1983) used shallow water beta-plane models in a motionless basic state and obtained similar results to those of Webster. In addition, they were able to simulate a western branch of the Walker circulation, which they interpreted as westward propagating Rossby modes. Similar results and analyses have been put forth by other authors such as Lau and Lim (1982) who used a beta-plane model with various mean winds in solid rotation. In accordance with the discussion above, this type of cellular motion has been termed "baroclinic" in the published literature. It might be noted that some work has been done using more sophisticated models to study the roles of various types of modes in tropical motions, including studies by Puri (1983), Kasahara (1984) and Errico (1984).

If we avoid some of the simplifying assumptions used in the above studies, then we allow for the possibility of producing the second type of response, which can propagate out of the tropics. For example, it is necessary to include a more realistic mean wind profile and to discard the long-wave approximation (Lighthill, 1969) that renders the Rossby modes nondispersive and causes them to be trapped near the equator. Unlike the cellular motions of the Walker or Hadley circulations, the propagating teleconnection response is characterized by flow having roughly the same vertical structure throughout the depth of the troposphere. Accordingly, this type of motion has been termed "barotropic" and corresponds to those vertical modes having the greatest equivalent depths or scale heights. Hoskins and Karoly (1981) used a linearized steady state version of a five-layer baroclinic model (Hoskins and Simmons, 1975) to study the

response of a spherical atmosphere to simple thermal and orographic forcing. Linearizing about a Northern Hemisphere winter zonal flow and using a low-latitude forcing, they obtained an extratropical response with equivalent barotropic structure, which they interpreted as nondivergent propagating Rossby waves. These authors successfully used ray tracing techniques to describe various properties of the teleconnection patterns. Simmons (1982) studied the effects of nonlinearity and nonuniform zonal flows on teleconnections in an effort to reveal the origin of systematic errors in the ECMWF spectral model. He found that both of these effects modified the intensity of the response, with a strong remote response occurring in the northern Pacific whenever the forcing was located just south of a region of maximum zonal flow. We may recall that the PNA teleconnection pattern is well documented in the observational studies of Horel and Wallace (1981) and Wallace and Gutzler (1981). The results of Simmons were supported by those of Webster (1982), who demonstrated that teleconnections occur in the winter hemisphere and depend strongly on the mean winds.

The structure of teleconnections was studied in further detail by Lim and Chang (1983), again using a linearized shallow water beta-plane model. They showed that the northward and eastward propagating response patterns could be interpreted in terms of lee-waves produced as the mean wind impinged on a tropical heat source. Performing a normal mode analysis in terms of Hermite functions, they further showed that these lee-waves were composed of several band-like Rossby modes with different meridional wave numbers superimposed on one another. Because each of these modes has a different spatial scale and phase speed, their interference produces the propagation patterns characteristic

of the teleconnection response pattern. Lim and Chang further showed that a propagating teleconnection response occurred only with a mean westerly wind, and then only when its speed fell within the range of the Rossby wave speed. This is in agreement with the results of some of the studies mentioned earlier (Simmons, 1982; Webster, 1982) concerning the influence of the mean wind on teleconnections. Similar results have been obtained by Lau and Lim (1984) who used ray tracing and compared the results of linear theory with those obtained from a nonlinear spectral model of the shallow water equations in various mean flows. More recently, Lim and Chang (1986,1987) have used simple models to examine the effects of internal heating, damping and vertical wind shear on the production of propagating responses from internal equatorial heat sources. Their findings may be relevant to simulating teleconnections using more sophisticated numerical models and will be discussed in detail in Chapter 3.

Naturally, the results of these and other similar studies show some disagreement concerning certain details of the teleconnection responses with regard to amplitude or sensitivity to the location of the tropical forcing. However, virtually all of the results thus far indicate that the meridionally propagating response is an equivalent barotropic phenomenon that has the same phase throughout the depth of the troposphere and amplitude that increases gradually with height. As a result, barotropic modeling studies have more or less successfully reproduced the qualitative nature of teleconnections demonstrated by observational studies and studies using more realistic models. In a study using the National Center for Atmospheric Research (NCAR) Community Climate Model (CCM) with an anomalous tropical vorticity source as forcing, Branstator (1985) compared the response of a linear nondivergent

barotropic version of the CCM with that of the complete CCM. He found that midlatitude circulation anomalies obtained in the simplified version of the model closely resembled those of the complete model when the former was linearized about a wavy (realistic) basic state.

1.2   Extension to Complex Systems

As with most atmospheric phenomena, much of what is known about the structure and dynamics of teleconnections has been learned from studies involving relatively simple models whose behavior can be easily interpreted. While the qualitative nature of the response appears to be well represented in these models, it is not known how well they describe the dynamics of the response in more realistic systems. As stated earlier, several investigators have observed teleconnections in studies with more sophisticated numerical models such as those by Rowntree (1972), Keshavamurty (1982), Blackmon *et al.* (1983) and Skukla and Wallace (1983). In most cases the response patterns were generally similar to those found in observational studies, with some variations in the amplitudes and geographical positions of the anomalies. More recently, some investigators have begun to examine the sensitivity of general circulation models (GCM) to changes in the location and strength of SST anomalies in light of growing evidence that these effects may significantly alter the flow in midlatitudes. Using the NCAR CCM, Geisler *et al.* (1985) found that the location of the SST anomaly had little impact on the location of the remote response pattern (a result common to some of the simple modeling studies discussed above), but found that its amplitude was greatest when the SST anomaly was located in the western Pacific. These and other modeling results

agree with a recent observational study by Hamilton (1988) who examined
various types of data covering the period from 1899–1982 and concluded that
the strength of the Northern Hemisphere response increases when the SST
anomaly is located farther westward in the Pacific. Geisler *et al.* also found that
the amplitude of the remote response showed limited sensitivity to the
amplitude of the SST anomaly. Their results were later supported by Pitcher *et
al.* (1988) who used the NCAR CCM to examine the response to the 1976/77
observed Pacific SST anomaly at various multiples of its original strength. They
found that the model response to the basic SST anomaly and to twice the basic
SST anomaly was a PNA pattern whose amplitude increased more slowly than
linearly as the magnitude of the SST anomaly was increased. Still other
researchers have investigated the responses of GCM's to observed SST anomalies
and found somewhat more variable results; examples include Fennessy *et al.*
(1985) who used the Goddard Laboratory for Atmospheric Sciences (GLAS)
climate model, and Palmer and Mansfield (1986) who used the British
Meteorological Office GCM, to study the midlatitude response to the 1982/83
observed SST anomaly. In both studies, the investigators found that the remote
response patterns showed considerable variations from the typical PNA pattern
described earlier and concluded that variations in the SST anomaly were crucial
to determining the variability of the remote response pattern.

Although there now exists a considerable amount of data documenting the
response of sophisticated numerical models to anomalous tropical forcing, little
is known about the details of the modal structure or dynamics of the response
in these models, nor to what extent these characteristics agree with results from
theoretical and basic modeling studies. Lau and Lim (1984) point out that an

analysis of the response in a multi-level baroclinic model with an interactive background state (*i.e.*, one in which the mean flow is modified by the anomalous response, rather than simply superimposed on it) is undoubtedly needed to understand completely the dynamics and effects of teleconnections. For example, it is well known that "El Niño years" are often associated with unusually stormy winters in certain locations, yet the mechanism for this effect is not completely understood. However, given the fact that teleconnections can alter the standing wave pattern in midlatitudes, it seems reasonable to assume that the position and intensities of synoptic-scale weather events are also likely to be influenced. The potential importance of transient eddy effects on the dynamics of teleconnections has been discussed by Kok and Opsteegh (1985) and others. Recently, Mechoso *et al.* (1987) used the UCLA GCM to show that the energy in midlatitude synoptic-scale transient eddies was in fact greater in an extended run with an SST anomaly in the eastern Pacific than in a similar run without the anomaly. Recent work by Zhong and Nogues-Paegle (1989) also indicates that baroclinic modes may be active in the midlatitude response. These results suggest that the midlatitude response to such forcing may in fact have a synoptic-scale component associated with changes in the behavior of the so-called Rossby regime. Thus, it appears likely that an understanding of the dynamic structure of the response in a realistic model that includes barotropic and baroclinic processes is needed to obtain a complete picture of the impact of anomalous tropical forcing on the general circulation. Unfortunately, the dynamic interactions in sophisticated numerical models are typically much less tractable than those in relatively simple models, making it difficult to use the former pedagogically.

The approach to this problem in the present study will be to exploit the tractability of the normal mode representations of the solutions to a sophisticated numerical model in order to examine the dynamics of tropical-midlatitude interactions. The normal modes are solutions to the linearized version of the model, and as such, provide a way of separating the model-simulated flow according to its fundamental spatial and temporal scales. Because the modes are exact solutions to the linearized model equations, they represent dynamic structures that often are governed by well-known relationships, which in turn, can be related to distinct types of atmospheric motions. The capability of isolating these structures without having to simplify the realism of the model dynamics will form the basis for conducting a more complete analysis of the impact of teleconnections on the general circulation than has been previously possible. The use of normal mode solutions as a diagnostic tool has been demonstrated by, among others, Kasahara and Puri (1981), Puri (1983), Errico and Rasch (1988) and Errico *et al.* (1988).

The primary focus of this study will be on improving our understanding of the processes that govern the *midlatitude* response to anomalous tropical diabatic forcing. The dynamics of the tropical response will be examined in somewhat less detail. From a numerical modeling point of view, it will be shown that errors in model-predicted tropical forcing may crucially influence midlatitude forecasts on time-scales as short as six to ten days. The model that will be used in this study is the forecast component of the Navy Operational Global Atmospheric Prediction System (NOGAPS). As is necessary for portraying the midlatitude response as accurately as possible, the model includes baroclinic processes and detailed vertical resolution, in addition to

realistic physical parameterizations and an interactive background state. The approach that will be taken in this study will be to analyze the model response to imposed SST anomalies in the tropical Pacific. The philosophy for choosing this approach is two-fold. First, perturbing the SST in a sophisticated global model represents one of the most fundamental and least artificial ways of permitting a tropical diabatic forcing anomaly to develop and evolve naturally via the physical processes in the model. Secondly, as discussed earlier, SST anomalies have been studied before using NWP models, so that the general characteristics and the statistical relevance of certain response patterns (*e.g.*, the PNA pattern) are well established. This is relevant in terms of the present study since we decided to analyze a limited number of simulations using as realistic a model as practically possible. Thus, the intention here is to investigate the structure and dynamics of interactions that might be considered typical of the sort associated with anomalous tropical forcing in a realistic setting, rather than to present an average of many cases. This is discussed in more detail when relevant issues arise throughout the course of the study.

The following chapter begins with a brief introduction to the NOGAPS spectral model and a description of the numerical simulations that were performed. These runs consist of a set of 50-day simulations with and without SST anomalies in the tropical Pacific Ocean, which we refer to as the anomaly and control runs, respectively. The anomalous response of the model is defined in terms of the difference between these runs. The main goal of this chapter is to describe the general characteristics of the simulation procedure and the numerical results, and to highlight some of the findings that are analyzed in detail in the remainder of the study. A more detailed description of the model

can be found in Hogan and Rosmond (1989).

In Chapter 3, a detailed normal mode analysis of the numerical results is performed. A new technique is developed whereby the normal modes are partitioned according to their latitudinal variances in order to estimate the tropical and extratropical contributions to the anomalous response energy. The dominant response modes in each region are identified and then related to the dynamics of the steady and temporally varying components of the anomalous response. The partitioning technique also reveals some interesting properties about the modal variances that may have implications concerning the initialization of models used for NWP. This is discussed further in Chapter 5.

Chapter 4 focuses on the midlatitude response of the model, and in particular, on the interactions between different horizontal scales of motion that ultimately determine how the SST anomaly influences the midlatitude flow. The anomalous stationary and transient eddies are decomposed in terms of zonal wave number bands and their temporal evolution is examined. This allows some inferences to be made concerning the growth of synoptic-scale anomalies in midlatitudes, and the roles of barotropic and baroclinic instability in the anomalous response.

The final chapter presents the conclusions of this study. Based on the current results, as well as on those from previous studies, we propose a scenario that describes the response of the midlatitude circulation in terms of a hierarchy of dynamic interactions beginning with the forcing from the tropical SST anomaly. This scenario is presented as one possible sequence of events that might occur in the atmosphere. Also, implications concerning peripheral issues such as nonlinear normal mode initialization (NNMI) are discussed in light of

some of the findings in this study. Finally, some of the limitations of the study are discussed and avenues for future research are suggested.

2. NUMERICAL SIMULATIONS

The most important difference between the analysis in the present study and those in previous studies of tropical-midlatitude interactions is that, in this study, the dynamics of the problem are analyzed within the context of a complete global model of the atmosphere, rather than in an idealized (say, linearized, barotropic) model. In this chapter, we provide an overview of the numerical aspects of this study. We begin by summarizing the general characteristics of the model, and then describe the simulations that were conducted in order to provide the data for the analysis. We then examine the general characteristics of the time-mean responses in each simulation. Finally, it is shown that the model response to anomalous tropical forcing exhibits certain characteristics that have not been observed in studies with idealized models. These results provide the motivation for the analysis that is conducted in the remaining chapters.

2.1 The NOGAPS Spectral Model

The model used in this study is version 3.0 of the Navy Operational Global Atmospheric Prediction System (NOGAPS) spectral model described by Hogan and Rosmond (1989). This version of the model served as the Navy's operational global atmospheric forecast model between January 1988 and March 1989. The current operational model—NOGAPS 3.1—is an updated version of the model used in this study. Any references to the NOGAPS spectral model during the remainder of this study are to version 3.0 unless otherwise stated.

For convenience in the following discussion, we separate the NOGAPS spectral model into adiabatic and diabatic components. The adiabatic component refers to the basic model formulation, including its vertical structure, representations of the dependent variables, differencing schemes, etc. The diabatic component refers to the set of physical parameterizations employed in the model. In this section, we describe the general features of each component. A more mathematically detailed description is given by Hogan and Rosmond (1989).

2.1.1 Adiabatic Component

In terms of its adiabatic component, the NOGAPS model is spectral in the horizontal dimensions and has 18 vertically discrete levels defined in terms of σ-coordinates of the form

$$\sigma_k = \frac{p_k - p_T}{p_s - p_T}, \tag{2.1}$$

where p_k is the pressure at level k, p_s is the pressure at the terrain surface, and p_T is the pressure at the top of the model. The value $p_T = 1$ mb is used to provide an acceptable (*i.e.*, nonzero) upper boundary for some of the physical parameterization schemes. The vertical index k is taken to increase toward the surface so that (2.1) implies $\sigma_1 < \sigma_2 < \ldots < \sigma_{18}$. The σ-levels are unevenly spaced in such a way as to provide increased vertical resolution in the boundary layer and at extremely high levels, and an energy-conserving finite difference scheme, described by Haltiner and Williams (1980), is used to compute vertical derivatives.

At each level, the dependent variables are represented in terms of a sum of spherical harmonics that, for now, we write in the general form

$$\xi(\lambda, \mu, t) = \sum_m \sum_n \xi_{m,n}(t)\, P_{m,n}(\mu)\, e^{i\, n\lambda}\, , \tag{2.2}$$

where $\xi_{m,n}(t)$ is a time-dependent expansion coefficient for a model variable ξ, $P_{m,n}(\mu)$ is an associated Legendre polynomial, λ and μ are the longitude and sine of the latitude, respectively, and m and n are integers. In the NOGAPS model, (2.2) is truncated triangularly such that $m = -M, \ldots, 0, \ldots, M$ and $n = |m|, \ldots, M - |m| + 1$, where $M = 47$ (henceforth referred to as a T47 truncation). With this resolution, the nonlinear terms in the model equations are computed most efficiently via the transform method, in which the dependent variables are first transformed into values on a grid of points, then multiplied together to form the appropriate nonlinear quantities, and finally, transformed back into spectral space as tendencies. The spectral-to-grid transform uses a vectorized fast Fourier transform in longitude, and the Legendre integrals in latitude are evaluated by Gaussian quadrature. For the T47 spectral truncation, the transform grid consists of 144 longitudinal points and 72 Gaussian latitudes, which corresponds very nearly to a resolution of 2.5° (approximately 275 km) in both horizontal dimensions.[1] A ∇^4-type spatial filtering is employed to smooth extremely small-scale features.

Finally, the time-integration scheme used in the NOGAPS model is a centered semi-implicit scheme (Kwizak and Robert, 1971) with a Robert (1966) time filter. The semi-implicit scheme is used to reduce the phase speeds of the most rapidly propagating gravity waves, and thus increase the maximum allowable time-step. For the T47 truncation of the NOGAPS spectral model, a time-step of 24 minutes is used.

---

[1] This spacing is exact in longitude but varies slightly in latitude as a result of the unequal spacing of the Gaussian latitudes. Gaussian latitudes correspond to the roots of the Legendre polynomials used in the spherical harmonic expansions of the dependent variables.

2.1.2 Diabatic Component

The diabatic component of the NOGAPS spectral model includes the following parameterized physical processes: gravity wave drag, vertical fluxes of mass and momentum, cumulus convection, large-scale precipitation, shallow cumulus mixing, and long-wave and short-wave radiation. In the NOGAPS model, the vertical fluxes (including gravity wave drag) and radiational forcing are computed as explicit tendencies analogous to those computed for the adiabatic terms in the model equations. The effects of the remaining physical processes are treated as adjustments to the dependent variables on the grid at each time-step. Thus, the value of a dependent variable ξ at some future time $t + \Delta t$ is computed from values at previous times t and $t - \Delta t$ using a three-step procedure. First, the total (adiabatic plus diabatic) tendency at time t is computed by the sum

$$\frac{\Delta \xi^{(t)}}{\Delta t} = \left.\frac{\Delta \xi^{(t)}}{\Delta t}\right|_{adiabatic} + \left.\frac{\Delta \xi^{(t)}}{\Delta t}\right|_{radiation} + \left.\frac{\Delta \xi^{(t)}}{\Delta t}\right|_{vertflux}, \qquad (2.3)$$

where Δt is the time-step. Next, the result of (2.3) is used to compute a "provisional" value of ξ at $t + \Delta t$ via

$$\xi'^{(t+\Delta t)} = \xi^{(t-\Delta t)} + 2\Delta t \left(\frac{\Delta \xi^{(t)}}{\Delta t}\right), \qquad (2.4)$$

where the prime indicates the provisional forecast value. Finally, the effects of the remaining physical processes are incorporated by making a series of adjustments to the provisional value of the form

$$\xi^{(t+\Delta t)} = \mathcal{F}\left(\xi'^{(t+\Delta t)}\right), \qquad (2.5)$$

where $\mathcal{F}$ is an implicit operator at time t. Figure 2.1 shows schematically the sequence of calculations that is performed during each integration step of the

NOGAPS model. A brief description of each of the physical parameterization schemes employed in the NOGAPS model is given below.

Gravity Wave Drag

The effect of vertically propagating energy (from say, air flow over a mountain) on the upper-tropospheric westerly momentum budget is parameterized at all resolvable scales using the formulation of Palmer *et al.* (1986). The vertical stress generated by the wind blowing across the terrain surface is assumed to remain constant at successively higher levels until the local Richardson number becomes less than its critical value, implying instability. At that level, and at successively higher ones, the vertical stress is systematically decreased as the gravity wave is assumed to "break."

Vertical Fluxes

The parameterizations of vertical fluxes of mass and momentum are based on the K-theory formulation of Louis (1979). In each model layer k, the turbulent fluxes are evaluated in terms of vertical mixing coefficients K_k, which determine the exchange with surrounding layers. In contrast to a bulk formulation for the planetary boundary layer, this formulation permits turbulent mixing to occur throughout extremely deep layers spanning several model levels. Also, unlike the bulk formulation, the K-theory formulation does not require the boundary layer to be well defined.

Cumulus Convection

The effects of penetrative cumulus convection are parameterized via the Arakawa-Schubert scheme (Arakawa and Schubert, 1974; Lord *et al.*, 1982).
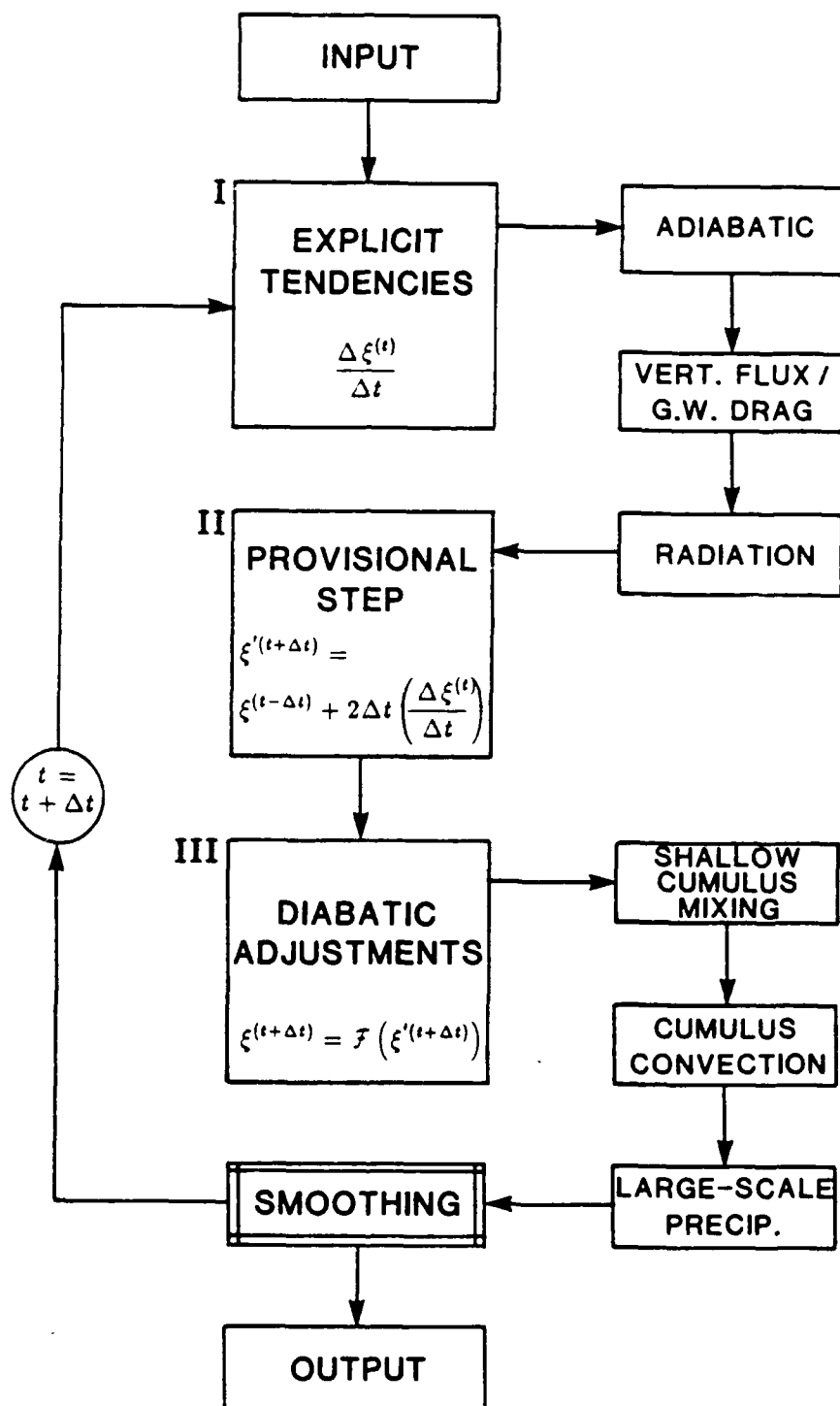
INPUT

I EXPLICIT
TENDENCIES

$$\frac{\Delta \xi^{(t)}}{\Delta t}$$

ADIABATIC

VERT. FLUX /
G.W. DRAG

RADIATION

$t = t + \Delta t$

II PROVISIONAL
STEP

$\xi'^{(t+\Delta t)} =$

$\xi^{(t-\Delta t)} + 2\Delta t \left(\dfrac{\Delta \xi^{(t)}}{\Delta t} \right)$

III DIABATIC
ADJUSTMENTS

$\xi^{(t+\Delta t)} = \mathcal{F} \left(\xi'^{(t+\Delta t)} \right)$

SHALLOW
CUMULUS
MIXING

CUMULUS
CONVECTION

SMOOTHING

LARGE-SCALE
PRECIP.

OUTPUT

Figure 2.1   Flow diagram depicting the sequence of adiabatic and diabatic
computations performed during each iteration of the NOGAPS
model. The three major steps outlined in the text are labeled I, II
and III.

This scheme is based on a theory that describes the interaction of an ensemble of cumulus clouds with the large-scale environment. The two most important features of the Arakawa-Schubert scheme are the quasi-equilibrium closure hypothesis and the allowance for a spectrum of cloud sizes at each grid point. Quasi-equilibrium assumes that the cloud ensemble reacts sufficiently rapidly to changes in the grid-scale flow that changes in the cloud work function (which is analogous to the positive area between the cloud parcels and their environment on a thermodynamic diagram) are minimized (Frank, 1983). In the NOGAPS spectral model, the quasi-equilibrium integral equation is solved using calculus of variations. Other improvements to the scheme used in the NOGAPS model include crude representations of the effects of ice physics in cloud anvils, and downdrafts caused by liquid water loading. The Arakawa-Schubert scheme has been shown to produce accurate rainfall rates in studies by Krishnamurti *et al.* (1980) and Lord (1982). Tiedtke (1984) showed that the Arakawa-Schubert scheme performs well over the tropical oceans.

Large-Scale Precipitation

The parameterization of large-scale, or "stable," precipitation is based on the relative humidity (RH) within each model layer. When RH exceeds 100%, moisture is rained out to the level below and the associated release of latent heat is distributed within the raining layer. The rain is evaporated in the layer below until RH exceeds 100% there as well, at which point the process repeats itself and continues in successively lower layers provided that each of these layers becomes supersaturated. An exception is made in the lowest model layer where all liquid water reaching this layer is assumed to reach the ground as well.

Shallow Cumulus Mixing

The effects of convective mixing by non-precipitating shallow cumulus clouds are parameterized according to Tiedtke (1984). The net result of this process is a vertical mixing of moisture and potential temperature from the top of the shallow cumulus layer to the surface. In the NOGAPS model, the necessary conditions for this mixing to occur are:

1. RH $\geq$ 70% in the lowest layer,

2. a negative air-surface temperature difference; *i.e.*, the vertical fluxes must be directed upward from the surface,

3. the presence of a moist unstable layer somewhere in the bottom 250 mb (bottom five or six σ-levels) of the model, and

4. the presence of the surface lifted condensation level somewhere in the bottom 250 mb of the model.

This scheme has been successful in producing a more realistic distribution of moisture in the lowest levels, and in augmenting the inversion above the trade wind moist layer.

Radiation

The effects of radiational forcing are parameterized according to the formulation of Harshvardhan *et al.* (1987) that was obtained from the National Atmospheric and Space Administration (NASA) Goddard Space Flight Center. The effects of both short-wave and long-wave radiational forcing are modeled, and a diurnal cycle is included. Due to its relatively high computational cost,

the radiational forcing is computed every fifth time-step; *i.e.*, only once every two forecast hours. This two-hour radiational forcing value is then distributed evenly over the interim time steps. Thus, for example, the cosine form of the diurnal heating cycle is approximated as a series of step functions, each having two hours duration.

The short-wave formulation parameterizes the effects of absorption by water and ozone according to Lacis and Hansen (1974). In addition, Rayleigh scattering owing to ozone is modeled. Short-wave absorption by clouds is parameterized for scattered-to-scattered radiation according to Sagan and Pollack (1967), and for direct-to-scattered radiation according to Coakley and Chylek (1975). The latter effect is computed as a function of the solar zenith angle. The long-wave radiation scheme includes broadband absorption in four bands; there are two bands for water and one each for ozone and carbon dioxide. The clear-sky radiation between model layers is decreased according to a calculation of the probability of a clear line-of-sight. The version of the NOGAPS model used in this study does not include a cloud-radiation interaction scheme. It may be noted that such a scheme has been introduced in the Navy's current operational model (NOGAPS 3.1) and has improved the predicted convective rainfall amounts substantially.

2.2 Numerical Procedure

As discussed in Chapter 1, much of the existing work on the effects of tropical forcing on the general circulation has focused on changes that occur on seasonal, or even annual, time-scales. In contrast, *the focus of this study will be on understanding the near-term impact of anomalous tropical diabatic forcing on*

the dynamics of midlatitude flow. Here, the phrase "near-term" refers to time-scales rang. ., from one week to one or two months. Although this may seem to be a rather broad definition in absolute terms, it represents a relatively narrow time-scale compared with those most often associated with tropical-midlatitude interactions. The experimental approach that will be used to examine tropical-midlatitude interactions in the present study will be to analyze the response of the NOGAPS spectral model to imposed SST anomalies in the tropical Pacific Ocean. In accordance with the discussion above, we will be interested primarily in changes that occur within, or slightly beyond, the range of useful predictability in current atmospheric forecast models. Thus, they may have a crucial impact on our ability to predict the global circulation for any extended pe iod of time.

The data set for this study is obtained from two separate cases involving a total of four pairs of 50-day runs with the NOGAPS model; *i.e.*, there are two pairs of simulations associated with each case. Based, in part, on the discussion above, it was decided that 50-day runs would be adequate in the present study. Each pair of runs consists of a control run and an anomaly run. The control and anomaly runs differ only in that, in the latter, a localized positive SST anomaly is added to the initial climatological SST values. In the first set, the SST anomaly is located in the eastern Pacific Ocean, and in the second, the SST anomaly is located in the western Pacific Ocean. Henceforth, these simulations will be referred to as the ESSTA and WSSTA simulations, respectively. In both the control and anomaly runs, the SST values are held constant throughout the simulations. From a physical point of view, this seems reasonable considering the time-scale of interest in this study. With regard to implications for

numerical modeling, we may think of the steady anomalous forcing (most of which is associated with the increased convective heating resulting from the higher SST's) in terms of a systematic error in the model-predicted tropical forcing at some location. It should be noted here that, although there remains much uncertainty regarding the effect of the longitudinal position of the SST anomaly on the response pattern, it is not the aim of this study to make a detailed comparison between the ESSTA and WSSTA simulations. Rather, the results of both simulations will be examined to check the consistency of the conclusions drawn from the results, and to point out uncertainties in these conclusions where appropriate.

The control run for the first pair of integrations in each simulation was started from initial conditions based on the NOGAPS analysis from 12 UTC on 15 December 1985, along with the corresponding climatological SST values for this date. The control run for the second pair of integrations in each simulation was started from initial conditions based on the NOGAPS analysis from 12 UTC on 13 December 1987, along with its corresponding SST climatology. In keeping with the premise in Chapter 1 that tropical-midlatitude interactions occur regularly in the atmosphere and play an integral part in the global circulation, it should be noted that the selection of these two particular sets of initial conditions was based solely on their availability, and not on any *a priori* knowledge concerning the outcome of the simulations. In fact, it should be noted that data from these periods was used to test and evaluate the NOGAPS spectral model during its operational implementation, and was used, in part, because it appeared to represent typical Northern Hemisphere wintertime conditions.

In the ESSTA simulation, the anomaly runs in each pair were started from the same initial conditions as the corresponding control runs, except that the climatological SST values in the eastern Pacific Ocean were perturbed positively as shown in Figure 2.2a. The anomaly is symmetric about the equator, extending latitudinally from approximately 14° N to 14° S, and longitudinally from 90° W to 155° W. (This corresponds to an area on the NOGAPS transform grid extending 11 grid spaces in latitude and 26 grid spaces in longitude.) The magnitude of the anomaly increases from $+1°$ C at its outer boundary to $+3°$ C at its center. In the WSSTA simulation, the climatological SST values in the anomaly runs in each pair of simulations were perturbed as shown in Figure 2.2b. The anomaly in this simulation has the same horizontal structure and magnitude as the one used in the ESSTA simulation, but is positioned longitudinally between 105° E and 170° E. The horizontal structure and magnitude of the SST anomalies in Figure 2.2 are very similar to those used by Keshavamurty (1982), who used a nine-level, global, spectral primitive equation model to study the effects of an SST anomaly in the central Pacific Ocean. Generally speaking, the horizontal structure and magnitude of the anomalies used in this study are comparable with those used in other modeling studies, such as those by Julian and Chervin (1978) and Shukla and Wallace (1983). A review of the different types of SST anomalies used in these and other studies is given by Shukla and Wallace (1983).

The 50-day simulations were carried out on the Cyber 205 computer at Fleet Numerical Oceanography Center (FNOC). The NOGAPS model required 550–600 seconds of computer time per forecast day; the time varied mostly in response to the number of times it was necessary to call certain physical
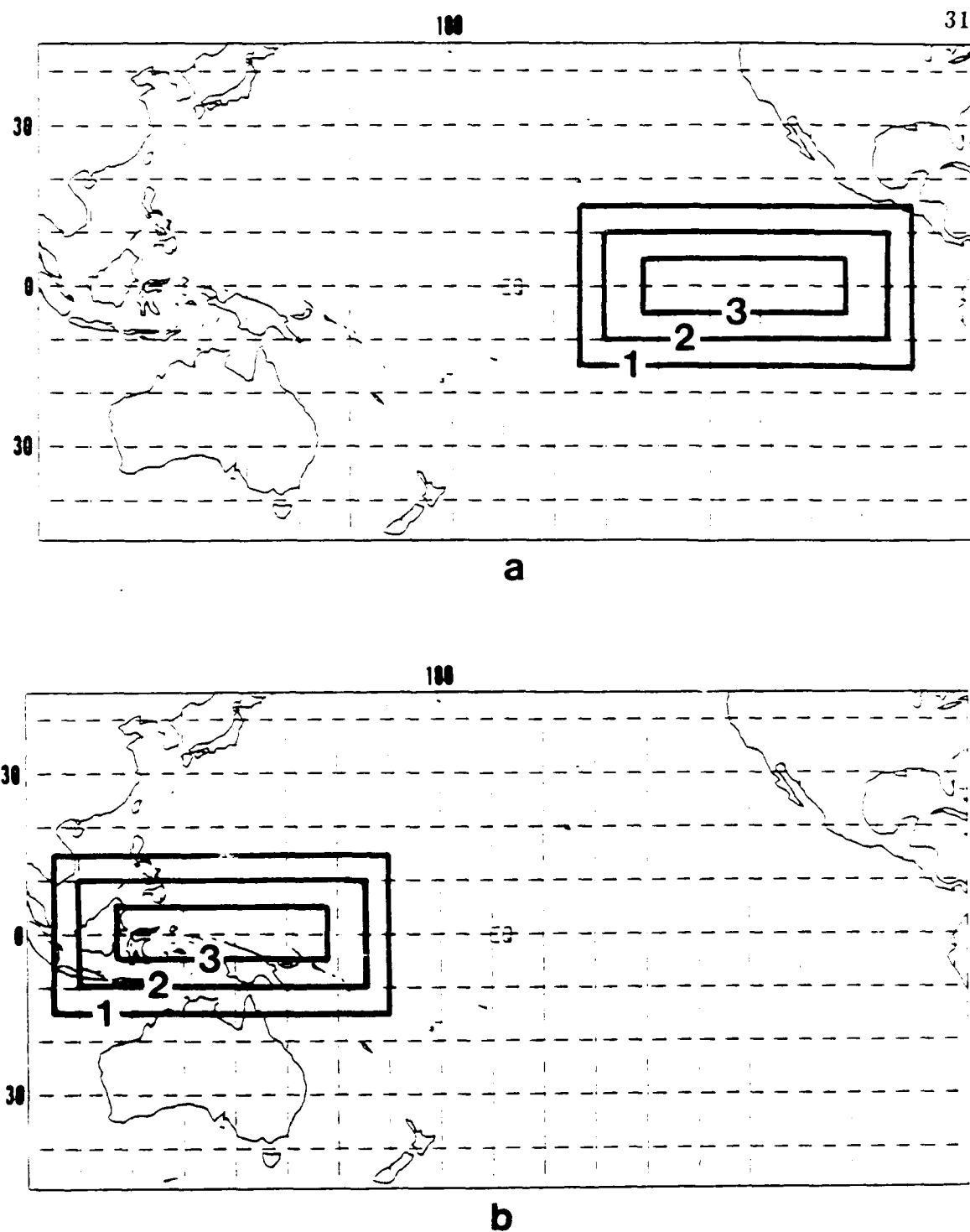
Figure 2.2   Schematic representations of the positive temperature anomalies
added to the climatological SST values in the anomaly runs of the
(a) ESSTA and (b) WSSTA simulations. The outermost contour
encloses a region of 1° C anomalous warming, while the innermost
contour encloses a region of 3° C anomalous warming.

parameterization schemes during a particular forecast. The forecast data were output to a "model history file" at 24-hr intervals, beginning with the initial conditions at 12 UTC for each case. The output data represents the instantaneous values of the fields at 12 UTC on each day of the simulation. Most of the data are output in the form of spectral coefficients, including those for each of the prognostic variables (vertical vorticity ς, horizontal divergence D, potential temperature θ, specific humidity q, and surface pressure p_*) as well as those for certain physical heating rates such as radiative, cumulus, and total diabatic heating. Actually, at each output time t, the spectral coefficients for the prognostic variables were saved from the two most recent time steps (i.e., times t and $t - \Delta t$) so that the model could be stopped and restarted at any point during the forecast without loss of continuity. This allowed each 50-day simulation to be divided into several shorter simulations, which helped to ease the considerable data management task, and to alleviate the strain on computational resources at a given time. It is clear that events having periods less than 24 hours are not resolvable in these data sets since the spectral coefficients were saved only once per forecast day. However, for the phenomena of interest in this study, we might expect there to be little variance associated with periods less than a few days (Hoskins et al., 1983).

For each simulation, "composite" control and anomaly data sets were formed by averaging the history file data for various numbers of days from both sets of initial conditions. Thus, for example, a 30-day mean composite control data set is based on 60 days of data—30 from the control run of 12 December 1985, and 30 from the control run of 13 December 1987. Most of the results that will be discussed in the following sections are based on the *differences* between

the composite control and anomaly data sets. The use of composite data is a standard practice in modeling studies of this type (see references in Section 1.2) because these data tend to highlight statistically significant features in the flow. From this point of view, it would have been preferable to consider more cases than the two used here in each simulation. However, as discussed in Section 1.2, this would have been impractical in the present study since it was decided to perform the analysis using as realistic a model as possible.

2.3 The Time-Mean Response

Many of the general characteristics of the time-mean atmospheric response to anomalous tropical forcing are well known and have been noted in both observational and modeling studies (*e.g.*, Horel and Wallace, 1981; Wallace and Gutzler, 1981; Blackmon *et al.*, 1983; Shukla and Wallace, 1983). Despite the variability among the results of these and other studies, there appear to be certain features in the anomalous response that are often present to some degree, even though the characteristics of the forcing anomaly may vary substantially from case to case. For example, among the most consistently observed features of the atmospheric response to tropical SST anomalies are changes in the magnitude of the Walker circulation and a redistribution of the convective precipitation maxima in the tropics, and to a lesser extent, the recurrence of certain standing wave patterns, such as the PNA pattern, in the extratropics. With the benefit of this *a priori* knowledge as a background, and with the dynamical framework discussed in Section 1.1 for interpreting tropical-midlatitude interactions, it will be useful to examine some of the general characteristics of the time-mean responses in the ESSTA and WSSTA

simulations described in Section 2.2. In addition to revealing some of the synoptic changes caused by the anomalous forcing in these simulations, this discussion serves as a comparison between the present results and those from previous studies discussed in Section 1.2. This comparison is particularly relevant for enhancing the degree of confidence in the results of the present study since we consider only a limited number of cases in each simulation.

In this study, the time-mean response will be represented by the composite 30-day average of the fields for days 21–50 in each simulation. The averaging was begun at day 21 in order to give the NOGAPS model sufficient time to approach an approximate state of balance. This will be verified in Chapter 3, where we examine the temporal evolution of the anomalous response. We may recall from Section 2.2 that the composite fields in each simulation consist of the combined results from two separate Northern Hemisphere wintertime cases. Unless otherwise stated, all of the results that will be shown in the following sections are based on the composite data from these two cases. For most of the fields considered in this section, we will examine the control run as well as the differences between the control and anomaly runs. The control fields are shown to ensure that the time-mean behavior of the unperturbed NOGAPS simulations is reasonable. We define the differences ξ_D between the control values ξ_C and the anomaly values ξ_A as $\xi_D = \xi_A - \xi_C$, so that a positive (negative) difference implies that the anomaly (control) values are greater.

2.3.1 The Tropical Response

Figures 2.3a-c show the 30-day mean 12-hr accumulated precipitation at 12 UTC over the Pacific Ocean for the control simulation and for the differences

between the control and anomaly runs in the ESSTA and WSSTA simulations, respectively. That is, the precipitation amounts in each figure correspond to the average amounts for the 12-hr period ending at the model output time on each day of the simulation.[2] The minimum contour in these figures is 0.1 in/12 hrs and there are contours every 0.2 in/12 hrs thereafter. The precipitation patterns in the control run (Figure 2.3a) are rather typical for the tropical Pacific Ocean during the Northern Hemisphere winter. There is a well defined inter-tropical convergence zone (ITCZ) centered near $5 - -10°$ N that spans most of the Pacific Ocean, with precipitation rates greater than 0.1 in/12 hrs. The location and strength of this feature seem reasonable for the middle of winter in the Northern Hemisphere. There are also locally larger maxima over the maritime continent and near the extreme west coast of South America. The precipitation rates in these regions are greater than 0.6 in/12 hrs and 0.4 in/12 hrs, respectively.

The 30-day mean differences between the anomaly and control runs in the ESSTA simulation are shown in Figure 2.3b. Although the difference field for this simulation is spotty in general, there is a localized positive anomaly of greater than 0.1 in/12 hrs in the east-central Pacific Ocean just south of the equator between 120° W and 150° W, and negative anomalies to the northeast and northwest. Note that the contour interval for the difference fields in this figure is one fourth of that used for the control run, or 0.05 in/12 hrs. The negative anomalies are roughly equal in magnitude to the positive anomaly, and

---

[2] Unfortunately, the precipitation amounts in the NOGAPS model are only quantified for 12-hr intervals before the "bucket" is emptied and the measuring process begins again. This makes it difficult to obtain more conventional precipitation measures such as the the actual 24-hr rainfall rate, which has no semi-diurnal bias.
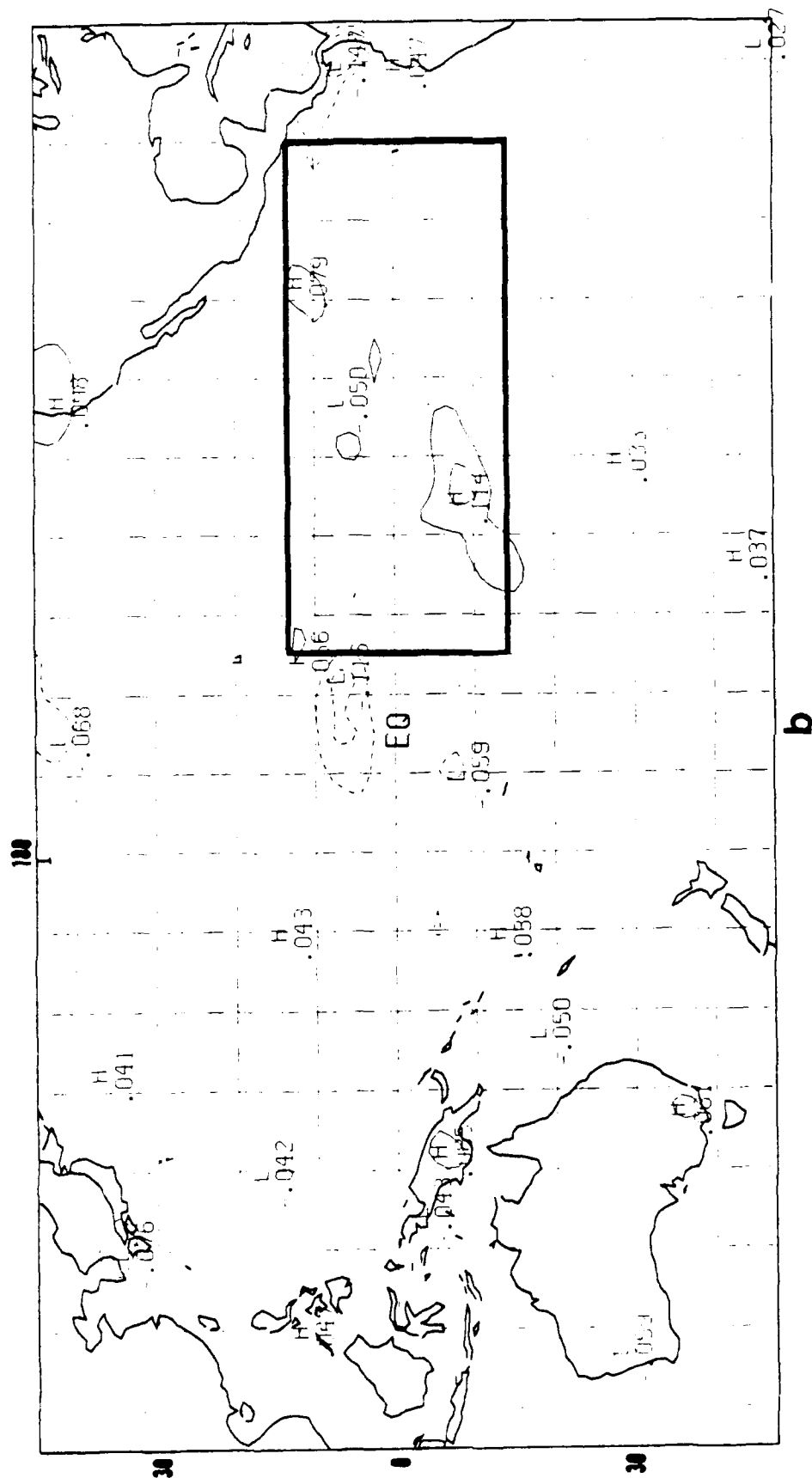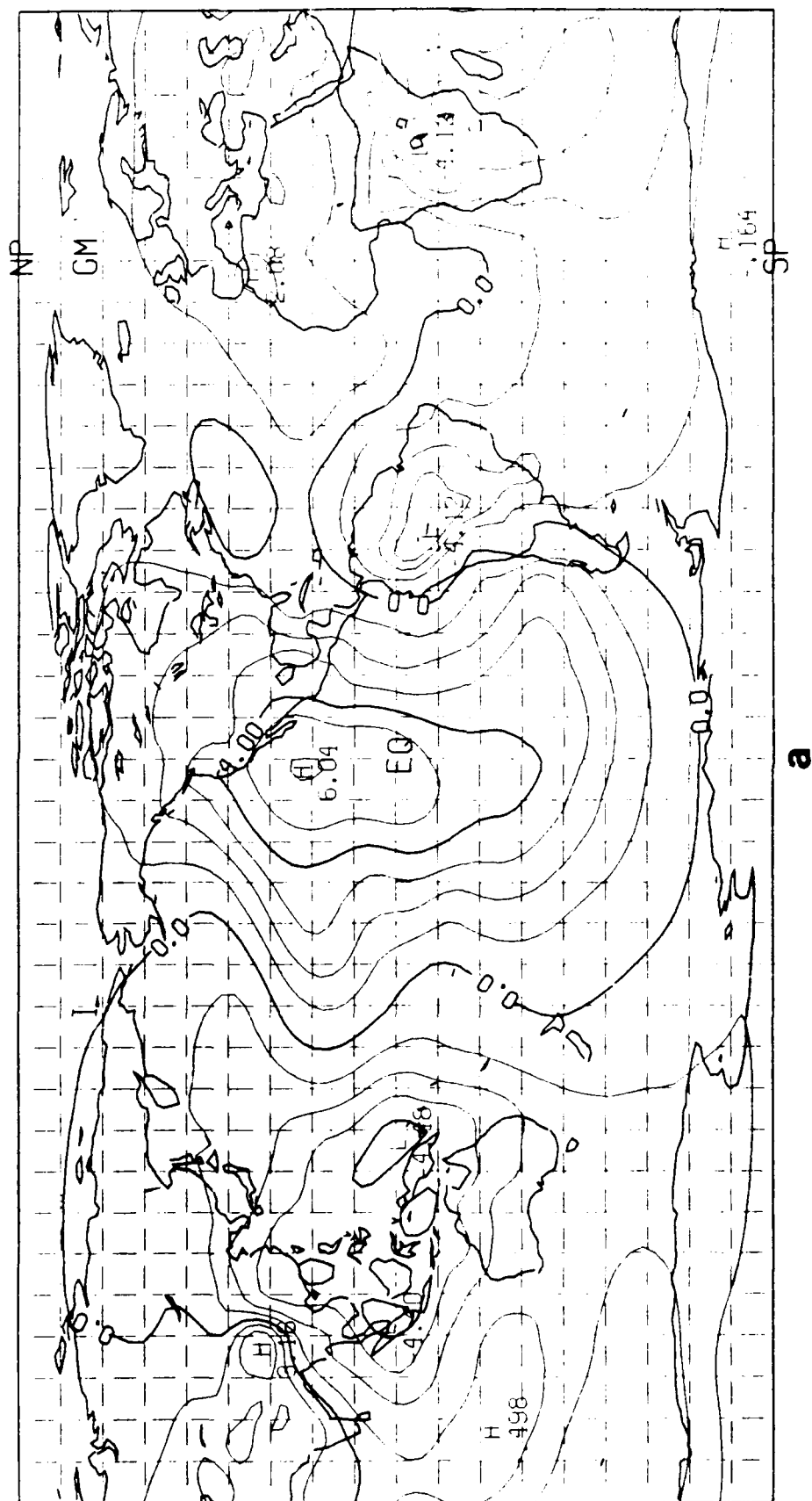
a

Figure 2.3 The 30-day mean 12-hr accumulated precipitation at 12 UTC over the Pacific Ocean for days 21–50 of the (a) control run, and for the difference between the anomaly and control runs in the (b) ESSTA and (c) WSSTA simulations. The minimum contour is 0.1 in/12 hr, with contours every 0.2 in/12 hr thereafter. Negative differences are denoted by dashed lines in (b) and (c), and the SST anomaly is indicated by the dark outline.

(continued on next page)

Figure 2.3 (continued)

Figure 2.3 (continued)

are located over Panama and to the east of the dateline. These results are physically reasonable in that the positive precipitation anomaly is located well within the region of increased SST (Figure 2.2a), while the negative precipitation anomalies are located just outside this region. There appear to be no significant changes in the western Pacific Ocean, except for a slight increase in precipitation over New Guinea.

In contrast to the ESSTA difference field, the WSSTA difference field in Figure 2.3c shows a much more dramatic anomalous response. In this case, the existing convective precipitation over the maritime continent in the control run (Figure 2.3a) has been enhanced substantially, especially over New Guinea and the extreme northeastern part of Australia. At the same time, there are negative precipitation anomalies over western South America and the eastern Pacific Ocean to the southwest of Mexico. This is consistent with the tendency for SST anomalies in the western Pacific Ocean to increase the strength of the Walker circulation with low-level easterlies over the central Pacific and upward motion over the maritime continent. This will be confirmed shortly when we examine the vector wind differences in this region. It should be noted that the differences between the magnitudes of the precipitation anomalies in the ESSTA and WSSTA simulations (Figures 2.3b,c) are not entirely unexpected since the western Pacific is one of the most convectively active regions in the world. Bjerknes (1969) proposed that the abundant precipitation associated with warm episodes in the western Pacific may be the result of increased moisture availability due to the higher climatological SST values in this region. At the same time, it should be mentioned that some of the differences between the two results may be related to the fact that the precipitation values shown in these

figures are based on 12-hr accumulations ending at 12 UTC. This would tend to favor the positive anomalies in the western Pacific where the measuring period extends over the nighttime and early morning hours when convective precipitation has its diurnal maximum.

In order to make a rough comparison with other studies, it is worth noting that if we assume that the magnitudes of the maximum 12-hr precipitation anomalies in the ESSTA and WSSTA simulations (which range from 0.1–0.24 in/12 hrs) are representative of those that occur over 24 hours, then we obtain values of 0.2–0.48 in/day, or approximately 5–12 mm/day. These values are comparable to those obtained by Keshavamurty (1982) and Blackmon *et al.*, (1983) who observed maximum values of 7 mm/day and 8.3 mm/day, respectively, in GCM studies of SST anomalies in the central Pacific.

The anomalous tropical precipitation patterns in Figure 2.3, and their implied longitudinal circulation anomalies, are strongly reflected in Figure 2.4, which shows the 30-day mean velocity potential χ at 150 mb for the control run and for the difference field in each simulation. These figures give an indication of the upper-level horizontal divergence associated with the convective outflow. The horizontal divergence is proportional to the Laplacian of the velocity potential so that the minimum values in these figures denote the regions of strongest divergence. The control run shown in Figure 2.4a shows the expected features of the time-mean flow, including strong upper-level divergence over the most convectively active regions in the tropics such as South America, Africa and the maritime continent. In addition, there is large-scale convergence over the central and eastern Pacific Ocean. The dipole pattern in the Pacific is consistent with the observations of Bjerknes (1969), who first noticed the
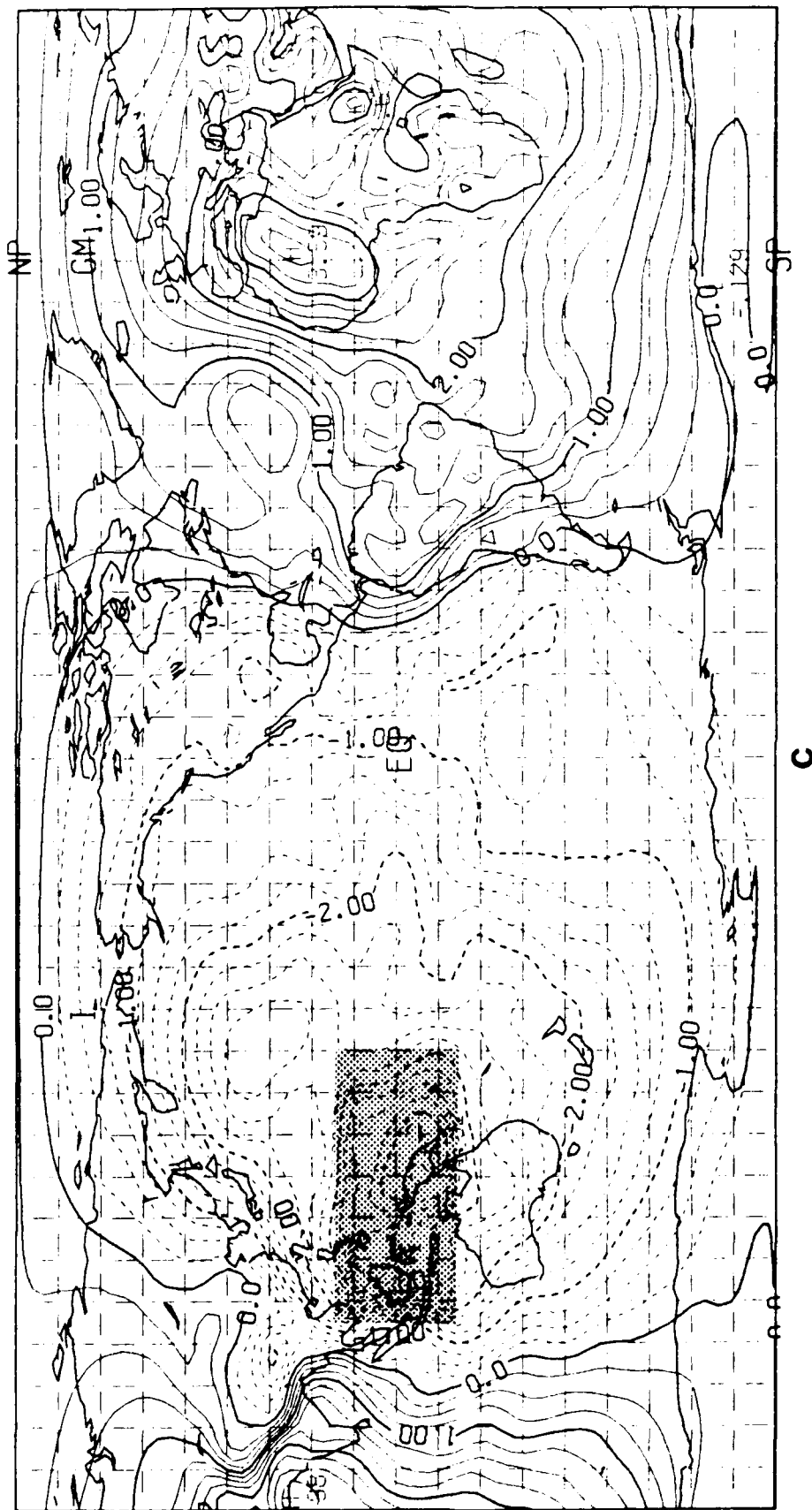
Figure 2.4 The 30-day mean velocity potential at 150 mb for days 21–50 of the (a) control run, and for the difference between the anomaly and control runs in the (b) ESSTA and (c) WSSTA simulations. The divergent (irrotational) component of the wind is directed perpendicular to the contours from lower to higher values. The contour interval is 1×10^6 m^2/sec in (a), and 0.25×10^6 m^2/sec in (b) and (c). Negative differences are denoted by dashed lines, and the SST anomaly is indicated by the stippled region. (continued on next page)

b

Figure 2.4 (continued)

Figure 2.4 (continued)

correlation between rising motion over the maritime continent and large-scale descending motion to the east.

The differences in the 30-day mean velocity potential in both simulations show that the most significant upper-level divergence occurs in the vicinity of the SST anomalies, with convergence in most other regions (Figures 2.4b,c). These results imply that, in both simulations, the convective activity has been enhanced in the region of the SST anomaly and suppressed in the surrounding regions. As with the precipitation anomalies in Figure 2.3, the anomalous upper-level divergence maximum appears to be a more localized phenomenon in the ESSTA simulation shown in Figure 2.4b. Based on this figure, we might expect the convection over the maritime continent to be suppressed in this simulation (i.e., there is anomalous upper-level convergence in this region), although this was not reflected in the precipitation anomaly in Figure 2.3b. In contrast, the maximum divergence anomaly in the WSSTA simulation (Figure 2.4c) is a larger-scale phenomenon that has a global dipole structure. Note that the maximum divergence in this figure is roughly collocated with, and equal in magnitude to, that in the control run over the maritime continent. These figures further indicate that the SST anomaly in the western Pacific Ocean has increased the strength of the existing Walker circulation in the tropics, while the SST anomaly in the eastern Pacific has increased the circulation in the opposite direction. A similar reversal in the anomalous Walker circulation was observed by Mechoso et al. (1988) who used the UCLA GCM to study the effects of SST anomalies in the eastern Pacific Ocean.

The anomalous longitudinal circulations implied by the vertical forcing in Figures 2.3b,c and 2.4b,c are plainly evident in Figures 2.5 and 2.6, which show

the 30-day mean vector wind differences between the control and anomaly runs in each simulation.

Figure 2.5 shows the vector wind differences at 925 mb and 200 mb in the ESSTA simulation. Restricting our attention to the tropics for the time being, we see that in Figure 2.5a there are anomalous westerlies at 925 mb over the equatorial central Pacific, indicating flow into the region of the SST anomaly that lies to the east. The maximum anomalies in this region are on the order of 5 m sec. There are also anomalous easterlies off the west coast of South America, indicating strong low-level convergence into the center of the SST anomaly. From continuity arguments, this is consistent with the strong upper-level divergence in this region shown in Figure 2.4b. As expected, the flow at 200 mb in Figure 2.5b shows anomalous easterlies over the equatorial central Pacific to the west of the maximum SST anomaly, indicating flow away from the SST anomaly at upper-levels. Again, this is consistent with the divergence pattern in Figure 2.4b and clearly demonstrates that the anomalous convective forcing in the eastern Pacific acts to oppose the existing Walker circulation.

The vector wind differences in the WSSTA simulation in Figure 2.6 are oriented in the opposite sense to those in the ESSTA simulation. Again restricting our attention to the tropics, we see that in Figure 2.6a there are anomalous easterlies at 925 mb over the equatorial central Pacific, indicating flow into the SST anomaly lying to the west. As in the ESSTA simulation, the maximum wind speed anomalies in this region are on the order of 5 m/sec. Note that the anomalous flow to the west and north of New Guinea shows that there is substantial convergence beneath the region of maximum upper-level divergence indicated in Figure 2.4c. The situation is reversed in Figure 2.6b,
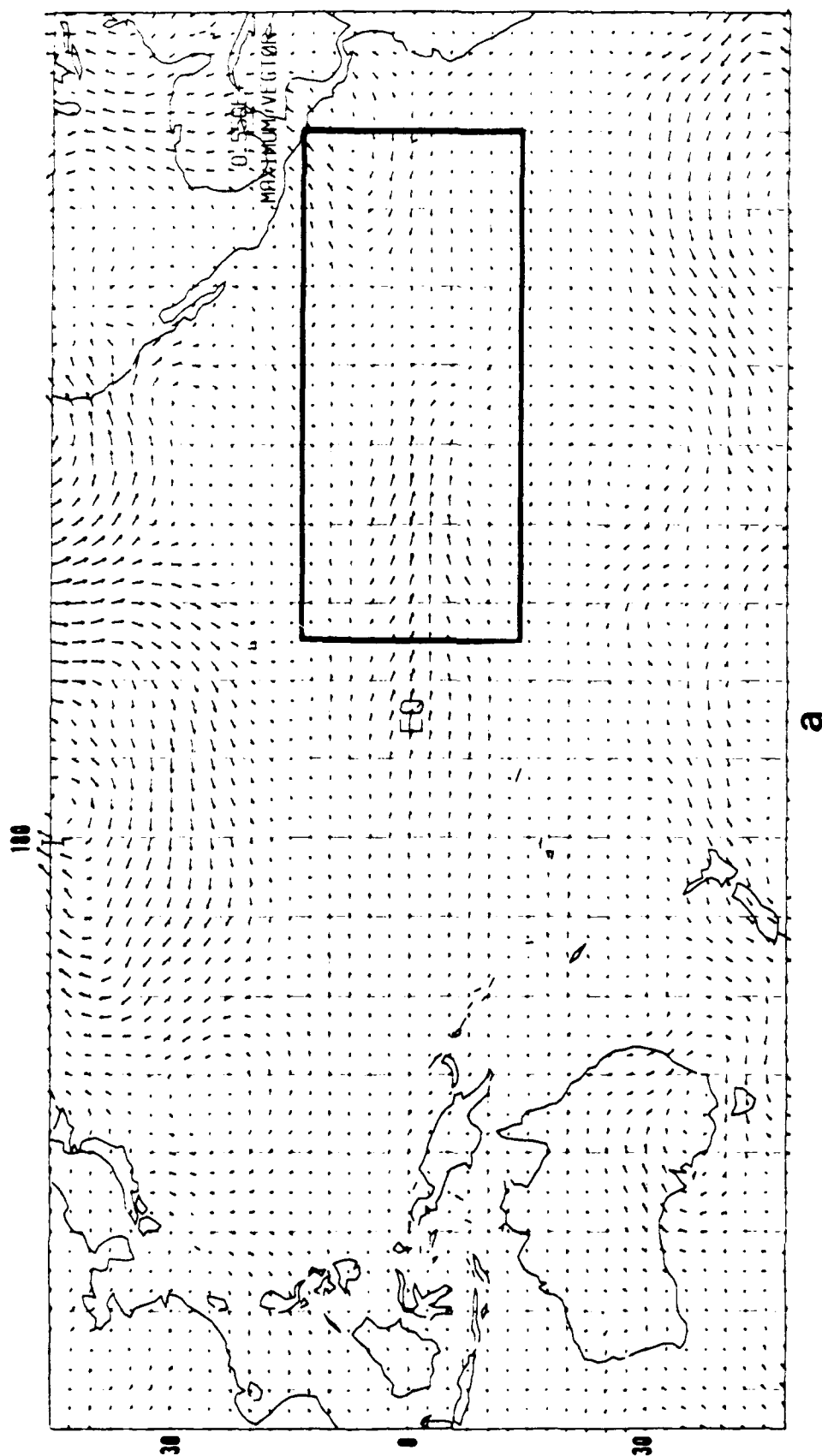
a

Figure 2.5 The 30-day mean vector wind differences between the anomaly and control runs over the Pacific for days 21–50 of the FSSTA simulation at (a) 925 mb and (b) 200 mb. The maximum vector length corresponds to a wind speed of approximately 6 m/sec in (a), and to a wind speed of approximately 14 m/sec in (b). The SST anomaly is indicated by the dark outline.
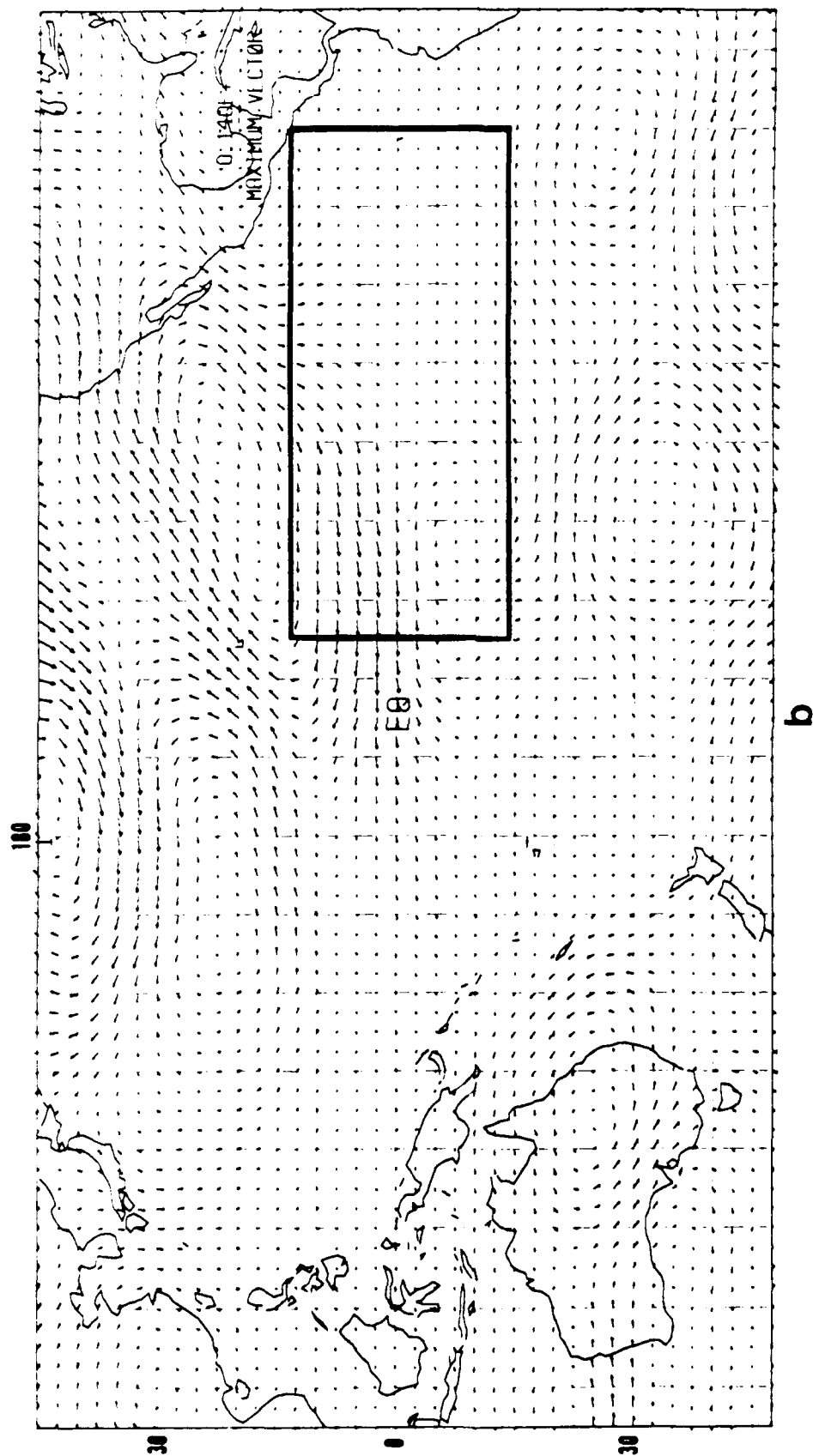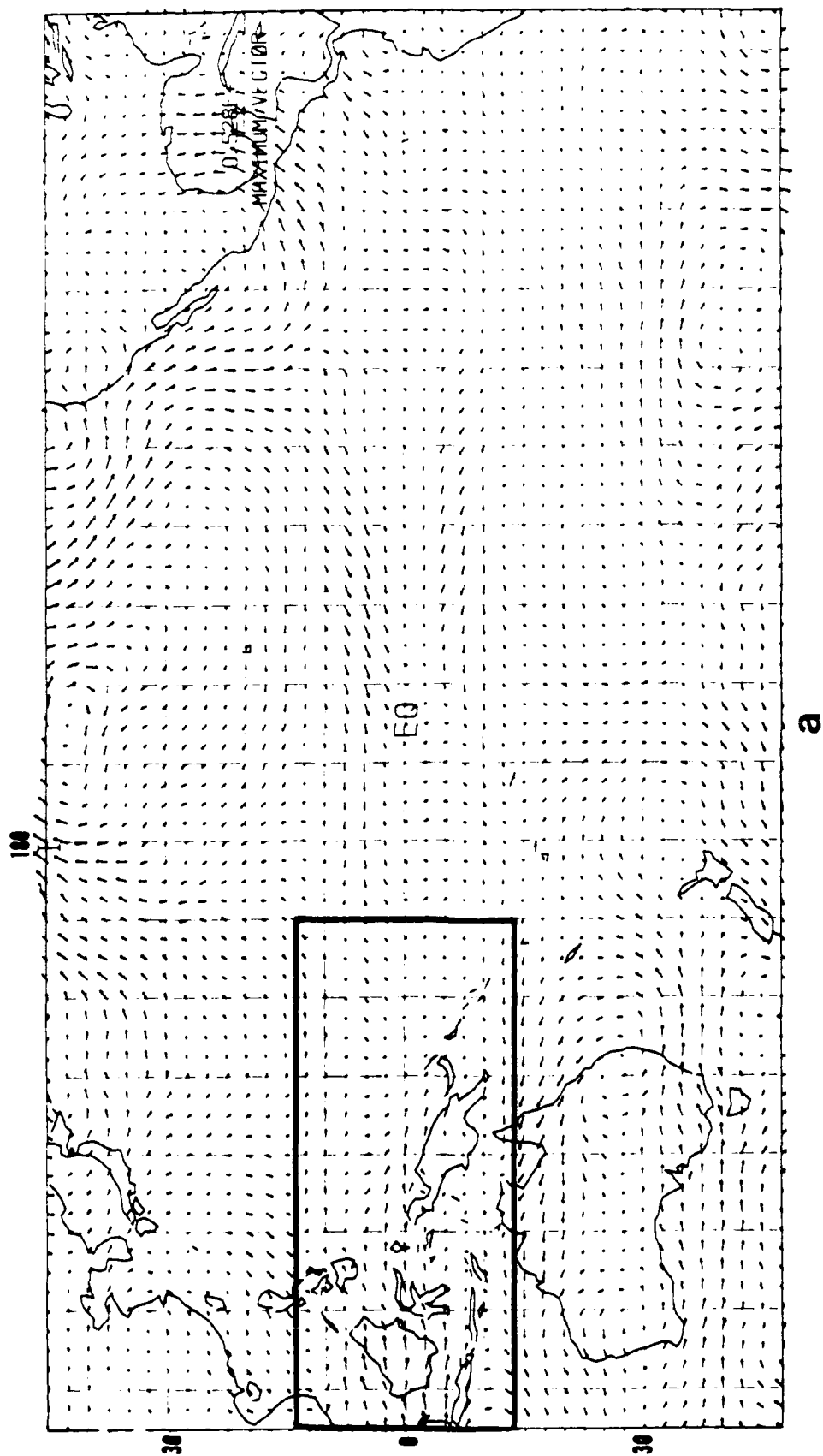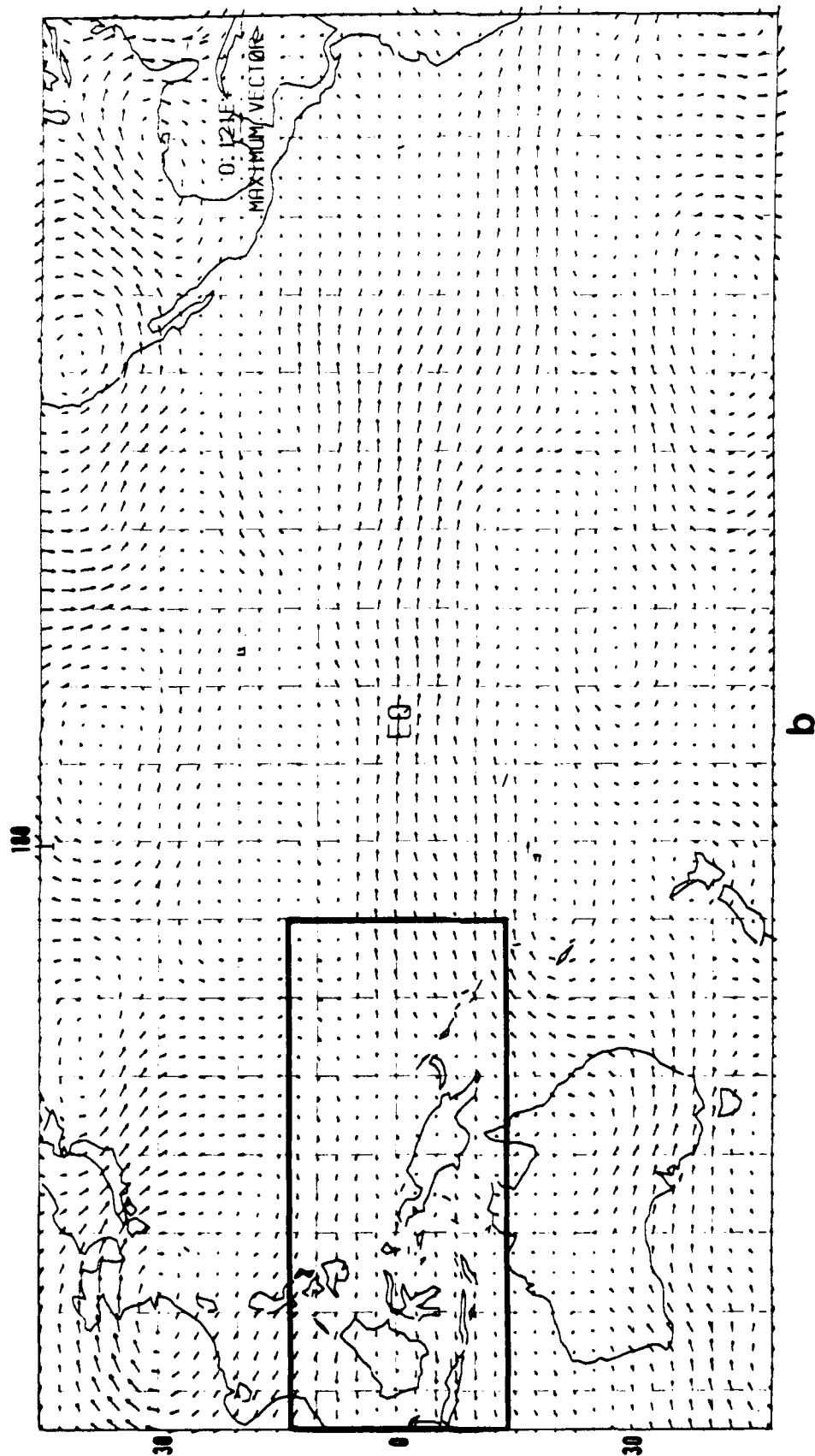
Figure 2.5 (continued)

MAXIMUM VECTOR

EQ

a

Figure 2.6 As in Figure 2.5, except for the WSSTA simulation. Here, the maximum vector length corresponds to a wind speed of approximately 5 m/sec in (a), and to a wind speed of approximately 12 m/sec in (b).

Figure 2.6 (continued)

which shows the anomalous flow at 200 mb in the WSSTA simulation. At this
level, the flow is divergent over New Guinea and there are strong westerlies on
the order of 12 m sec extending across most of the equatorial Pacific. The
band-like structure and negligible meridional velocity component of the wind
anomalies in this figure are consistent with equatorially trapped Kelvin waves,
which are low-frequency eastward propagating gravity waves. These results are
qualitatively similar to those obtained in the idealized modeling study of
Webster (1972). Using a two-level linear model, Webster interpreted a similar
type of response to the east of an equatorial heat source in terms of Kelvin
waves. His results were reproduced in other idealized modeling studies such as
those by Gill (1980), Silva Dias *et al.* (1983) and Lim and Chang (1983). Again,
note that the results in Figures 2.6a and 2.6b confirm that the SST anomaly in
the western Pacific has strengthened the usual sense of the Walker circulation.

It is interesting to note that there is a significant difference between the
vertical structures of the tropical and midlatitude wind anomalies in Figures 2.5
and 2.6. The vertical structure of the tropical wind anomalies described above is
consistent with the cellular, or baroclinic type of response discussed in
Section 1.1, in which the flow is in opposite directions at upper and lower levels.
As pointed out in Section 1.1, this vertical structure is typical of tropical
motions, and is associated with medium-depth internal vertical modes that tend
to be equatorially trapped by the Coriolis force. This will be confirmed by the
normal mode analysis performed in Chapter 3. In contrast, the midlatitude
wind anomalies in these figures have the same sign at both levels. For example,
in Figure 2.5 there is an anomalous anticyclonic circulation centered to the east
of the date line at approximately 40° N (extreme top center of the figure) in

which the flow is clearly oriented in the same direction at both 925 mb and 200 mb. This feature also appears in approximately the same location in Figure 2.6. Here again, the circulation is in the same sense at both levels. Similar features can be seen at other locations in the midlatitudes in the Northern and Southern Hemisphere in each figure. The vertical structure of these anomalies is consistent with there being a barotropic type of response, as discussed in Section 1.1, in which the flow remains relatively constant throughout the depth of the troposphere. We may recall that this type of response is associated with extremely deep vertical modes that can propagate into the midlatitudes as shown schematically in Figure 1.1. The structure of the midlatitude anomalies will be examined in more detail in the following section.

2.3.2 The Midlatitude Response

Figure 2.7 shows the 30-day mean geopotential height field at 300 mb for the control run and for the differences between the control and anomaly runs in the ESSTA and WSSTA simulations. As shown by the composite control run in Figure 2.7a, the main features of the time-mean Northern Hemisphere wintertime flow are generally well represented during this 30-day period. In particular, the zonal asymmetries in the Northern Hemisphere height field indicate that the major midlatitude jets are reasonably well positioned along the east coasts of Asia and North America. As expected, the East Asian jet is somewhat stronger than the North American jet, although the longitudinal extent of the former appears to be exaggerated. The strong ridge along the west coast of North America is also reasonably positioned. In contrast, there is relatively little zonal asymmetry in the Southern Hemisphere midlatitude height

field during this period. as expected. Finally. there appears to be some noise in the central and eastern tropical Pacific Ocean.

The 30-day mean differences between the 300 mb height fields in the control and anomaly runs in each simulation are shown in Figures 2.7b and 2.7c. In both simulations. the anomalous tropical forcing leads to a remarkably strong remote (*i.e.*, midlatitude) response. The magnitudes of the anomalies are generally comparable to those found by other investigators such as Blackmon *et al.* (1983) and Shukla and Wallace (1983), and more recently by Mechoso *et al.* (1987), although the present values may be slightly greater owing to the shorter averaging period used in this study. Note that the magnitudes of the anomalies are generally greater in the Northern Hemisphere, especially for the WSSTA simulation in Figure 2.7c. This is consistent with the findings of Simmons (1982) and Webster (1982), among others, who demonstrated that the strength of the remote response depends on the mean westerly wind in the subtropics, and thus, is usually strongest in the winter hemisphere. Based on these results, and for the sake of brevity, we will focus the remainder of this discussion on the Northern Hemisphere anomalies.

Figures 2.8 and 2.9 are polar stereographic projections of the Northern Hemisphere height anomalies at 300 mb and 700 mb in each simulation. Restricting our attention to the 300 mb anomalies for the time being (Figures 2.8a and 2.9a), we see that in both simulations, the largest anomalies occur in the vicinity of North America and its surrounding waters, although there are some substantial anomalies over Europe as well. The anomalies over North America in both simulations form arcing patterns of alternating highs and lows that are suggestive of the PNA teleconnection pattern described by
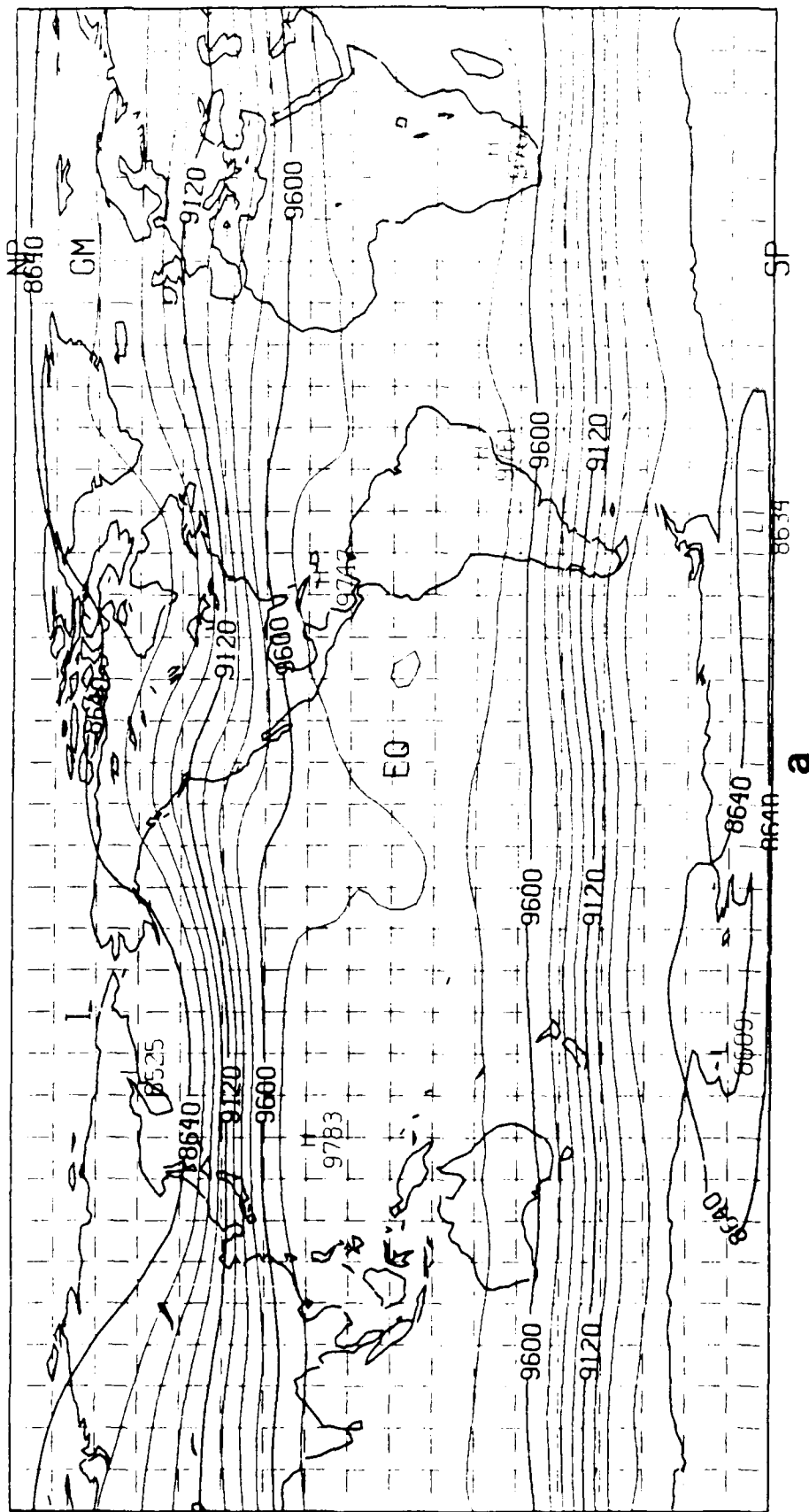
Figure 2.7 The 30-day mean geopotential height field at 300 mb for days 21-50 of (a) the control run, and for the differences between the anomaly and control runs in the (b) ESSTA and (c) WSSTA simulations. The contour interval is 120 m in (a), and 30 m in (b) and (c). Negative differences are denoted by dashed lines, and the SST anomaly is indicated by the stippled region.
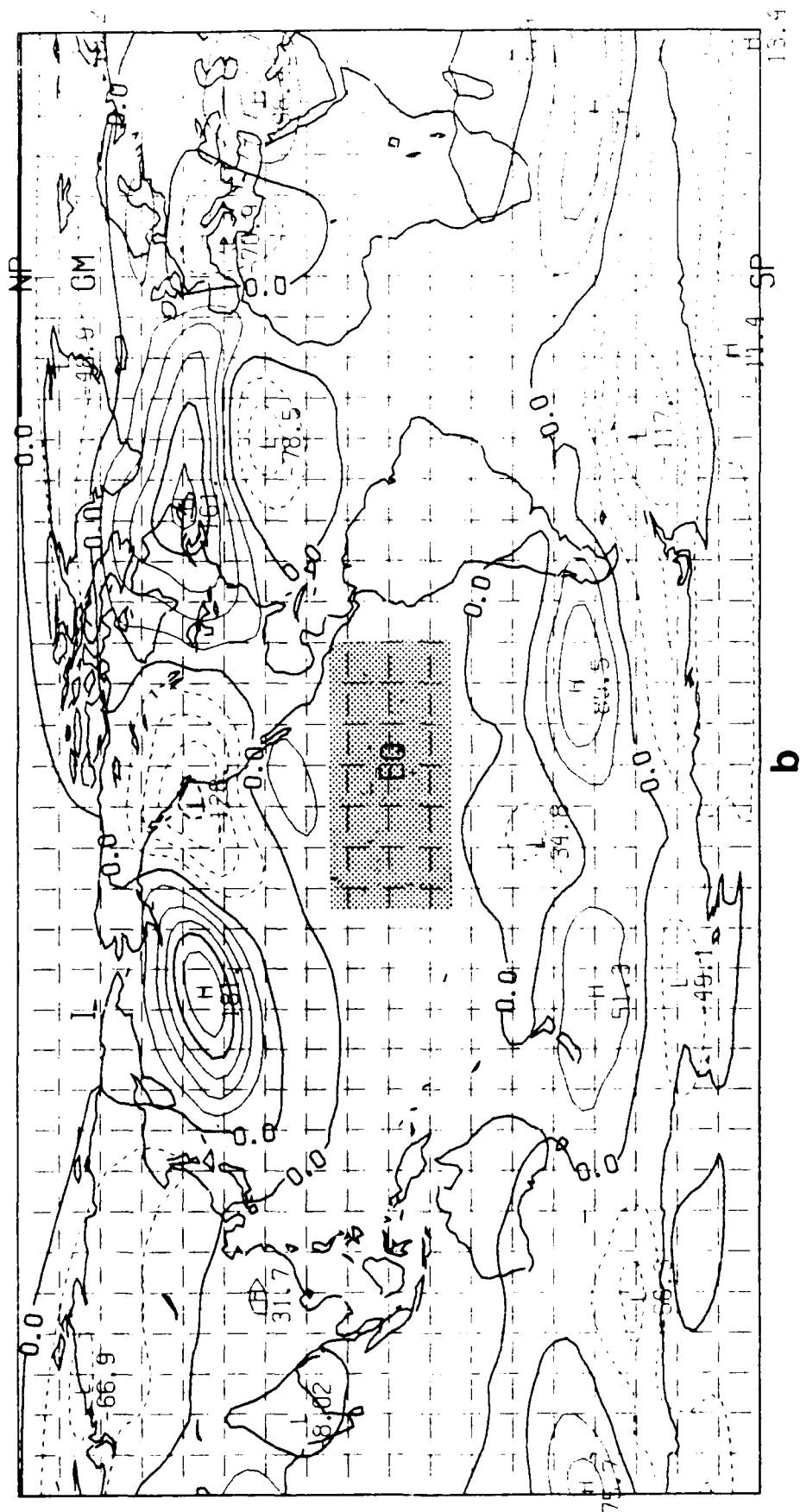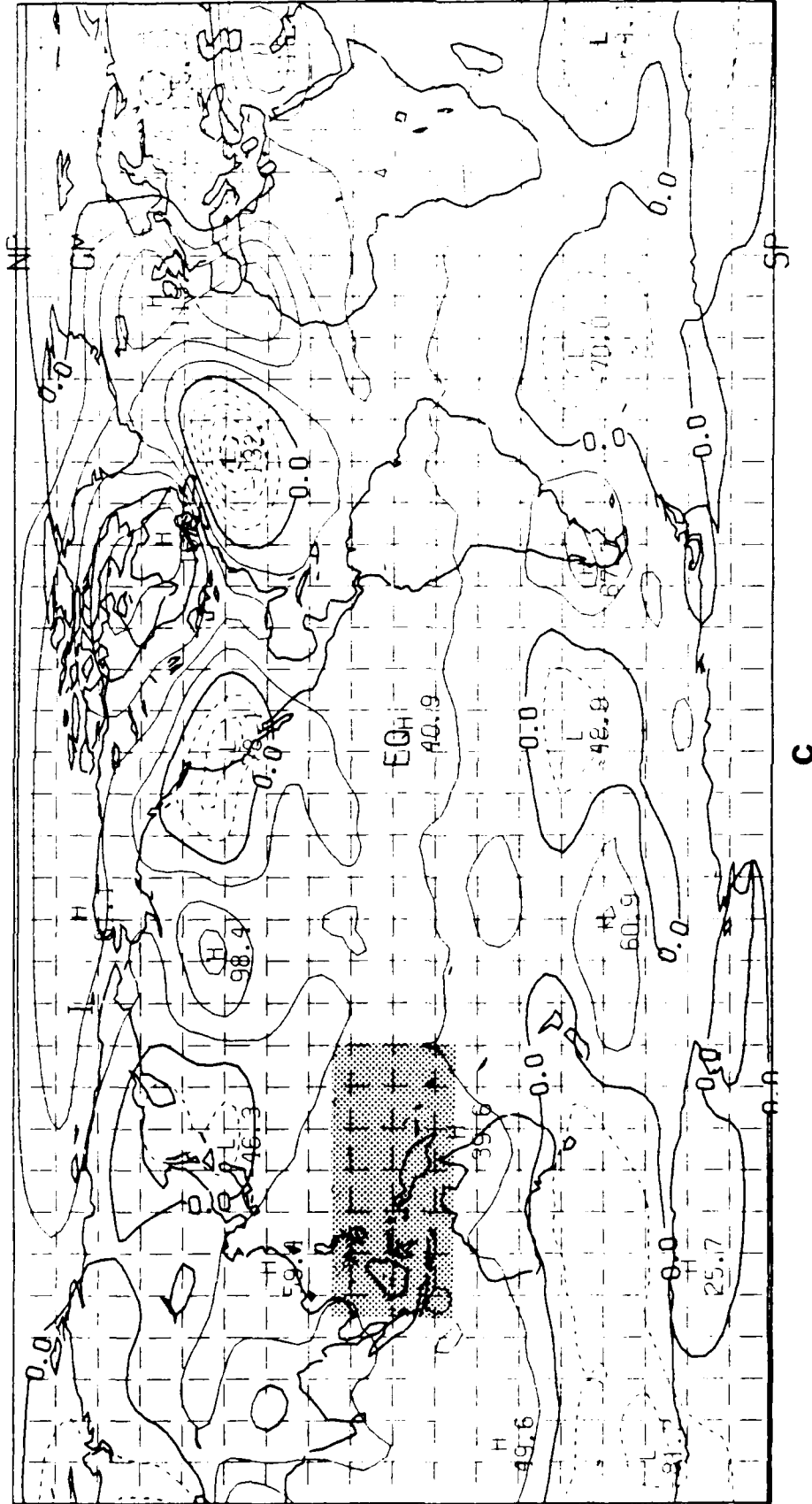
Figure 2.7 (continued)

Figure 2.7 (continued)

Horel and Wallace (1981), and shown schematically in Figure 1.1. This pattern is especially evident in the WSSTA simulation in Figure 2.9a. The anomaly pattern in this figure (including the response over Europe) is very similar to that in Figure 11 of Shukla and Wallace (1983), who examined the response of the GLAS climate model to the composite SST anomaly of Rasmusson and Carpenter (1982). The anomalies in the ESSTA simulation in Figure 2.8a resemble a PNA pattern that has been shifted eastward.

The fact that the general forms of the patterns are similar in the ESSTA and WSSTA simulations reflects a certain amount of insensitivity to the longitudinal position of the SST anomaly. As mentioned in Chapter 1, this behavior has been observed in studies with both idealized models and GCM's, and may be due to the horizontal shear of the mean westerly wind. At the same time, it should be noted that the differences between the two patterns in these figures are consistent with the findings of other investigators, such as Simmons *et al.* (1983), Geisler *et al.* (1985) and Palmer and Mansfield (1986), who found that the magnitude of the classical PNA response pattern is greatest when the SST anomaly is located in the western Pacific.

The equivalent barotropic structure of the time-mean response in the midlatitudes is revealed by comparing the height anomalies at 300 mb with the corresponding anomalies at 700 mb in Figures 2.8b and 2.9b. It is clear from these figures that the anomalies at both levels are in phase with one another and have amplitudes that increase with height. For example, the three major anomalies surrounding North America in the WSSTA simulation in Figure 2.9 occur in roughly the same locations at 700 mb as they do at 300 mb, but their amplitudes at 300 mb are larger by at least 50%. In particular, the amplitude of
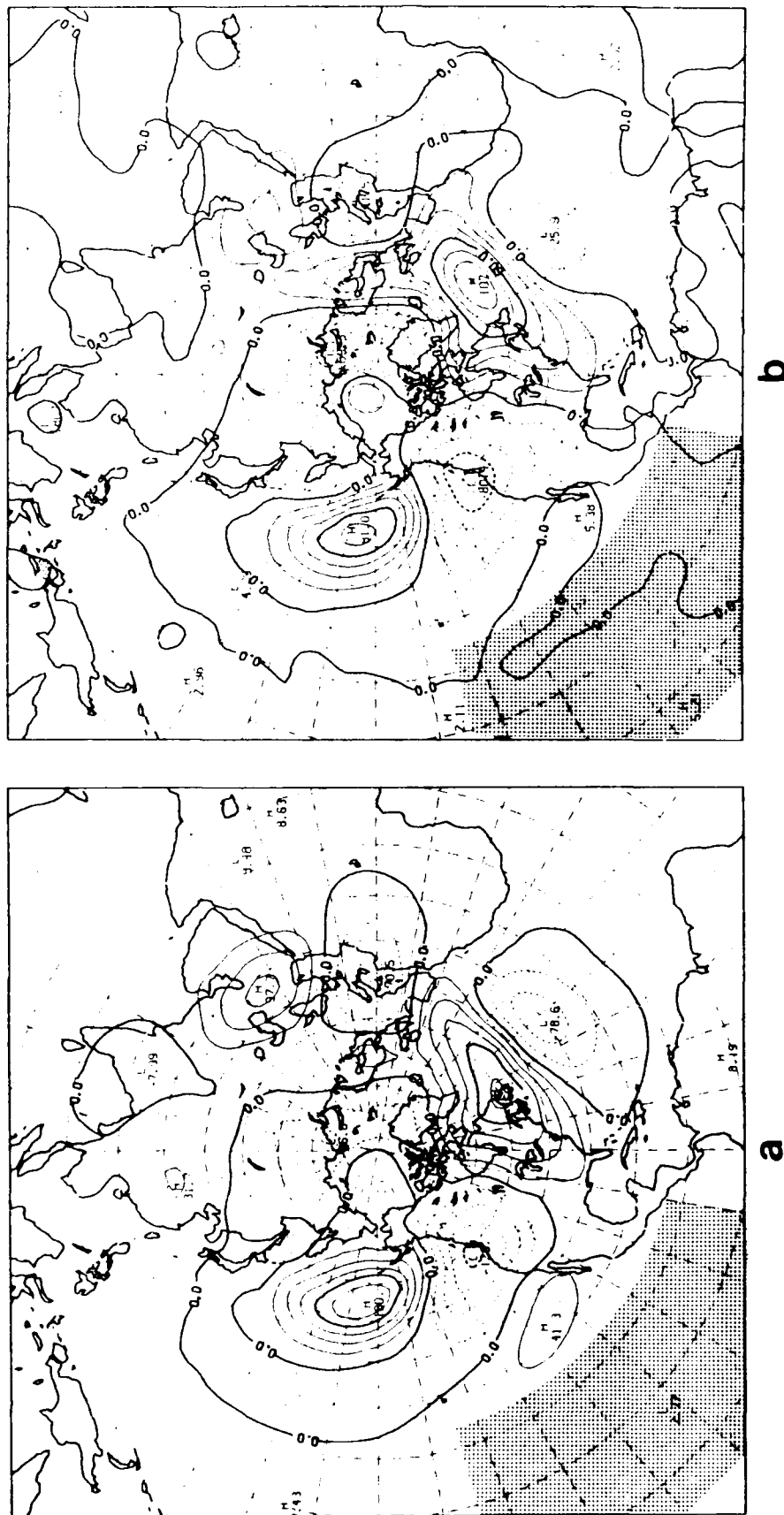
57

Figure 2.8 Polar stereographic projection of the 30-day mean Northern Hemisphere geopotential height anomalies from days 21–50 of the ESSTA simulation at (a) 300 mb and (b) 700 mb. The equivalent barotropic structure of the anomalies is indicated by their similar phases at upper and lower levels. The contour interval is 30 m, with negative anomalies denoted by dashed lines, and the SST anomaly, by the stippled region.
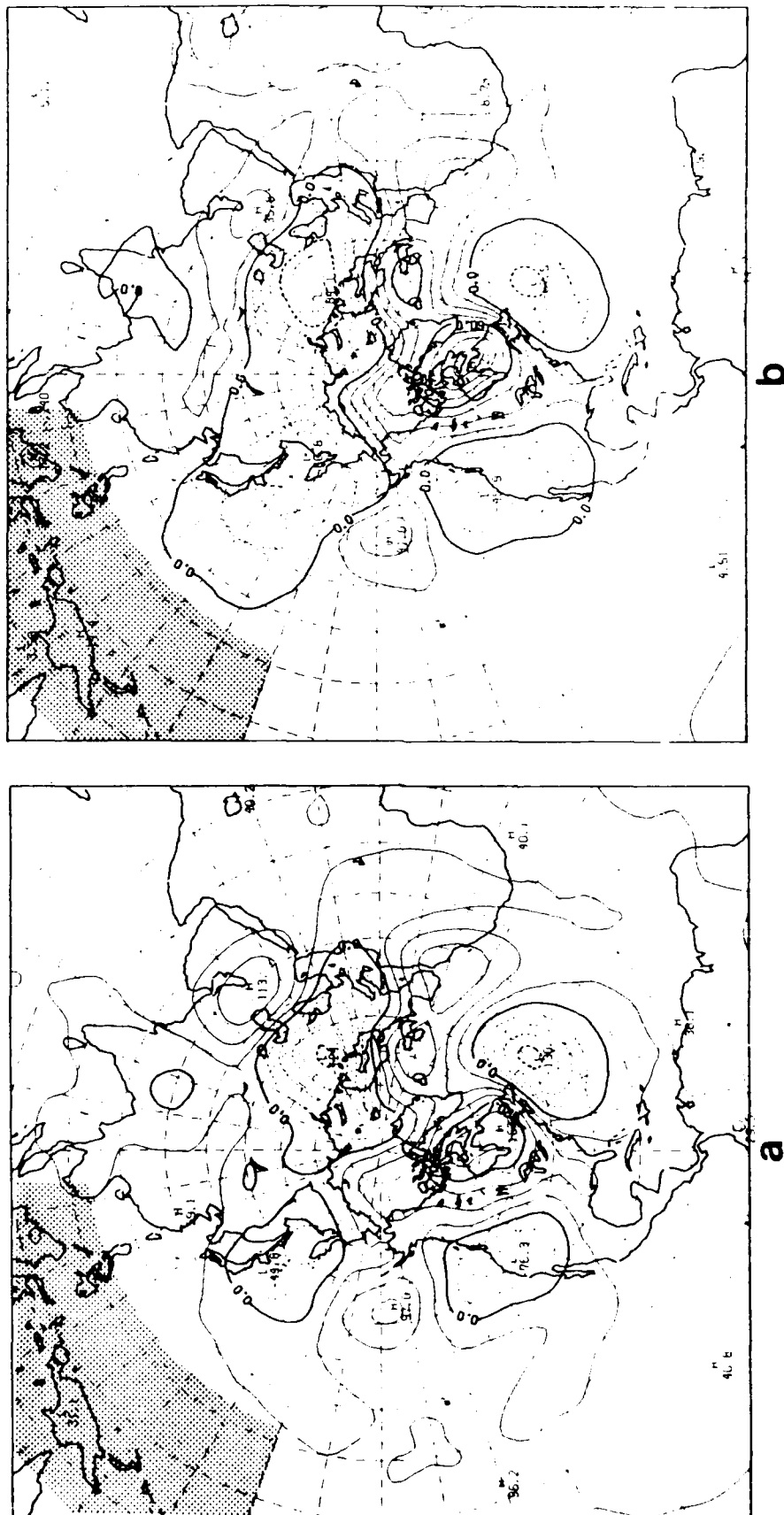
Figure 2.9   As in Figure 2.8, except for the WSSTA simulation.

58

the anomalous low off the east coast of the United States has nearly doubled between the two levels. Again, the equivalent barotropic structure of these anomalies is in contrast to the baroclinic structure of the tropical anomalies discussed earlier, and suggests that the anomalous standing wave pattern at high latitudes is composed of extremely deep vertical modes. This is reasonable considering the differences in the meridional propagation characteristics between shallow modes and deep modes, as discussed in Chapter 1. We will examine the structure of these anomalies in more detail in Section 2.4.

In summary, the general characteristics of the 30-day mean responses of the NOGAPS spectral model in the ESSTA and WSSTA simulations agree quite well with the time-mean responses obtained in similar modeling studies. Based on the preceding results alone, it appears that the model responses fit the conceptual framework outlined in Chapter 1, whereby anomalous diabatic forcing in the tropics can stimulate a significant response both locally and at locations far removed from the forcing anomaly. In further agreement with this framework, the local and remote responses appear to have different vertical structures. These structures are consistent with the two general classes of vertical modes discussed in Section 1.1. On the one hand, the time-mean response in the tropics has a vertical structure in which the flow reverses sign in the middle troposphere. This type of structure has been associated with relatively slowly propagating internal, or baroclinic modes that tend to be equatorially trapped to a high degree by the Coriolis force. On the other hand, the time-mean response in the midlatitudes has a predominant vertical structure in which there is little or no phase difference between the flow at upper and lower levels. This type of structure has been associated with external and deep

internal barotropic modes that can overcome the trapping effect of the Coriolis force and propagate to high latitudes, and it is examined in more detail in Chapters 3 and 4. In the ESSTA and WSSTA simulations, the anomalous standing waves in the midlatitudes form arcing patterns similar to those observed in other modeling and observational studies. A PNA-type pattern is especially evident in the WSSTA simulation.

2.4   Vertical Mode Projections

As discussed in Chapter 1, much of what is known about the dynamics of tropical-midlatitude interactions has been learned from theoretical and idealized modeling studies. While the results in the preceding section corroborate many aspects of the response predicted by idealized models, it is reasonable to assume that a complete description of the impact of tropical-midlatitude interactions on the general circulation must include the effects of certain dynamical processes that are excluded from these simpler systems. For example, processes that depend on more detailed vertical resolution (e.g., baroclinic development) and realistic physical forcing may play an important role in the anomalous response, especially in the midlatitudes. In this section, we examine some examples in which the anomalous midlatitude response discussed in Section 2.3.2 is projected onto the vertical modes of the NOGAPS model. These results highlight some aspects of the response that have not been observed in idealized models, and that are investigated in detail in the remainder of this study.

The dynamical framework mentioned in the preceding sections, in which tropically forced motions may be interpreted in terms of a spectrum of vertical modes of varying equivalent depths, derives from the fact that the linear

solutions to many hydrodynamical systems are separable in terms of their horizontal and vertical structures. A similar separation can be obtained for the adiabatic linearized version of the NOGAPS model. except that the resulting modes have discrete, rather than continuous vertical structures. This occurs because the dependent variables in the NOGAPS model are defined on a finite set of σ-surfaces, as described in Section 2.1. In the NOGAPS model. there are 18 vertical modes (corresponding to the number of σ-surfaces) numbered $\ell = 1,\ldots,18$. in which $\ell = 1$ denotes the deepest. or external mode, while $\ell = 18$ denotes the shallowest internal mode (Figure A.1). A summary of the derivation of the horizontal and vertical structures (or normal modes) of the NOGAPS equations is given in the Appendix, and a detailed description of the energetics of these modes is given in Chapter 3. For now, it is of interest to note simply that data obtained from the complete (i.e., nonlinear, forced) model can be projected onto these modes in order to determine the relative importance of the different modal structures. A description of how the model data is projected onto the modes is also given in the Appendix.

As noted above, theoretical and simple modeling studies have shown that the teleconnection response observed in the midlatitudes typically is manifested by a series of equivalent barotropic centers of action (highs and lows) in the upper-tropospheric geopotential height or stream function field that arc from the tropics toward high latitudes and then back toward the tropics again. Note that this is the form of the responses over North America observed in Figures 2.8 and 2.9; the equivalent barotropic structure of the midlatitude anomalies in these figures was discussed in Section 2.3.2. In accordance with their vertical structure, we might expect the midlatitude anomalies in the

NOGAPS model to be primarily an external ($\ell = 1$) mode response. Not only do the external modes have equivalent barotropic structure as shown in Figure A.1a, but their phase speeds are greater than 300 m/sec, allowing them to overcome the equatorial trapping by the Coriolis force. Lim and Chang (1983) have proposed that, in addition to external modes, deep internal modes with phase speeds greater than 120 m/sec are also essentially equivalent barotropic throughout most of the troposphere, and thus are capable of substantial meridional propagation. Therefore, based on meridional propagation characteristics alone, it seems reasonable to assume that the response in the midlatitudes should be comprised of only very deep vertical modes.

In order to determine whether this is indeed the case in a realistic model with complex vertical structure, the 30-day mean geopotential anomalies in Figures 2.8 and 2.9 were projected onto the vertical modes of the NOGAPS spectral model. To accomplish this, a procedure was used whereby the contribution to the anomalous response from vertical mode ℓ was computed as a residual between the total difference field and a difference field from which the contribution from vertical mode ℓ had been removed. It was decided to use this indirect method, rather than to compute the filtered amplitudes directly, because of the difficulty involved in reconstructing a reliable geopotential field from only a single vertical mode. Thus, the following procedure was employed:

1. The geopotential Φ_C from the control data set is computed.

2. A type of normal mode filtering is performed on the control data in which the data are projected onto the normal modes, then the mode amplitudes corresponding to vertical mode ℓ are set to zero and the data are projected back into physical space.

3. The geopotential $\Phi_C^{(f)}$ from the filtered control data set produced in step (2) is computed.

4. Steps (1)-(3) are repeated for the anomaly data set in order to obtain the geopotential fields Φ_A and $\Phi_A^{(f)}$.

5. The geopotential of the total difference field Φ_D is computed via

$$\Phi_D = \Phi_A - \Phi_C.$$

6. The geopotential of the filtered difference field $\Phi_D^{(f)}$ is computed via

$$\Phi_D^{(f)} = \Phi_A^{(f)} - \Phi_C^{(f)}.$$

7. Finally, the geopotential of the residual difference field $\Phi_D^{(r)}$ is computed via $\Phi_D^{(r)} = \Phi_D - \Phi_D^{(f)}$, where $\Phi_D^{(r)}$ represents the *contribution to the difference field from vertical mode ℓ* removed in steps (2) and (4).

Figure 2.10 shows the contributions from the first five vertical modes of the NOGAPS model to the midlatitude anomalies in the WSSTA simulation, based on the procedure outlined above. (Qualitatively similar results were obtained for the ESSTA simulation and thus are not shown.) The phase speeds of these modes are approximately 308, 178, 89, 55, and 36 m/sec, respectively. Using as a guideline the cut-off for meridional propagation of approximately 120 m/sec proposed by Lim and Chang (1983), we might expect to see very little amplitude in the projections onto modes greater than $\ell = 2$ or $\ell = 3$. However, the results in Figure 2.10 show that this is clearly not the case. Figures 2.10a and 2.10b show the contributions from $\ell = 1$, and from all modes *except* $\ell = 1$, respectively, to the total geopotential height anomaly at 300 mb in Figure 2.9a. Comparing Figures 2.9a and 2.10a, we see that the contributions from the external modes are large, which agrees with theoretical and idealized modeling

results. For example. it appears that between 40% and 70% of the amplitudes of the anomalies over North America project onto the external mode. Accordingly, Figure 2.10b shows that the contributions from the remaining (internal) modes are also significant. (The sum of the maxima in Figure 2.10a and 2.10b may not exactly match those in Figure 2.9 owing to the nonorthogonality of the vertical modes and the fact that the maxima are not necessarily collocated in each of the projections.) The substantial contributions from the internal modes in Figure 2.10b may not seem surprising initially. since vertical modes $\ell = 2$ and $\ell = 3$ may be capable of substantial meridional propagation. However, the projections onto these modes shown in Figures 2.10c and 2.10d are clearly insufficient to account for the remainder of the response in the internal modes shown in Figure 2.10b.

Moving on to the contributions from vertical modes $\ell = 4$ and $\ell = 5$ in Figures 2.10e and 2.10f, we see that much of the remaining amplitude projects onto the latter vertical mode. In general. it appears that the amplitude of vertical mode $\ell = 4$ is comparable with that of $\ell = 2$. but the amplitude of vertical mode $\ell = 5$ is significantly larger than all vertical modes except the external one. It may be noted that the contributions from $\ell \geq 6$ are insignificant, and therefore, are not shown here. Thus, Figure 2.10 indicates that the anomalous response in the midlatitudes has a substantial secondary maximum at $\ell = 5$. This is confirmed in Chapter 3, and is clearly in contrast to the conceptual framework described in previous sections, in which the midlatitude response is described as an essentially equivalent barotropic phenomenon.

It is interesting to note that while the total midlatitude response in Figure 2.9 appears to be equivalent barotropic. a significant portion of its
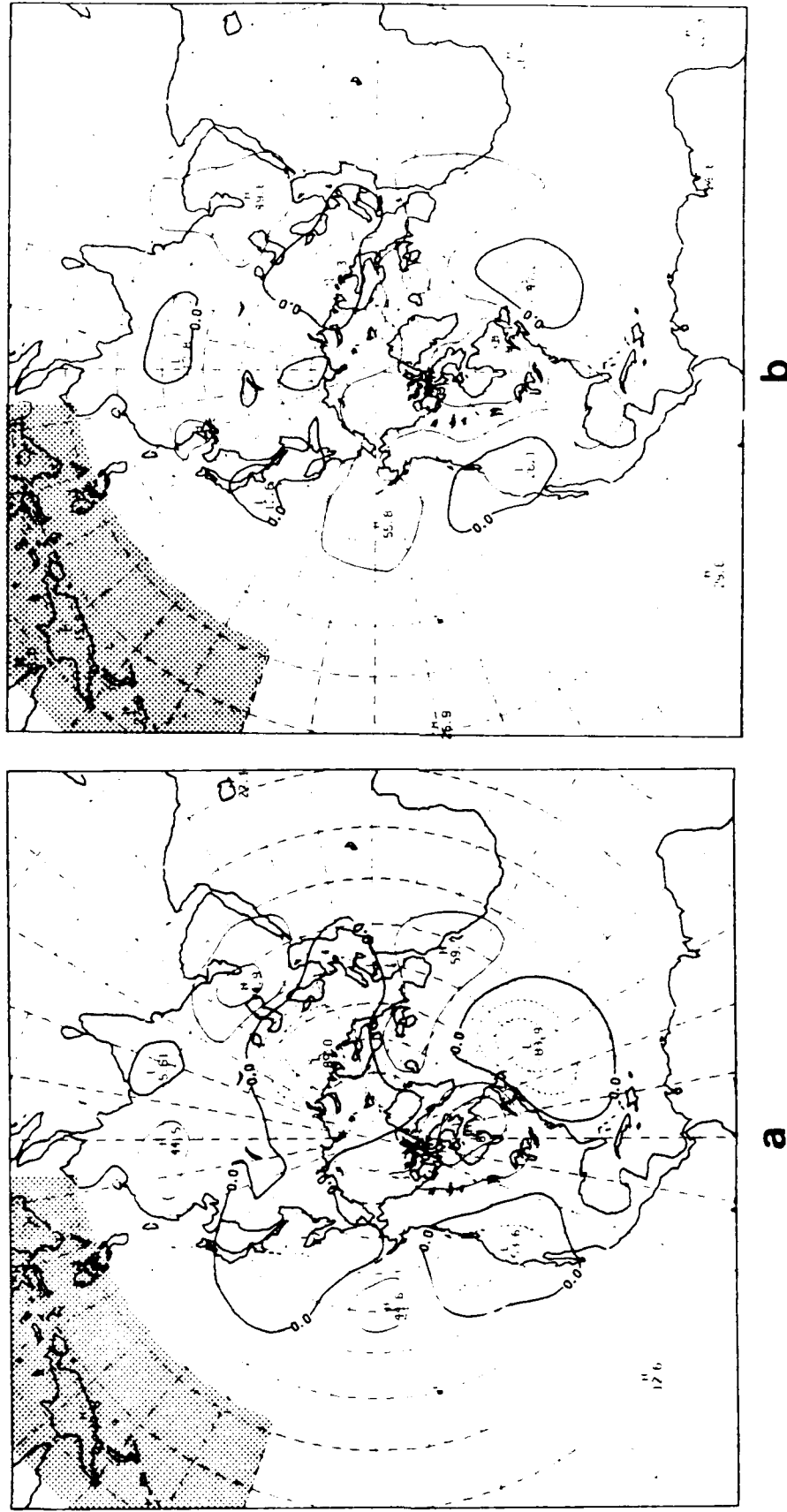
b

a

Figure 2.10 Polar stereographic projections of the Northern Hemisphere geopotential height anomalies shown in Figure 2.9a onto the vertical modes of the NOGAPS model. The projection onto the external ($\ell = 1$) modes is shown in (b). The projections onto vertical modes $\ell = 1$ is shown in (a), and onto all modes *except* $\ell = 1$ is shown in (c)-(f), respectively. The contour interval is 30 m, with negative differences $\ell = 2, 3, 4$ and 5 are shown in (c)-(f), respectively. The contour interval is 30 m, with negative differences denoted by dashed lines, and the SST anomaly indicated by the stippled region. (continued on next page)
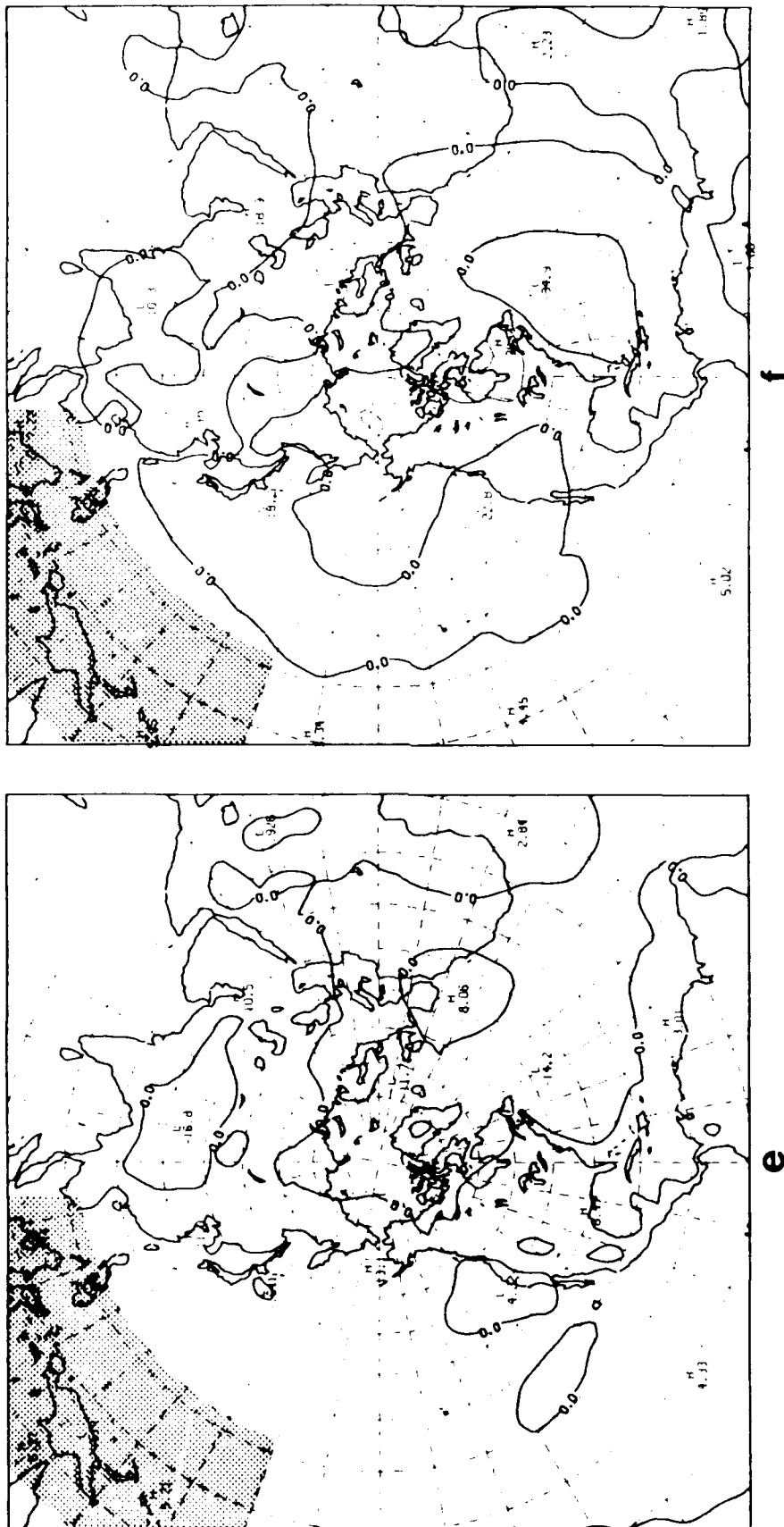
d

c
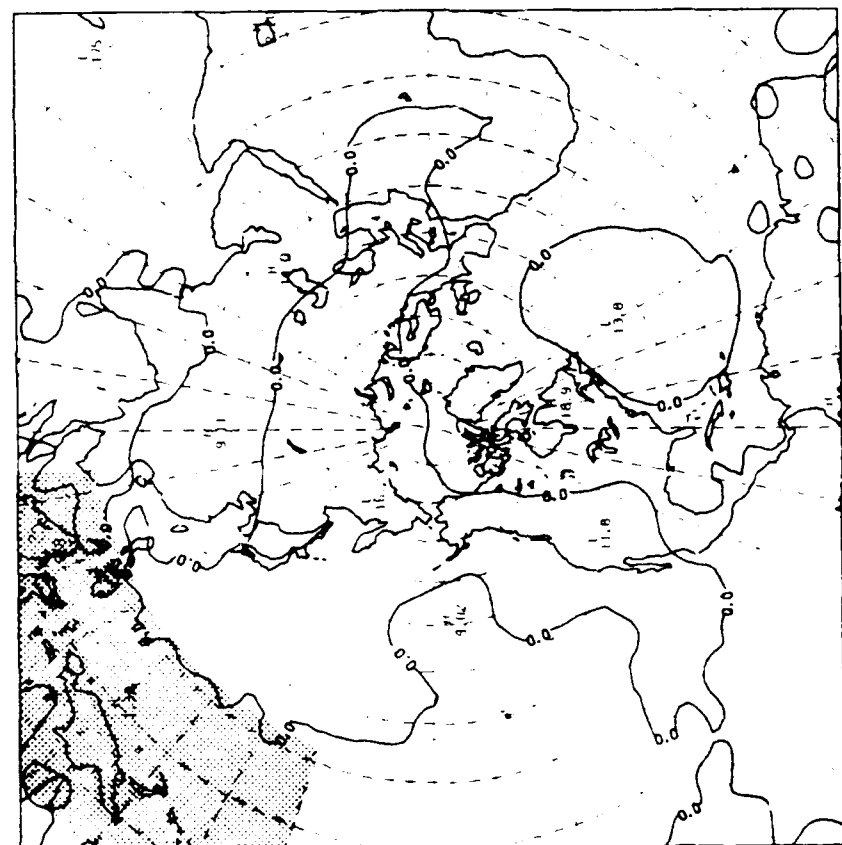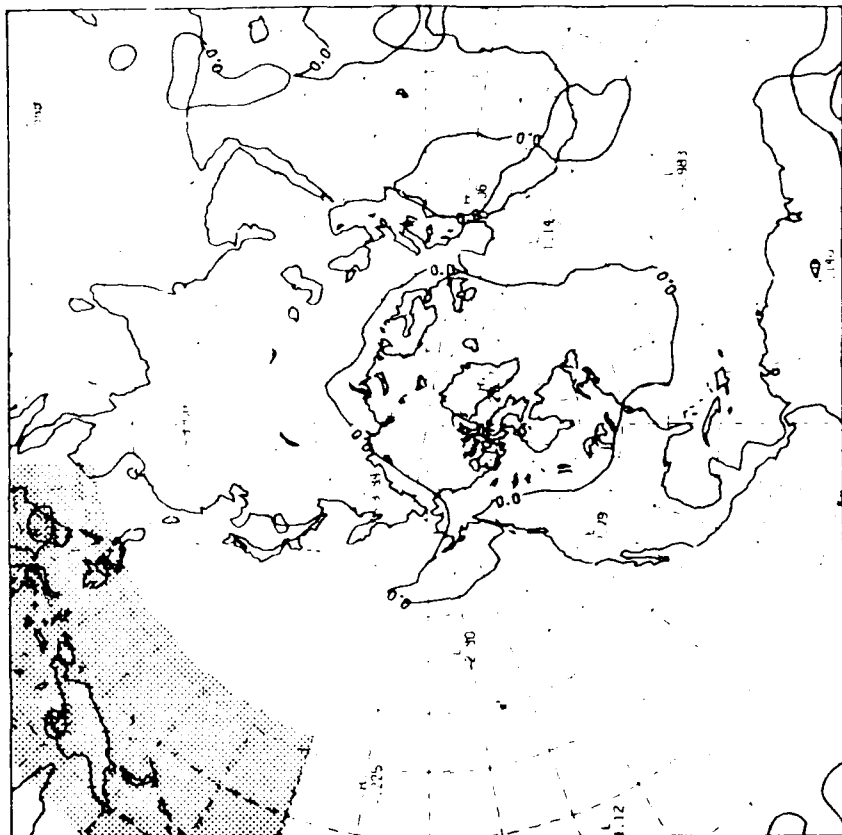
Figure 2.10 (continued)

Figure 2.10 (continued)

amplitude projects onto a mode ($\ell = 5$) whose vertical structure is usually associated with baroclinic motions. We may recall that this type of vertical structure is more often observed in the tropical response discussed in Section 2.3.1. However, based on the relatively slow phase speed of this vertical mode, and on its associated divergent characteristics, it seems unlikely that meridional propagation alone can explain its amplitude at such high latitudes. One possible explanation might be that its presence is related to secondary baroclinic processes in the midlatitudes that are driven by the primary barotropic response to anomalous tropical forcing. If this is the case, then it is not surprising that this component of the response is not accounted for in the dynamical framework obtained from idealized (*i.e.*, barotropic) modeling studies. In Chapters 3 and 4, we exploit the tractability of the normal mode solutions to the NOGAPS model in order to substantiate the existence of the $\ell = 5$ (baroclinic) component of the anomalous response, and thus, gain a better understanding of how the tropics and midlatitudes might interact in a more realistic setting.

3. NORMAL MODE ANALYSIS

As indicated by the results in Chapter 2, anomalous tropical forcing in the atmosphere can generate a complex response on various spatial and temporal scales. As with most complex atmospheric phenomena, an attractive approach to studying the dynamics of this response might be to design a modeling study that obtains the best compromise between the simplicity of the model we choose, and the degree of realism we hope to portray in its results. However, a key step in designing such a study is first to identify those components of the flow that describe the essential dynamic behavior of the phenomenon in question. For example, a great deal has been learned about the dynamical and mathematical properties of the large-scale atmospheric flow using severely truncated hydrodynamical models that retain the basic nonlinearity of the Navier-Stokes equations (*e.g.*, Vickroy and Dutton, 1979; Shirer and Dutton, 1979; Shirer and Wells, 1983; Shirer, 1980,1986; Gelaro and Shirer, 1986).

In a similar manner, one of the goals of this study is to identify those components of the flow that are essential for describing the dynamics of tropical-midlatitude interactions in a realistic setting. It was proposed in Chapters 1 and 2 that, in addition to barotropic processes, these interactions may depend on detailed vertical structure and baroclinic processes, as well as on realistic parameterizations of diabatic forcing. From this point of view, it seems that a sophisticated numerical model may be necessary to understand completely the dynamics of tropical-midlatitude interactions in the atmosphere. Unfortunately, the results obtained from experiments with such a model are

likely to be much less tractable than those obtained from a simpler model.

Recently however, investigators have begun to examine many aspects of the behavior of complicated numerical models in terms of the normal modes of linearized versions of these models (Puri, 1983; Errico, 1984; Errico *et al.*, 1988). As described in the Appendix, the normal modes provide a way of separating the model-simulated flow according to its different spatial and temporal scales. Because the normal modes are exact solutions to the linearized model equations, they obtain two basic forms: high-frequency *inertia-gravity* modes and low-frequency *rotational* (or *Rossby*) modes. It is shown here that by projecting the model output onto the normal modes, we can isolate the behavior of selected scales of motion. Furthermore, because the behavior of the different types of modes (eastward gravity, westward gravity and rotational) is often governed by well known prognostic and diagnostic relationships, the modal responses can be related to distinct types of atmospheric motions. Provided that the results of the normal mode analysis are interpreted within the proper framework, this technique represents a powerful tool for simplifying and understanding the results of a sophisticated numerical model.

3.1 Energetics in Terms of Normal Modes

One of the advantages of analyzing the model output in terms of the normal modes is that certain energy relationships obtain a relatively simple form. To begin with, we recall that in the continuous, hydrostatic system, the total kinetic plus available potential energy E per unit mass is given by

$$E = \frac{1}{8\pi} \int_0^1 \int_0^{2\pi} \int_{-1}^1 [\varphi \tau^{-1} \varphi - \psi \nabla^2 \psi - \chi \nabla^2 \chi] \, d\mu \, d\lambda \, d\sigma , \qquad (3.1)$$

where ψ is the stream function, χ is the velocity potential, φ is the pseudo-geopotential (hereafter referred to as simply the geopotential) and τ is an integral-differential operator of the vertical coordinate σ. It turns out that the separation of the model equations into horizontal and vertical structures depends significantly on the operator τ. In the discrete model equations, τ is expressed in terms of a matrix operator $\mathbf{S}$, as described in the Appendix. The variables λ and μ are the longitude and sine of the latitude respectively, and ∇^2 is the horizontal Laplacian in spherical coordinates, given approximately by

$$\nabla^2 = \frac{1}{a^2(1 - \mu^2)} \frac{\partial^2}{\partial \lambda^2} + \frac{1}{a^2} \frac{\partial}{\partial \mu} \left[(1 - \mu^2)\frac{\partial}{\partial \mu} \right], \qquad (3.2)$$

where a is the radius of the earth. Actually, the NOGAPS spectral model is formulated in terms of vorticity ς and divergence D rather than stream function and velocity potential, and so it is convenient to use the former in the rest of the derivation. Substituting the usual definitions

$$\varsigma = \nabla^2 \psi, \qquad (3.3)$$

$$D = \nabla^2 \chi, \qquad (3.4)$$

into (3.1), we obtain

$$E = \frac{1}{8\pi} \int_0^1 \int_0^{2\pi} \int_{-1}^1 \left[\varphi \tau^{-1}\varphi - \varsigma\nabla^{-2}\varsigma - D\nabla^{-2}D \right] d\mu \, d\lambda \, d\sigma. \qquad (3.5)$$

Although the inverse Laplacian (∇^{-2}) in (3.5) may seem awkward, it is computed easily in spectral space when the dependent variables are expanded in terms of spherical harmonics of the form

$$Y_{m,n}(\mu, \lambda) = P_{m,n}(\mu) \, e^{im\lambda}, \qquad (3.6)$$

in which $P_{m,n}(\mu)$ is an associated Legendre polynomial and m and n are integers. In that case, it can be shown readily that

$$\nabla^{-2} Y_{m,n} = -r_n Y_{m,n} , \qquad (3.7)$$

where

$$r_n = \frac{a^2}{n(n+1)} . \qquad (3.8)$$

To obtain the normal mode form of (3.5), we must express the dependent variables in terms of horizontal and vertical modes. Using a notation similar to that of Ko et $al.$ (1989), we can expand the vorticity, divergence and geopotential in the forms

$$\begin{pmatrix} \varsigma \\ D \\ \varphi \end{pmatrix} = \sum_J \alpha_J \begin{pmatrix} \hat{\varsigma}_J \\ \hat{D}_J \\ \hat{\varphi}_J \end{pmatrix} z_\ell , \qquad (3.9)$$

in which α_J is the time-dependent normal mode expansion coefficient (or normal mode amplitude), $\hat{\varsigma}_J$, $\hat{D}_J$ and $\hat{\varphi}_J$ are horizontal Hough functions corresponding to the vorticity, divergence and geopotential respectively, and z_ℓ is the vertical mode. The index J denotes the normal mode index set (m, j, ℓ), where m is the zonal wave number index, j is the horizontal mode index, and ℓ is the vertical mode index (Appendix); each normal mode is associated with a unique value of J. The range of the triple summation in (3.9) is left general for now, but will be discussed later in this section. As shown in the Appendix, the Hough functions in (3.9) are the horizontal modes (eigenvectors) of the linear system, which may be expanded in terms of spherical harmonics such that

$$\begin{pmatrix} \hat{\varsigma}_J \\ \hat{D}_J \\ \hat{\varphi}_J \end{pmatrix} = \sum_n \begin{pmatrix} \varsigma_{n,J} \\ D_{n,J} \\ \varphi_{n,J} \end{pmatrix} Y_{m,n} , \qquad (3.10)$$

where $\zeta_{n,J}$, $D_{n,J}$ and $\varphi_{n,J}$ are spherical harmonic expansion coefficients, and n is the degree of the spherical harmonic $Y_{m,n}$. Owing to the triangular truncation of the NOGAPS model, the range of n varies as a function of the zonal wave number m.

The expression for the total energy E given by (3.5) can be written in terms of the normal modes as

$$E = \frac{1}{8\pi} \int_0^1 \int_0^{2\pi} \int_{-1}^1 \sum_J \sum_{J'} \{[(\hat{K}_\zeta)_{J,J'} + (\hat{K}_D)_{J,J'} + (\hat{P})_{J,J'}] \, \alpha_J \alpha_{J'}^* \, z_\ell z_{\ell'}\} \, d\mu \, d\lambda \, d\sigma \,.$$

(3.11)

where

$$(\hat{K}_\zeta)_{J,J'} = -\hat{\zeta}_J \nabla^{-2} \hat{\zeta}_{J'}^* \,, \tag{3.12}$$

$$(\hat{K}_D)_{J,J'} = -\hat{D}_J \nabla^{-2} \hat{D}_{J'}^* \,, \tag{3.13}$$

$$(\hat{P})_{J,J'} = \frac{\hat{\varphi}_J \hat{\varphi}_{J'}^*}{gH_\ell} \,. \tag{3.14}$$

Here, g is gravity, H_ℓ is the equivalent depth, obtained as an eigenvalue of the vertical structure equation (A.10), and an asterisk denotes a complex conjugate. The first two terms on the right side of (3.11) involving (3.12) and (3.13) represent the rotational and divergent components of the kinetic energy and have been discussed in some detail by Ko et al. (1989). Also, it should be noted that the form of the available potential energy (3.14) in (3.11) is obtained via the vertical structure equation (A.10) and application of the appropriate vertical boundary conditions.

Combining (3.9) and (3.10), and substituting the result into (3.11)-(3.14), we obtain the total energy E in terms of the normal modes expanded in spherical harmonics

$$E = -\frac{1}{8\pi}\int_0^1\int_0^{2\pi}\int_{-1}^1 \sum_J\sum_{J'}\sum_n\sum_{n'}[(\varsigma_{n,J}\,\varsigma_{n',J'}^*\,Y_{m,n}\nabla^{-2}Y_{m',n'}^*$$
$$+ D_{n,J}D_{n',J'}^*\,Y_{m,n}\nabla^{-2}Y_{m',n'}^* - \frac{\varphi_{n,J}\,\varphi_{n',J'}^*}{gH_\ell}Y_{m,n}Y_{m',n'}^*)\,\alpha_J\alpha_{j'}^*\,z_\ell z_{\ell'}]$$
$$\times\ d\mu\,d\lambda\,d\sigma\ . \tag{3.15}$$

Equation (3.15) can be greatly simplified provided that both the horizontal and vertical structure functions (modes) are orthogonal in the sense of (A.12) and (A.32). If this is the case, then those terms involving products of unlike indices (e.g. when $n \neq n'$) are orthogonal to one another, and hence, vanish. It follows from (A.32) that the Hough harmonics $\varsigma_{n,J}$, $D_{n,J}$ and $\varphi_{n,J}$ are orthogonal. The vertical structure functions z_ℓ of the linearized NOGAPS spectral model do not satisfy (A.12) strictly, and therefore, are not orthogonal. However, they do satisfy (A.12) to a very high degree, especially for the ten or so largest equivalent depths H_ℓ. This has been verified quantitatively, but is not shown here. As the results in the following sections show, we are concerned with only the first five or six largest equivalent depths, which is well within the range where orthogonality is a good assumption. Other investigators (e.g., Errico, 1984) have carried out analyses using vertical structure functions that were nearly orthogonal and have demonstrated the validity of this approach.

Proceeding as stated above, we may now drop the primes in (3.15) and assume that the vertical integral satisfies (A.12), leaving

$$E \approx -\frac{1}{8\pi}\int_0^{2\pi}\int_{-1}^1 \sum_J\sum_n [(\varsigma_{n,J}\,\varsigma_{n,J}^*\,Y_{m,n}\nabla^{-2}Y_{m,n}^* + D_{n,J}D_{n,J}^*\,Y_{m,n}\nabla^{-2}Y_{m,n}^*$$
$$- \frac{\varphi_{n,J}\,\varphi_{n,J}^*}{gH_\ell}Y_{m,n}Y_{m,n}^*)\,\alpha_J\alpha_j^*]\,d\mu\,d\lambda\ , \tag{3.16}$$

where we use the approximate equality sign "$\approx$" as a reminder that the vertical modes are not strictly orthogonal. Equation (3.16) is further simplified by recalling that $Y_{m,n} = P_{m,n}(\mu)\, e^{im\lambda}$ (where $P_{m,n}(\mu)$ is an associated Legendre polynomial) and applying the definition (3.7), then performing the integration over longitude to obtain

$$E \approx \frac{1}{4} \int_{-1}^{1} \sum_{J} \sum_{n} \left\{ \left[r_n (\varsigma_{n,J} \varsigma_{n,J}^{*} + D_{n,J} D_{n,J}^{*}) + \frac{\varphi_{n,J}\, \varphi_{n,J}^{*}}{gH_{\ell}} \right] P_{m,n}^2\, \alpha_J \alpha_J^{*} \right\} d\mu . \quad (3.17)$$

The final step in obtaining a simplified expression for the total energy E in terms of the normal modes is to nondimensionlize the Hough vector functions in such a way as to facilitate the use of the horizontal orthogonality condition (A.32). For the NOGAPS spectral model, the appropriate dimensionless forms, denoted by the tildes, are

$$\tilde{\varsigma}_{n,J} = \frac{h_n^{\ell}}{\sqrt{2\,\Omega^2 a}}\, \varsigma_{n,J} . \quad (3.18)$$

$$\tilde{D}_{n,J} = \frac{i\, h_n^{\ell}}{\sqrt{2\,\Omega^2 a}}\, D_{n,J} . \quad (3.19)$$

$$\tilde{\varphi}_{n,J} = \frac{1}{\sqrt{2\,\Omega^2 a^2}}\, \varphi_{n,J} . \quad (3.20)$$

where

$$h_n^{\ell} = \left(\frac{gH_{\ell}}{n(n+1)} \right)^{1/2} . \quad (3.21)$$

and Ω is the angular velocity of the earth. It may be noted that these dimensionless forms also ensure that the horizontal structure equations (A.30) obtain a simple symmetric form suitable for a numerical eigenvalue problem based on the method of Andersen (1977). After substitution of (3.18)–(3.21) into (3.17), we obtain

$$E \approx \gamma \int_{-1}^{1} \sum_{J} \sum_{n} \left[(\tilde{\varsigma}_{n,J} \tilde{\varsigma}_{n,J}^{*} + \tilde{D}_{n,J} \tilde{D}_{n,J}^{*} + \tilde{\varphi}_{n,J} \tilde{\varphi}_{n,J}^{*}) P_{m,n}^2 \alpha_J \alpha_J^{*} \right] d\mu . \quad (3.22)$$

where $\gamma = \Omega^4 a^4 2 g H_\ell$ scales E to the correct magnitude and gives it dimensions of energy per unit mass. In this form, the inner-product of the Hough harmonics $\hat{u}_{n,J}$, $\dot{D}_{n,J}$ and $\hat{z}_{n,J}$ is unity via the orthogonality condition (A.32). (As discussed in Section 3.2.2. each of the three terms in this inner-product do not necessarily contribute equally to the sum.) In addition, we note that only $P_{m,n}$ in (3.22) is a function of μ so that the integral satisfies the Legendre polynomial property

$$\int_{-1}^{1} P_{m,n} P_{m',n'} \, d\mu = \delta_{m,n}^{m',n'}, \tag{3.23}$$

where $\delta_{m,n}^{m',n'}$ is the Kronecker delta defined by

$$\delta_{m,n}^{m',n'} = \begin{cases} 1 & \text{for } (m,n) = (m',n') \\ 0 & \text{for } (m,n) \neq (m',n') \end{cases}.$$

With these simplifications, (3.22) is reduced to the form

$$E \approx \gamma \sum_{J} \alpha_J \alpha_J^* . \tag{3.24}$$

Recall that J denotes the index set (m, j, ℓ) where, for each vertical mode ℓ, the sum over the indices m and j includes all three types of modes (eastward and westward gravitational and rotational modes) since the mode types are defined in terms of frequency bands (Appendix). Equation (3.24) states that the total kinetic plus available potential energy E is given simply by the sum of the squares of the normal mode amplitude coefficients, scaled by the proper dimensional constants. Actually, (3.24) is exact when summed over all modes having equivalent depth H_ℓ (i.e., when ℓ is fixed). When summed over all the modes for all ℓ, (3.24) does not yield the total energy of all the modes because the vertical structure functions z_ℓ are not orthogonal, and therefore, do not contribute independently to the total energy (Errico, 1984). However, as stated earlier, the vertical structure functions of the NOGAPS spectral model are very

nearly orthogonal so that the resultant quantity is very close to the total energy of the complete system.

Aside from obtaining a simple form, (3.24) provides a convenient way of separating the energy into the contributions from rotational and gravitational modes. For example, in Figures 3.1 and 3.2, (3.24) has been used to compute the contributions to the total energy from the external ($\ell = 1$) and first internal ($\ell = 2$) vertical modes from day 20 of the December 1985 control run discussed in Chapter 2. For each vertical mode, the model data has been projected onto the normal modes and the contributions from the eastward (EG) and westward (WG) gravity modes and the rotational (RT) modes are plotted as functions of the natural frequencies of the modes (we may recall that these frequencies are the eigenvalues of the horizontal structure equation (A.30) and so are easy to identify). The format used to display the values of E in Figures 3.1 and 3.2 is based on the method of Errico (1984). Only a brief description of this method is given below, but further details may be found in Errico (1984) or Errico et al. (1988).

For convenience, the modes of each type are ordered according to the absolute values of their frequencies, from smallest to largest, and then placed into forty bins. Each bin contains the same number of modes (28) except the last, which contains that number plus any remaining (36). Note that (A.31) shows that there is a unique horizontal spatial eigenvector for each frequency, making it easy to project data onto the various modes and obtain temporal information. The zonally symmetric (m=0) modes have been omitted because there is a zero-frequency ambiguity for three of the modes resulting from a formal problem in defining zero-valued velocity fields; the horizontal
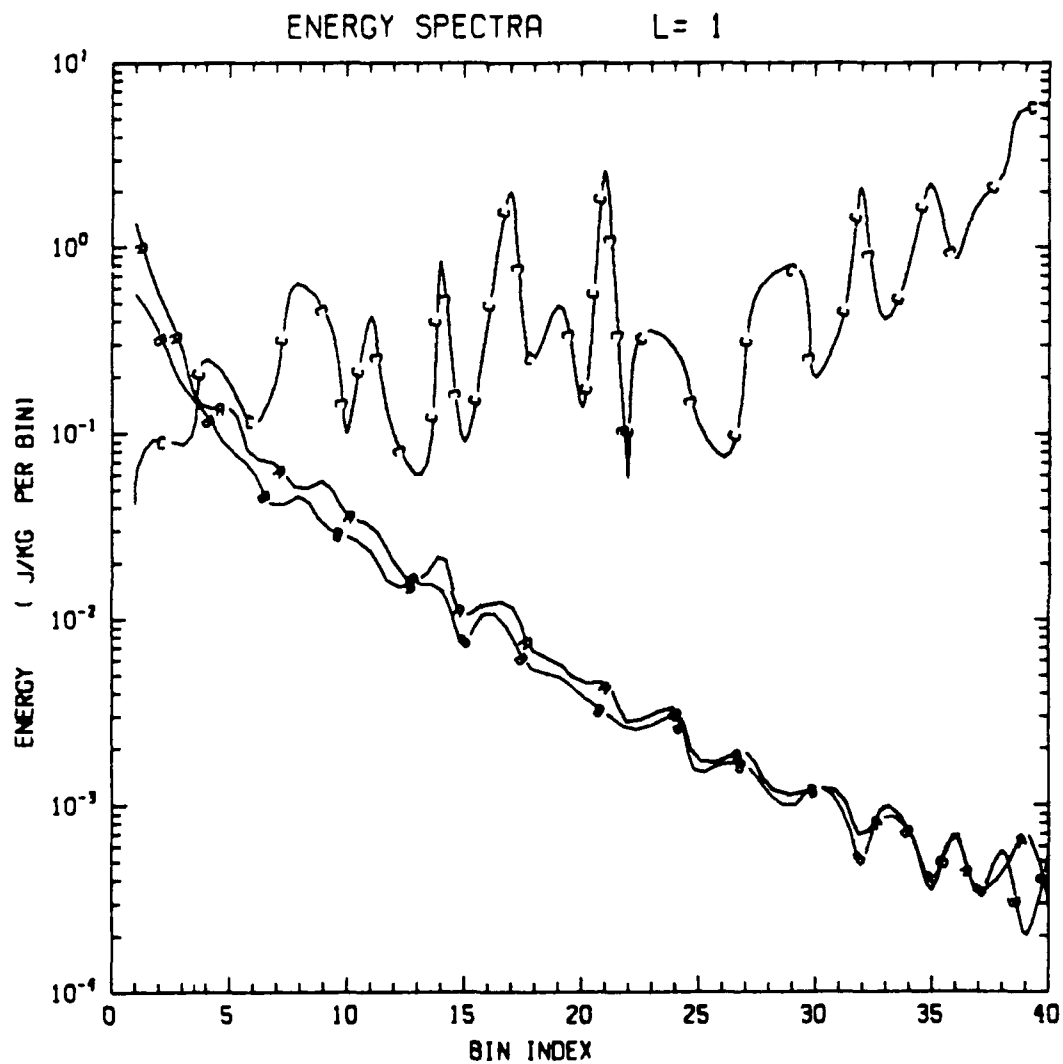
Figure 3.1   Energy spectra based on (3.24) for the external ($\ell = 1$) RT (curve
A), EG (curve B) and WG (curve C) modes from day 20 of the
control run. The bin index along the abscissa corresponds to an
ordering of the frequencies of the modes. This ordering is from
largest to smallest scales for the EG and WG modes, and from
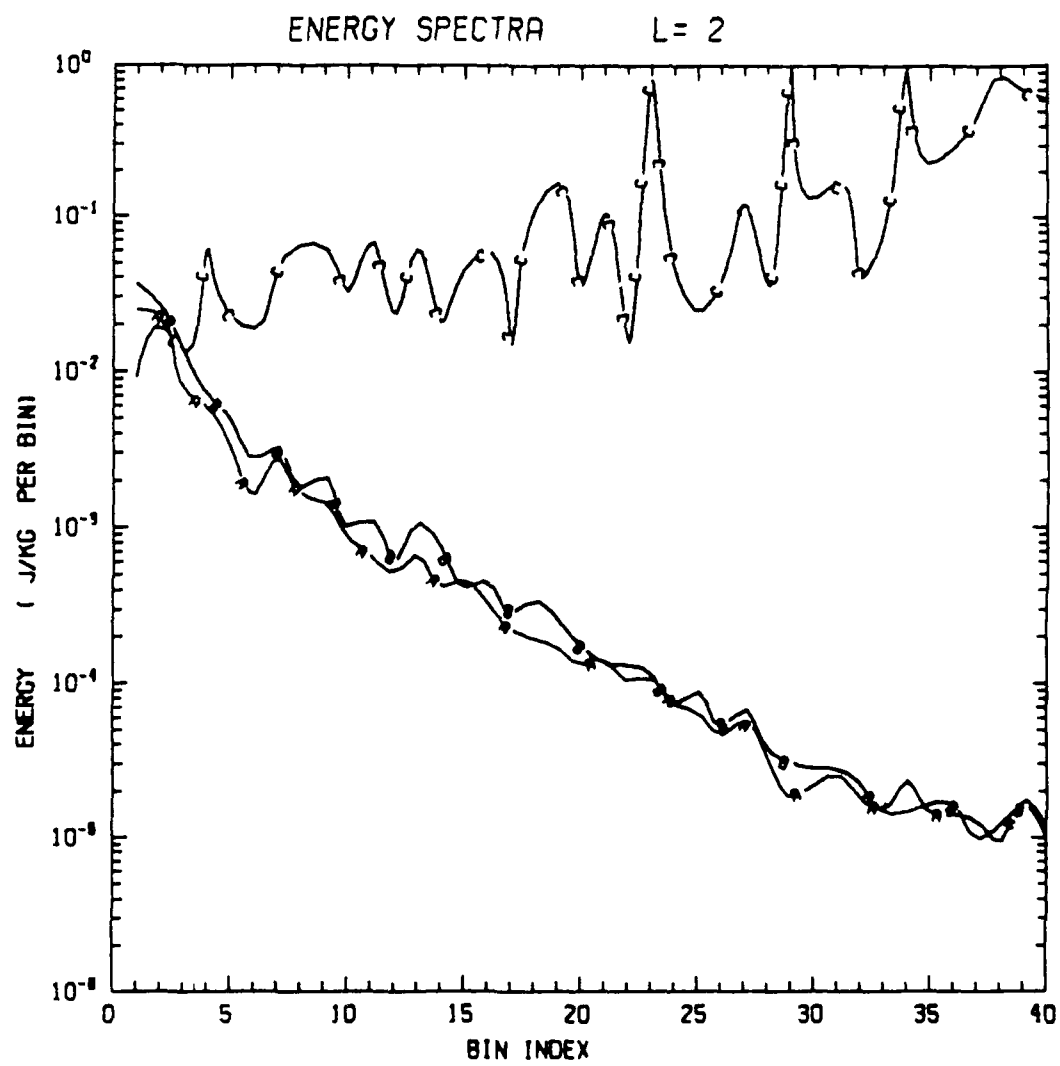smallest to largest scales for the RT modes (see text for details).

Figure 3.2   As in Figure 3.1, except for $\ell = 2$.

eigenvectors for these modes are not uniquely defined. This problem has been investigated by Kasahara (1978). However, at the moment, omitting these modes has no appreciable impact on the qualitative characteristics of the results. For each bin, the value of E is taken as the average value for all the modes in that bin. Because the frequency of the gravitational and rotational modes are respectively proportional to a wave number and an inverse wave number, the ordering is from largest to smallest scales for the EG or WG modes and from smallest to largest scale for the RT modes.

The most striking aspect of both figures is that, over most of the range of frequencies, the values of E for the RT modes (curve C) are several orders of magnitude greater than those for the EG modes (curve A) and WG modes (curve B). Of course this is in agreement with atmospheric data in which the meteorologically significant waves typically are far more energetic than the gravity waves. The highly energetic gravity modes in the first few bins in Figures 3.1 and 3.2 are most likely due to the contributions from low frequency Kelvin modes and mixed Rossby-gravity modes, which are believed to play significant roles in tropical circulations (Webster, 1972; Gill, 1980; Lim and Chang, 1983).

Another feature common to both figures is that the mean RT mode energy is roughly constant over the entire range of frequencies, increasing somewhat at higher frequencies (larger scales), whereas the mean EG and WG mode energy decreases significantly at higher frequencies (smaller scales). This indicates that the large-scale Rossby waves for these equivalent depths are somewhat more energetic than the small-scale Rossby waves, and that the large-scale gravity waves are far more energetic than their highly transient small-scale

counterparts. Again, these characteristics are reasonable for the atmosphere in a mean sense and reflect the fact that, after 20 simulated days, the model is in a state of balance in which high frequency gravity wave noise is an insignificant part of the overall energy balance. It may also be noted that the $\ell = 1$ modes of all types (Figure 3.1) are more energetic than those for $\ell = 2$ (Figure 3.2). This indicates that, at this time, the external mode motions in the model, which are equivalent barotropic and nearly nondivergent, are more energetic than the first internal mode motions, which have more baroclinic structure in the stratosphere, and thus, greater divergence (see Figure A.1a). The differences between internal and external mode characteristics, and their associated circulations, are discussed in greater detail in the following sections in the context of tropical-midlatitude interactions.

In summary, by selectively summing certain terms in (3.24) we have a convenient and dynamically meaningful way of quantifying the importance of different scales of motion in a flow with many degrees of freedom. It should be noted that other investigators such as Kasahara, 1984 and Errico, 1984 have successfully used some form of (3.24) to examine the energy of the different mode types in both model-simulated and observational data sets; their results are in general agreement with the examples in Figures 3.1 and 3.2. In the following sections, we will exploit some of the results of the preceding analysis in order to understand better the tropical and midlatitude responses to anomalous tropical forcing.

3.2 A Latitudinal Partitioning Technique for Normal Modes

The normal modes of the NOGAPS spectral model derived in the Appendix are global functions that describe the spectrally truncated fields of vertical vorticity ς, horizontal divergence D and geopotential φ. Accordingly, a truncated version of the energy equation (3.24) derived in Section 3.1 yields the *global* total energy for some subset of the modes (henceforth, the total energy is taken to mean the sum of the kinetic plus available potential energy). Indeed the simple form of (3.24) results, in part, from the Legendre polynomial property (3.23), which holds only when the integral is evaluated from pole to pole, that is from $\mu = -1$ to $\mu = 1$. As mentioned in Section 3.1, some investigators have used (3.24) to analyze the energy properties of various types of data sets. Likewise, we can use certain terms of (3.24) in its present form to examine the global total energy contributions from various modes to the anomaly patterns discussed in Chapter 2. Examples of these calculations are shown below. However, as discussed in Chapter 1, (and as demonstrated by the results in Chapter 2), there is much evidence from both observational and modeling studies that the tropics and midlatitudes respond quite differently to anomalous tropical forcing. Thus, it would be useful to have the capability to examine the results in Chapter 2 from a *regional* standpoint. With this in mind, we develop a new technique in this section for partitioning the energy of the normal modes in terms of latitude and type (*i.e.*, kinetic or available potential) in order to help us understand the differences between the tropical and midlatitude responses.

3.2.1 Global Energy

Before developing the partitioning technique, we briefly examine some of the results in Chapter 2 in terms of the global total energy given by (3.24). As before, we are interested in examining the *differences* between the control and anomaly data sets in order to reveal the anomalous response. The general procedure for obtaining the energy of the difference field is first to project the control and anomaly fields of ς, D and φ onto the normal modes as described in the Appendix. Then, having obtained the normal mode amplitude coefficients α_J for each data set, we form the differences $(\alpha_J)_D = (\alpha_J)_A - (\alpha_J)_C$ of the corresponding modes in the anomaly (A) and control (C) data sets. Finally, the values of $(\alpha_J)_D$ are used to obtain the energy of the difference field via (3.24), except that now α_J is replaced by $(\alpha_J)_D$.

We begin with the 30-day mean composite control and anomaly data sets for the ESSTA and WSSTA simulations discussed in Chapter 2. Again, the 30-day mean fields are obtained from days 21–50 of each model run and are intended to represent a quasi-steady solution. It is shown in Sections 3.3 and 3.4 that this is fairly well supported by the evolution of the modal responses. As in Chapter 2, the results from both simulations are shown to check the consistency of the results, not to make a detailed comparison between them. Figures 3.3a–d and Figures 3.4a–d show the global eddy total energy of the RT, EG and WG modes (and their sum, denoted ALL) for the 30-day mean difference fields in the ESSTA and WSSTA simulations, respectively, as a function of vertical mode ℓ. The abscissas are numbered such that vertical mode $\ell = 1$ corresponds to the external mode. For comparison, all vertical modes are includes in these figures although, as discussed in Section 3.1, the higher vertical modes are of little

GLOBAL EDDY ENERGY (RT)
ESSTA DIFFERENCE FIELD d(21-50)

a

GLOBAL EDDY ENERGY (EG)
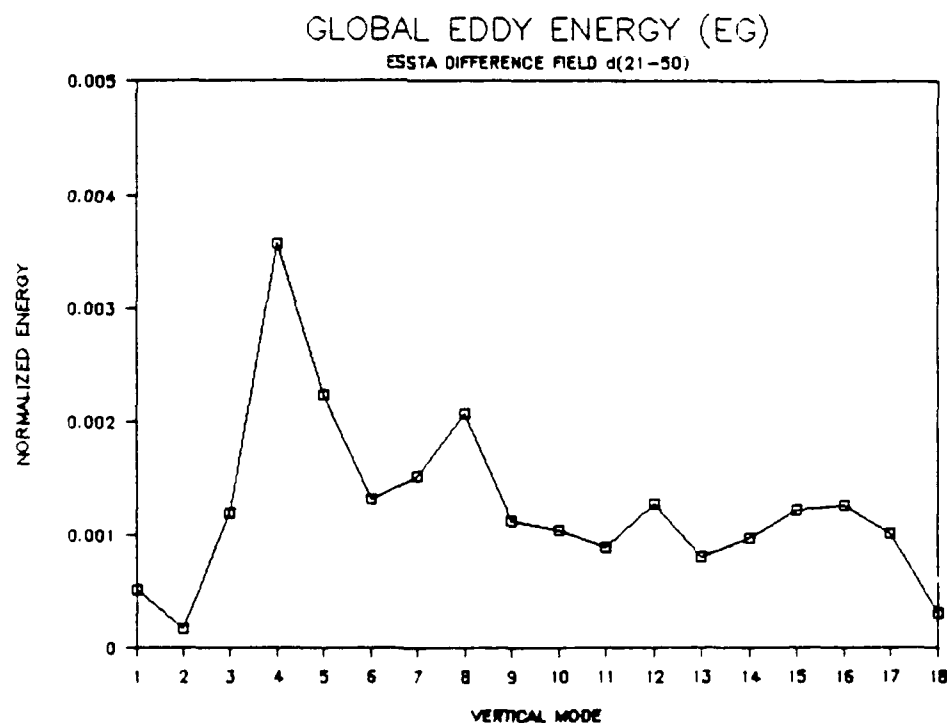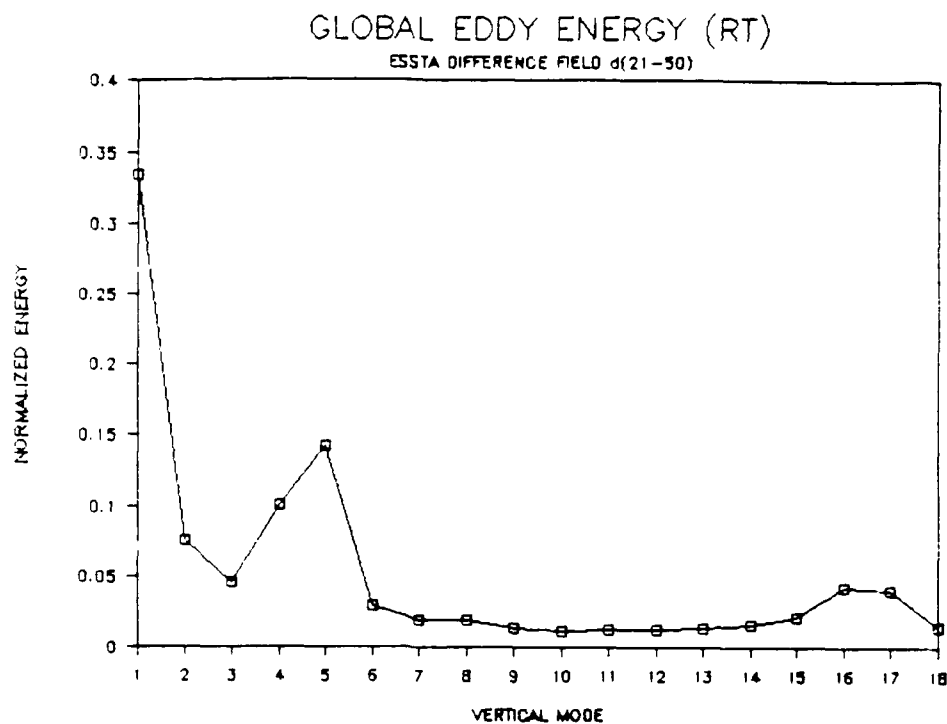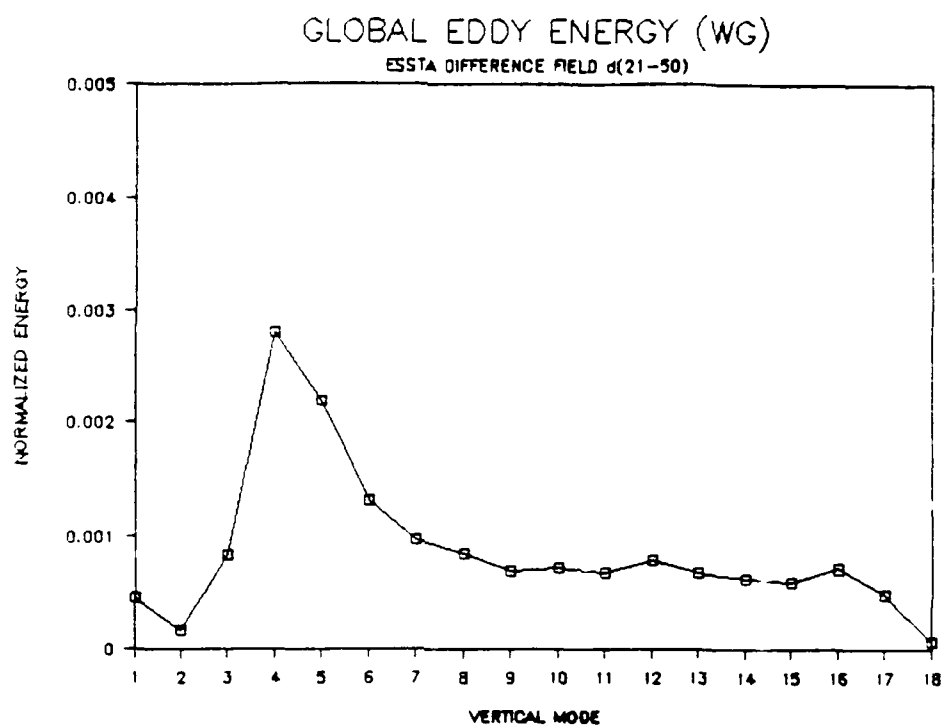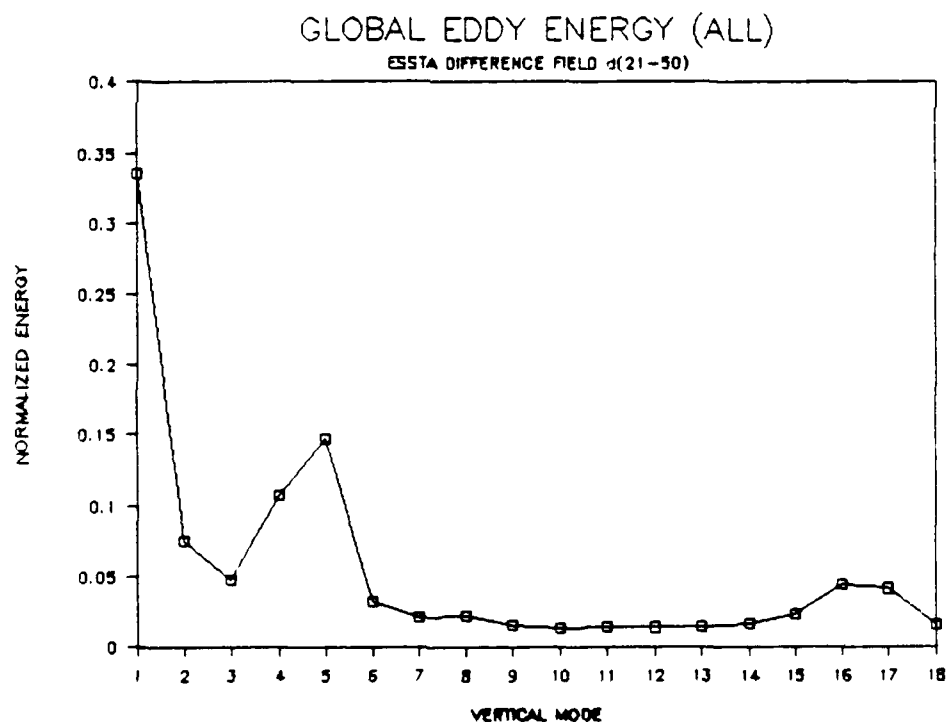ESSTA DIFFERENCE FIELD d(21-50)

b

Figure 3.3 The total eddy global energy of the (a) RT, (b) EG, (c) WG and
(d) ALL modes, as a function of vertical mode ℓ for the 30-day
mean difference field in the ESSTA simulation.

GLOBAL EDDY ENERGY (WG)

ESSTA DIFFERENCE FIELD d(21-50)

GLOBAL EDDY ENERGY (ALL)

ESSTA DIFFERENCE FIELD d(21-50)

Figure 3.3 (continued)

86
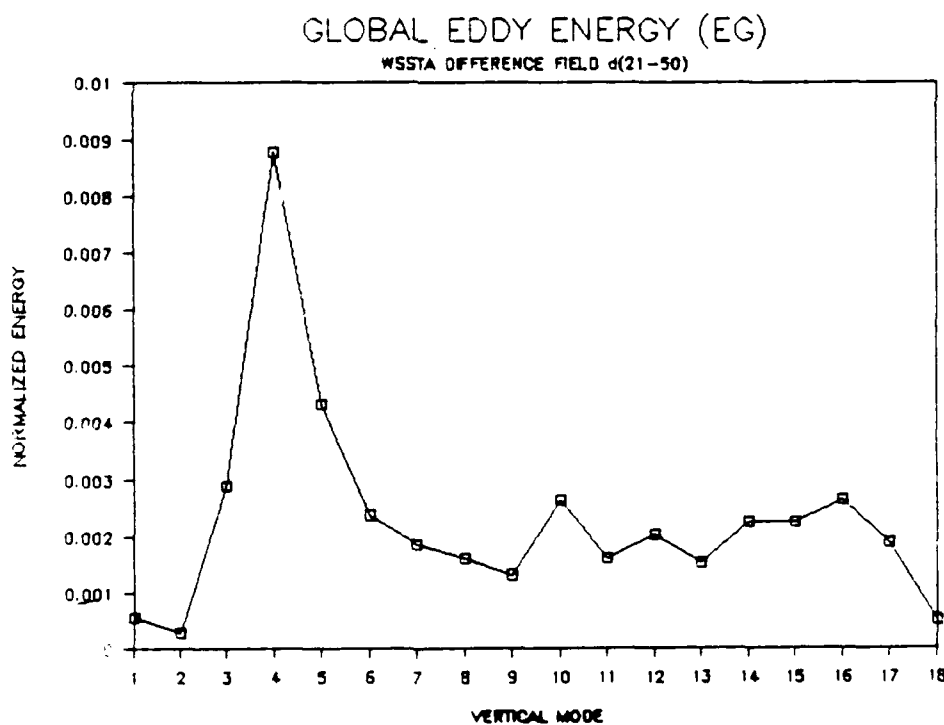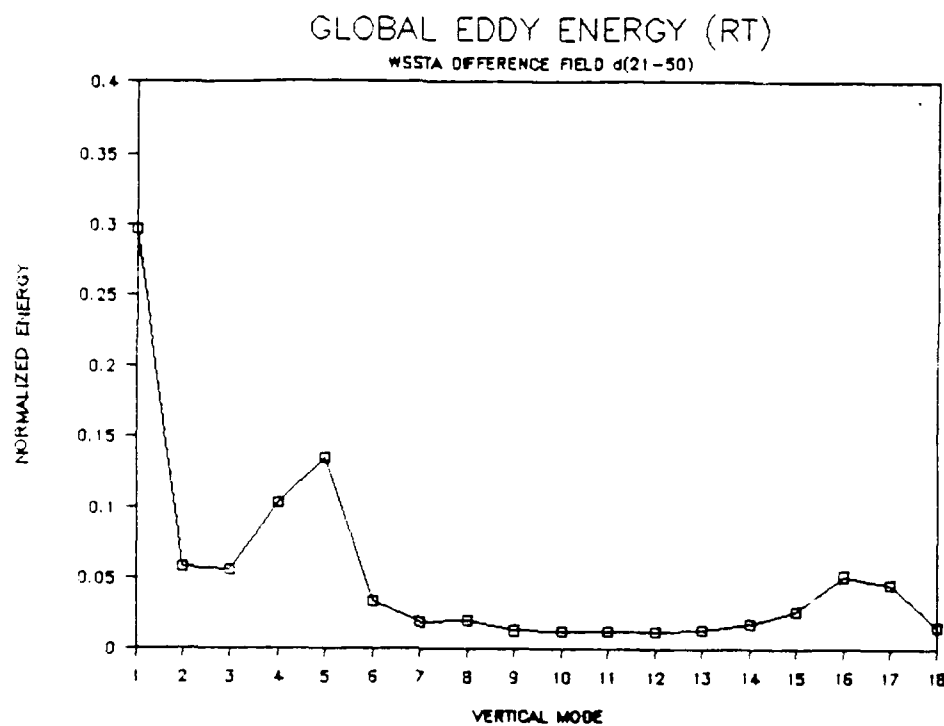
Figure 3.4   As in Figure 3.3, except for the WSSTA simulation.

(continued on next page)

GLOBAL EDDY ENERGY (WG)

WSSTA DIFFERENCE FIELD d(21-50)

c

GLOBAL EDDY ENERGY (ALL)

WSSTA DIFFERENCE FIELD d(21-50)
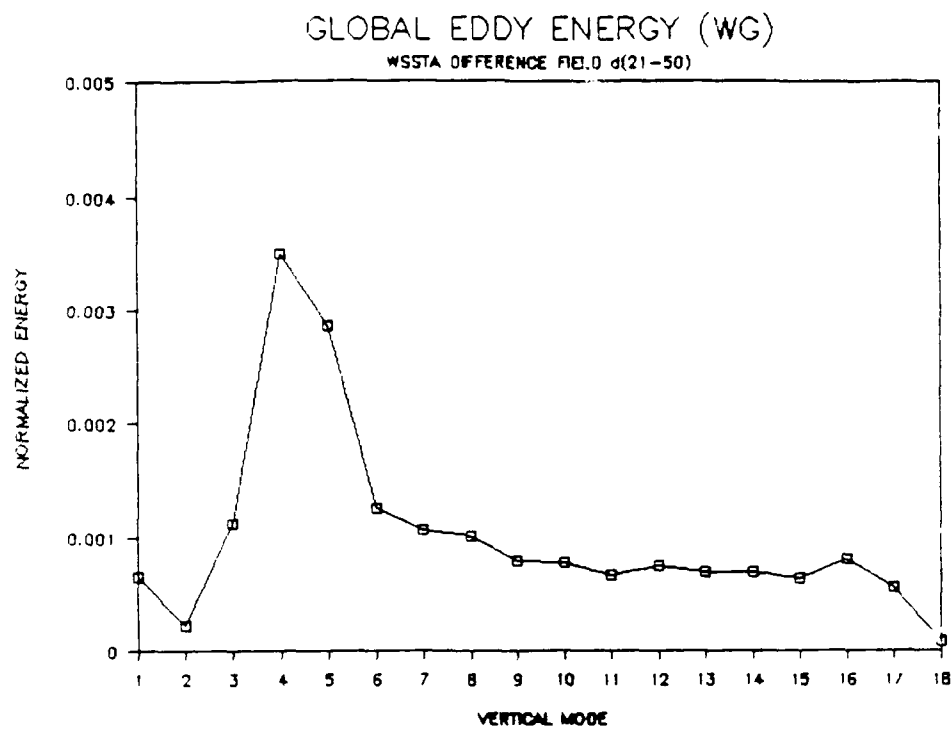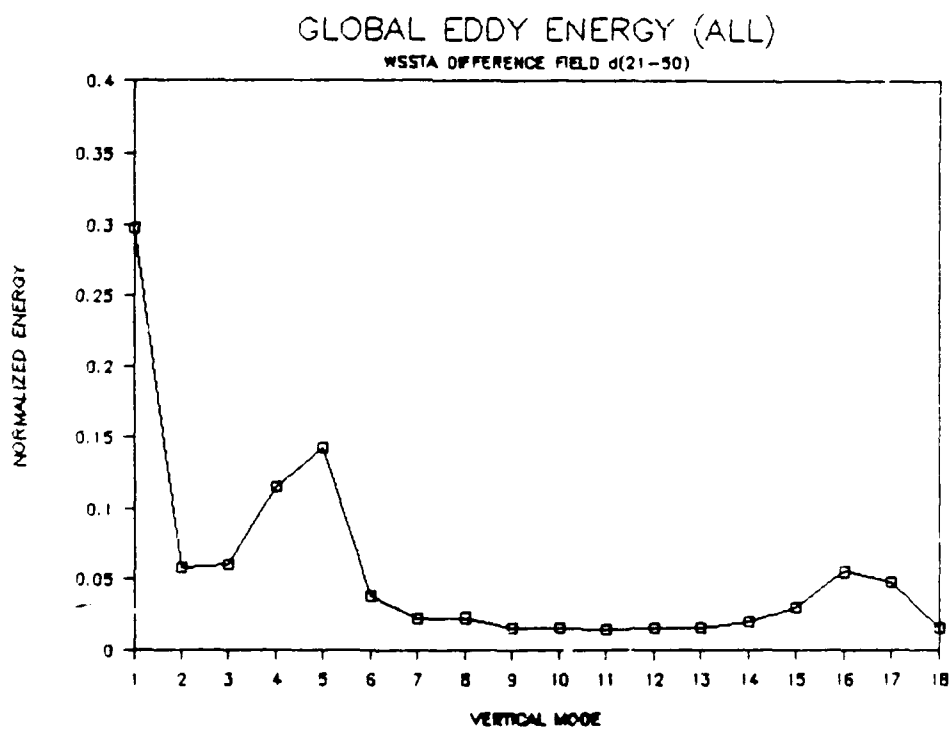
d

Figure 3.4 (continued)

physical relevance here. The plotted values are normalized by the quantity obtained when (3.24) is summed over all the mode types (RT, EG and WG) for all ℓ. Although this quantity is not equal to the total energy of all the modes (Section 3.1), its use as a normalization factor still provides a way of closely approximating the contribution of the different vertical modes to the total energy of the system. In the discussion that follows we will adopt this convention. For example, according to Figure 3.3a, the external ($\ell = 1$) RT modes contribute approximately 34% of the global energy, while the $\ell = 3$ RT modes contribute just under 5%. As a final comment on the format of the figures, it should be noted that, as in Figures 3.1 and 3.2, the zonally symmetric ($m = 0$) modes are excluded so that the plotted quantity is actually the global *eddy* energy unless otherwise stated. It turns out that this has no appreciable impact on the qualitative characteristics of the difference fields.

Figures 3.3a and 3.4a show the contributions of the RT modes to the global energy for the ESSTA and WSSTA difference fields respectively. Both cases have very similar profiles, with the external modes clearly dominating all others by contributing nearly one third of the total global energy of all the modes. This is qualitatively consistent with the results of the control run, as indicated by Figure 3.1. A secondary peak at $\ell = 5$ (although $\ell = 4$ is also quite energetic) is also common to both simulations, contributing approximately 15% of the global energy. These results clearly support those in Figures 2.10a and 2.10f, which show that the 30-day mean difference fields of 300 mb geopotential height project strongly onto the the first and fifth vertical modes. In fact, it appears from Figures 3.3a and 3.4a that the contribution of the fifth vertical mode is nearly half as large as that of the external mode. The fact that the

energy profiles in Figures 3.3a and 3.4a so strongly support the vertical mode projections of the difference field of geopotential in Figure 2.10 clearly suggests that the rotational modes dominate the 30-day mean response.

This result is confirmed by Figures 3.3b–d and 3.4b–d. Figures 3.3d and 3.4d, which show the contributions of ALL modes, have few discernible differences from Figures 3.3a and 3.4a, which show only the RT modes. Only for $\ell = 4$ do the plots of ALL modes show visible differences when compared with those of the RT modes alone, especially in Figure 3.4d for the WSSTA simulation. This small difference is explained by Figures 3.3b–c and 3.4b–c, which show that the energy of the EG and WG modes in both simulations is contributed mostly at $\ell = 4$, especially for the WSSTA simulation in Figures 3.4b–c. The peak in the gravity mode energy at this vertical mode is discussed in further detail in Section 3.3. It should be noted that the vertical scaling in the EG and WG figures is much smaller than in the RT and ALL mode figures, so that even the $\ell = 4$ gravity modes contribute less than 1% of the total global energy of the anomalous response. Although the gravity mode energy may be reduced somewhat by the averaging process, this result reflects the fact that, after this length of time, the response is in an approximate state of equilibrium dominated by the meteorologically significant waves. Also, we might mention that the small increase in energy for the $\ell = 16, 17$ RT modes in Figures 3.3a and 3.4a may be due to direct thermal forcing by extremely shallow boundary layer processes in response to the SST anomaly. However, the exact values of the energy at these extremely shallow modes may be uncertain as a result of nonorthogonality (Section 3.1) and because the available potential energy at these equivalent depths may not be well defined (Errico, personal

communication). In any case, these modes are of little dynamical interest in the present context.

As demonstrated by the results in Figures 3.3 and 3.4, (3.24) provides a useful way of quantifying the energy contributions of selected modes to the anomalous responses in the ESSTA and WSSTA simulations. These figures especially highlight two points concerning the character of the time-mean response of the NOGAPS spectral model to anomalous tropical forcing. The first point, which agrees well with existing knowledge, is that the external *rotational* modes seem to dominate the response, contributing 30% or more of the global total energy. This agrees well with the difference maps of geopotential discussed in Chapter 2, and supports the premise that nondivergent Rossby waves may be an important part of the anomalous response. However, at this point it appears that only Lim and Chang (1986) have made a quantitative estimate of energy in the external mode response, using a relatively simple two-layer model. Depending on the strength of the specified vertical wind shear in their model, they found that the kinetic energy in the external modes accounted for between 20% and 60% of the total kinetic energy once the model had reached a quasi-steady state. Their results clearly are in agreement with those in Figures 3.3 and 3.4.

The second point highlighted by Figures 3.3 and 3.4 is that there is a significant internal mode response at $\ell = 5$ (and to a lesser degree, at $\ell = 4$) with approximately half the amplitude of the external mode response. Based on the assumption that baroclinic modes tend to be trapped at low latitudes, this is a surprising result that raises several questions concerning the origin and propagation properties of these modes. Clearly, the vertical mode projection

shown in Figure 2.10f demonstrates that the $\ell = 5$ response is present in the midlatitudes where the anomalous geopotential height response is prominent. Although it is not clear from that figure, nor from the global energy calculations in Figures 3.3 and 3.4, whether this internal mode response is present in the tropics as well, it has been shown by many investigators (*e.g.*, Webster, 1981; Lim and Chang, 1983; Silva Dias *et al.*, 1983) that the tropical response has a strong baroclinic component. Typically, the vertical structure of this response exhibits a single sign reversal in the middle troposphere implying low-level inflow and upper-level outflow indicative of deep convection. Assuming this to be the case here as well, we are left with the question of whether these modes have somehow managed to propagate to the midlatitudes, or appear there as the result of some entirely independent process. In either case, their presence in the midlatitudes represents a significant departure from the conceptual framework ordinarily used to describe the midlatitude response to anomalous tropical forcing, in which this response has been thought to be predominantly equivalent barotropic in nature. In an effort to address these and other questions, we next introduce a way of isolating differences in the tropical and midlatitude responses in terms of the energy contributions from the normal modes.

3.2.2 Tropical and Midlatitude Energy

It was shown in Section 3.1 that the *total global* energy expressed in terms of the normal modes takes the simple form (3.24), upon application of the Legendre polynomial property (3.23) and the orthogonality condition (A.32) to the dimensionless energy equation (3.22). However, if we wish to consider some component of the total global energy (*e.g.*, the available potential energy) rather

than the total global energy itself, then we must consider the more general expression (3.22) without these simplifications. Recalling that only $P_{m,n}$ in (3.22) is a function of μ, we can rewrite this equation as

$$E \approx \gamma \sum_J \alpha_J \alpha_J^* \sum_n (\tilde{\varsigma}_{n,J} \tilde{\varsigma}_{n,J}^* + \tilde{D}_{n,J} \tilde{D}_{n,J}^* + \tilde{\varphi}_{n,J} \tilde{\varphi}_{n,J}^*) \int_{\mu_1}^{\mu_2} P_{m,n}^2 \, d\mu, \quad (3.25)$$

where the limits of integration over latitude are now general. We can further generalize (3.25) by writing the Hough functions in the vector form

$$\mathbf{h}_{n,J} = [(h_{n,J})_1, \ (h_{n,J})_2, \ (h_{n,J})_3]^T = \begin{pmatrix} \tilde{\varsigma}_{n,J} \\ \tilde{D}_{n,J} \\ \tilde{\varphi}_{n,J} \end{pmatrix}, \quad (3.26)$$

so that the inner-product of the Hough functions in (3.25) can be expressed

$$\langle \, \mathbf{h}_{n,J} \cdot \mathbf{h}_{n,J} \, \rangle = \sum_{k=1}^{3} (h_{n,J})_k \, (h_{n,J}^*)_k = (\tilde{\varsigma}_{n,J} \tilde{\varsigma}_{n,J}^* + \tilde{D}_{n,J} \tilde{D}_{n,J}^* + \tilde{\varphi}_{n,J} \tilde{\varphi}_{n,J}^*). \quad (3.27)$$

It follows from (3.12)–(3.14), that the terms $\tilde{\varsigma}_{n,J} \tilde{\varsigma}_{n,J}^*$, $\tilde{D}_{n,J} \tilde{D}_{n,J}^*$ and $\tilde{\varphi}_{n,J} \tilde{\varphi}_{n,J}^*$ in (3.27) represent the independent contributions to the total energy from the rotational kinetic, divergent kinetic and available potential energies respectively. Combining (3.25) and (3.27), we can write a general energy expression that includes any or all components of the total energy for any or all latitude bands in the form

$$E \approx \gamma \sum_J \alpha_J \alpha_J^* \, \Delta_J, \quad (3.28)$$

where Δ_J is given by

$$\Delta_J = \sum_n \underbrace{[\sum_k (h_{n,J})_k \, (h_{n,J}^*)_k]}_{a} \underbrace{[\int_{\mu_1}^{\mu_2} P_{m,n}^2 \, d\mu \,]}. \quad (3.29)$$

As shown schematically in (3.29), the factor Δ_J is composed of two parts. Part (a) describes the ratios for the various forms of energy that project onto

mode J, while part (b) describes the latitudinal variance of the mode. It should be noted that $0 \leq \Delta_J \leq 1$. For example, if we consider the global total energy, then for all modes, k is summed from 1 to 3 in (a), and each integral in (b) is evaluated from -1 to 1. Obviously, in that case we have $\Delta_J = 1$, so that (3.28) takes the simple form of (3.24). However, if we consider only the global available potential energy, then k in part (a) of (3.29) takes on only the value 3, and we have

$$(\Delta_J)_{APE} = \sum_n \left[\sum_{k=3}^{3} (h_{n,J})_k \, (h_{n,J}^*)_k \right] \left[\int_{-1}^{1} P_{m,n}^2 \, d\mu \right] = \sum_n (\check{\varphi}_{n,J} \check{\varphi}_{n,J}^*) . \quad (3.30)$$

In this case, the value of Δ_J may be different for each mode depending on how strongly the available potential energy projects onto mode J. Recall that each mode is uniquely defined by the triplet of indices $J = (m, j, \ell)$. Also, note that the values of Δ_J are independent of the data. The projections of the various energy forms onto the modes are examined in further detail later in this chapter.

Part (b) of Δ_J is of primary concern in the present study as it provides a way of partitioning the normal modes according to their latitudinal structure. For each mode, this structure is determined by the sum of the Legendre polynomials $P_{m,n}$ in its horizontal expansion (3.10). Because the NOGAPS spectral model is truncated *triangularly* at zonal wave number $m = M = 47$, these expansions may include as few as $n = 1$ (for zonal wave number m=47), or as many as $n = 1, 2, \ldots, 47$ (for zonal wave number m=1) different $P_{m,n}$ for each mode; *i.e.*, the latitudinal structures of those modes corresponding to small wave numbers are better resolved than those corresponding to large wave numbers. For each mode, the sum of the $P_{m,n}$ describes the total latitudinal variance of that mode. We may think of the integrals in (b) as summing the latitudinal "pieces" of this variance. Thus, they obtain a value of 1 when

evaluated from $\mu = -1$ to $\mu = +1$, implying, of course, that 100% of the modal variance exists between the poles. Accordingly, for each mode, the value that (b) obtains over some range of latitude $\delta\mu$ gives an indication of the percentage of its total variance accounted for in that range of latitude. Thus, by choosing $\delta\mu$ judiciously, we can determine whether a given normal mode has most of its variance in the tropics, or in the extratropics, and whether this distinction reveals any differences in its behavior, energy balances, etc. For example, if, for a given mode, part (b) obtains a value of 0.9 when integrated between 20° N and 20° S, then this implies that most (approximately 90%) of the variance of that mode is accounted for within this latitudinal band.

It should be pointed out that these calculations provide only a close estimate of the latitudinal variance of each mode. This is because the Legendre polynomial property (3.23) holds only when the limits of integration range from $\mu = -1$ to $\mu = +1$. Otherwise, there are nonzero cross-terms in (3.25). Therefore, strictly speaking, we cannot say that the value 0.9 in the example above implies that exactly 90% of the variance of the mode is accounted for between 20° N and 20° S. However, the results in the following sections indicate that the cross-terms are small and so the estimates of the variances hold to a close approximation. Therefore, for convenience in the remainder of this study, we adopt the above convention of equating the value of (b) to the fraction of the modal variance within a given latitudinal band.

In practice, the use of (b) in (3.29) as a way of partitioning the modes requires that we make some further considerations. The first of these involves the selection of the latitude range $\delta\mu$. It should be noted that the integral in (b) involves the *squares* of the Legendre polynomials, which we can evaluate

numerically using Gaussian quadrature in the form

$$\int_{\mu_1}^{\mu_2} P_{m,n}^2(\mu)\, d\mu \approx \sum_i P_{m,n}^2(\mu_i)\, w_i , \qquad (3.31)$$

where the w_i are the weights given to the functional values $P_{m,n}^2(\mu_i)$ at the Gaussian latitudes μ_i (Abramowitz and Stegun, 1965). Because the functional values of the polynomials are squared at each point, any information concerning the asymmetry of the mode about the equator is lost. That is, this effect is transparent to those $P_{m,n}$ that are symmetric about the equator, but it improperly portrays the effect of those $P_{m,n}$ that have equal but opposite structure in the Northern and Southern Hemispheres. Therefore, only the modal variances in equatorially symmetric ranges of $\delta\mu$ can be distinguished from one another. For example, a distinction can be made between the modal variances in the ranges 5° N – 5° S and 20° N – 20° S, but not between the ranges 0° – 5° N and 0° – 5° S. It should be noted that acceptable ranges of $\delta\mu$ need not be contiguous across the equator, as long as they are symmetric about it. In this study, we define the "tropics" as the belt extending eight Gaussian latitudes from the equator in both hemispheres. For the NOGAPS spectral model, this corresponds to Gaussian latitudes μ_{29} thru μ_{44} and translates to the latitudinal belt between approximately 19° N and 19° S. For convenience, the remaining area in both hemispheres (approximately 19°–90°) is defined as the "midlatitudes." Note that the midlatitude region is symmetric, but not contiguous, about the equator. Unless otherwise stated, any references to the tropics or midlatitudes will be in terms of these definitions. Also, in the context of this study, and for grammatical convenience, the terms "midlatitude" and "extratropical" are used interchangeably. When appropriate, any necessary distinction between the two are also stated.

Another important consideration in the use of (b) in (3.29) as a latitudinal partitioning factor is to apply it in a way that optimally exposes any differences between tropical and midlatitude modes. In this study, two approaches are considered, both of which use some form of energy as the diagnostic quantity. In either approach, it is necessary to compute the normal mode coefficients of the difference field $(\alpha_J)_D$.

As stated at the beginning of Section 3.2, the normal modes are global functions, implying that their structures are defined at all latitudes. With this in mind, the philosophy of the first approach, which is based on a study by Ko *et al.* (1989), is simply to determine the tropical and midlatitude variances of each mode using (3.29), and then compute the energy from *all* the modes that is contributed by these portions of the variance. To do this, we first compute the factors $(\Delta_J)_{trop}$ and $(\Delta_J)_{mid}$ for each mode corresponding to the tropical and midlatitude portions of their variances. In accordance with the tropical and midlatitude ranges of $\delta\mu$ given above, these factors are given by

$$(\Delta_J)_{trop} = \sum_n \sum_{i=29}^{44} P_{m,n}^2(\mu_i)\, w_i \, , \qquad (3.32)$$

and

$$(\Delta_J)_{mid} = \sum_n \sum_{i=1;\, i=45}^{28;\, 72} P_{m,n}^2(\mu_i)\, w_i \, , \qquad (3.33)$$

where μ_1 represents the southernmost Gaussian latitude at approximately 88° S and μ_{72} represents the northernmost Gaussian latitude at approximately 88° N. To compute the anomalous tropical or midlatitude energy using the first approach, we would now apply these factors in a manner analogous to that of (3.28), in which each term in the sum is multiplied by the appropriate factor for

mode J. For example, the anomalous tropical energy would be given by

$$(E_D)_{trop} \approx \gamma \sum_J (\alpha_J)_D \, (\alpha_J^*)_D \, (\Delta_J)_{trop} \, . \qquad (3.34)$$

Note that, with this method, the total energy of the difference field is given by the sum of the tropical and midlatitude energies; $i.e.$, $E_D = (E_D)_{trop} + (E_D)_{mid}$. However, when the above procedure is implemented, and the results displayed in the format of Figures 3.3 and 3.4, there appear to be only minor differences between the tropical and midlatitude energy profiles, with a slightly more energetic response in the tropics at vertical mode $\ell = 4$. It is shown later that this increase in anomalous energy at $\ell = 4$ is indeed a characteristic of the tropical response, but it is underestimated in these results. Because the differences between these results and those of the global energy in Figures 3.3 and 3.4 are not very revealing, the former are not shown here. We discuss some of the reasons for the apparent failure of this approach later, in light of the results obtained from the second approach described below.

Although the first method described above seems to follow as a direct application of (3.28), it is difficult to interpret physically the result of extracting and quantifying only a portion of the total variance of each mode. In the second partitioning technique employed in this study, we take a different tack in that only selected subsets of the modes are used to define the tropical and midlatitude energy contributions, rather than the entire set of modes used in the previous method. With the new approach, we use the values of the variance factors $(\Delta_J)_{trop}$ and $(\Delta_J)_{mid}$ themselves as criteria for determining whether a mode should be classified as tropical or extratropical, and then group the modes accordingly. (Recall that the values of $(\Delta_J)_{trop}$ and $(\Delta_J)_{mid}$ are independent of the data, and thus, may be calculated in advance.) In this way, the energy

profiles for the tropics or midlatitudes can be computed using the simple expression (3.24), except that now the sum includes *only modes from the appropriate group.* Moreover, unlike the first approach, the total variance of mode J is included in each term in (3.24). This technique has the advantage of being easier to interpret physically, owing to the fact that each term in the sum in (3.24) represents the contribution from a theoretically complete entity.

To apply this technique, we must define some threshold values for the variance factors $(\Delta_J)_{trop}$ and $(\Delta_J)_{mid}$ that will be used to determine whether a mode should be classified as tropical or extratropical. However, there is no *a priori* way of knowing what threshold values of $(\Delta_J)_{trop}$ and $(\Delta_J)_{mid}$ adequately separate the two groups of modes. Instead, the most successful way to apply this technique is simply to plot the values of $(\Delta_J)_{trop}$ or $(\Delta_J)_{mid}$ as functions of the natural frequency of the corresponding mode, in order to see where a natural separation might exist.

Figures 3.5–3.7 show the values of $(\Delta_J)_{trop}$ corresponding to the RT, EG and WG modes respectively for the external ($\ell = 1$) vertical mode. Again, the values of $(\Delta_J)_{trop}$ are computed for $\delta\mu$ corresponding to the latitudinal belt from approximately 19° N – 19° S. Thus, for example, a value of $(\Delta_J)_{trop} = 0.8$ implies that 80% of the variance of mode J occurs within this range of latitude (in accordance with the convention discussed earlier). The value of $(\Delta_J)_{trop}$ for each mode is indicated by a "+" plotted as a function of the natural frequency of the mode; the frequencies are ordered from smallest to largest according to their absolute values. As explained in Section 3.1, this ordering is from largest to smallest spatial scales for the EG and WG modes, and from smallest to largest spatial scales for the RT modes. As before, all modes are represented

except those corresponding to zonal wave number $m = 0$

As we might expect, the tropical variances of the EG and WG modes in Figures 3.6 and 3.7 are more similar to one another than to those of the RT modes in Figure 3.5. However, for all mode types, there appears to be a lower cut-off of $(\Delta_J)_{trop} \approx 0.2$, implying that very few modes have less than 20% of their variance in the tropics. Put another way, it can be said that there are no purely extratropical modes (i.e., values at, or near, $(\Delta_J)_{trop} = 0$) accordi. to this definition. In contrast, we note that for all mode types in Figures 3.5–3.7, there are modes for which $(\Delta_J)_{trop} = 1$, implying that 100% of their variance occurs within the tropics. These modes are discussed in greater detail shortly. The value of the lower cut-off in Figures 3.5–3.7 depends on the latitudinal range $\delta\mu$, and increases or decreases in accordance with the limits of integration in part (b) of (3.29). For example, if $\delta\mu$ were to extend from pole to pole, then *all* modes would lie at $(\Delta_J)_{trop} = 1$, implying that 100% of the variance of all the modes is accounted for within this range of latitude.

The values of $(\Delta_J)_{trop}$ in Figures 3.5–3.7 appear to be organized into discrete bands that arc downward from left to right for the RT modes in Figure 3.5, and downward from right to left for the EG and WG modes in Figures 3.6 and 3.7. It turns out that each band represents a family of modes having the same normal mode index j (Section 3.1). Each mode in a given band, or j-family, corresponds to a different zonal wave number m. In the NOGAPS spectral model there are forty-seven such families, excluding the zonally symmetric ($m = 0$) modes. Because of the triangular truncation of the model, the number of modes in each band varies from forty-seven (for $j = 1$) down to one (for $j = 47$). For the RT modes, the $j = 1$ family is the upper-right
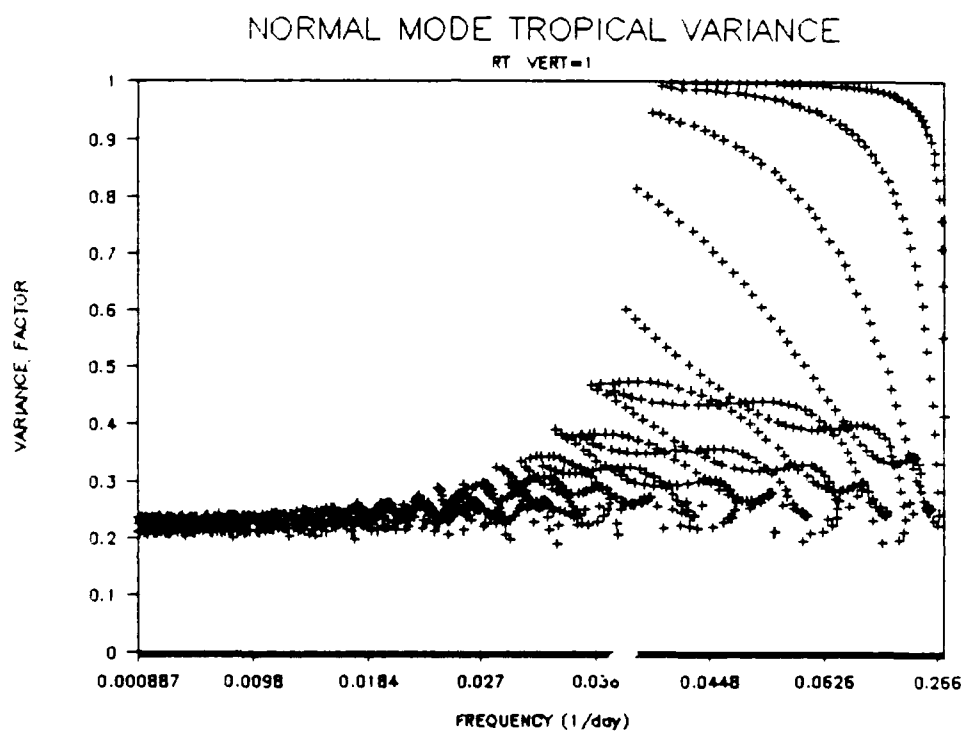
NORMAL MODE TROPICAL VARIANCE

RT VERT=1

Figure 3.5   Values of the variance factors $(\Delta_J)_{trop}$ for the external RT modes
as functions of the mode frequencies. The values along the
ordinate correspond to the fraction of the modal variance between
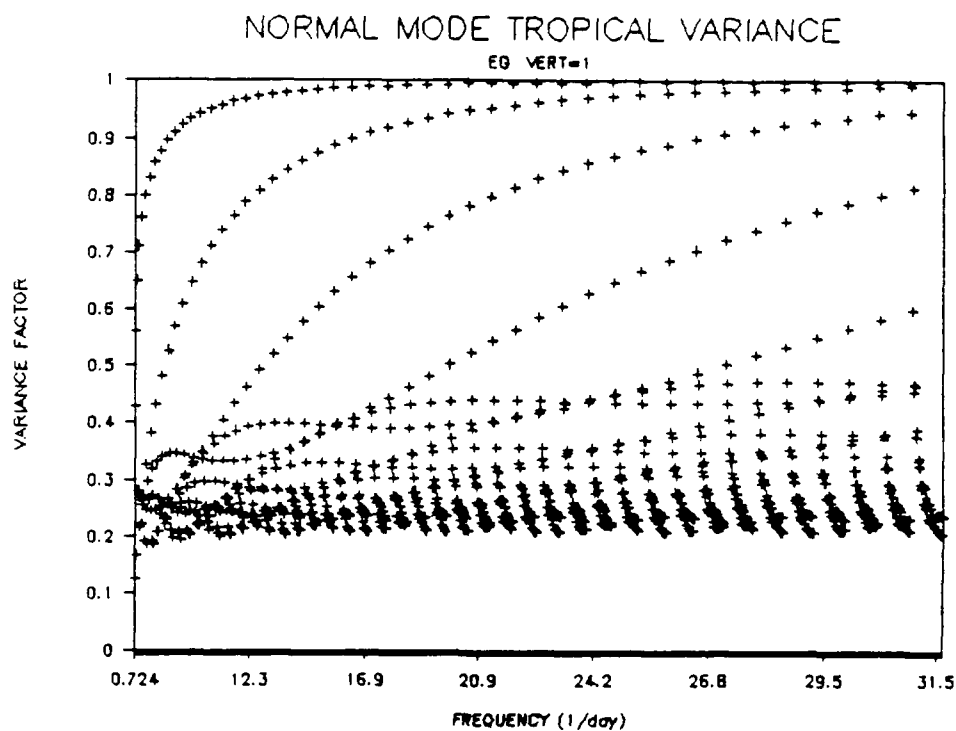19° N and 19° S.

NORMAL MODE TROPICAL VARIANCE

Figure 3.6   As in Figure 3.5, except for the external EG modes.
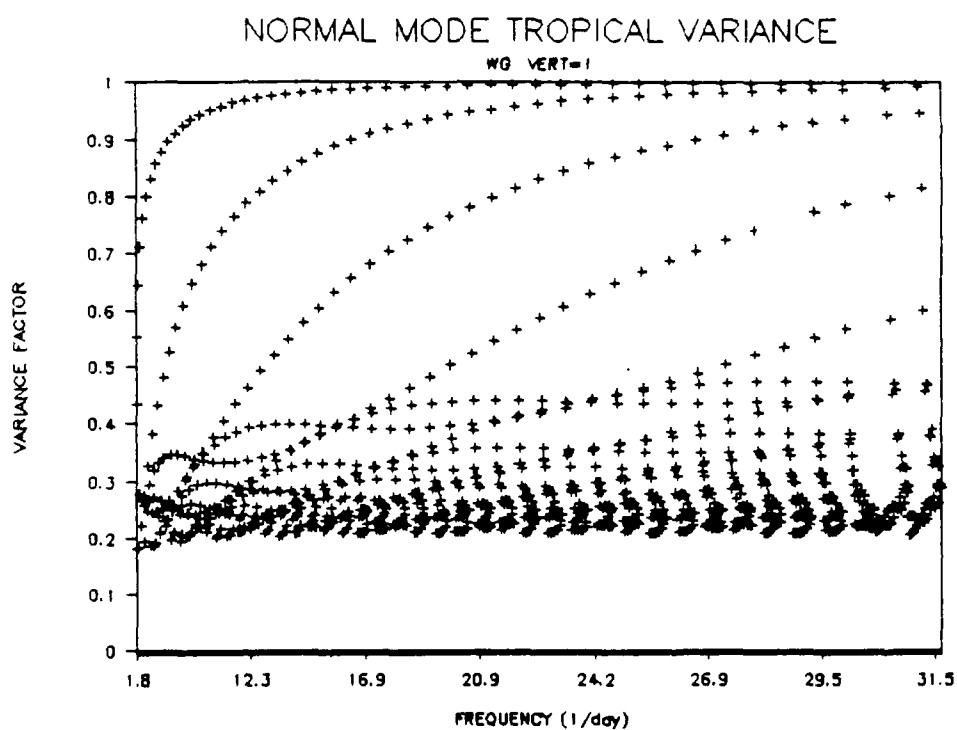
Figure 3.7   As in Figure 3.5, except for the external WG modes.

most band in Figure 3.5, and represents the mixed Rossby-gravity modes. Note that many of these modes are tropically trapped, having relatively large values of $(\Delta_J)_{trop}$. The $j = 1$ families for the EG and WG modes are the upper-left most bands in Figures 3.6 and 3.7 respectively. For the EG modes in Figure 3.6, the $j = 1$ family represents the low-frequency Kelvin modes discussed earlier. Again, it has been shown that these modes are important in tropical circulations. This is consistent with Figure 3.6, which shows that most of the modes in the $j = 1$ family have values at, or very close to, $(\Delta_J)_{trop} = 1$. For all mode types, we note that the bands become less distinguishable from one another as the value of j increases (i.e., as we move toward the bottoms of the figures). Also, it seems that for all mode types, those modes with large meridional structure (small values of j) have more of their variance in the tropics than those with smaller meridional structure (large values of j). For example, in Figures 3.8 and 3.9, we have isolated values of $(\Delta_J)_{trop}$ corresponding to the two families $j = 5$ and $j = 20$ respectively for the $\ell = 1$ EG modes in Figure 3.6. Note that several of the $j = 5$ modes in Figure 3.8 have more than 50% of their variance in the tropics, while none of the $j = 20$ modes in Figure 3.9 has even 30% of their variance in this region. Also note that there are more $j = 5$ modes (43) than there are $j = 20$ modes (28) because of the triangular truncation of the NOGAPS spectral model.

In contrast to Figures 3.8 and 3.9, Figures 3.10 and 3.11 show values of $(\Delta_J)_{trop}$ corresponding to the two zonal wave numbers $m = 5$ and $m = 20$ for the EG modes in Figure 3.6. When separated by zonal wave number m instead of by normal mode index j, the modes fall into less coherent patterns that are not individually identifiable when all the modes are present as in Figure 3.6. For

example, the $m = 5$ Kelvin mode is well separated from the remaining modes in Figure 3.10, appearing on the far left of the figure with the value $(\Delta_J)_{trop} \approx 0.76$. Similarly, the $m = 20$ Kelvin mode in Figure 3.11 has the value $(\Delta_J)_{trop} \approx 0.98$, although the $j = 2$ and $j = 3$ modes for this zonal wave number also exhibit considerable variance in the tropics, having values of $(\Delta_J)_{trop}$ of approximately 0.85 and 0.59 respectively. Neither the pattern in Figure 3.10, nor the one in Figure 3.11, is apparent in Figure 3.6.

Clearly, there is much more information that can be gleaned from plots of Δ_J for various ranges of $\delta\mu$. For example, it is interesting to note that the RT modes in Figure 3.5 exhibit very little tropical variance at frequencies less than 0.036 per day. This is manifested by the absence of modes in the center- and upper-left portions of Figure 3.5. At this time, it is unclear whether there is some theoretical basis for this sharp cut-off. Although the plots themselves are not the primary interest in this study, they may have applicability in other areas, such as in nonlinear normal mode initialization, or in the development of limited (severely truncated) atmospheric models. These are discussed briefly in Chapter 5. Presently, we are interested in using these plots to distinguish between tropical and midlatitude modes. To do this, it is only necessary to consider values of $(\Delta_J)_{trop}$ in order to identify both the tropical and midlatitude modes since $(\Delta_J)_{trop}$ and $(\Delta_J)_{mid}$ sum to one according to their present definitions (3.32) and (3.33). Also, it should be noted that plots for the remaining vertical modes (not shown) analogous to those in Figures 3.5–3.7, reveal similar patterns for their corresponding frequency ranges.

In all of these figures, it appears that the first five or six families of modes demonstrate a definite increase in tropical variance compared with the
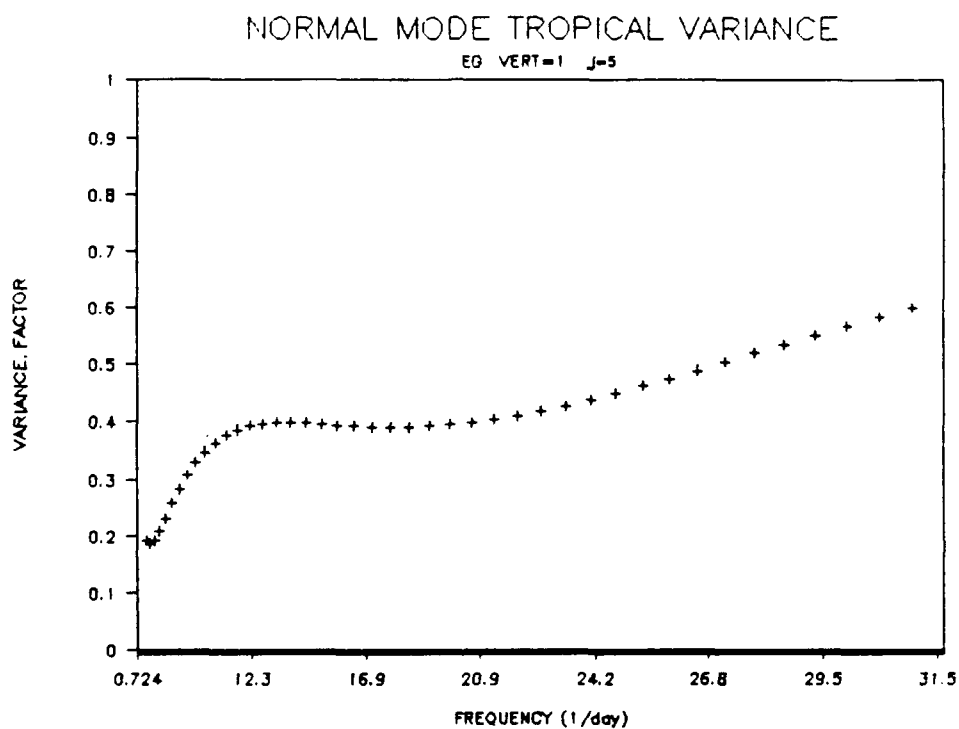
NORMAL MODE TROPICAL VARIANCE

EG VERT=1 J=5

Figure 3.8   Values of the variance factors $(\Delta_J)_{trop}$ corresponding to the $j = 5$ family of external EG modes in Figure 3.6.

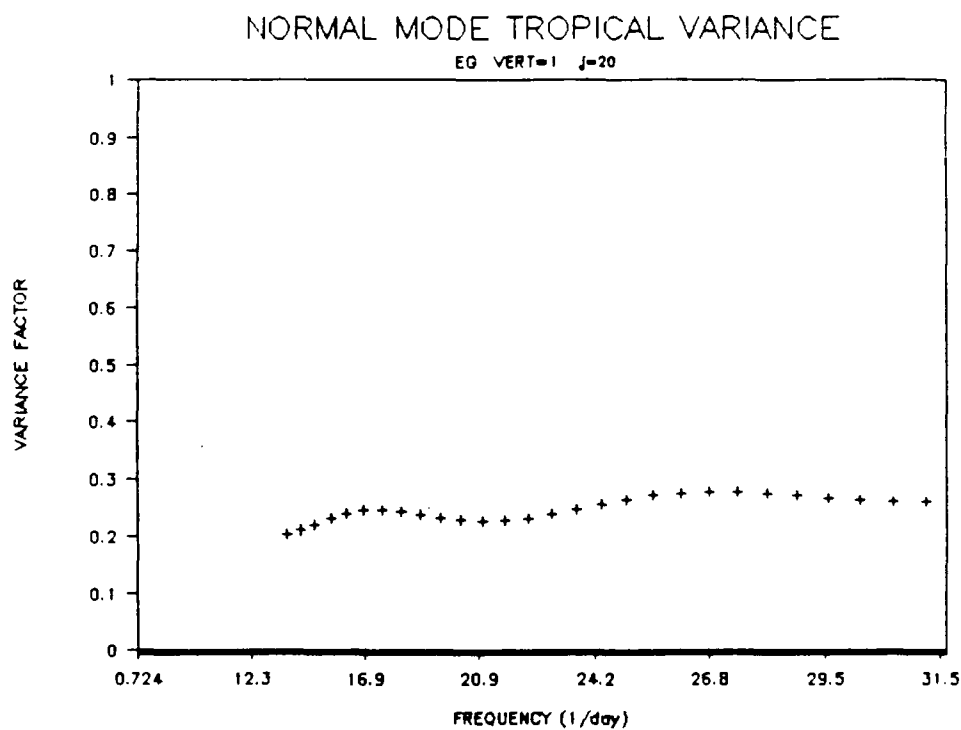## NORMAL MODE TROPICAL VARIANCE

EG VERT=1 J=20

Figure 3.9   As in Figure 3.8, except for the $j = 20$ family of external EG modes in Figure 3.6. Note that, in this case, there are fewer modes (28) than in Figure 3.8 (43), owing to the triangular truncation of the model.

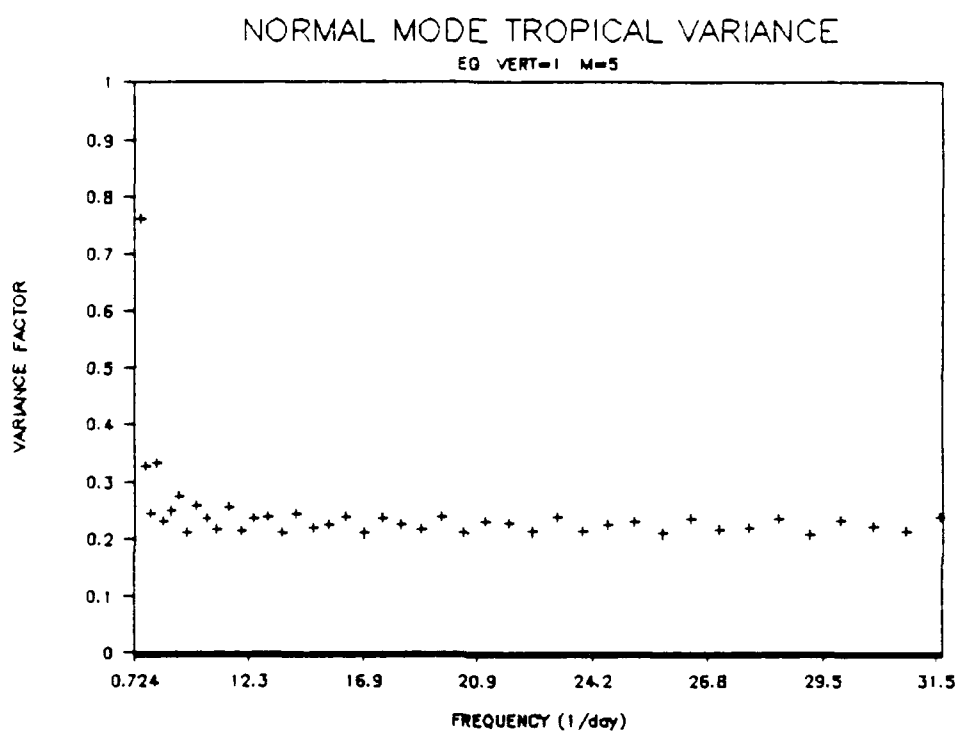NORMAL MODE TROPICAL VARIANCE
EG VERT=1 M=5

Figure 3.10   Values of the variance factors $(\Delta_J)_{trop}$ corresponding to the $m = 5$ external EG modes in Figure 3.6. The Kelvin mode appears at the extreme left and has the value $(\Delta_J)_{trop} \approx 0.76$.

NORMAL MODE TROPICAL VARIANCE
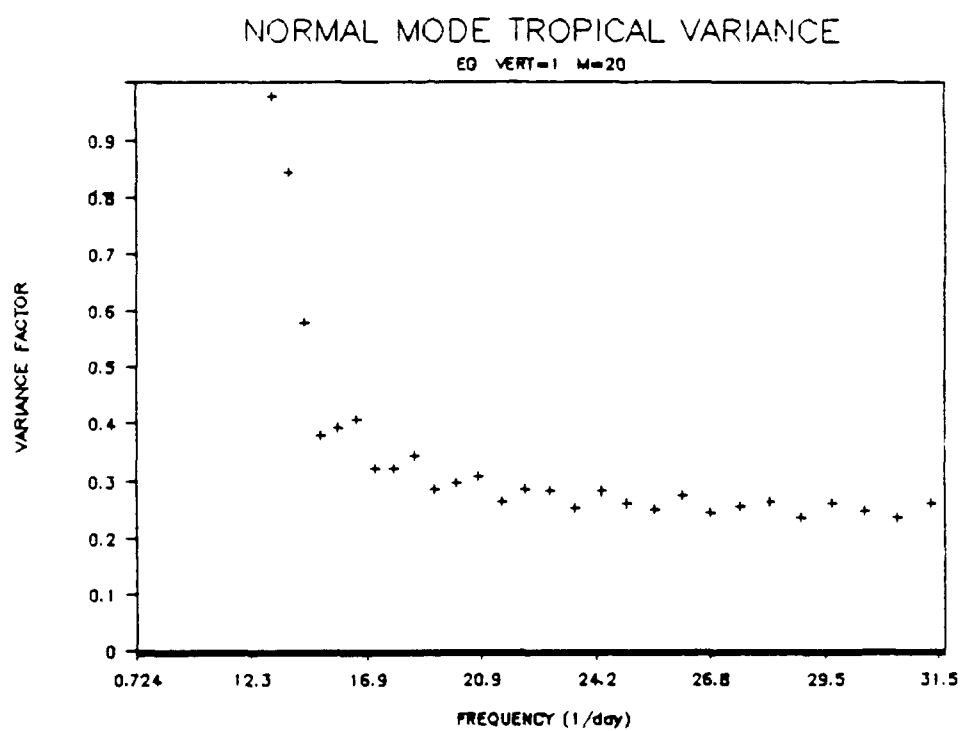
EG VERT=1 M=20

Figure 3.11   As in Figure 3.10, except for the $m = 20$ external EG modes in Figure 3.6. In this case, the Kelvin mode has the value $(\Delta_J)_{trop} \approx 0.98$.

remaining families. Most of the modes in these families have values of approximately $(\Delta_J)_{trop} \geq 0.4$. Based on these observations, we will classify modes for which $(\Delta_J)_{trop} \geq 0.4$ as "tropical" modes, and those for which $(\Delta_J)_{trop} \leq 0.3$ as "midlatitude" modes (recall that the latter is synonymous with $(\Delta_J)_{mid} \geq 0.7$). Those modes for which $0.3 < (\Delta_J)_{trop} < 0.4$ are difficult to classify as belonging entirely in one group or the other, and so are excluded. Therefore, with this approach, $E_D \neq (E_D)_{trop} + (E_D)_{mid}$. However, compared with the first approach, the values of $(E_D)_{trop}$ and $(E_D)_{mid}$ provide a sharper (but still physically realistic) separation between the characteristics of the tropical and midlatitude contributions to the energy of the anomalous response.

It is important to note that, with the threshold values selected above, the first several vertical modes contribute roughly the same number of horizontal modes to the energy *within* each group. Table 3.1 shows the numbers of RT, EG and WG modes in the "tropical" and "midlatitude" groups for each vertical mode, based on these threshold values. Note that, for approximately the first eight vertical modes, the number of horizontal modes of each type is fairly evenly distributed within each group; there are between 200-220 tropical modes of each type, and 710-740 midlatitude modes of each type for a given value of ℓ. This allows a fair comparison to be made between the relative contributions of each vertical mode to either the tropical or midlatitude energies in a manner similar to that in Figures 3.3 and 3.4. The numbers of modes of each type begin to increase or decrease more quickly for $\ell > 10$, but these modes are of little interest in the present analysis. There are, of course, more midlatitude modes than tropical modes because of the difference in the latitudinal ranges $\delta\mu$ that we use to define each region. It turns out that, for each vertical mode, the two

Table 3.1 The numbers of RT, EG and WG modes classified as "tropical" or "midlatitude" for each vertical mode ℓ, based on the threshold values $(\Delta_J)_{trop} \geq 0.4$ and $(\Delta_J)_{mid} \geq 0.7$, respectively.

ℓ	Tropical			Midlatitude		
	RT	EG	WG	RT	EG	WG
1	204	204	204	748	748	748
2	203	203	204	746	748	748
3	205	204	204	744	748	744
4	208	205	204	739	747	741
5	215	210	211	733	740	732
6	216	212	217	726	733	722
7	217	215	214	719	729	713
8	224	217	216	709	716	701
9	231	225	227	688	698	675
10	238	234	234	671	679	650
11	241	237	238	657	666	631
12	245	240	246	646	655	620
13	246	245	249	634	651	612
14	254	248	253	630	643	609
15	258	250	259	630	637	604
16	256	254	263	630	634	598
17	255	256	265	632	634	596
18	250	255	271	633	634	593

groups account for roughly 85% of the total number of modes in the complete (global) set. That is, 15% of the complete set have values $0.3 < (\Delta_J)_{trop} < 0.4$, and are not included in either group.

We can view the subsets of modes in each group as "tracer" modes, because they exhibit a predominant portion of their variance in either the tropics or midlatitudes. Henceforth, when computing the tropical or midlatitude energy via (3.24), we will be considering only these tracer modes in order to emphasize any differences between the tropical and midlatitude energy profiles. Further justification for the threshold values of $(\Delta_J)_{trop}$ and $(\Delta_J)_{mid}$ discussed above are given in later sections. In Sections 3.3 and 3.4, we use this latitudinal partitioning technique to re-examine the normal mode energy profiles in Figures 3.3 and 3.4.

3.3 Tropical Modes

The normal mode partitioning technique developed in Section 3.2.2 is now used to analyze the tropical response of the NOGAPS spectral model for the anomalous forcing simulations described in Chapter 2. As stated earlier, there is much evidence that the tropical response may be quite different from that of the midlatitudes. By isolating the vertical and horizontal modes that contribute significantly to this response, we hope to gain some insight into the dynamical processes that shape the anomalous tropical circulation.

As in Section 3.2.1, we begin by examining the quasi-steady anomalous response, which we approximate from the 30-day mean composite difference fields for the ESSTA and WSSTA simulations described in Chapter 2. Figures 3.12 and 3.13 show the tropical energy of the various mode types for the

TROPICAL EDDY ENERGY (RT)

ESSTA DIFFERENCE FIELD d(21-50)

a

TROPICAL EDDY ENERGY (EG)

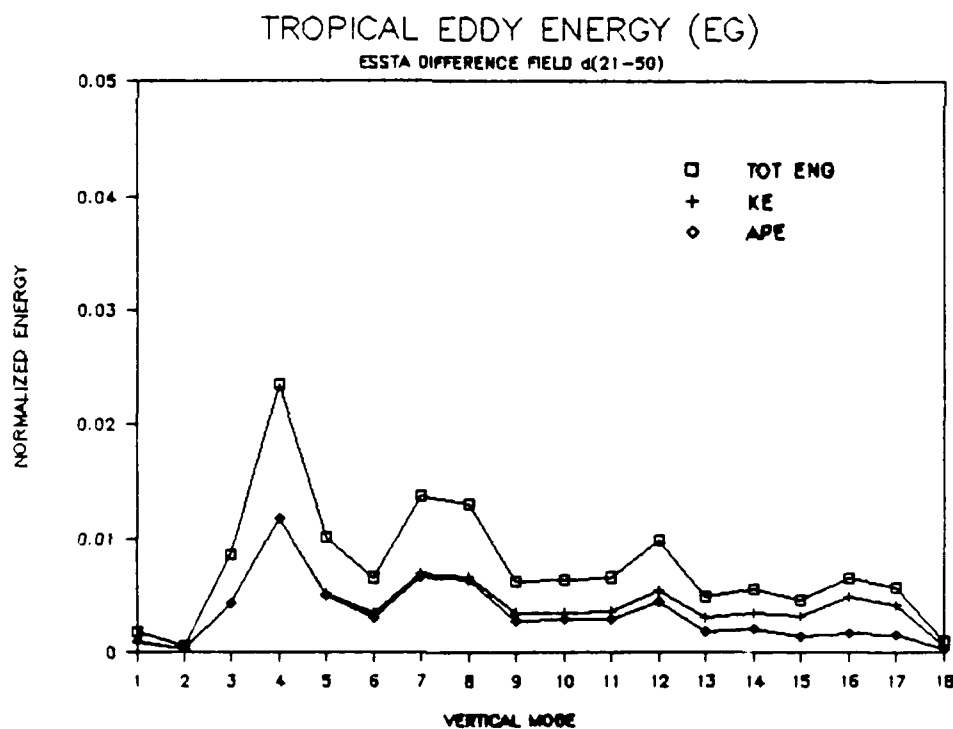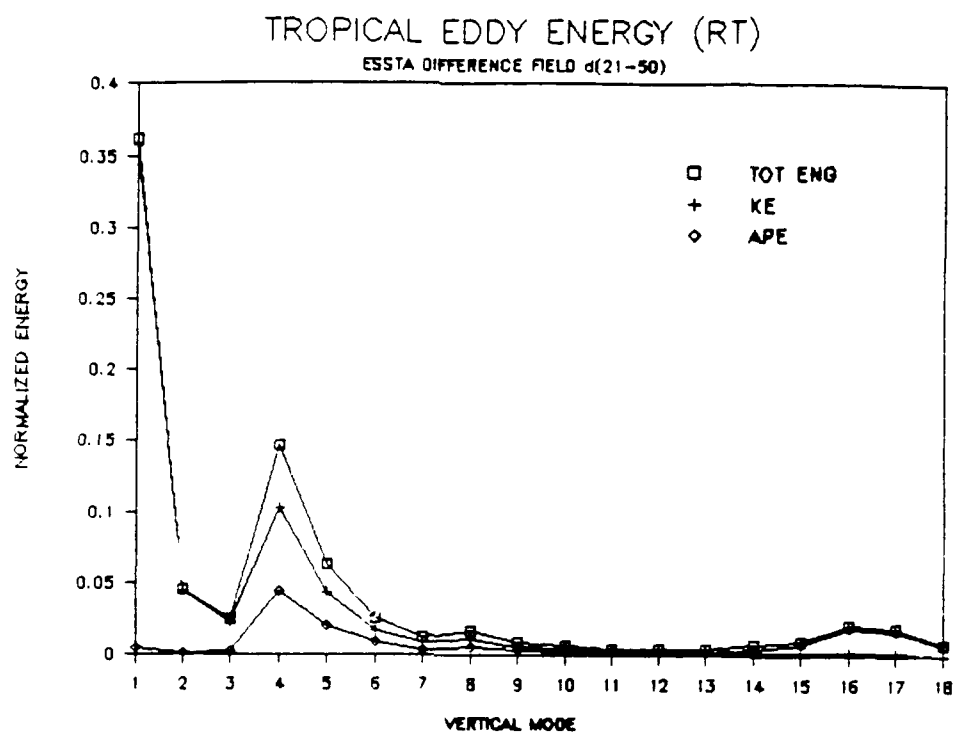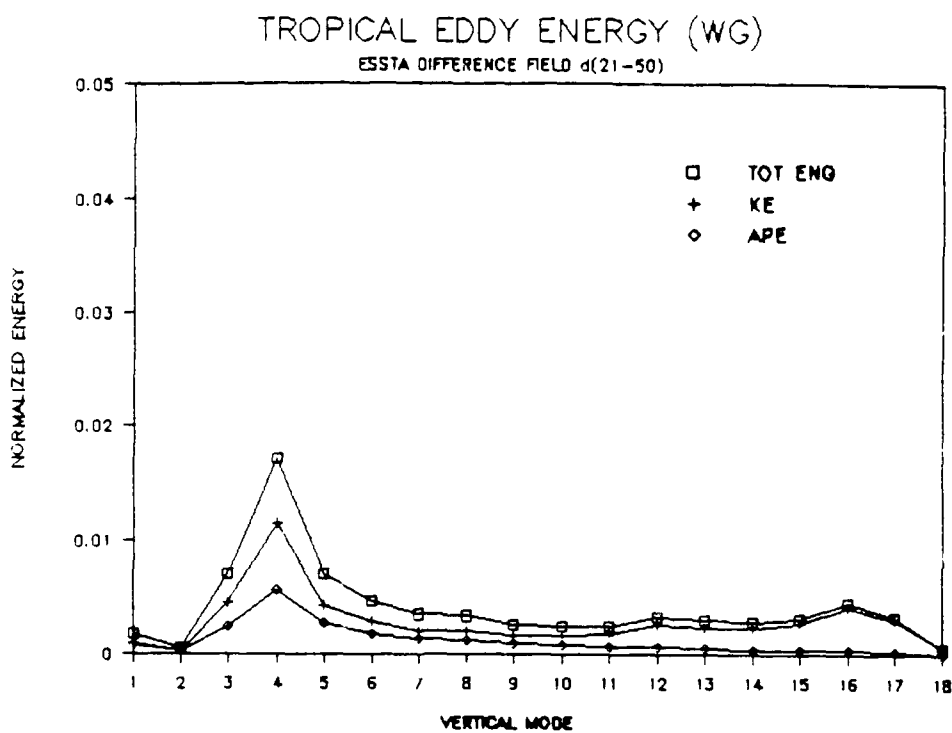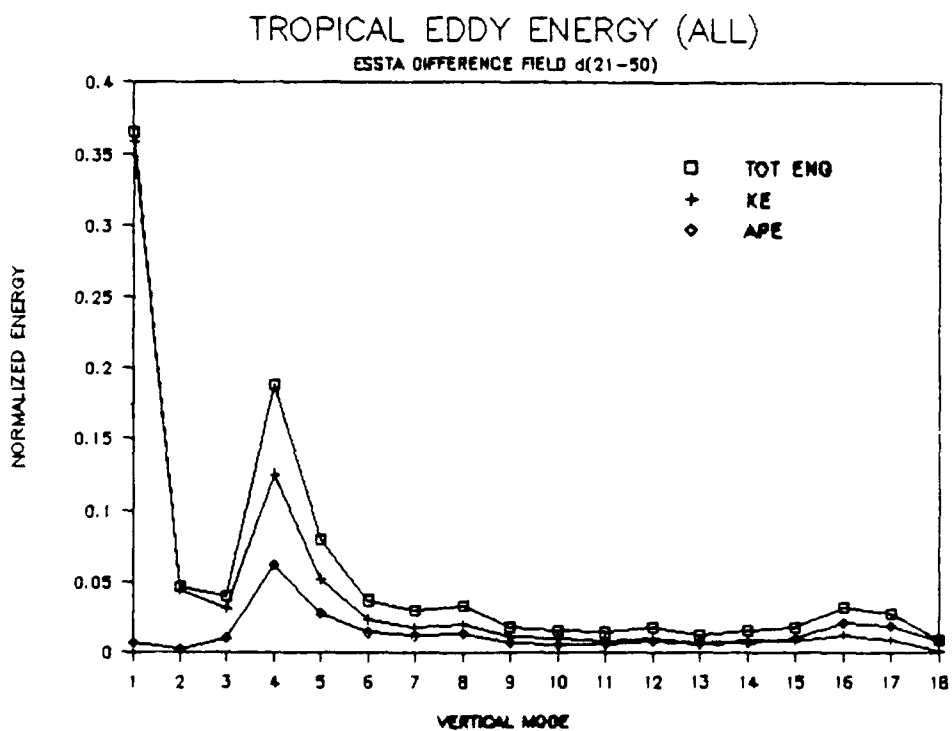### ESSTA DIFFERENCE FIELD d(21-50)

b

Figure 3.12   The contributions to the tropical eddy energy of the 30-day mean difference field for days 21–50 in the EsSTA simulation from the (a) RT, (b) EG, (c) WG and (d) ALL modes, as a function of vertical mode ℓ. Only modes for which $(\Delta_J)_{trop} \geq 0.4$ are included.

TROPICAL EDDY ENERGY (WG)

ESSTA DIFFERENCE FIELD d(21-50)

c

TROPICAL EDDY ENERGY (ALL)

ESSTA DIFFERENCE FIELD d(21-50)

d

Figure 3.12 (continued)

TROPICAL EDDY ENERGY (RT)

WSSTA DIFFERENCE FIELD d(21-50)

a

TROPICAL EDDY ENERGY (EG)

WSSTA DIFFERENCE FIELD d(21-50)

b
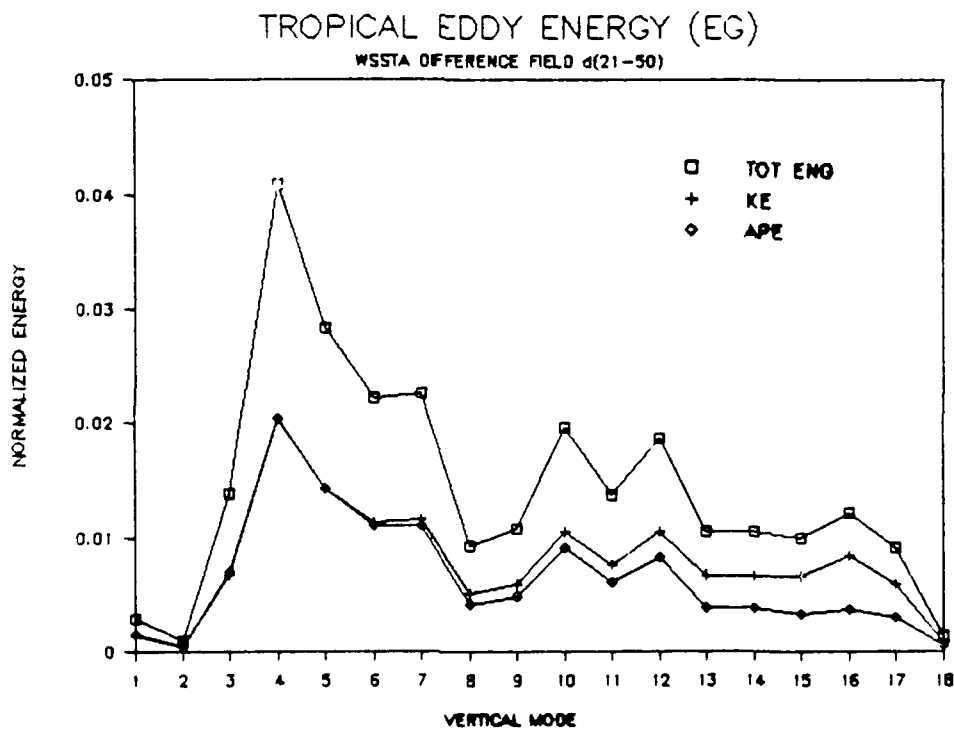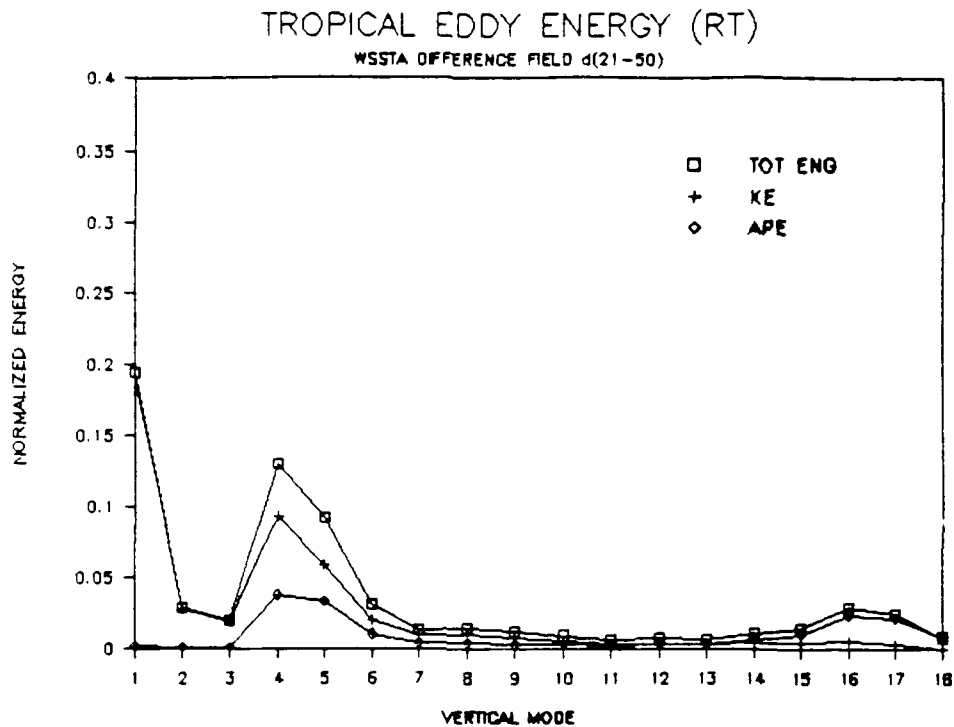
Figure 3.13   As in Figure 3.12, except for the WSSTA simulation.

TROPICAL EDDY ENERGY (WG)

c

TROPICAL EDDY ENERGY (ALL)
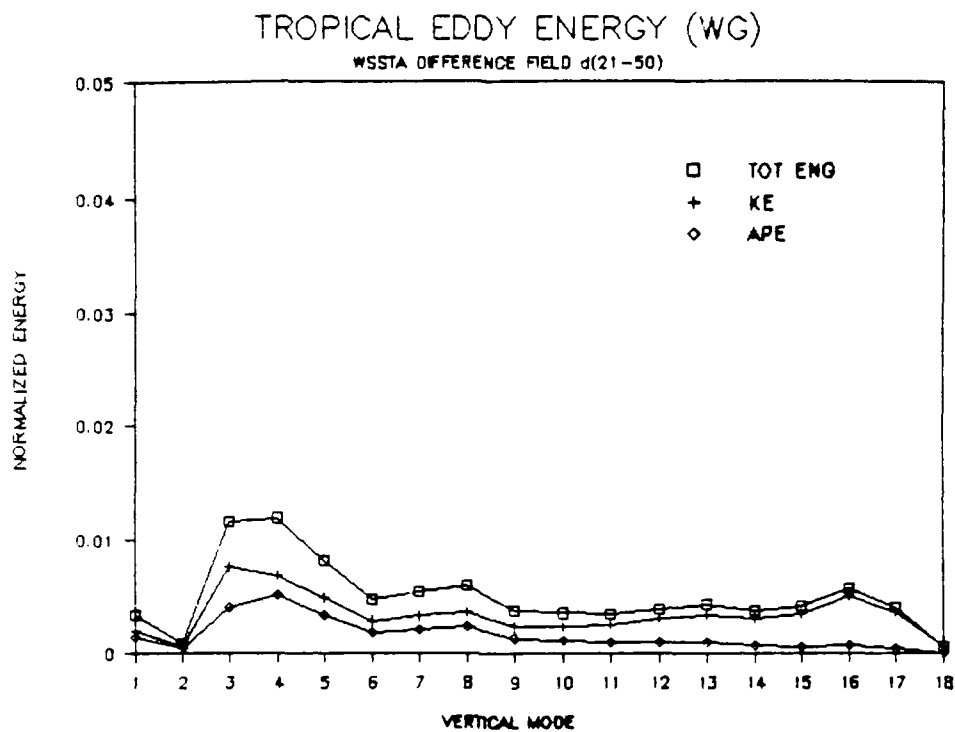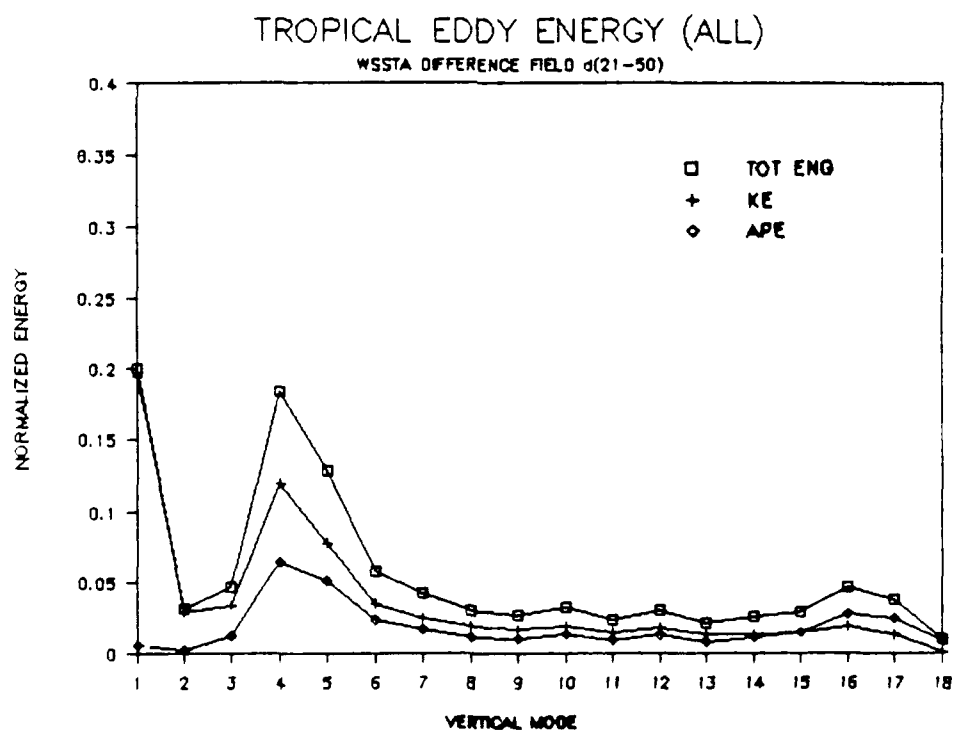
d

Figure 3.13 (continued)

ESSTA and WSSTA simulations respectively, as a function of vertical mode ℓ.
In accordance with the technique developed in Section 3.2.2, these figures only
depict the energy of those modes for which $(\Delta_J)_{trop} \geq 0.4$. In these figures, each
plotted value is normalized by the sum of the values over all ℓ for all mode types
corresponding to the *tropical* modes only. Thus, each value gives an estimate of
the contribution from vertical mode ℓ to the tropical energy of the total
difference field. In addition to the tropical total energy, Figures 3.12 and 3.13
show the tropical kinetic and tropical available potential energy for each vertical
mode. These quantities are obtained by multiplying each term in (3.24) by the
factors

$$(\Delta_J)_{KE} = \sum_n (\tilde{\varsigma}_{n,J} \, \tilde{\varsigma}_{n,J}^* + \tilde{D}_{n,J} \, \tilde{D}_{n,J}^*) \,, \tag{3.35}$$

or

$$(\Delta_J)_{APE} = \sum_n (\tilde{\varphi}_{n,J} \, \tilde{\varphi}_{n,J}^*) \,, \tag{3.36}$$

which are derived from (3.29) and represent the projections onto mode J of the
kinetic and available potential energies respectively. Recall that $\tilde{\varsigma}_{n,J}$, $\tilde{D}_{n,J}$ and
$\tilde{\varphi}_{n,J}$ are the dimensionless spherical harmonic expansion coefficients for the
Hough functions, or horizontal modes.

Figure 3.12a shows the contribution of the RT modes to the tropical
energy of the 30-day mean difference field for the ESSTA simulation. This figure
may be compared with Figure 3.3a (bearing in mind that they are normalized
differently), which shows the contributions of the modes to the global energy.
Both figures exhibit a prominent external $(\ell = 1)$ mode response with
comparable amplitude. It can be seen in Figure 3.12a that the total energy of
the external modes is composed almost entirely of kinetic energy. This is
consistent with the fact that the external modes are essentially barotropic, and

therefore, describe motions in which there are no conversions between available potential energy and kinetic energy. The prominence of the external RT modes in both Figures 3.3a and 3.12a suggests that these modes may play an important role in tropical-midlatitude interactions. It is shown in Chapter 4 that they in fact behave like nondivergent barotropic Rossby waves that have propagated out of the tropics toward higher latitudes, and represent a significant component of the quasi-steady response. As discussed in Chapter 1, many investigators have observed this phenomenon in simulations with both simple and sophisticated models to study the global response to anomalous tropical forcing. In addition, observational studies, such as those by Horel and Wallace (1981) and Wallace and Gutzler (1981), have revealed the existence of nondivergent barotropic centers of action in the atmosphere during years with anomalously warm tropical SST. It is shown in Chapter 4 that these meridionally propagating waves partially explain the standing wave patterns in the mean difference fields of stream function and geopotential height discussed in Chapter 2. We note a similar external mode response in Figure 3.13a for the WSSTA simulation, although it is not as strong as that in Figure 3.12a. At this time, it is unclear whether the weaker external mode response in the WSSTA simulation is a manifestation of the natural variability of the model, or the effect of some other dynamical process.

Although we emphasize again that it is not the goal of this study to make a detailed comparison between the ESSTA and WSSTA simulations, the difference in strength between the external mode responses in Figures 3.12a and 3.13a highlights an important point concerning the formation and growth of the propagating response. One important factor in this process may be local

differences in the vertical wind shear in the regions of the SST anomalies. It has been shown by Lim and Chang (1986) that this may be of critical importance in determining the strength of an internally forced external mode response. Lim and Chang point out that internal forcing such as convective heating (which is the primary heat source in the presence of an SST anomaly) is expected to excite essentially only internal (baroclinic) motions. They argue that the response amplitude A of a vertical mode with structure $Z(p)$ excited by a heat source $Q(p)$ is given by

$$A = - \int_0^{p_0} Z(p) \frac{\partial}{\partial p} \left[\frac{R Q(p)}{c_p \, p \, \sigma} \right] dp \,, \tag{3.37}$$

where R, c_p, σ and p_0 are the gas constant, specific heat at constant pressure, static stability parameter and surface pressure, respectively. For the external mode, $Z(p)$ is nearly constant in the troposphere as shown in Figure A.1a. If $Q(p)$ is negligible above the troposphere, then (3.37) is closely approximated by

$$A \approx - \left[Z(p_0) \frac{R Q(p)}{c_p \, p \, \sigma} \right]_0^{p_0} = - Z(p_0) \frac{R Q(p_0)}{c_p \, p_0 \, \sigma(p_0)} \,. \tag{3.38}$$

Now, with internal forcing, the surface heating $Q(p_0)$ is negligible, which implies that the response amplitude A of the external mode is negligible as well. However, Lim and Chang go on to show that other processes, such as vertical wind shear and differential damping, act to couple the internal and external modes, allowing an external mode response to develop over a period of time. In their two-layer model, it takes approximately two weeks or more for an internal forcing to develop a nearly steady external mode response. Once developed, the external mode accounts for 20% to 60% of the kinetic energy of the total response, depending on the strength of the vertical wind shear in their model.

The magnitudes of the steady state responses for the external RT modes in Figures 3.12a and 3.13a agree well with these results. In the present study,

the 30-day mean vertical wind shears have not been calculated, so we are unable to determine explicitly whether this effect accounts for the differences between the external mode responses in the ESSTA and WSSTA simulations. However, the evolution of the external mode energy in the ESSTA and WSSTA simulations is very similar to that observed by Lim and Chang. For example, Figure 3.14a shows the evolution of the energy in the tropical RT modes for the WSSTA difference field. Here, consecutive five-day mean values of the energy are plotted for the first five vertical modes of the NOGAPS spectral model (the remaining vertical modes are of little dynamical interest in the present context and have been omitted for clarity). Each plotted value has been normalized as in previous figures. The curve for the external mode in Figure 3.14a (denoted by boxes) clearly suggests a period of growth that lasts up to three weeks before settling into an approximate steady state. After this time, the external RT modes remain the most energetic of all the modes, although the $\ell = 4$ response is obviously important as well. As indicated by Figures 3.14b and 3.14c, at no time do the external gravity modes contribute significantly to the anomalous tropical response.

The main point here is that the evolution of the external mode response clearly displays the behavior associated with the growth mechanism suggested by Lim and Chang. If we assume that this mechanism operates to some degree in the atmosphere, then there are implications concerning our ability to forecast the impact of SST anomalies on the general circulation. For example, we might speculate that a significant amount of energy may escape to the midlatitudes even when the tropics are only marginally disturbed, provided that the prevailing vertical wind profile can maximize the coupling between the internal

TROPICAL ENERGY GROWTH (RT)

WSSTA DIFFERENCE FIELD

a

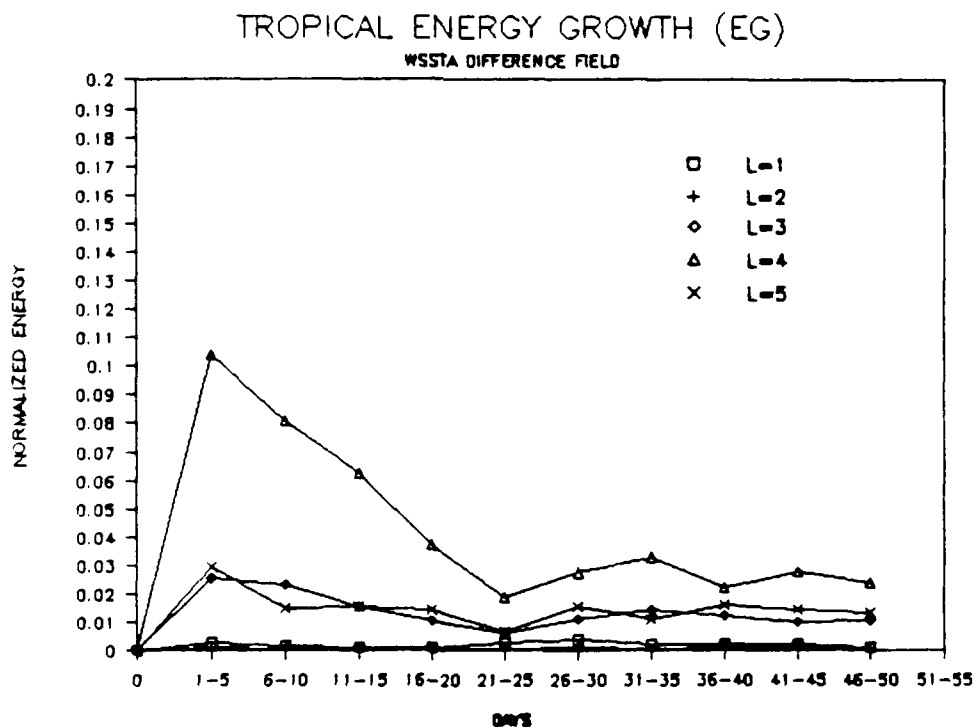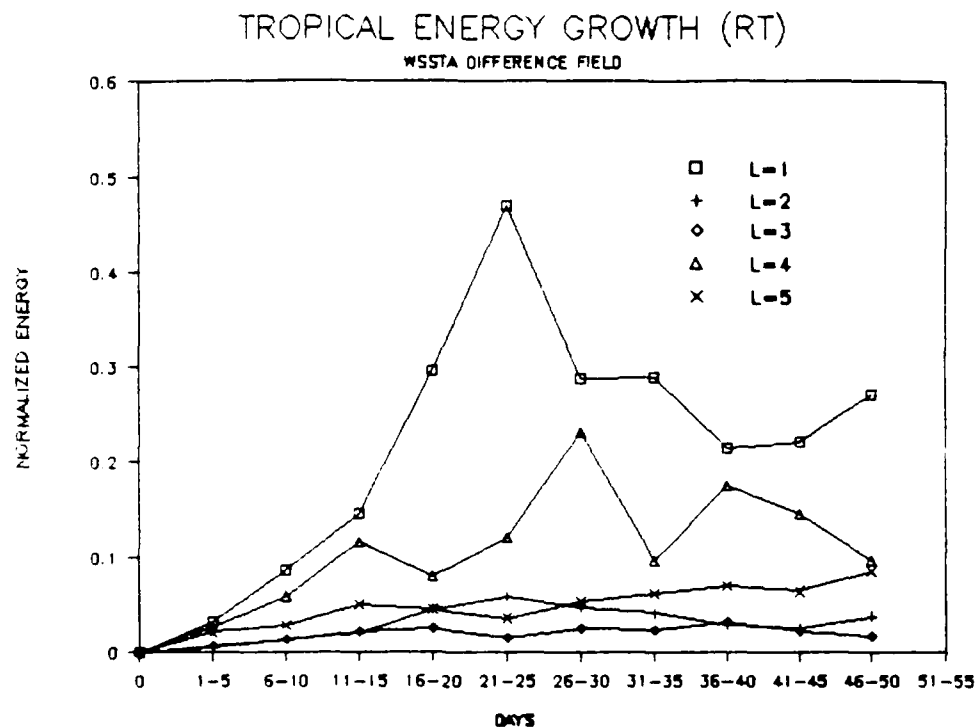## TROPICAL ENERGY GROWTH (EG)

WSSTA DIFFERENCE FIELD

b

Figure 3.14   The evolution (in terms of five-day means) of the total tropical eddy energy in the first five vertical modes of the NOGAPS model for the difference field in the WSSTA simulation, for the (a) RT, (b) EG, (c) WG and (d) ALL modes.

TROPICAL ENERGY GROWTH (WG)

WSSTA DIFFERENCE FIELD

c

TROPICAL ENERGY GROWTH (ALL)
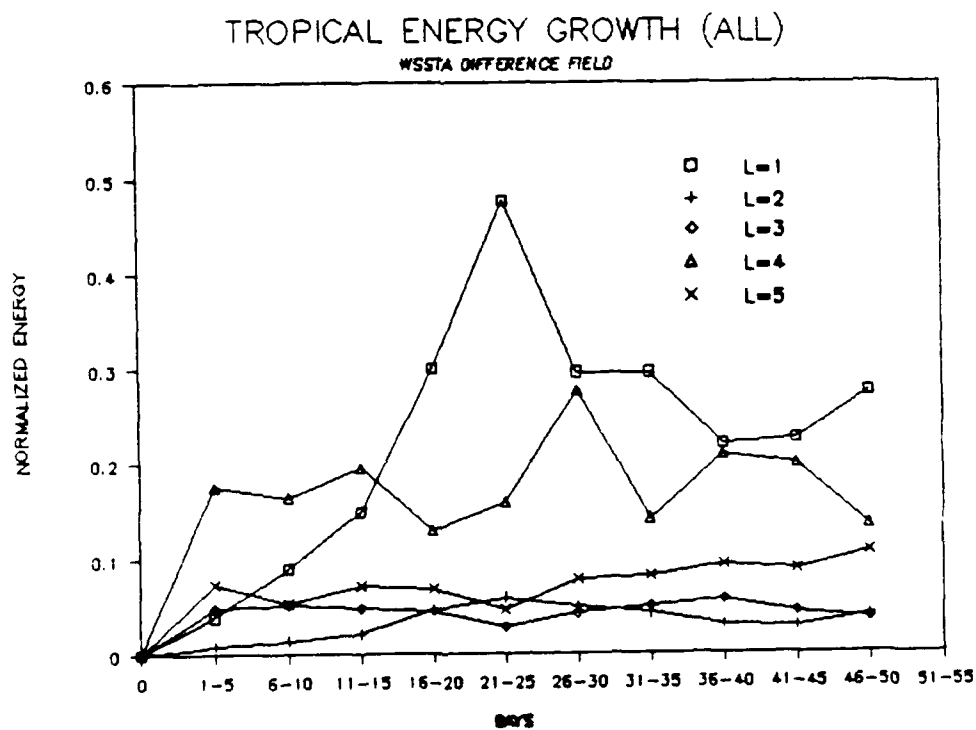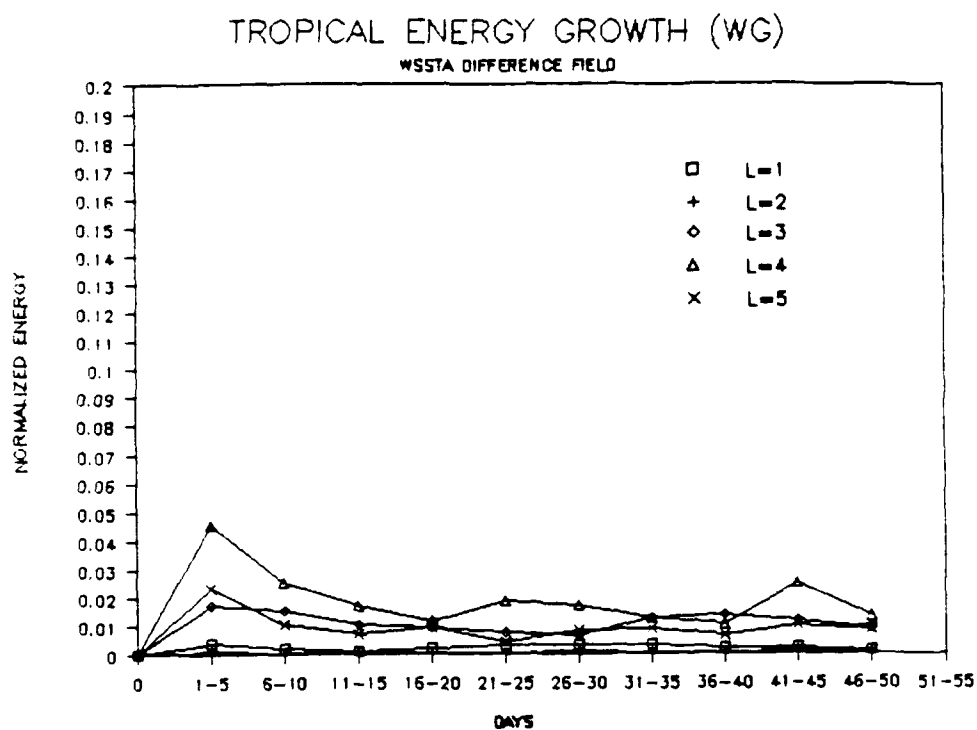
WSSTA DIFFERENCE FIELD

d

Figure 3.14 (continued)

and external modes. Conversely, episodes of extreme anomalous forcing may have little or no impact at all at higher latitudes under less favorable tropical wind conditions. The variability of the atmospheric response to anomalous warmings in the tropical SST has been documented in both observational and modeling studies such as those by Hamilton (1988) and Palmer and Mansfield (1986). It should be noted that other factors also may influence the propagating response, such as the horizontal shear of the mean zonal wind and the location of the SST anomaly. The impact of this propagating response on the midlatitude circulation is demonstrated in Chapter 4. In any case, the growth mechanism suggested by Lim and Chang may provide the first link in a chain of dynamic interactions whereby localized atmospheric forcing can eventually influence the general circulation.

In contrast to the external RT mode response in Figure 3.12a, the internal RT mode response in the tropics differs significantly from its global counterpart in Figure 3.3a. The tropical $\ell = 4$ response in Figure 3.12a is clearly dominant among the internal modes, contributing 15% of the tropical total energy in the anomalous response. This is more than twice the energy of the $\ell = 5$ response which, in contrast, is clearly the dominant internal mode in terms of the global energy in Figure 3.3a. At the same time, the substantial response at $\ell = 4$ in Figure 3.3a is consistent with the results in Figure 3.12a and reflects the fact that these are the dominant internal modes in the tropics. A similar, but less dramatic, reversal in the relative magnitudes of the $\ell = 4$ and $\ell = 5$ responses in the tropics is observed in the WSSTA simulation (Figures 3.4a and 3.13a). The fact that the $\ell = 4$ RT modes are the dominant internal modes in the tropics, while the $\ell = 5$ RT modes are dominant globally, implies that the $\ell = 5$ modes

contribute significantly to the *midlatitude* response. This is an important result that we verify in Section 3.4 and in Chapter 4. For now, it suffices to say that the strong response of the $\ell = 5$ RT modes in the global energy profiles appears to be more of a midlatitude, rather than a tropical, phenomenon.

As discussed in Chapter 1, it is well known that the local response to anomalous tropical forcing has a significant baroclinic component that is associated with deep convection. Because deep tropical convection often fills the depth of the troposphere, with inflow at lower levels and outflow aloft, we might expect this component of the response to project strongly onto medium depth internal modes that exhibit a single sign reversal somewhere in the middle troposphere. For example, it has been suggested by Puri (1983) that convective forcing may project strongly onto those modes whose vertical profile resembles the inflow-outflow structure of the Hadley cell. In contrast, Lim and Chang (1983) suggest that the distribution of energy among the vertical modes depends very sensitively on the vertical profile of the heating. While these theories may partially explain the strong response of the tropical $\ell = 4$ RT modes in Figures 3.12a and 3.13a, there remain two issues that need to be addressed in the present case. The first is that cumulus convection, with its compensating inflow and outflow, represents a *strongly divergent* circulation (*cf.*, Figure 2.4 or Figure 3.16), which tends to imply a significant gravity mode response, rather than the rotational mode response in Figure 3.12a or 3.13a. The second issue is that the baroclinic responses in these figures project strongly onto vertical mode $\ell = 4$, even though other vertical modes in the NOGAPS spectral model, such as $\ell = 5$, more closely resemble the heating and momentum profiles associated with convection (Figure A.1b).

With regard to the former, it turns out that the gravity modes do play an important part of the internal mode response in the tropics, as indicated in Figure 3.12b,c and 3.13b,c, which show the time-mean responses of the tropical EG and WG modes in each simulation. In all of these figures, the gravity modes are relatively much more energetic than in the corresponding global plots in Figures 3.3 and 3.4 (note the different scaling on the ordinates). A comparison reveals that the relative contributions from the gravity modes are typically on the order of ten times greater in the tropics than they are globally. The main thing to note is that, with the possible exception of the $\ell = 3$ WG modes in Figure 3.13c, it is the $\ell = 4$ gravity modes in these figures that are clearly the most energetic.

The fact that the rotational and gravity mode energy have their peaks at the same vertical mode is indicative of the close relationship between the rotational and divergent components of the wind above the region of anomalous heating. The horizontal divergence of the wind above this heating may be viewed as driving the upper tropospheric rotational wind field (Sardeshmukh and Hoskins, 1988). These two components of the wind field are related through the vorticity equation, in the form

$$
\left(\frac{\partial}{\partial t} + \mathbf{v} \cdot \nabla \right) \varsigma = -\varsigma D + F , \tag{3.39}
$$

where ς is the absolute vertical vorticity, D is the horizontal divergence, $\mathbf{v}$ is the horizontal wind velocity and F is the frictional term (Sardeshmukh and Hoskins, 1985). The vertical advection and tilting terms are neglected in (3.39) because the vertical velocity is small at the level of convective outflow. Recall that the vorticity projects mainly onto the RT modes, while the divergence projects mainly onto the EG and WG modes. Thus, (3.39) implies that the

prominent response of the $\ell = 4$ RT modes may result from the divergent forcing by the $\ell = 4$ EG and WG modes through the term $-\varsigma D$. Although this cannot be inferred directly from Figure 3.14 alone, the evolution of the responses of the different mode types are at least consistent with this forcing.

In Figure 3.14a, the $\ell = 4$ RT mode energy (denoted by triangles) grows gradually from zero, increasing steadily until days 11–15. After this time, the energy appears to oscillate about an approximate steady state, contributing between 10% and 20% of the tropical total energy. This agrees with Figure 3.13a, which shows that the $\ell = 4$ RT modes contribute approximately 14% of the total energy to the tropical steady state in this simulation. Note that the growth time of the $\ell = 4$ response in Figure 3.14a is considerably shorter than that of the external mode response, which continues to grow until days 21–25. This is indicative of the fact that these two responses result from different dynamical forcings. However, it is interesting that the energy in the external modes grows much more rapidly after the $\ell = 4$ response begins to level off at days 11–15. It seems reasonable to speculate that the growth process for the external modes suggested by Lim and Chang (1986) may become more efficient after the internal modes have reached their maximum amplitude.

In contrast to the gradual growth of the $\ell = 4$ RT modes, the $\ell = 4$ EG and WG modes in Figures 3.14b,c attain their maximum energies almost immediately after the simulation begins, and then slowly settle into a steady state after two to three weeks (Figure 3.14b). It is during this time that the divergent forcing from these gravity modes should begin to "spin up" the RT mode response via (3.39). Although the gravity modes quickly react to the increased boundary layer and cumulus forcing associated with the heating

anomaly, there is little doubt that a significant portion of the initial jump in energy in Figures 3.14b,c results from the "model shock" induced by suddenly perturbing the SST at the beginning of the simulation. Both of these effects are visible in Figure 3.15, which shows the evolution of the EG mode energy in the WSSTA simulation at 24-hour intervals during the first ten days of the simulation (this is the period corresponding to the first two pentads in Figure 3.14b). The initial jump to over 12% at day 1 is due almost certainly to model shock. After this time, a slower growth to about 17% occurs up to day 4 as the boundary layer and cumulus convection adjust to the anomalous heating. From day 5 on, the gravity mode energy decreases as these processes begin to approach their new steady state.

With regard to the second issue mentioned above concerning the projection of the baroclinic response onto vertical mode $\ell = 4$, the preceding analysis indicates that the vertical structure of this response may be governed to a large extent by the divergent forcing associated with the anomalous heating. Therefore, we might expect the baroclinic response to project most strongly onto those modes whose vertical structures closely resemble the vertical profile of the divergence, rather than the profiles of heating or momentum themselves. Based on continuity arguments, we can infer the divergent forcing from the vertically integrated height anomaly associated with the net heating in the column. In a vertically discrete system such as the NOGAPS spectral model, we can compute the height anomaly in each layer using the hypsometric equation

$$\Delta h_k = -\frac{R \overline{T}_k}{g} \ln \left(\frac{p_k^{(top)}}{p_k^{(bot)}} \right) , \qquad (3.40)$$

where Δh_k is the height anomaly in layer k, bounded above and below by pressures $p_k^{(top)}$ and $p_k^{(bot)}$, respectively, and $\overline{T}_k$ represents the mean temperature

TROPICAL ENERGY GROWTH (EG)
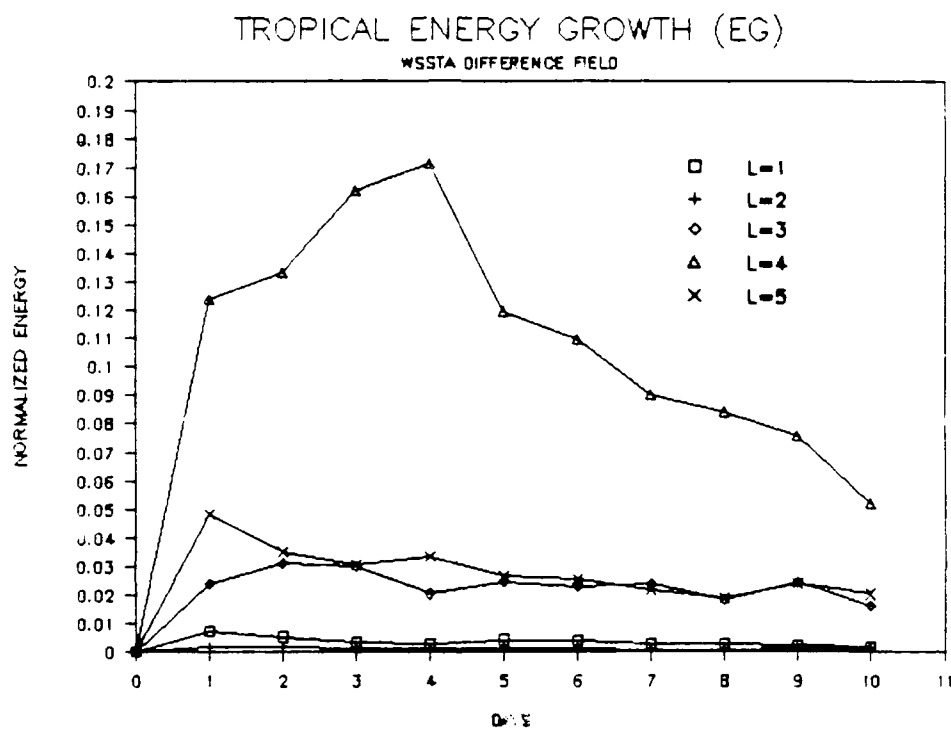
WSSTA DIFFERENCE FIELD

Figure 3.15   The daily evolution of the tropical EG mode total eddy energy in the first five vertical modes of the NOGAPS model during days 1–5 for the difference field in the WSSTA simulation.

change in the layer due to the net diabatic heating. The vertically integrated height anomaly is thus approximated by the sum of the Δh_k. For example, Figure 3.16a shows the area-averaged net diabatic heating profile over the region of anomalous SST during days 11–15 of the anomaly run in the WSSTA simulation. Figure 3.16b shows the corresponding vertically integrated height anomaly obtained via (3.40). Note the strong resemblance between the heating profile in Figure 3.16a and the structure of vertical mode $\ell = 5$ in Figure A.1b. Yet, the baroclinic response projects mainly onto vertical mode $\ell = 4$, whose vertical structure (Figure A.1b) is, instead, remarkably similar to that of the height anomaly in Figure 3.16b. Therefore, the divergent forcing associated with the height anomaly in Figure 3.16b projects mainly onto the $\ell = 4$ gravity modes, which in turn, force the $\ell = 4$ RT modes via (3.39). Presumably, this forcing is strongest at the level of convective outflow in the tropics, which coincides reasonably well with the levels of maximum amplitude in Figures A.1b and 3.16b.

The strong projection of the upper-level tropical divergence onto vertical mode $\ell = 4$ is further illustrated in Figure 3.17, which shows two vertical mode projections of the 30-day mean difference in velocity potential χ at 150 mb for the WSSTA simulation shown in Figure 2.4c. Figure 3.17a shows the projection of the difference field in Figure 2.4c onto vertical mode $\ell = 4$, while Figure 3.17b shows the projection onto all vertical modes *except* $\ell = 4$.

As discussed in Section 2.3, the most obvious feature in these figures is the dipolar structure of the anomalous velocity potential, with divergence over the maritime continent and the western Pacific, and convergence over Africa and the Atlantic. Again, this pattern shows that the SST anomaly in the western
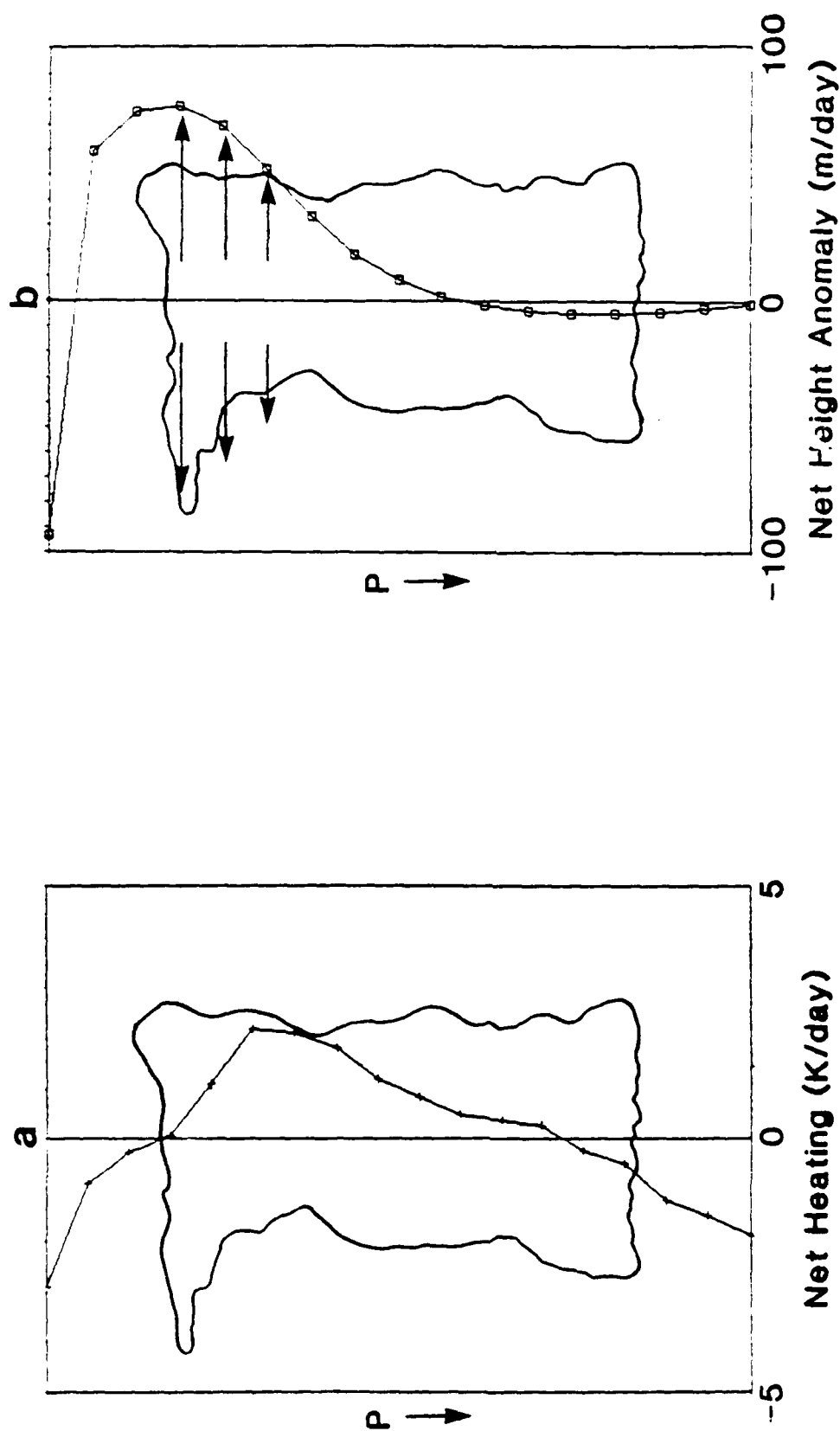
129

Figure 3.16   The area-averaged (a) net diabatic heating profile (K/day), and (b) vertically integrated height anomaly (m/day) based on (3.40), over the region of anomalous SST during days 11–15 of the anomaly run in the WSSTA simulation. The horizontal arrows in (b) denote schematically the region of maximum divergence near the level of convective outflow.
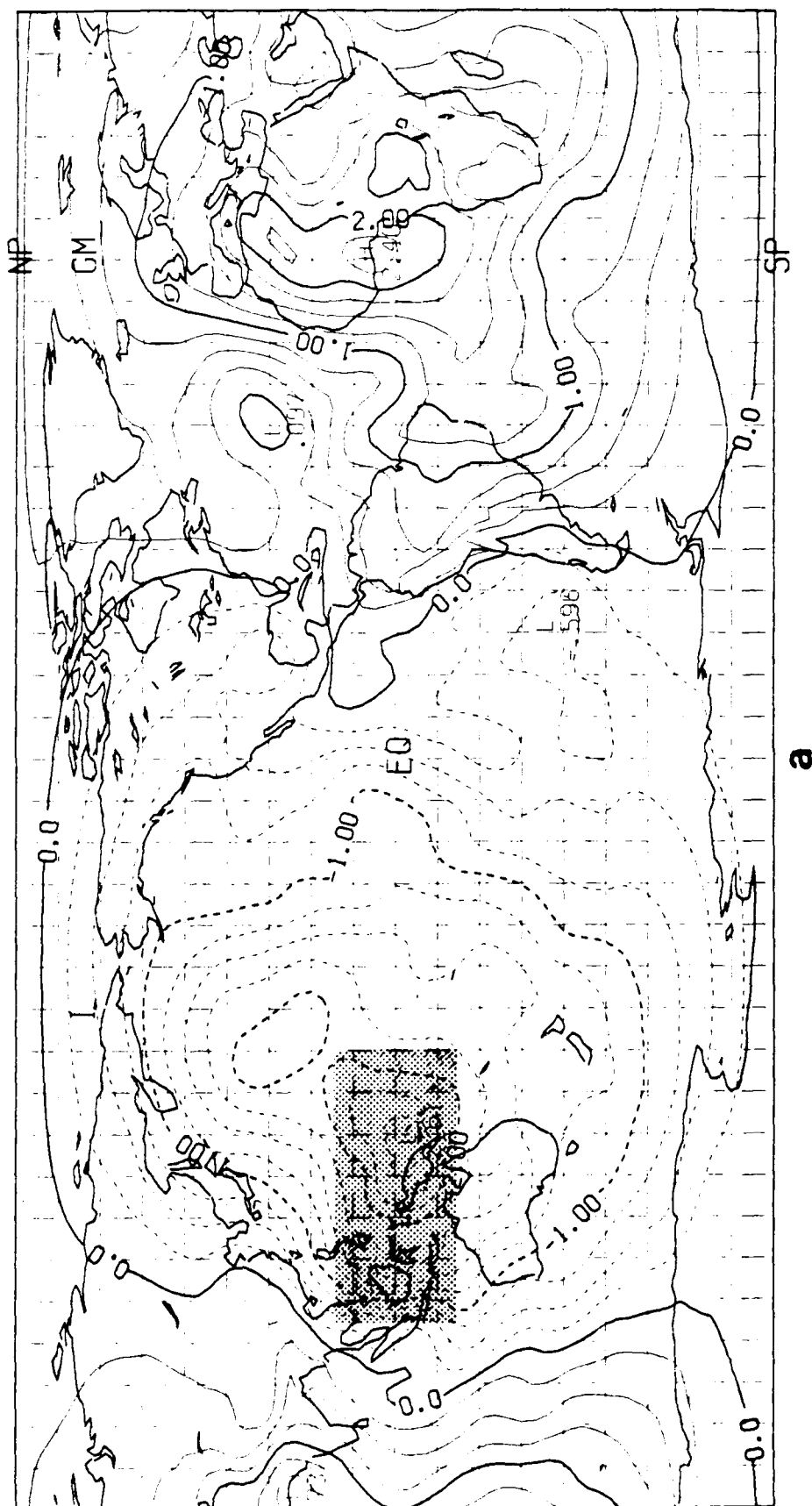
Figure 3.17 The projection of the 30-day mean difference in velocity potential at 150 mb in Figure 2.4c onto (a) vertical mode $\ell = 4$, and (b) all modes *except* $\ell = 4$. The contour interval is 0.25×10^6 m^2/sec, with negative differences denoted by dashed lines, and the SST anomaly indicated by the stippled region.
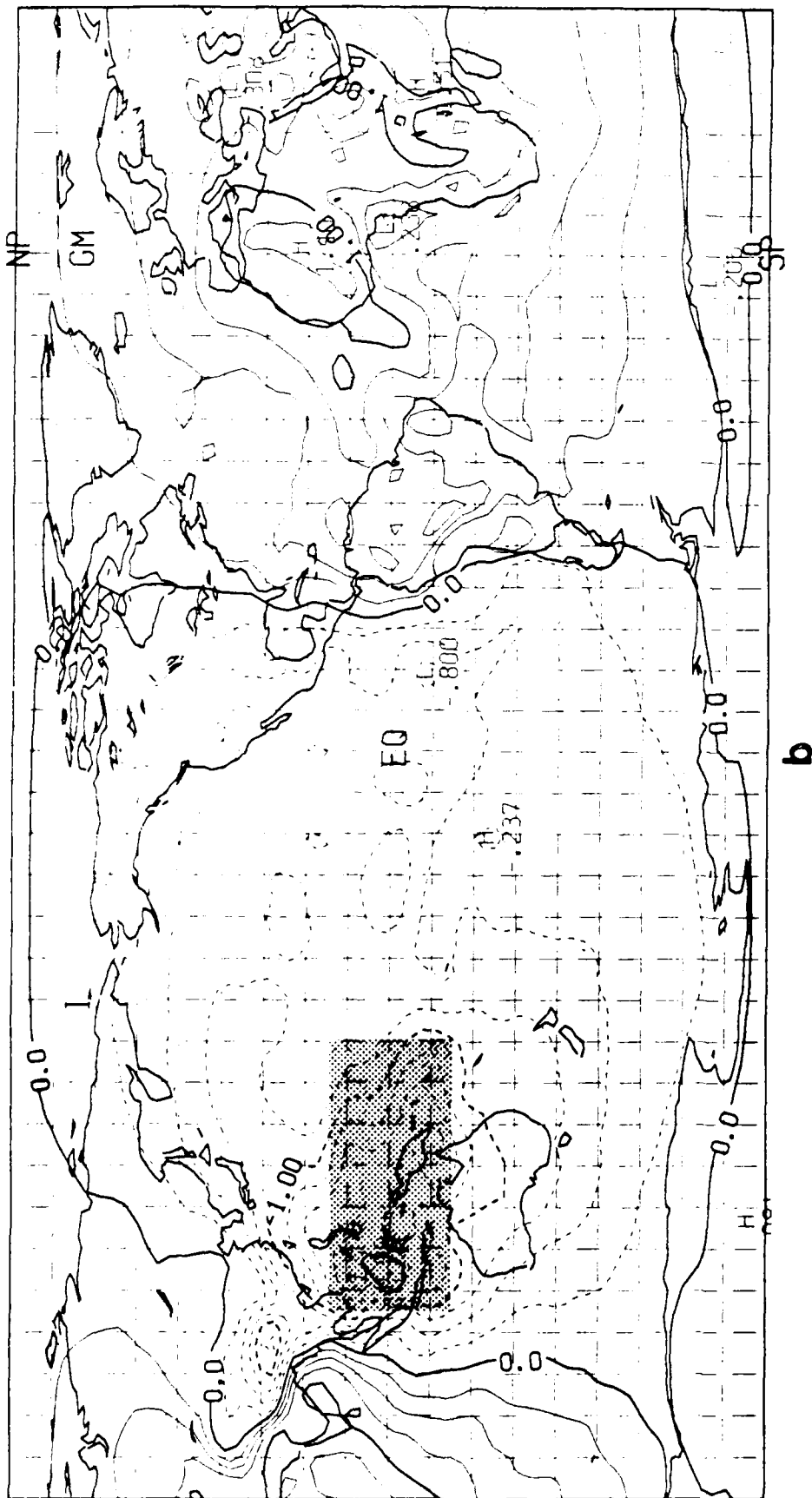
Figure 3.17 (continued)

Figure 3.18 The 30-day mean difference in the stream function at 150 mb in the WSSTA simulation for (a) the total difference field, and for the projections of the difference field onto (b) $\ell = 4$, and (c) all modes *except* $\ell = 4$. The contour interval is $0.5 \times 10^6 \ m^2/sec$, with negative differences denoted by dashed lines, and the SST anomaly indicated by the stippled region.
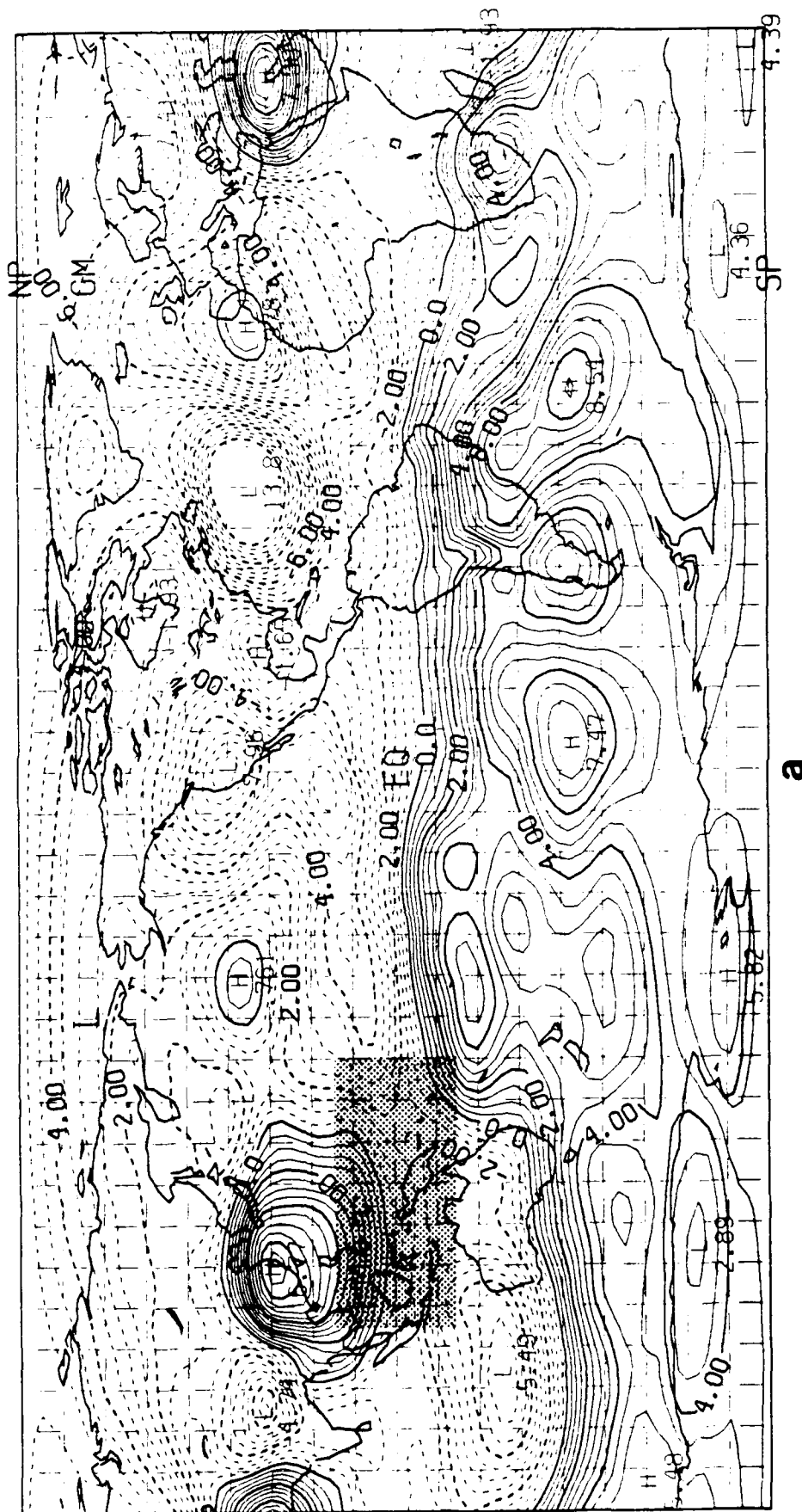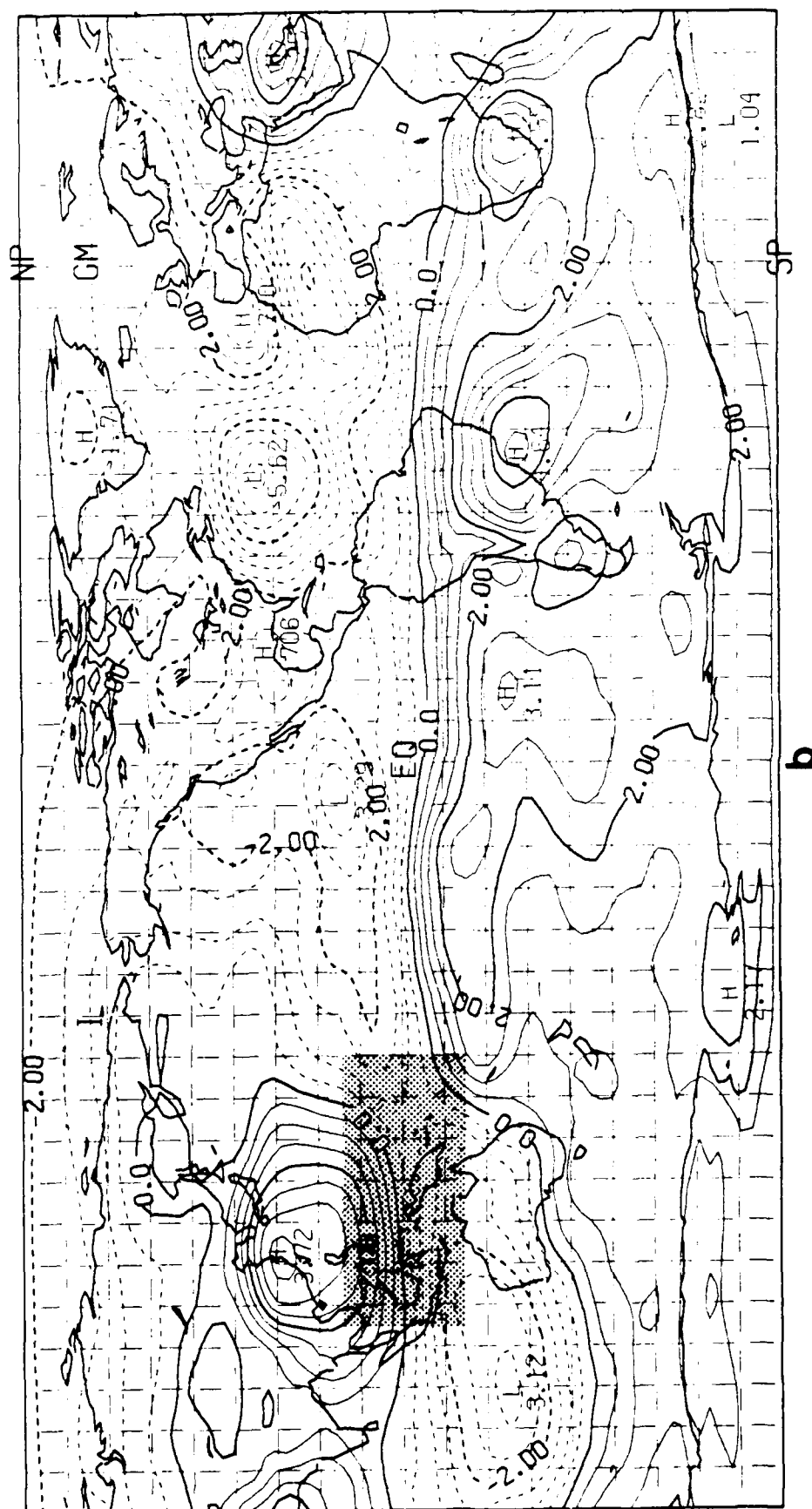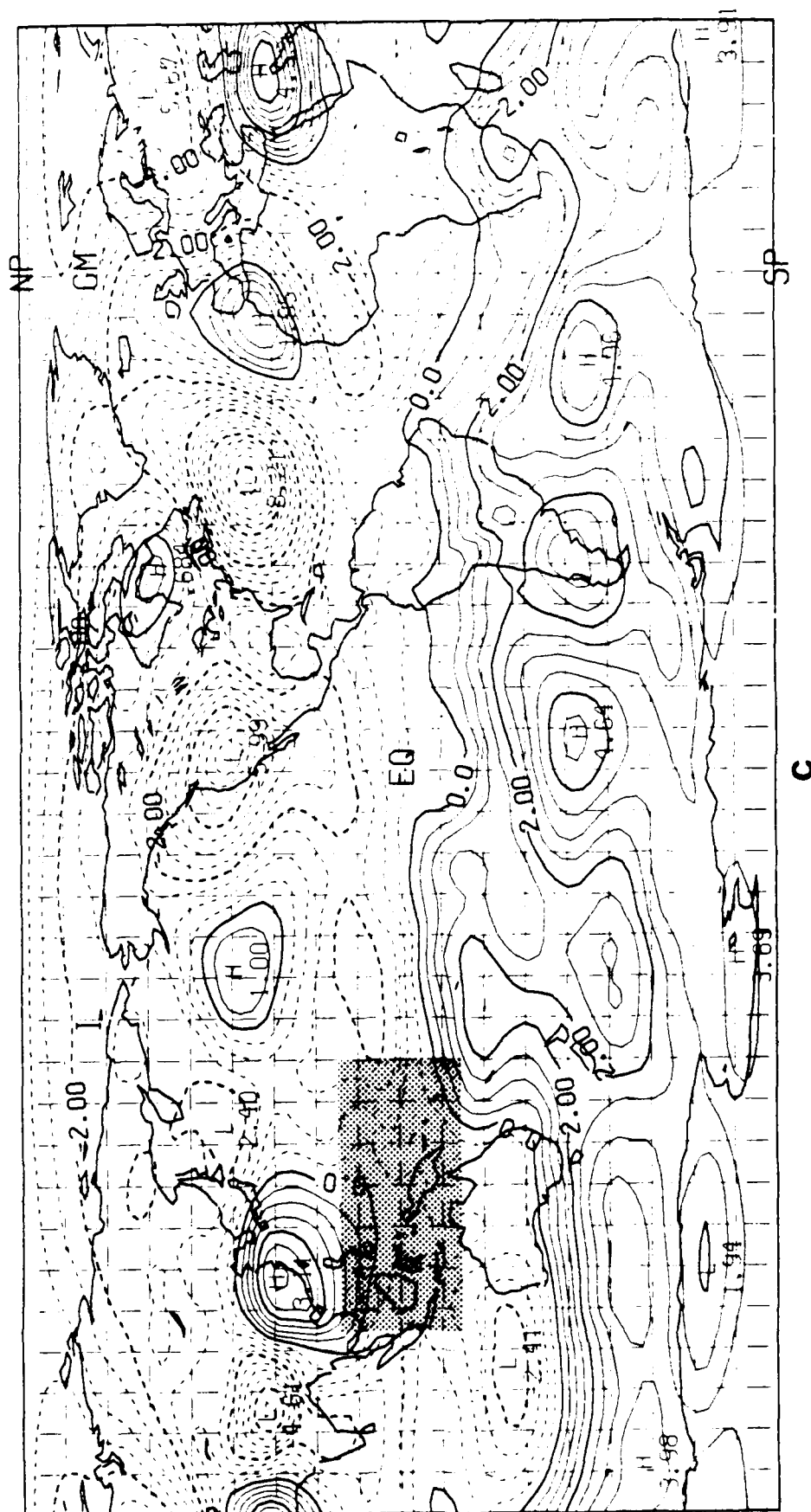
133

Figure 3.18 (continued)

b

C

Figure 3.18 (continued)

Pacific has intensified the usual sense of the Walker circulation. In agreement with the results above, it appears that most of the variance of the total difference field in Figure 2.4c projects onto vertical mode $\ell = 4$ in Figure 3.17a. The remaining vertical modes shown Figure 3.17b account for a relatively small portion of the variance. The strongest divergent flow in Figures 2.4c and 3.17a occurs on the western flank of the SST anomaly. Therefore, it is in this region that we might expect significant divergent forcing of the rotational wind field. This is confirmed in Figure 3.18, which shows the 30-day mean difference in the stream function ψ at 150 mb in the WSSTA simulation. In this figure, the total difference field is shown in Figure 3.18a, while the projections of the total difference onto vertical mode $\ell = 4$ and onto all vertical modes except $\ell = 4$ are shown in Figures 3.18b and 3.18c, respectively. Note the two strong anticyclones to the west of Australia[1] and to the north of the Philippines in Figure 3.18a. These coincide well with the regions of strong divergent flow in Figures 2.4c and 3.17a. This result is consistent with the findings of Sardeshmukh and Hoskins (1988) who used a single-level vorticity model to study the effects of an anomalous vorticity source in the subtropics. They showed that the advection of vorticity by the divergent wind in this region played an important role in the Rossby wave source term in their model. It can be seen in Figure 3.18b that the two anticyclones in Figure 3.18a project strongly onto vertical mode $\ell = 4$, demonstrating the importance of the divergent forcing mechanism described by (3.39). The appearance of similar anticyclones to the west of an equatorial heat source has been documented by other investigators such as Blackmon *et al.* (1983), Palmer and Mansfield (1986) and Sardeshmukh and Hoskins (1988).

---

[1] The sign of the stream function in the Southern Hemisphere is reversed, so that this feature appears as a low to the west of Australia.

We may recall from Figures 3.12a and 3.13a that, although the $\ell = 4$ RT modes are dominant among the internal modes in the tropics, it is the external RT modes that account for most of the energy in the tropical difference field. Thus, unlike the projection of the velocity potential in Figure 3.17a, the projection of the stream function onto the $\ell = 4$ modes in Figure 3.18b does not account for most of the variance in the total difference field in Figure 3.18a. Instead, the projection onto the remaining vertical modes (Figure 3.18c) accounts for more of the variance than the projection onto vertical mode $\ell = 4$. Obviously, most of the variance in Figure 3.18c is accounted for by the external modes. With this in mind, it is revealing to note some fundamental differences between Figures 3.18b and 3.18c. It can be seen that most of the features in Figure 3.18c appear in the middle to high latitudes in both hemispheres. For example, note that the anomaly pattern over North America discussed in Chapter 2 shows up clearly in this figure, as do the anomalies surrounding the southern tip of South America. In the tropics however, the anomalies that appear in the total difference field in Figure 3.18a have a relatively weaker signature in Figure 3.18c. In contrast, most of the features that project onto vertical mode $\ell = 4$ in Figure 3.18b appear in the tropics and subtropics. Note that the two western Pacific anticyclones discussed earlier are prominent in this figure. Also, meridional gradients in the stream function along the equator show up in this figure. These observations indicate that the $\ell = 4$ response describes more of the tropical variance of the total difference field, while the external mode (which dominates the response in Figure 3.18c) describes more of the extratropical or midlatitude variance. Moreover, these results are in general agreement with those in Figures 3.12 and 3.13, which showed the relative

contributions of the various vertical modes and mode types to the anomalous tropical energy. In particular, Figures 3.12 and 3.13 highlighted the importance of the $\ell = 1$ and $\ell = 4$ RT modes in the tropics, as well as the $\ell = 4$ EG and WG modes. It is important to recall that the results in Figures 3.12 and 3.13 depend on the factors $(\Delta_J)_{trop}$, which were derived in Section 3.2.2 as a way of distinguishing between tropical modes and midlatitude modes. Thus, the general agreement between the results in Figures 3.12–3.13 and those in Figures 3.17–3.18 (which are independent of the values of $(\Delta_J)_{trop}$) helps substantiate the validity of these factors, and in particular, the validity of the choice of the threshold value $(\Delta_J)_{trop} \geq 0.4$, which defines the subset of tropical modes.

In summary, the local (*i.e.*, tropical) response to anomalous tropical forcing consists of a barotropic and a baroclinic component. The barotropic component projects onto the external ($\ell = 1$) RT modes and appears to be associated with meridionally propagating nondivergent Rossby waves. This is verified in Section 3.4, where the impact of these modes on the general circulation is assessed. Although the anomalous forcing in the tropics is due predominantly to internal heating from cumulus convection, the external mode response appears to grow via the mechanism suggested by Lim and Chang (1986), in which vertical wind shear acts to co.. .e the internal and external modes. The primary evidence of this is the time-scale of the growth, which takes two to three weeks, as well as the amplitude of the steady response, which accounts for between 20% and 35% of the tropical total energy. The barotropic response is examined in more detail in Section 3.4 and in Chapter 4.

The baroclinic response in the tropics projects mainly onto vertical mode

$\ell = 4$, although vertical modes $\ell = 3$ and $\ell = 5$ also appear to be important. The baroclinic response to enhanced convection projects initially onto the divergence field, and is therefore manifested in the $\ell = 4$ EG and WG modes. It was shown that these modes have vertical structures resembling a typical profile of divergence associated with convection in the tropics, with maximum amplitude near or above 150 mb. The anomalous divergent forcing above the heating anomaly can induce a response in the rotational wind field through the divergence term in the vorticity equation (3.39). This undoubtedly explains the strong secondary response in the $\ell = 4$ RT modes. The time-scale for the growth of this response is on the order of several days. These results are supported by projections of anomalous stream function and velocity potential onto various vertical modes.

In Section 3.4 we conduct a similar analysis of the remote response to anomalous tropical forcing in terms of the midlatitude modes defined in Section 3.2.2.

3.4   Midlatitude Modes

The most striking result of the anomalous forcing simulations in Chapter 2 is that the largest amplitude responses occur far from the region of anomalous tropical heating. The standing wave patterns in the difference field of geopotential height over North America in Figures 2.8 and 2.9 are examples of the most prominent of these responses. Although, as discussed previously, many investigators have observed similar features in both modeling and observational studies, little is known about their influence on the dynamics of the midlatitudes, or about their effect on the general circulation as a whole. At the

same time, it has become increasingly clear that the success of extended-range forecasts of the midlatitudes is highly dependent on our ability to simulate the global impact of tropical forcing (Tiedtke, 1984; Donner *et al.*, 1982). However, in order to accomplish this, we first must develop a basic understanding of the structure and dynamics that govern the remote responses to tropical forcing. With this in mind, we now use the normal mode partitioning technique developed in Section 3.2 to analyze the midlatitude response of the NOGAPS spectral model obtained from the anomalous forcing simulations described in Chapter 2.

Figures 3.19 and 3.20 show the midlatitude energy of the various mode types for the 30-day mean composite difference fields in the ESSTA and WSSTA simulations, respectively. In accordance with the definition for midlatitude modes developed in Section 3.2.2, these figures depict the energy of those modes for which $(\Delta_J)_{mid} \geq 0.7$. The formats of these figures are analogous to those of Figures 3.12 and 3.13, so that the plotted values represent the contributions to the midlatitude total energy.

Figures 3.19a and 3.20a show the contributions of the RT modes to the midlatitude energy in each simulation. In both cases, it is clear that the midlatitude steady response is dominated by the external ($\ell = 1$) RT modes, which account for approximately one third of the total energy in the midlatitudes. Also, it can be seen that the total energy of the external mode response is composed almost entirely of kinetic energy. As discussed in Section 3.3, this reflects the fact that the external modes are essentially barotropic. Thus, the prominence of the external mode response in Figures 3.19a and 3.20a is consistent with the findings of other investigators (see

MIDLAT EDDY ENERGY (RT)

ESSTA DIFFERENCE FIELD d(21-50)

a

MIDLAT EDDY ENERGY (EG)

ESSTA DIFFERENCE FIELD d(21-50)

b
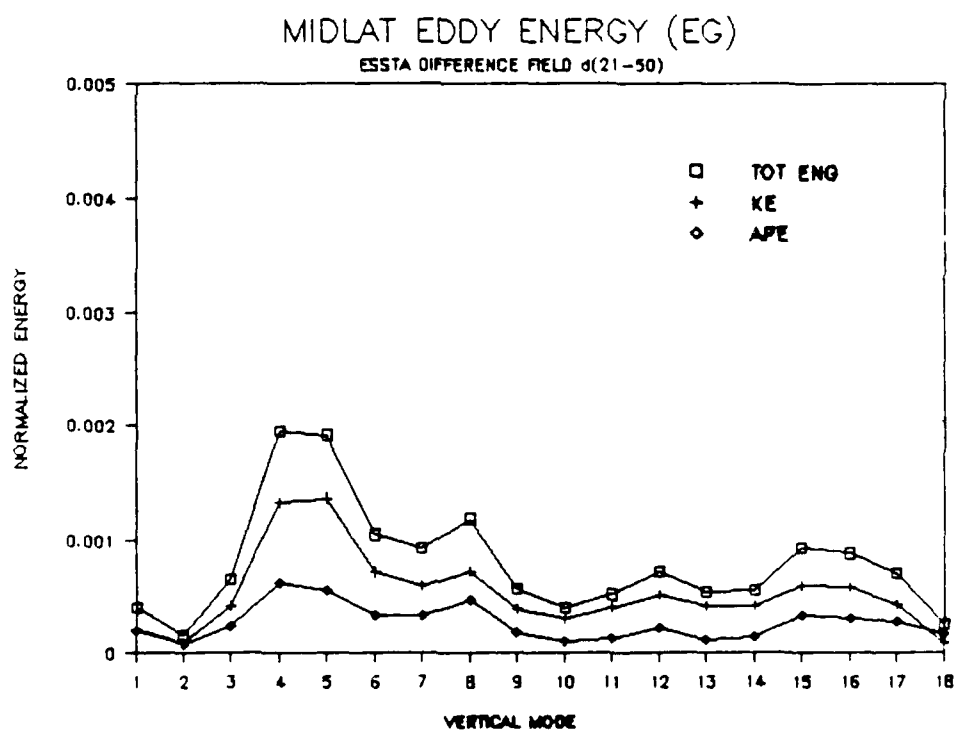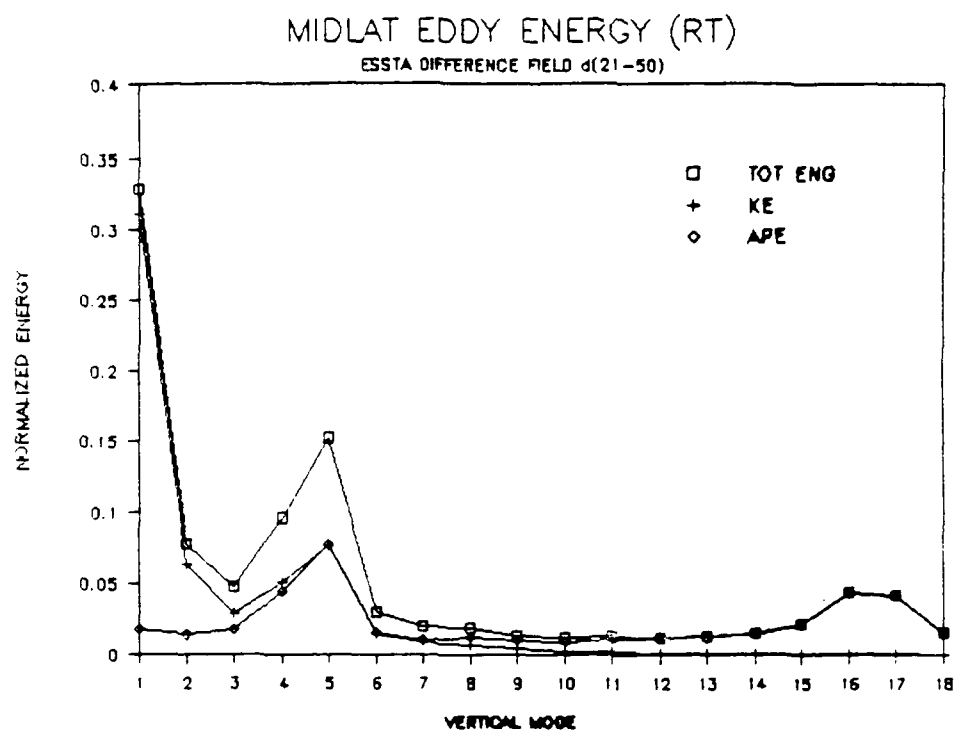
Figure 3.19 The contributions to the midlatitude eddy energy of the 30-day mean difference field for days 21–50 in the ESSTA simulation from the (a) RT, (b) EG, (c) WG and (d) ALL modes, as a function of vertical mode ℓ. Only modes for which $(\Delta_J)_{mid} \geq 0.7$ are included.

MIDLAT EDDY ENERGY (WG)

ESSTA DIFFERENCE FIELD d(21-50)

c

MIDLAT EDDY ENERGY (ALL)

ESSTA DIFFERENCE FIELD d(21-50)

d

Figure 3.19 (continued)

MIDLAT EDDY ENERGY (RT)

WSSTA DIFFERENCE FIELD d(21-50)

a

MIDLAT EDDY ENERGY (EG)

WSSTA DIFFERENCE FIELD d(21-50)
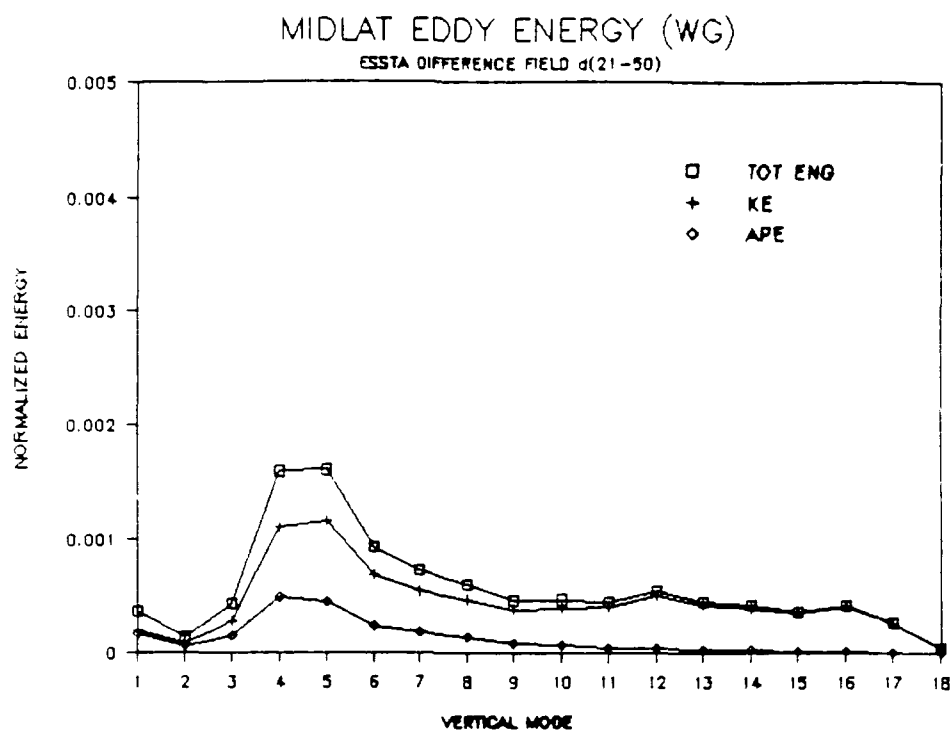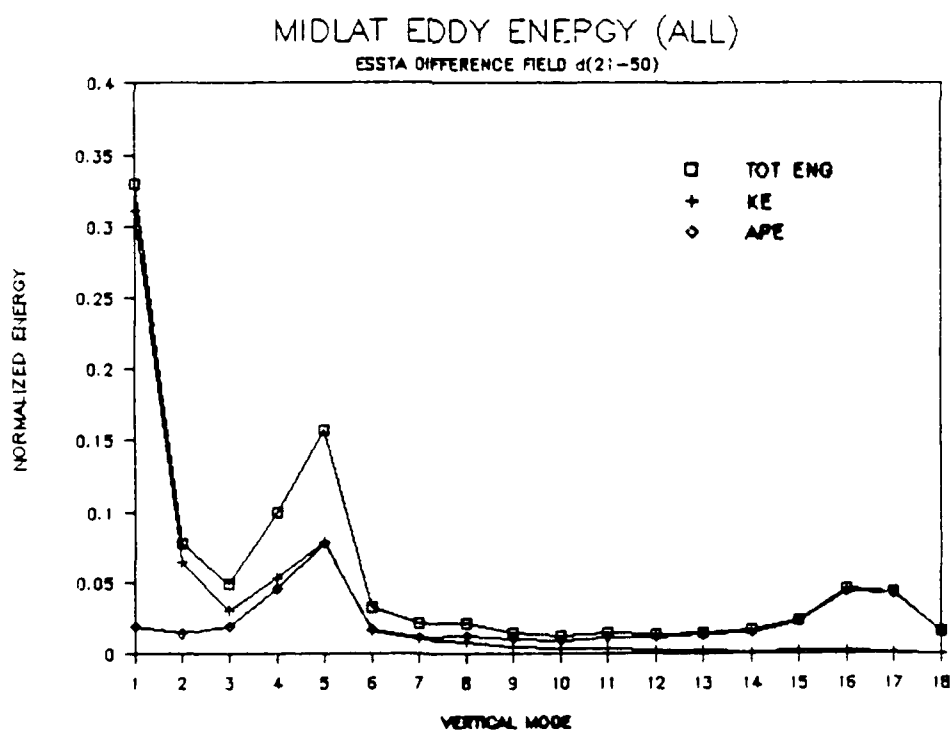
b

Figure 3.20   As in Figure 3.19, except for the WSSTA simulation.

(continued on next page)

MIDLAT EDDY ENERGY (WG)

WSSTA DIFFERENCE FIELD d(21-50)

c

MIDLAT EDDY ENERGY (ALL)

WSSTA DIFFERENCE FIELD d(21-50)

d

Figure 3.20 (continued)

references in Chapter 1) who have demonstrated that the remote response to anomalous tropical forcing has equivalent barotropic structure, similar to the well known PNA pattern described by Hore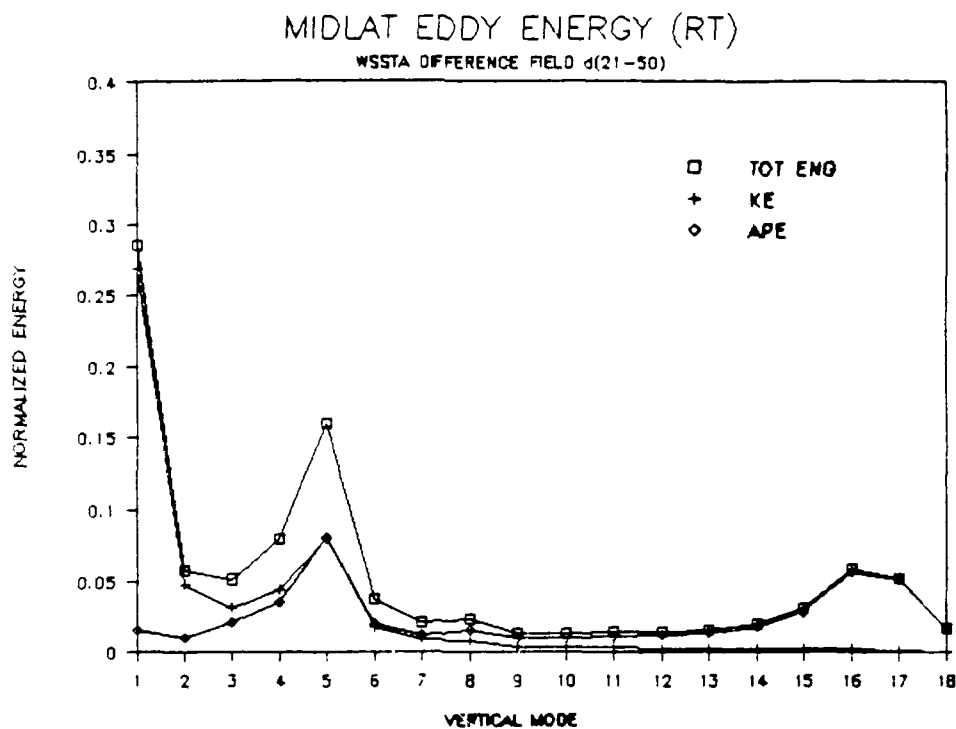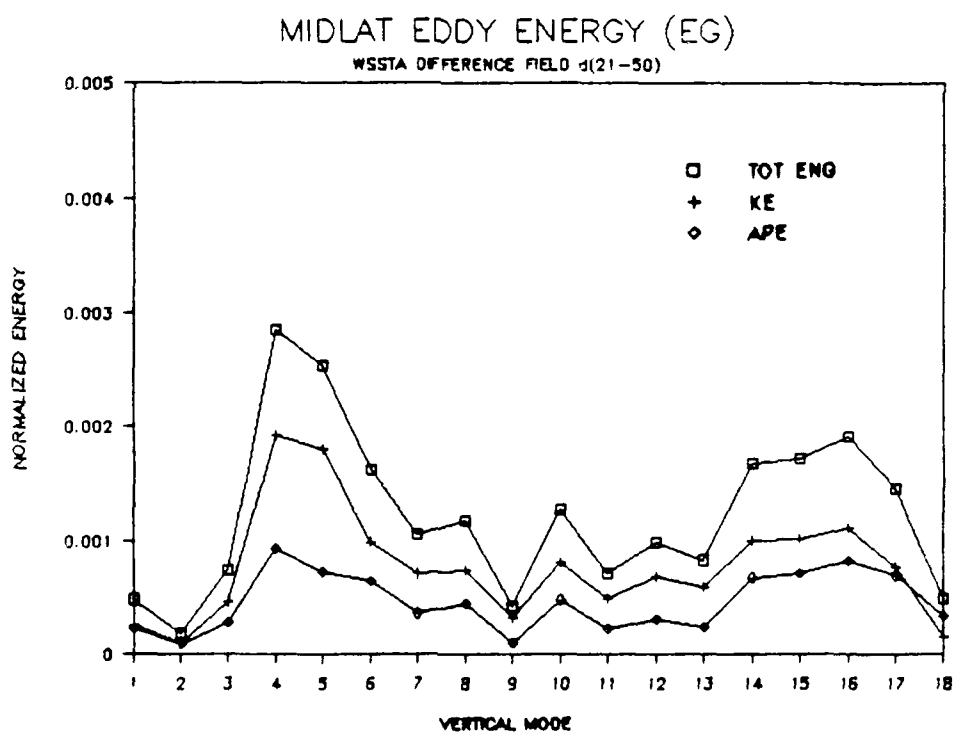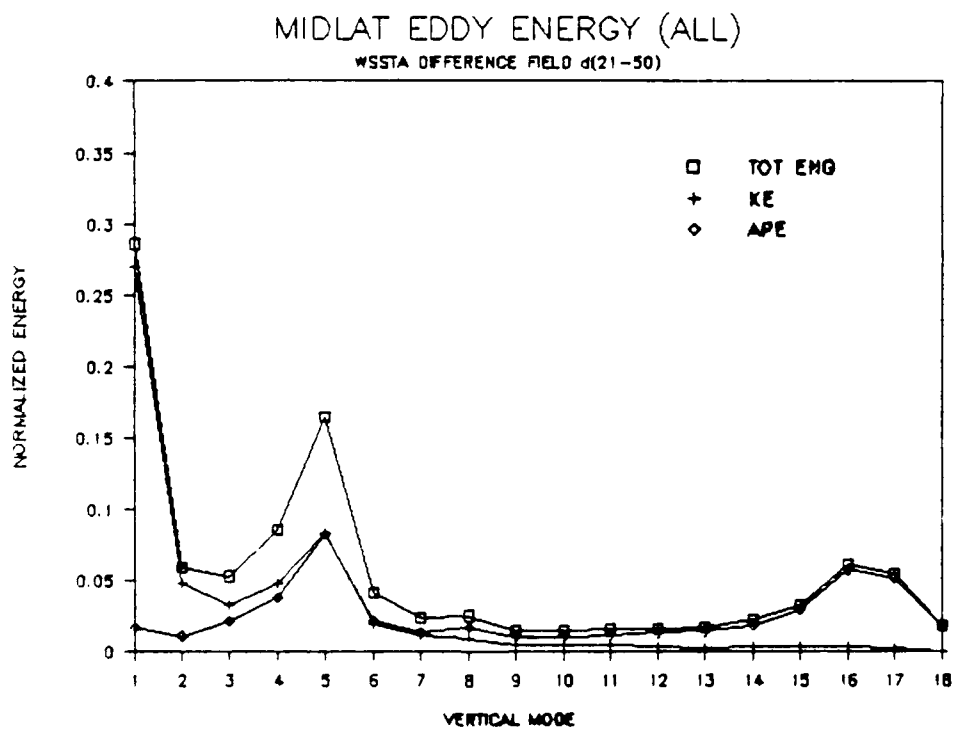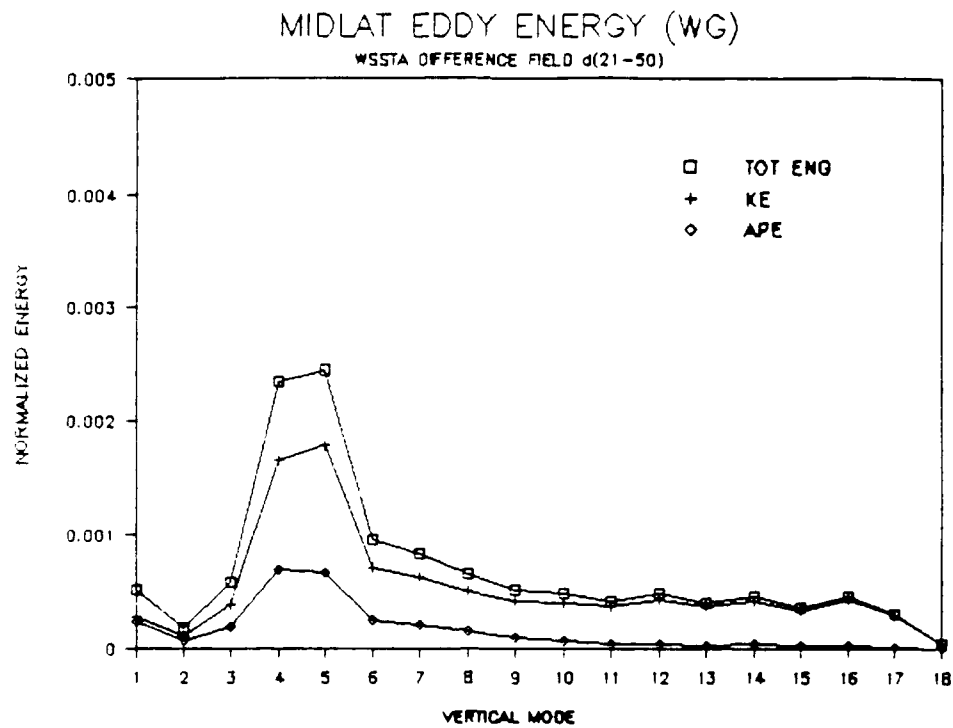l and Wallace (1981). Typically, these studies have shown that difference fields of stream function or geopotential height reveal midlatitude anomalies that have the same sign at all levels (*i.e.*, highs over highs, lows over lows), and increasing amplitude with height. We may recall that the difference fields of geopotential height at 300 mb and 700 mb in Figures 2.8 and 2.9 show that the anomalies over North America in the ESSTA and WSSTA simulations exhibit this structure. Again, these features have been interpreted in terms of nondivergent Rossby waves that have propagated out of the tropics toward higher latitudes. Based on this theory, only very deep (*i.e.*, barotropic) modes with large phase speeds can overcome the trapping effect of the Coriolis force and propagate out of the tropics. We may recall from Section 2.4 that Lim and Chang (1983) proposed that these modes must have phase speeds $c \geq 120$ m/sec. As stated in Section 3.3, this appears to be a reasonable explanation for the energy in the external modes in Figures 3.19a and 3.20a since these modes have phase speeds of $c \approx 308$ m/sec and equivalent barotropic structure as shown in Figure A.1a. With regard to this point, a comparison of Figures 3.19a and 3.20a with Figures 3.12a and 3.13a reveals the remarkable similarity between the external mode responses in the tropics and midlatitudes. Note that in each region, the external modes account for roughly the same portion of the difference field energy, and that this response is composed almost entirely of kinetic energy. These results are a further indication that the external mode responses in the tropical and midlatitude energy profiles are actually manifestations of the same propagating

phenomenon. This is confirmed in Chapter 4.

Although the external modes in Figures 3.19a and 3.20a are the most energetic, it is the secondary energy peak at vertical mode $\ell = 5$ that is perhaps the most interesting feature in these figures. In both simulations these modes contribute approximately 15% of the midlatitude total energy, equaling more than half that of the external modes. This indicates that the midlatitude response to anomalous tropical forcing has a significant *baroclinic* component, in agreement with the vertical mode projections shown in Figure 2.10. This is remarkable in light of the fact that most studies, such as those cited earlier in Chapters 1 and 2, have focused almost exclusively on the equivalent barotropic structure of the midlatitude response. Accordingly, midlatitude anomalies such as those over North America in Figures 2.8 and 2.9 have been viewed strictly in terms of meridionally propagating waves. However, it is shown below that this only partially explains the patterns in Figures 2.8 and 2.9. Clearly, the internal mode response at $\ell = 5$ does not fit this theory, since these modes have phase speeds $c \approx 38$ m/sec, and baroclinic structure as shown in Figure A.1b. Furthermore, we may recall from the analysis in Section 3.3 that the baroclinic response in the tropics is dominated by the $\ell = 4$ RT modes (although the $\ell = 5$ response is not negligible), as shown in Figures 3.12a, 3.13a and 3.14a. This implies that, even if conditions prevailed in which medium-depth tropical internal modes became untrapped, we might expect to see the maximum internal response in the midlatitudes at vertical mode $\ell = 4$, rather than at $\ell = 5$.

The importance of vertical mode $\ell = 5$ in the midlatitude response is even more dramatic in Figure 3.21a, which shows the evolution of the energy in the midlatitude RT modes for the WSSTA difference field. This figure is the

MIDLAT ENERGY GROWTH (RT)

WSSTA DIFFERENCE FIELD

a

MIDLAT ENERGY GROWTH (EG)

WSSTA DIFFERENCE FIELD
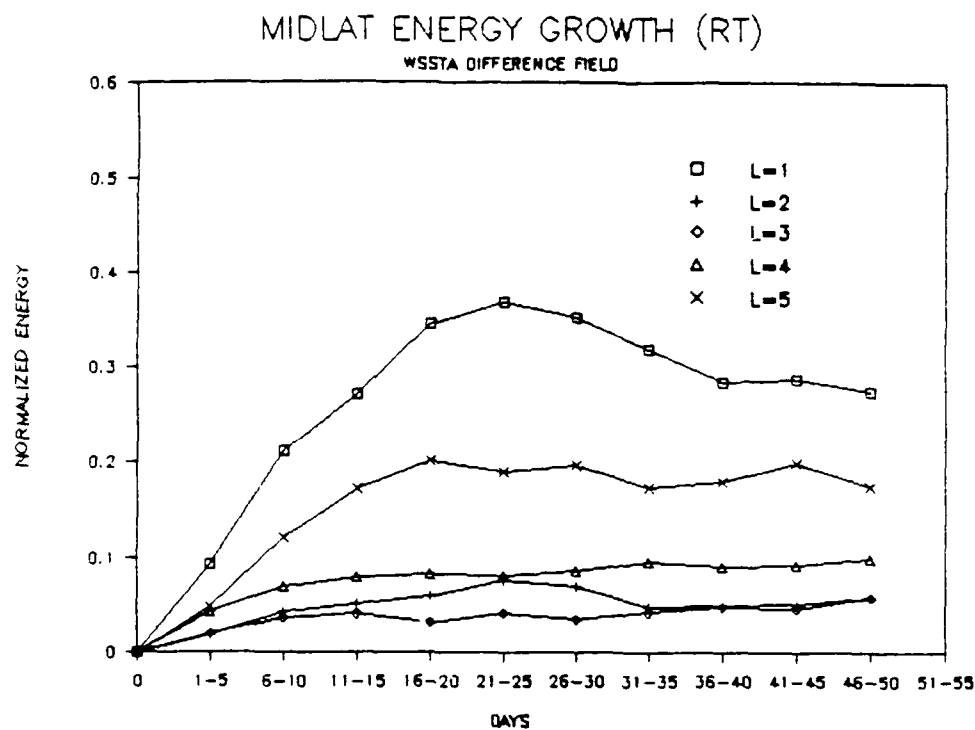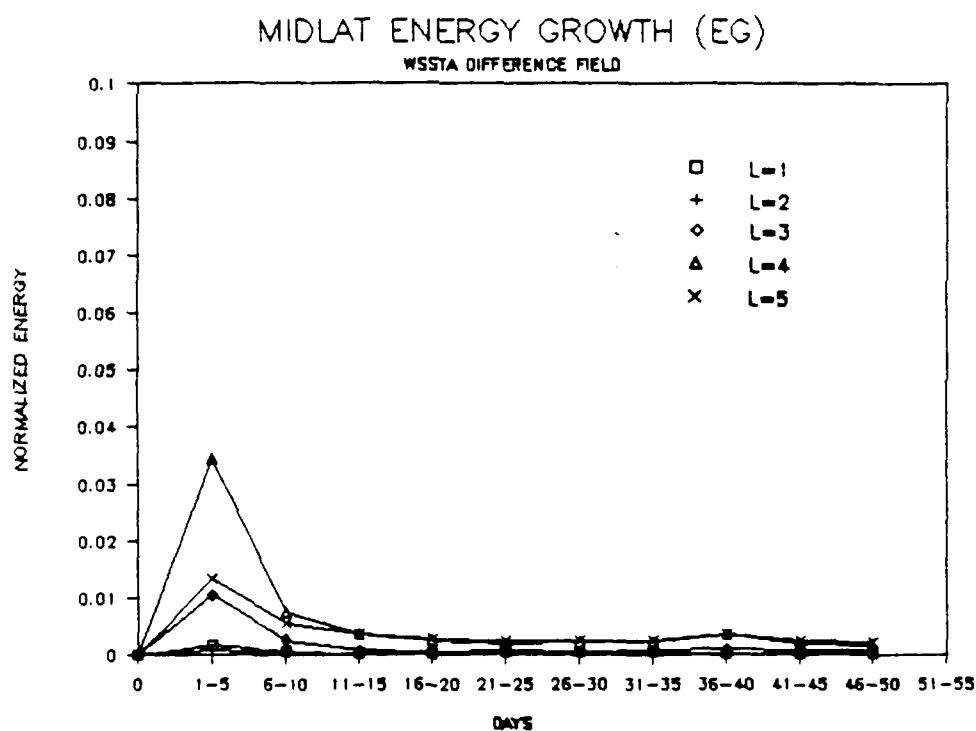
b

Figure 3.21   The evolution (in terms of five-day means) of the total midlatitude eddy energy in the first five vertical modes of the NOGAPS model for the difference field in the WSSTA simulation, for the (a) RT, (b) EG, (c) WG and (d) ALL modes.

MIDLAT ENERGY GROWTH (WG)

WSSTA DIFFERENCE FIELD

□ L=1
+ L=2
◇ L=3
△ L=4
× L=5

NORMALIZED ENERGY

0.1
0.09
0.08
0.07
0.06
0.05
0.04
0.03
0.02
0.01
0

0   1-5   6-10   11-15   16-20   21-25   26-30   31-35   36-40   41-45   46-50   51-55

DAYS

c

MIDLAT ENERGY GROWTH (ALL)

WSSTA DIFFERENCE FIELD

□ L=1
+ L=2
◇ L=3
△ L=4
× L=5

NORMALIZED ENERGY

0.6
0.5
0.4
0.3
0.2
0.1
0

0   1-5   6-10   11-15   16-20   21-25   26-30   31-35   36-40   41-45   46-50   51-55
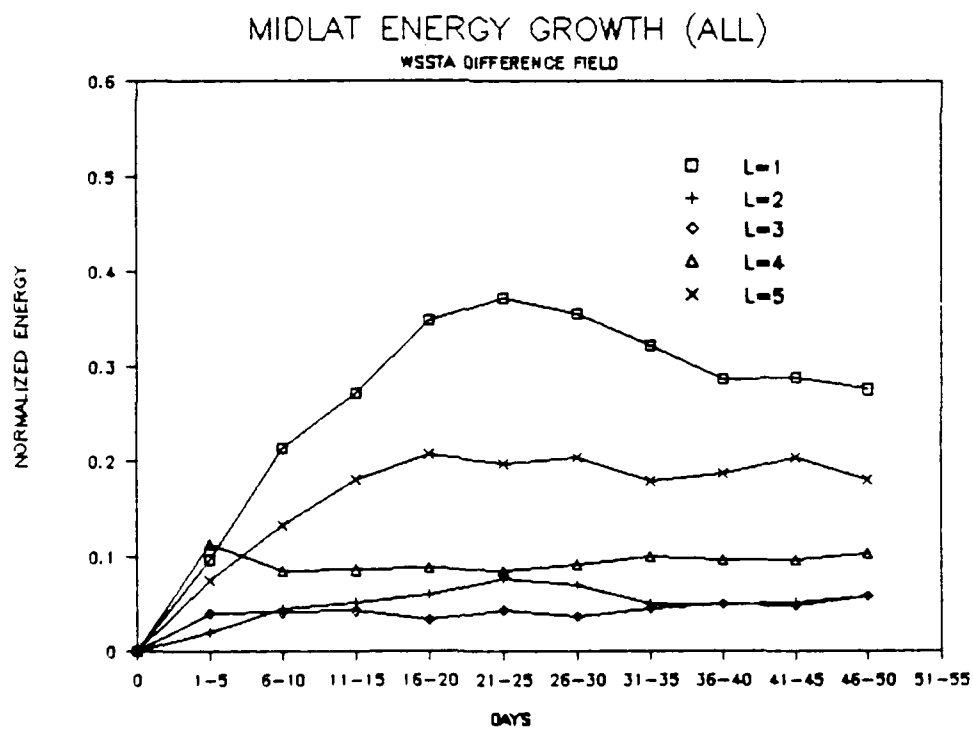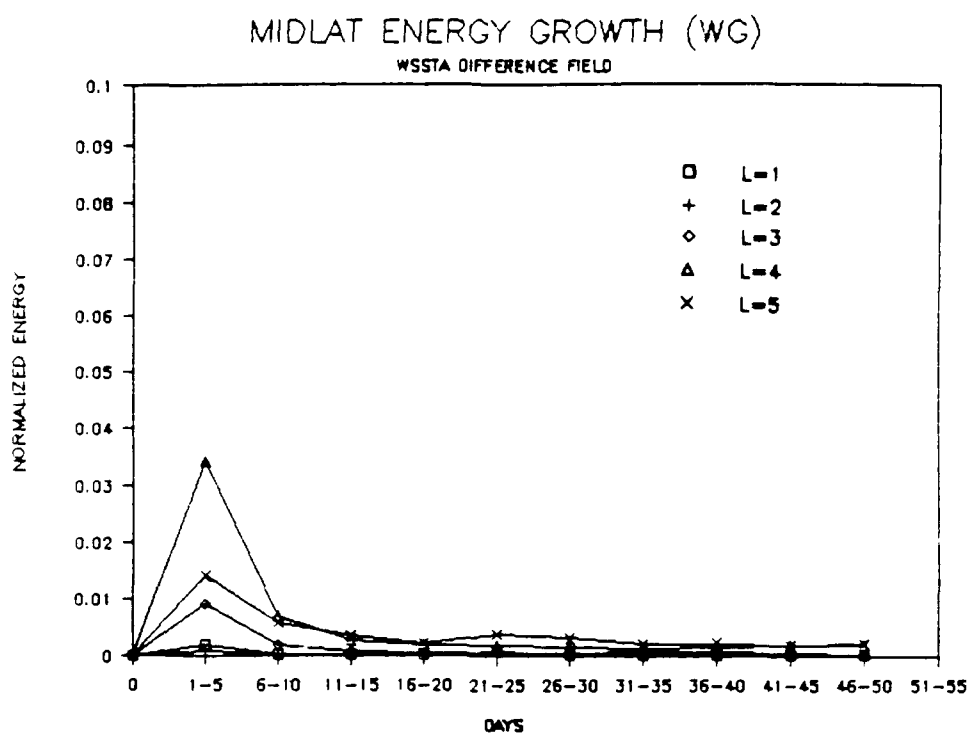
DAYS

d

Figure 3.21 (continued)

midlatitude analogue of Figure 3.14a. Note the dramatic difference between the relative importance of vertical modes $\ell = 4$ and $\ell = 5$ in the tropics and midlatitudes. Clearly the midlatitude baroclinic response in Figure 3.21a is dominated by vertical mode $\ell = 5$ (denoted by x's), while the tropical baroclinic response in Figure 3.14a is dominated by vertical mode $\ell = 4$ (denoted by triangles). Based on these results, it is unlikely that the response at vertical mode $\ell = 5$ in Figures 3.19a and 3.20a has its origin in the tropics. The considerable amount of energy at vertical mode $\ell = 4$ in Figures 3.19a and 3.20a is undoubtedly due to the fact that the definition of "midlatitudes" used in this study extends equatorward as far as 19° latitude. Thus, for example, the $\ell = 4$ RT modes associated with the low-latitude anticyclones to the northwest and southwest of the SST anomaly (Figure 3.18) also contribute to the energy in these figures.

It was concluded in Section 3.3 that the strong baroclinic response of the tropical RT modes was most likely a result of convective heating and the associated upper-level divergence (*e.g.*, Sardeshmukh and Hoskins, 1988). Intuitively, we would not expect this process to be of much importance in the midlatitudes. This is supported by Figures 3.19b,c and 3.20b,c which show the steady response of the midlatitude EG and WG modes in each simulation. Although the $\ell = 5$ gravity modes contribute a significant portion of the energy in each of these figures, their contributions are only on the order of 0.2% to 0.3% of the total energy of the midlatitudes. In order for divergent forcing to be important, we might expect the gravity modes to contribute more significantly than this to the total energy. For example, we may recall that the contributions from the tropical $\ell = 4$ gravity modes in Figures 3.12b,c and 3.13b,c were on the

order of ten times greater than those in Figures 3.19b,c and 3.20b,c. Similarly,
the evolution of the energy in the midlatitude EG and WG modes in
Figures 3.21b,c shows no indication of divergent forcing by the $\ell = 5$ modes.
Not only is the energy dominated by $\ell = 4$ instead of $\ell = 5$, but the energy in all
gravity modes becomes negligible after days 1 to 5.

This indicates that almost all of the gravity mode energy in the
midlatitudes during the early part of the simulation is due only to the initial
shock of the SST anomaly. For example, Figure 3.22 shows the evolution of the
midlatitude EG mode energy in the WSSTA difference field at 24-hour intervals
during the first ten days of the simulation.   This figure may be compared with
Figure 3.15 corresponding to the tropical EG modes. In Figure 3.22, the energy
in vertical mode $\ell = 4$ decreases rapidly after the initial jump at day 1 (note
that the energy in the $\ell = 5$ modes is never significant), and then rapidly
reaches a nearly trivial steady state. This is in contrast to the evolution of the
tropical EG modes in Figure 3.15 which shows a period of growth *after* the
initial jump that lasts until day 4, and then a slow decrease toward a
quasi-steady state as shown in Figure 3.14b. As shown in this figure, the gravity
mode energy in the tropics takes approximately three weeks to reach its new
steady state, during which time the rotational response develops. Based on
these results, it seems reasonable to conclude that the $\ell = 5$ rotational response
in the midlatitudes is not associated with convectively driven motions.

Another indication that the baroclinic responses in the tropics and
midlatitudes represent dynamically different phenomena is the differences in
their ratios of kinetic and available potential energy to the total energy. For the
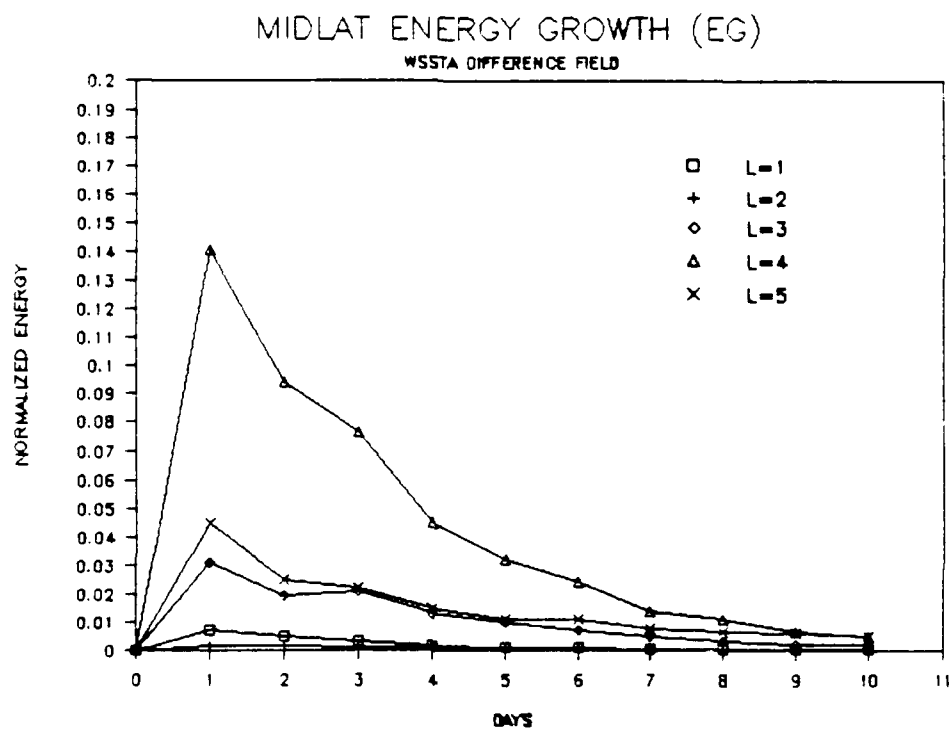30-day mean tropical response in Figures 3.12a and 3.13a, it can be seen that

Figure 3.22   The daily evolution of the total midlatitude EG mode eddy energy
in the first five vertical modes of the NOGAPS model during days
1-5 for the difference field in the WSSTA simulation.

the total energy in vertical mode $\ell = 4$ is dominated by the kinetic energy. Its contribution is more than twice that of the available potential energy in both the ESSTA and WSSTA simulations. The small contribution from the available potential energy reflects the fact that the horizontal temperature gradients within the tropics are relatively weak. In contrast, for the 30-day mean response in the midlatitudes in Figures 3.19a and 3.20a, we see that the kinetic and available potential energies contribute equally to the total energy in the $\ell = 5$ RT modes. This not only reflects the fact that there are strong horizontal temperature gradients in the midlatitudes, but also may indicate that conversions between available potential and kinetic energy play an important role in this component of the response. Again, it is also interesting to note the difference between the relative contributions of each type of energy to the barotropic ($\ell = 1$) and baroclinic ($\ell = 4, 5$) responses in each figure. The preceding analysis strongly suggests that the prominent response of the $\ell = 5$ RT modes is an innate phenomenon of the midlatitudes. This is in agreement with Figure 2.10f, which showed the projection onto vertical mode $\ell = 5$ of the 30-day mean difference in geopotential height at 300 mb in the WSSTA simulation. We may recall from Figure 3.18 that most of the features that project onto this vertical mode appear in the middle or high latitudes in both hemispheres.

In summary, the normal mode partitioning technique developed in this chapter provides a way of highlighting some fundamental characteristics of the tropical and midlatitude responses of the NOGAPS spectral model to the anomalous forcing configurations described in Chapter 2. With this technique, we examined the energy contributions from subsets of "tracer" modes in each region. These are the modes that exhibit a substantial portion of their

latitudinal variance in either the tropics or midlatitudes, and presumably, play important roles in the dynamics in each of these regions (Section 3.2). Based on this partitioning technique, we showed that the anomalous energy in both the tropics and midlatitudes was dominated by the external ($\ell = 1$) rotational modes, indicating a strong barotropic response component in both regions. This is consistent with the difference fields of geopotential height discussed in Chapter 2, and with the results of several of the studies discussed in Chapter 1, that have demonstrated that tropically forced midlatitude anomalies have significant equivalent barotropic structure.

It was also shown that there is a significant baroclinic component to the anomalous response in each region. In the tropics, the baroclinic response projects mainly onto vertical mode $\ell = 4$. This is because the vertical structure of these modes closely resembles the vertical profile of the divergence anomaly associated with the enhanced cumulus convection in the tropics. The prominence of these modes in the tropical response is qualitatively consistent with the results of theoretical and idealized modeling studies that have demonstrated that the local response to anomalous tropical forcing has significant baroclinic structure. In contrast, the prominent baroclinic response in the midlatitudes at vertical mode $\ell = 5$ appears to be a relatively unexplored phenomenon. As stated above, the midlatitude response to anomalous tropical forcing has been discussed previously in terms of propagating equivalent barotropic waves. However, given the fact that the midlatitude response is usually most prominent in the winter hemisphere (Webster, 1982; Simmons, 1982), it seems reasonable to assume that it may exhibit a significant baroclinic component as well. Indeed, the results of Kok and Opsteegh (1985) and

Mechoso *et al.* (1988), among others, indicate that there may be some correlation between episodes of anomalously warm tropical SST and increased transient eddy activity at higher latitudes. At the very least, it is clear that the response at vertical mode $\ell = 5$ in the present study is an indication that the anomalous tropical forcing has led to changes in the energy balance of certain midlatitude baroclinic modes. A logical next step is to investigate the origin of this response, and to attempt to assess its significance in terms of the global response to tropical forcing.

4. THE MIDLATITUDE RESPONSE

The normal mode analysis conducted in Chapter 3 revealed that the anomalous midlatitude response of the NOGAPS spectral model has a significant baroclinic component with approximately half the energy of the more well-known equivalent barotropic response. Based on that analysis, and on the propagation properties of the modes, we concluded that while the barotropic component may originate in the tropics and then propagate to higher latitudes, the baroclinic component is a more local phenomenon that develops in response to conditions in the midlatitudes. However, in conjunction with this, we showed in Figure 3.21a that the evolution of the energy in the baroclinic modes closely follows that of the barotropic modes, with the energy in the former growing at a somewhat slower rate. This behavior suggests that there may be a cause-and-effect relationship between the two components of the response. Moreover, we might expect this relationship to play an important role in determining how forcing in the tropics can eventually influence the climate in midlatitudes. The focus of this chapter is on interpreting in a physically meaningful way the results of the normal mode analysis in Chapter 3, in order to gain insight into how these various response components interact with one another to alter the general circulation in the midlatitudes.

4.1 Horizontal Scales of Motion

The fact that the anomalous midlatitude response has both a barotropic and a baroclinic component suggests that this response may be separated into

contributions from two distinct *horizontal* as well as vertical scales of motion. This is because barotropic motions in the midlatitudes generally tend to be associated with large-scale quasi-stationary waves with long wavelengths (small zonal wave numbers), while baroclinic motions tend to be associated with more rapidly moving synoptic-scale waves with relatively shorter wavelengths (larger zonal wave numbers). The anomalous response at each of these scales of motion is represented in Figures 4.1a and 4.1b, which show the contributions from those modes corresponding to zonal wave numbers 1–3 and 5–9, respectively, to the 30-day mean difference in the 300 mb stream function for the WSSTA simulation. Clearly, there is a dramatic difference between the response patterns at each of these scales of motion. Similar results are obtained in the ESSTA simulation, although the long-wave response in this case is somewhat more difficult to interpret than in the WSSTA simulation. For clarity, the results of the ESSTA simulation are discussed in Section 4.3, in light of the results obtained from the WSSTA simulation.

The long waves in Figure 4.1a are zonally elongated, and are aligned in patterns that reveal distinct meridional wave trains emanating from the tropics toward higher latitudes. It should be noted that the zonal elongation of the anomalies is characteristic of two-dimensional Rossby wave propagation (*e.g.*, Hoskins and Karoly, 1981; Webster, 1981). The strongest of these patterns originates from the north   stern tip of South America and arcs northeastward along the east coast of the United States, and then toward the southern tip of Greenland. The strength of the wave train increases with increasing latitude. The counterpart of this wave train in the Southern Hemisphere arcs southeastward along the west coast of South America, but it is noticeably
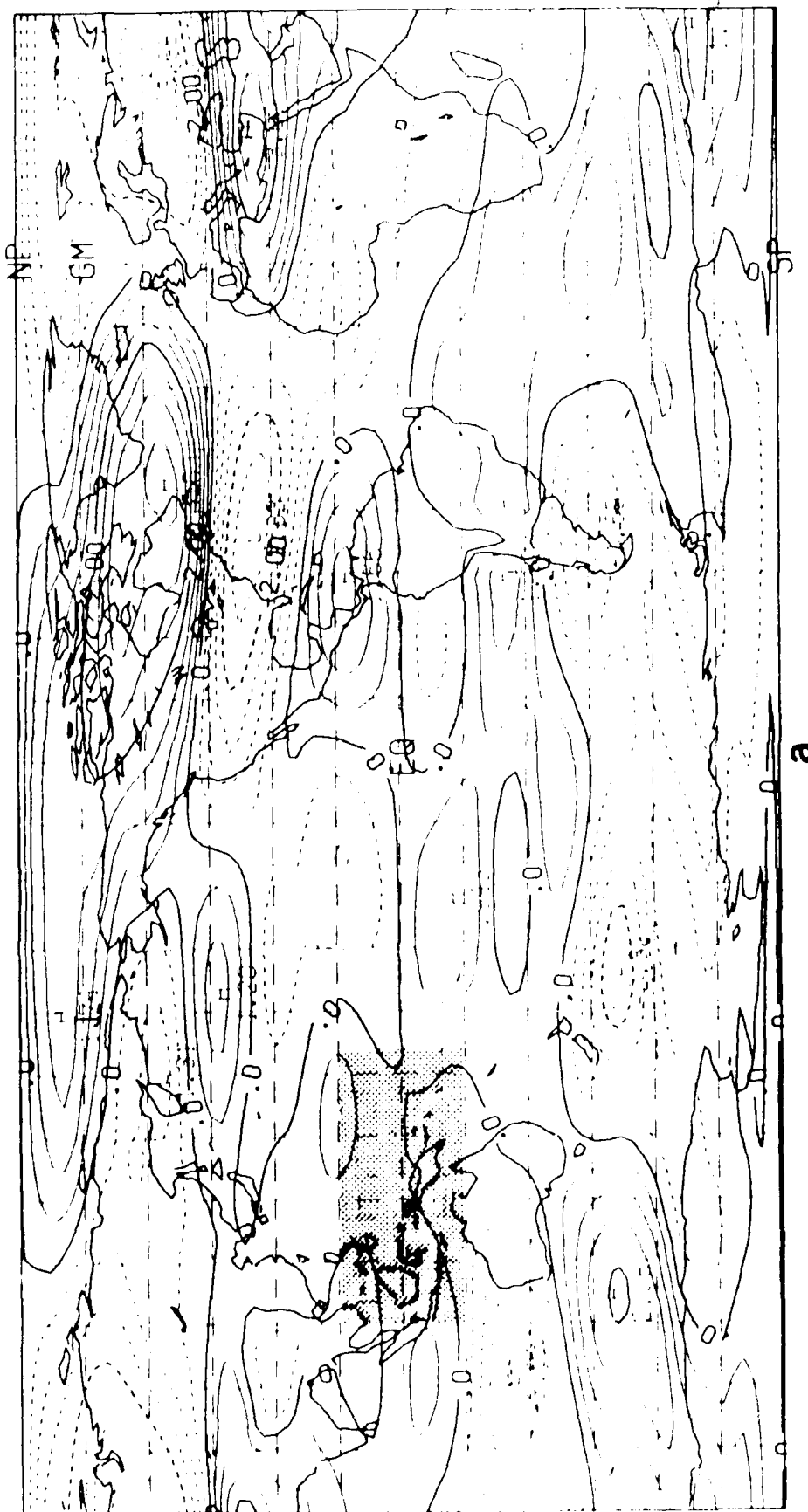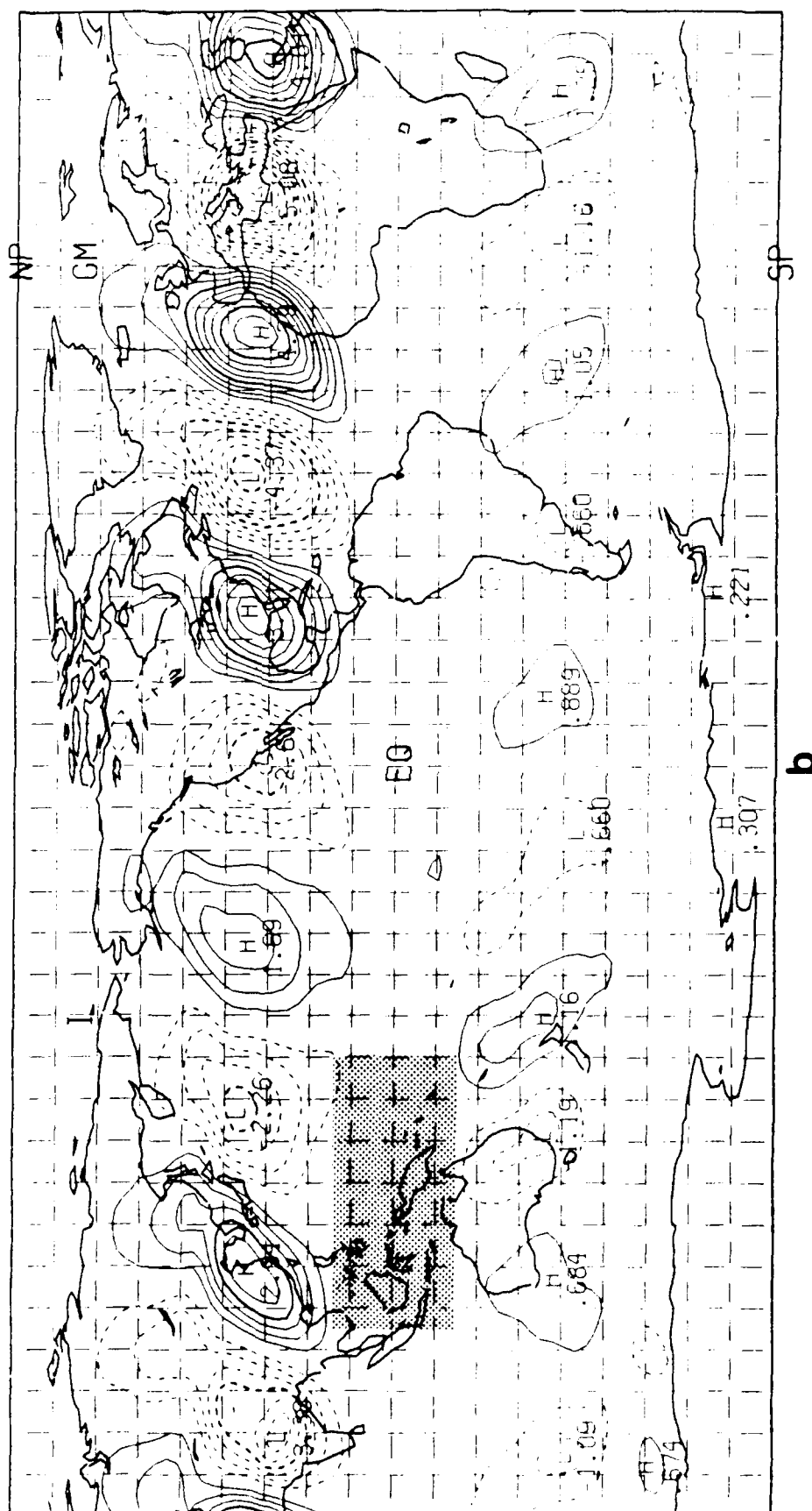
156

Figure 4.1 The contributions from zonal wave numbers (a) 1-3 and (b) 5-9 to the 30-day mean difference in the stream function at 300 mb for the WSSTA simulation. The contour interval is $0.5 \cdot 10^6$ m^2 sec. with negative differences denoted by dashed lines. and the SST anomaly indicated by the stippled region.

Figure 4 1 (continued)

weaker than the wave train in the Northern Hemisphere. The difference in the strengths of the two wave trains is consistent with the findings of Simmons (1982), Webster (1982) and others, who have shown that the strength of the meridionally propagating response depends on the equatorward extent of the midlatitude westerlies, and thus, is usually strongest in the winter hemisphere. Also, there appears to be a secondary region of meridional propagation emanating from just west of Indonesia and propagating into the Southern Hemisphere along the west coast of Australia. In this case, the northern branch of the wave train is conspicuously absent.

It is interesting to note that the main propagating response in this figure emanates from near South America, even though the SST anomaly in this simulation is located in the vicinity of the maritime continent. It has been shown by other investigators that, in the presence of realistic horizontal mean winds, the locations of the tropically forced midlatitude anomalies may be independent of the longitudinal position of the tropical forcing (Simmons *et al.*, 1983; Branstator, 1985). It is believed that the midlatitude anomaly patterns may be geographically "phase-locked" as a result of the horizontal shear in the tropical wind field. Recently, Webster and Chang (1988) have demonstrated that the longitudinal stretch of the mean equatorial zonal wind (*i.e.*, $\partial \bar{u}/\partial x$) can create preferred regions for meridional propagation known as "energy accumulation" zones. They argue that energy from anomalous heat sources near the equator may remain trapped at low latitudes and propagate zonally for great distances before accumulating in these preferred locations and then escaping to higher latitudes. This may explain why the strongest propagating response in Figure 4.1a occurs near the Americas rather than near Indonesia,

although an analysis of the tropical wind field in this simulation remains a topic for future research. It will be shown in Section 4.3 that the position of the American wave train in Figure 4.1a appears to be shifted to the west in the ESSTA simulation in response to .ie SST anomaly being located just off the west coast of South America. Also, the region of weak meridional propagation emanating from west of Indonesia in Figure 4.1a is not present in the ESSTA simulation. The remaining features in Figure 4.1a, such as those over eastern Europe and the Mediterranean Sea, do not appear to be associated with distinct meridional wave trains but may be related to other recurrent teleconnection patterns such as the Eastern Atlantic or Eurasian patterns discussed by Wallace and Gutzler (1981), and may be forced indirectly by the anomalous heating. We may recall that the total difference field shown in Figure 2.7c exhibits anomalies in this region that are similar to those observed by Shukla and Wallace (1983).

The synoptic-scale waves in Figure 4.1b also contribute significantly to the 30-day mean difference in the 300 mb stream function. However, it is clear from this figure that these waves represent a component of the anomalous response that is dramatically different from that represented by the long waves in Figure 4.1a. In contrast to the long waves, these waves are elongated meridionally rather than zonally, and appear as if they may propagate zonally rather than meridionally. This is confirmed in Section 4.2 where the evolution of these waves is examined. It is also clear from Figure 4.1b that these waves contribute primarily to the anomalous response in the midlatitudes, since nearly all of the anomalies in this figure are located poleward of 30° in both hemispheres. In both hemispheres, the time-mean response shown here is dominated by zonal wave number $m = 5$. Given that the anomalies propagate

from west to east, their alignment in Figure 4.1b can be viewed as delineating the mean path of the anomalous synoptic-scale waves. A latitudinal meandering in the path is especially visible in the Northern Hemisphere where the anomalies tend to be displaced slightly poleward over the oceans, and slightly equatorward over the continents. The anomalies themselves display the "tilted trough" structure of baroclinic eddies, showing a southwest-northeast orientation in the Northern Hemisphere, and a northwest-southeast orientation in the Southern Hemisphere. Not surprisingly, the magnitudes of the anomalies are much greater in the Northern (winter) Hemisphere, but in both hemispheres there are zonal asymmetries in the magnitudes and degree of tilt of the eddies. These are important points that are discussed in detail in Section 4.2. In general however, it is most important to note that the results in Figure 4.1b demonstrate that anomalous tropical forcing may alter both the positions and *magnitudes* of the midlatitude synoptic-scale disturbances. The forcing for these disturbances is investigated in the following sections.

The differences between the orientations of the anomalies in Figures 4.1a and 4.1b closely resemble the findings of Hoskins *et al.* (1983), who examined the shape and propagation of large-scale transient eddies during the Northern Hemisphere winter of 1979–80. Using a horizontal velocity correlation tensor as a diagnostic quantity, they found that the time-averaged eddy structure at periods less than ten days differed dramatically from that at periods greater than ten days. The anisotropic part of the horizontal velocity correlation tensor provides a measure of the characteristic horizontal eddy shape and is given by

$$\mathbf{T} = \begin{pmatrix} M & N \\ N & -M \end{pmatrix},$$ (4.1)

where

$$M = \frac{1}{2} \overline{\left(u'^2 - v'^2\right)} , \qquad (4.2)$$

and

$$N = \overline{u'v'} . \qquad (4.3)$$

The quantities M and N describe the eddy dimensions in the longitudinal and latitudinal directions, respectively. Here, the bar signifies a time-mean operator and the prime signifies a deviation from this mean. Hoskins *et al.* found that high-pass filtered eddies (*i.e.*, those with periods less than ten days) were elongated meridionally with southwest-northeast tilt and a ratio of zonal to meridional scales of about two to three, while low-pass filtered eddies (*i.e.*, those with periods greater than ten days) were elongated zonally with much greater anisotropy implying a ratio of zonal to meridional scales of about five to two. These investigators demonstrated that the low-pass eddies in their study corresponded to slowly varying barotropic waves, while the high-pass eddies corresponded to synoptic-scale baroclinic waves. Their results, including the greater anisotropy for the zonally elongated low-pass eddies, are remarkably similar to those in Figures 4.1a and 4.1b. It is interesting to note that the results in Figure 4.1 were obtained using a spatial (*i.e.*, wave number) filter rather than a temporal filter as used by Hoskins *et al.* The similarity between their results and the results in Figure 4.1 demonstrates the relationship between the temporal and spatial scales of these waves. Moreover, it strongly implies that the long waves in Figure 4.1a show the 30-day mean positions of eddies associated with the slowly varying or quasi-stationary component of the anomalous response, and that the synoptic-scale waves in Figure 4.1b show the 30-day mean positions of eddies associated with more rapidly fluctuating

162

midlatitude baroclinic disturbances.

It seems reasonable to try to relate the different structures in Figures 4.1a and 4.1b to the barotropic and baroclinic responses at vertical modes $\ell = 1$ and $\ell = 5$ in Figure 3.20a. Figure 4.2 shows the projections of the long waves in Figure 4.1a onto vertical modes $\ell = 1$ (Figure 4.2a) and $\ell = 5$ (Figure 4.2b). Both of the meridionally propagating wave trains observed in Figure 4.1a project strongly onto the external modes in Figure 4.2a. In contrast, neither of these wave trains projects strongly onto vertical mode $\ell = 5$ in Figure 4.2b. Although some features of the North American wave train can be seen in the latter figure, it is difficult to associate these features with meridionally propagating waves without pre-existing knowledge of the position of the wave train. These figures confirm that the meridionally propagating long waves in Figure 4.1a are indeed a barotropic phenomenon.

Figure 4.3 shows the projections of the synoptic-scale waves in Figure 4.1b onto vertical modes $\ell = 1$ and $\ell = 5$. Although the baroclinic character of these waves is demonstrated by their projection onto vertical mode $\ell = 5$ in Figure 4.3b, it is clear from Figure 4.3a that they project even more strongly onto the external modes. This may be due, in part, to the fact that these figures represent 30-day mean fields. For example, Ghil (1987) points out that averaging over this length of time substantially increases the barotropic character of the flow, which in turn, projects onto the external modes. This barotropization, or barotropic adjustment, has been explained in different ways by several investigators (Holloway, 1986; Simmons and Hoskins, 1978; Held, 1988), and appears to indicate a pre-eminence of external Rossby waves over internal ones. In the present case, other calculations involving shorter averaging

a

Figure 4.2 The projections of zonal wave numbers 1–3 of the 300 mb stream function anomalies in Figure 4.1a onto vertical modes (a) $\ell = 1$, and (b) $\ell = 5$. The format is the same as in Figure 4.1.

(continued on next page)
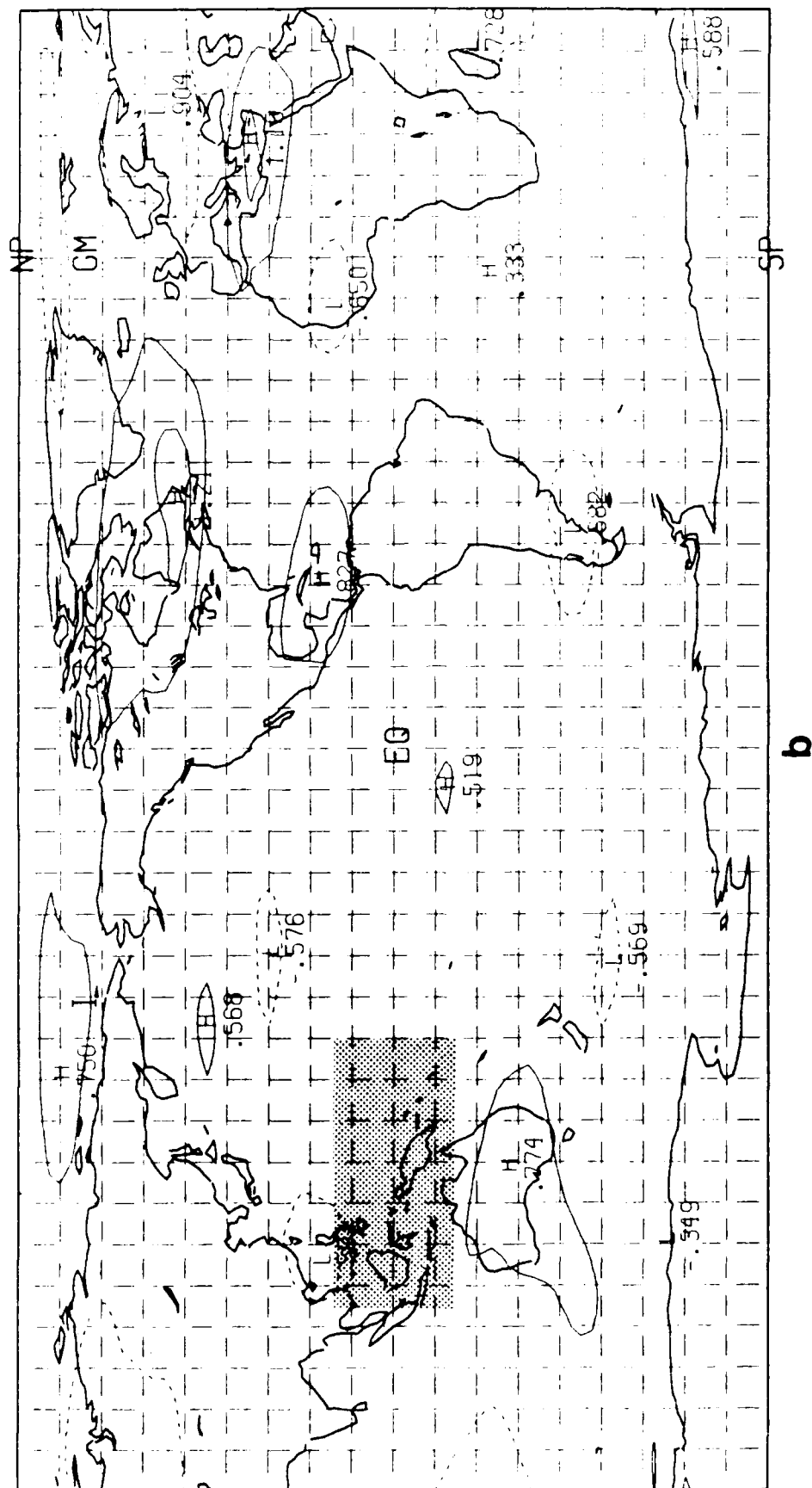
Figure 4.2 (continued)

b

periods of five days (roughly equal to the synoptic period) indicate that these waves actually project nearly equally onto vertical modes $\ell = 1$ and $\ell = 5$. Nonetheless, based on these projections it appears that both baroclinic and barotropic processes may contribute to the growth of these disturbances. Again. note that the zonal asymmetries in the magnitudes of the eddies are especially evident in these figures.

In summary, the time-mean midlatitude response of the NOGAPS spectral model to anomalous tropical forcing is separable into two distinct types of horizontal wave motion. The first type is associated with long waves (*e.g.*, zonal wave numbers 1–3), which appear to originate from localized regions in the tropics and then to propagate meridionally toward higher latitudes. The horizontal structure of these waves is consistent with that of low-pass filtered or slowly varying eddies (those having periods greater than ten days) that have been examined by other investigators. These waves project almost exclusively onto the external normal modes of the anomalous midlatitude response, indicating that they are indeed a barotropic phenomenon analogous to the Rossby wave trains obtained in simple modeling studies such as those discussed in Chapter 1.

The second type of wave motion is associated with synoptic-scale waves (*e.g.*, zonal wave numbers 5–9) that, as shown in Section 4.2, propagate zonally along latitudes between 30° and 45°. For the WSSTA simulation discussed above, the quasi-stationary solution is dominated by zonal wave number 5. It is shown in Section 4.3 that, in the ESSTA simulation, zonal wave number 6 appears to be dominant. It is not clear whether the preferred zonal wave number depends on the structure of the tropical forcing or on the stability characteristics
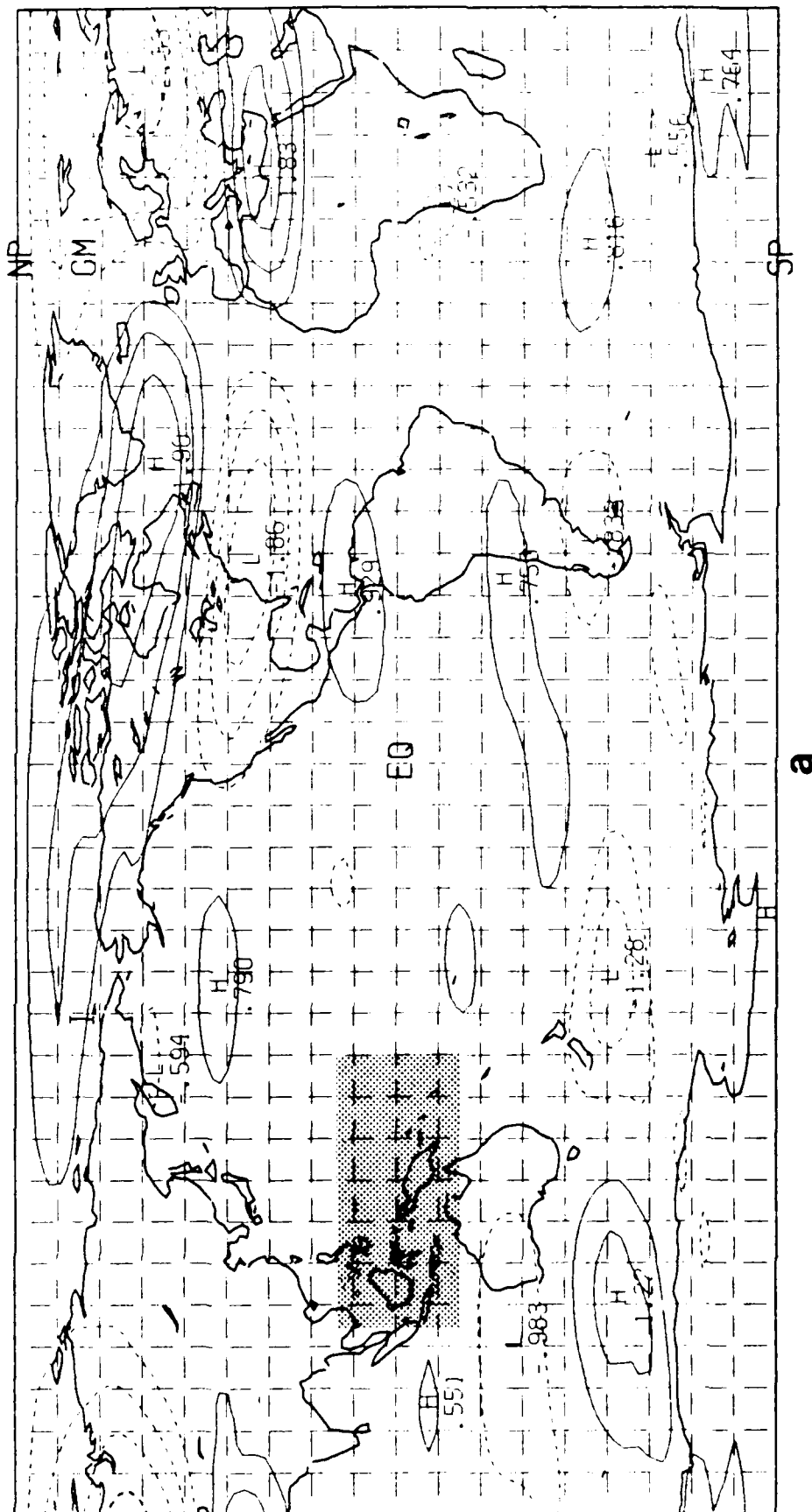
a

Figure 4.3   The projections of zonal wave numbers 5-9 of the 300 mb stream function anomalies in Figure 4.1a onto vertical modes (a) $\ell = 1$, and (b) $\ell = 5$.   The format is the same as in Figure 4.1.

Figure 4.3 (continued)

b

of the midlatitude flow. At this point, the latter seems more likely in view of the fact that a similar SST anomaly was used in both simulations. The horizontal structure and tilt of these waves are consistent with high-pass filtered eddies (those having periods less than ten days) that are associated with midlatitude baroclinic waves. This is further supported by differences in the energy spectra of the modes for the control and anomaly simulations. For example, Figure 4.4 shows the difference in the 30-day mean energy in zonal wave numbers 0–10 for vertical mode $\ell = 5$ (note that this figure shows the *difference of the energy*, rather than the energy of the difference field). This difference is defined by subtracting the control values of energy from the anomaly values, so that a positive (negative) difference indicates that the anomaly (control) simulation is more energetic. Given that instability is defined by a preferential transfer of energy *between the zonal mean flow and the eddies* (Pedlosky, 1979), we have included the zonally symmetric ($m = 0$) modes in Figure 4.4 in order to compare the distributions of eddy and zonal mean energy in the control and anomaly simulations. Accordingly, the most striking result in this figure is that the anomaly simulation shows a dramatic decrease in zonal mean available potential energy, combined with a moderate increase in zonal mean kinetic energy. In addition, the anomaly simulation shows an increase in energy in the synoptic-scale wave numbers 5 and 6. These results are consistent, at least qualitatively, with energy conversions associated with baroclinic instability, and with the subsequent increase in zonal mean momentum associated with mature and decaying cyclones (Simmons *et al.*, 1983). This also supports the results in Figures 4.3a and 4.3b in which the normal mode projections of these waves indicated the presence of both baroclinic and barotropic structures.
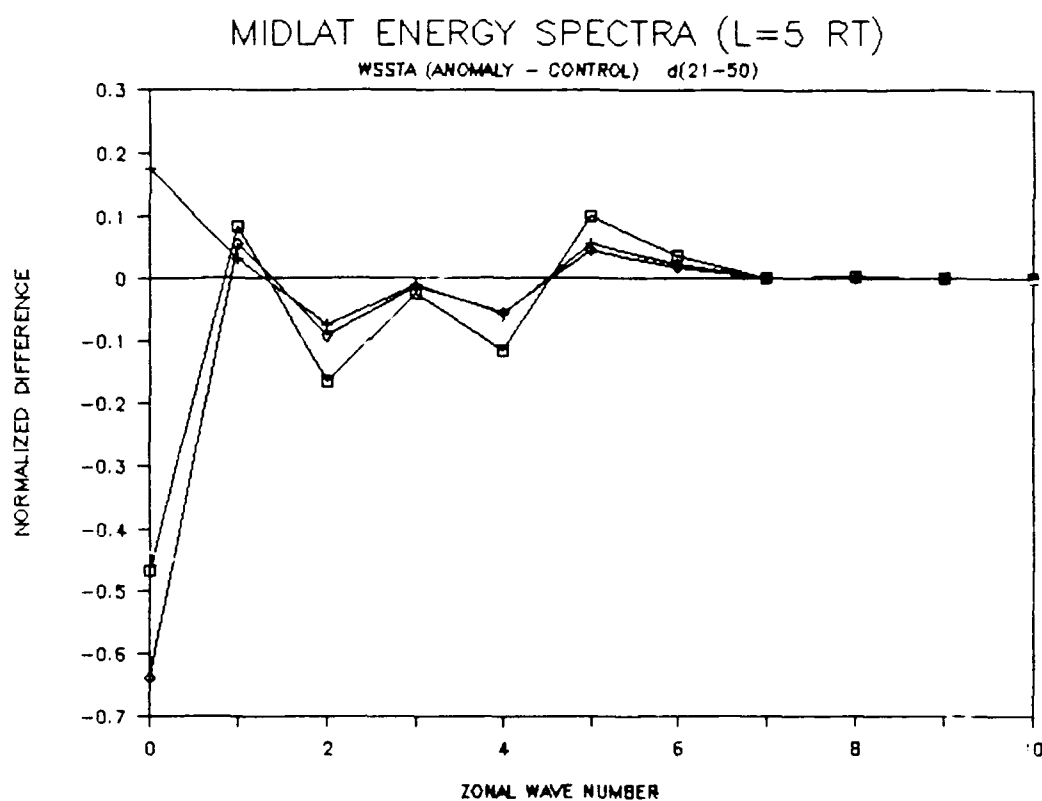
Figure 4.4   The normalized differences between the 30-day mean energy
spectra for zonal wave numbers 0-10 in the control and anomaly
runs in the WSSTA simulation, for the midlatitude $\ell = 5$ RT
modes. Positive differences indicate that the anomaly values are
greater.

The results in Figures 4.1b, 4.3b and 4.4 are consistent with the strong response at vertical mode $\ell = 5$ obtained in the midlatitude energy profile in Figure 3.20a and suggest that *the SST anomaly in the Western Pacific has significantly modified the synoptic-scale baroclinic development in the midlatitudes.* This assertion is verified in Section 4.2, and it goes beyond the idea of an equivalent barotropic response in the midlatitudes, in which the upper-tropospheric circulation is simply displaced geographically by anomalous standing waves in the troposphere. It should be noted that these results are consistent with those of Mechoso *et al.* (1987) who observed an increase in midlatitude synoptic-scale transient energy in response to a tropical SST anomaly in the UCLA GCM.

The extent to which these results can be considered general is of course an important issue for future research. Certainly, the quantitative nature of the results will vary somewhat from case to case, and from model to model. However, in accordance with the discussion in Section 2.3, the degree of confidence that can be attached to these results is certainly enhanced by the fact that the total difference field in this simulation (Figure 2.9) reveals anomaly patterns that are typical of those known to occur in response to localized SST anomalies in the tropics (*e.g.*, Horel and Wallace, 1981; Shukla and Wallace, 1983; Branstator, 1985). This is especially evident in the WSSTA simulation, in which the standing wave pattern over North America closely resembles the well-known PNA pattern.

Finally, it should be noted that these results may have important implications with regard to atmospheric predictability, and more directly, the prospect for making extended-range forecasts of midlatitude flow. For example,

on the one hand, we might expect the midlatitudes to be less predictable during periods of anomalously strong tropical forcing since the resulting increase in synoptic-scale wave development would tend to be associated with a more variable weather pattern in midlatitudes. A recent study by Palmer (1988) of Northern Hemisphere winter data over several seasons has in fact shown that variations in predictive skill may be correlated with fluctuations of the PNA mode. On the other hand, the preceding results imply that our ability to predict midlatitude flow may be greatly increased if we correctly simulate the tropical forcing in atmospheric models.

4.2 The Synoptic-Scale Response

It is clear from Figure 4.1a that the anomalous long-wave response in midlatitudes is associated with meridionally propagating waves that originate in the tropics. This is consistent with its strong projection onto the external modes as shown in Figure 4.2 and with the normal mode analysis in Chapter 3, which revealed that the external RT modes contributed approximately one third of the anomalous total energy in both the tropics and midlatitudes. In simple modeling studies such as those described in Chapter 1, this type of response has been interpreted in terms of Rossby wave dispersion on a sphere from a tropica' vorticity source (e.g., Hoskins and Karoly, 1981). In contrast, the synoptic-scale response shown in Figure 4.1b is strictly a midlatitude phenomenon whose horizontal structure appears to be consistent with that of baroclinic waves. This also is supported by the results of the normal mode analysis in Chapter 3, which revealed a secondary energy peak at vertical mode $\ell = 5$ in the midlatitudes. Because baroclinic processes have been neglected in most of the simple modeling

studies of teleconnections, there is as yet no body of knowledge concerning the origin or forcing mechanism for this component of the anomalous response. The focus of this section is to gain some insight into these issues.

One of the most interesting characteristics of the anomalous synoptic-scale eddies in Figure 4.1b is that they exhibit a marked zonal asymmetry in intensity. Restricting our discussion to the Northern Hemisphere for the time being, we observe a pronounced increase in the strength of the anomalies in Figure 4.1b that begins over the eastern United States and continues across the Atlantic Ocean before reaching a maximum negative value of -4.9×10^6 m^2/sec over the Mediterranean Sea. The anomalies in this region have more than twice the amplitude of those in the Pacific. After this point, the anomalies decrease in intensity monotonically until they approach the west coast of the United States. This zonal asymmetry is even more pronounced in Figure 4.3b, which shows the projection of these eddies onto vertical mode $\ell = 5$. It is interesting to note that there is no corresponding increase in the strength of the anomalies off the East Asian coast, which ordinarily is a region of intense synoptic-scale development during the winter and which is close to the SST anomaly. We may recall from Figure 2.7a that the 30-day mean geopotential height field at 300 mb for the control simulation represents a fairly typical Northern Hemisphere wintertime pattern. In particular, the East Asian jet does not appear to be unusually weak during this period. Thus, it is not likely that the zonal asymmetry in the magnitudes of the anomalous synoptic-scale eddies is associated with any pre-existing weakness in the Pacific storm track. Based on these 30-day mean fields alone, it can be concluded only that the anomalous synoptic-scale eddies have their maximum preferred locations between the eastern United States and

the Mediterranean Sea. However, this information is in itself of interest because it demonstrates the potential impact of erroneous tropical forcing in numerical models. For example, if we consider the SST anomaly used in these simulations to be a measure of the difference between the observed and model-predicted forcing over the western Pacific, then these figures indicate that there would be substantial 30-day mean errors in the midlatitude synoptic-scale waves, and moreover, that there would be a preferred region in which these errors obtain a maximum. Clearly, it is important to understand the forcing and dynamics that produce such an error pattern.

Further insight into the origin of the anomalies is obtained by examining the evolution of the difference field. Figure 4.5 shows three consecutive five-day mean fields of the anomalous stream function at 300 mb corresponding to days 1–5, 6–10 and 11–15 of the WSSTA simulation. As before, only those modes corresponding to zonal wave numbers 5–9 are shown. It can be seen from this sequence that the character of the difference field changes dramatically over the first two weeks of the simulation. As indicated by the near absence of anomalies poleward of approximately 20° in Figure 4.5a, there is little difference in the midlatitude flow between the control and anomaly simulations during days 1–5. However, as shown in Figure 4.5b, by days 6–10 there are closed anomalies over a region stretching from the southern United States to Spain. Although there are some weak anomalies in the western Pacific at this time, the midlatitude flow in the Northern Hemisphere is relatively undisturbed downstream of extreme western Europe. Figure 4.5c shows that by days 11–15, the anomalies have spread across Asia and into the northern Pacific, with only the western Pacific remaining relatively undisturbed. Note that the strongest anomalies are
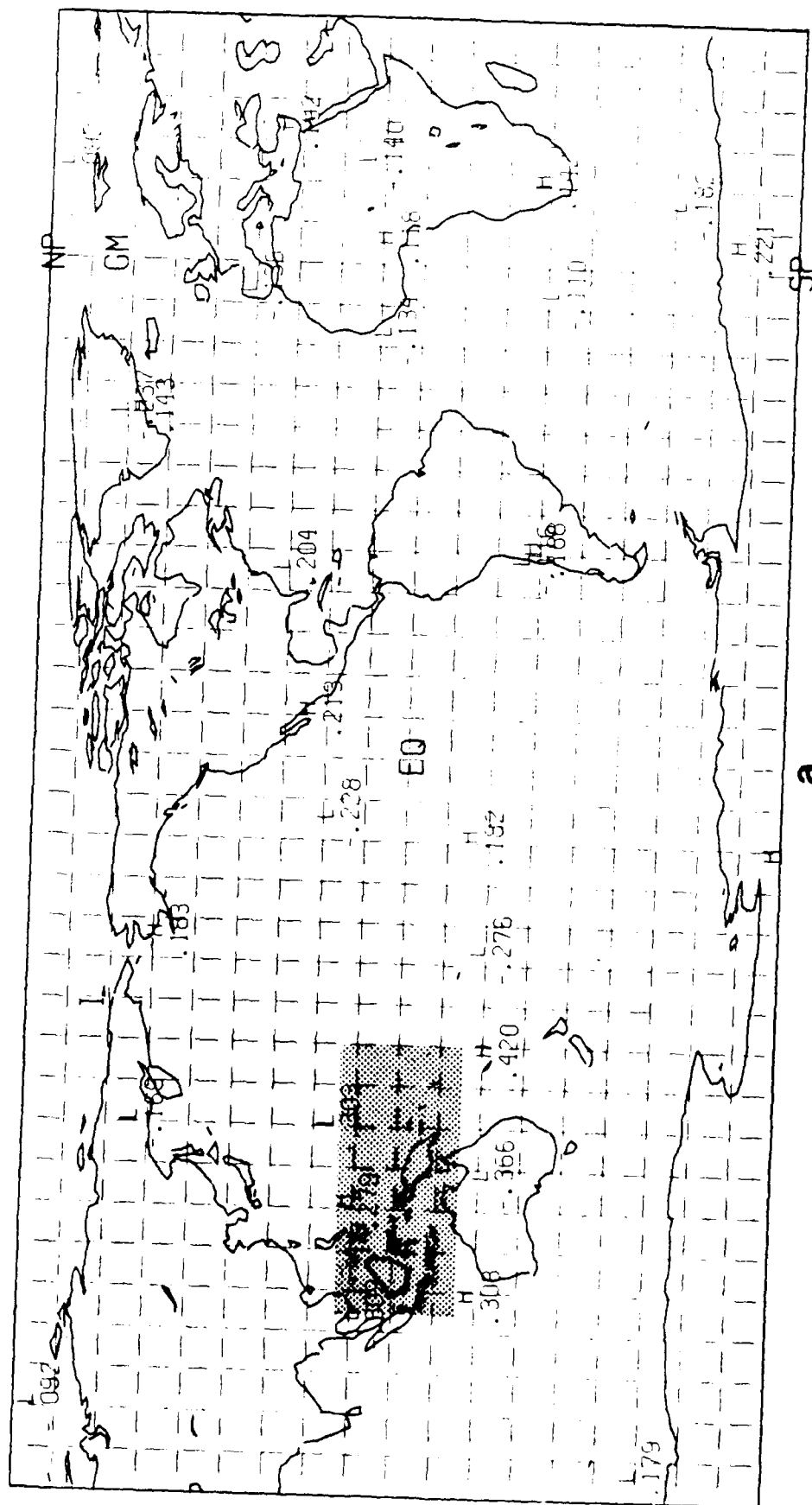
Figure 4.5 Five-day mean anomalies for zonal wave numbers 5-9 of the stream function at 300 mb for days (a) 1-5, (b) 6-10 and (c) 11-15 of the WSSTA simulation. The format is the same as in Figure 4.1.
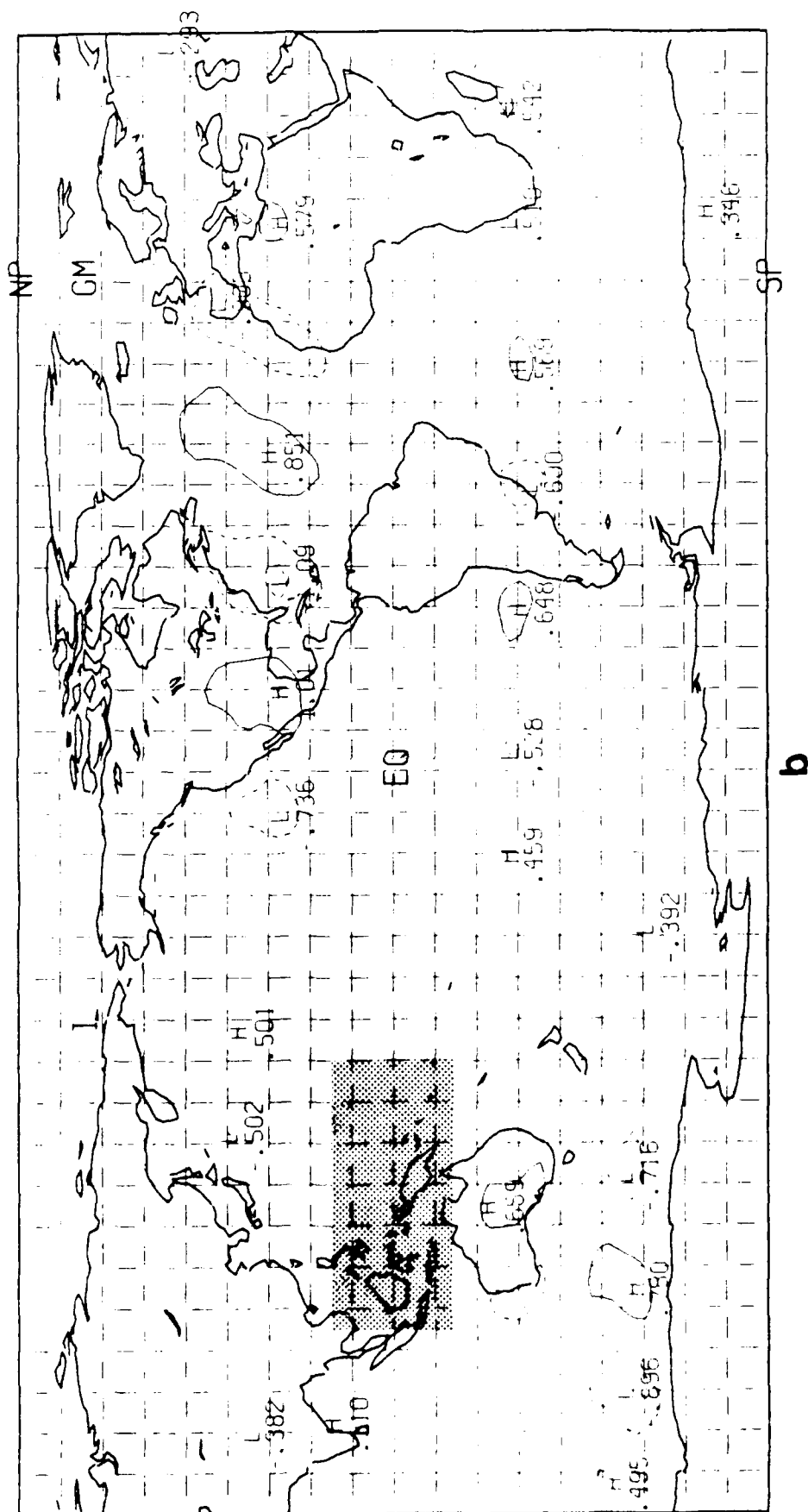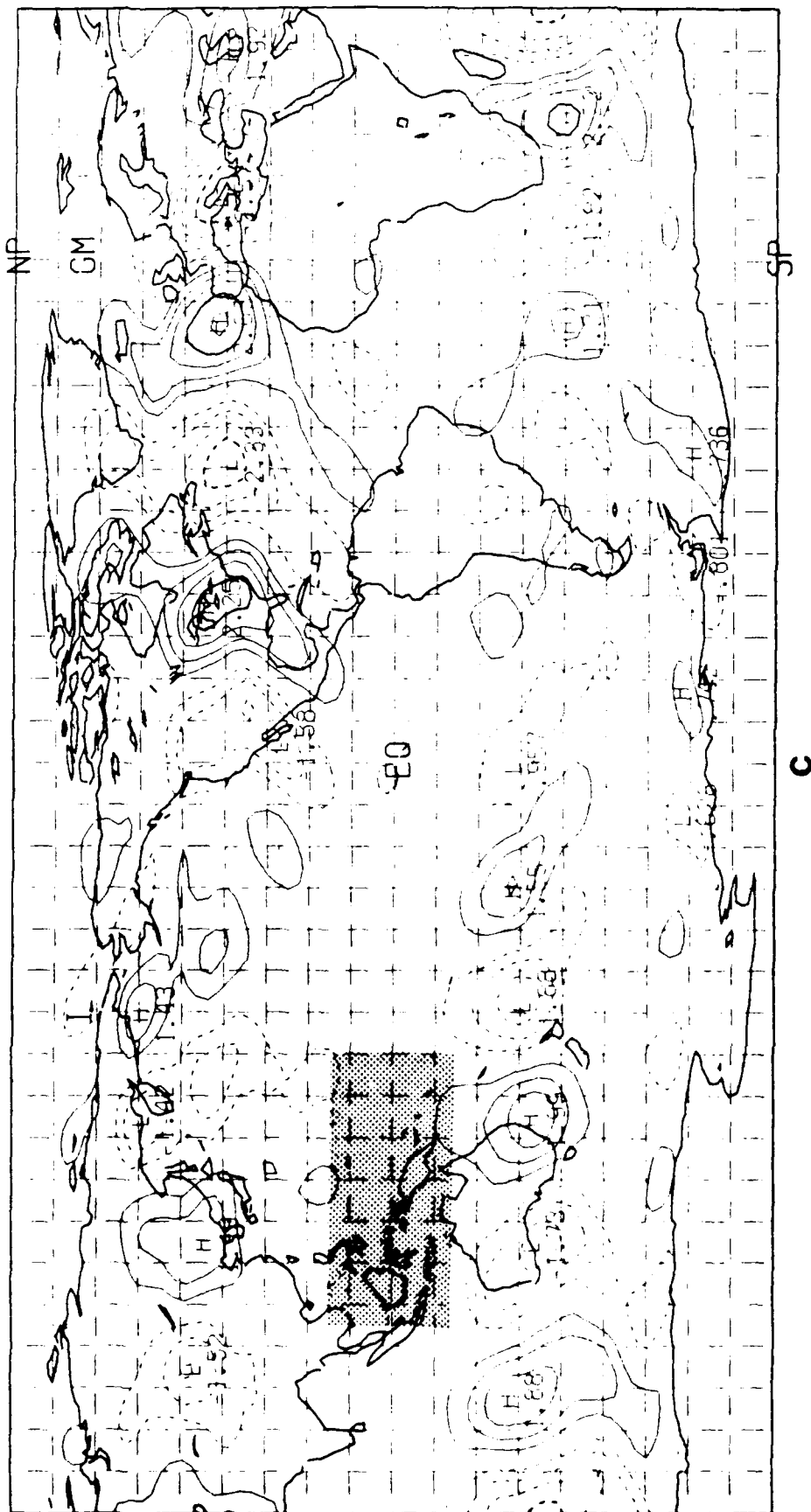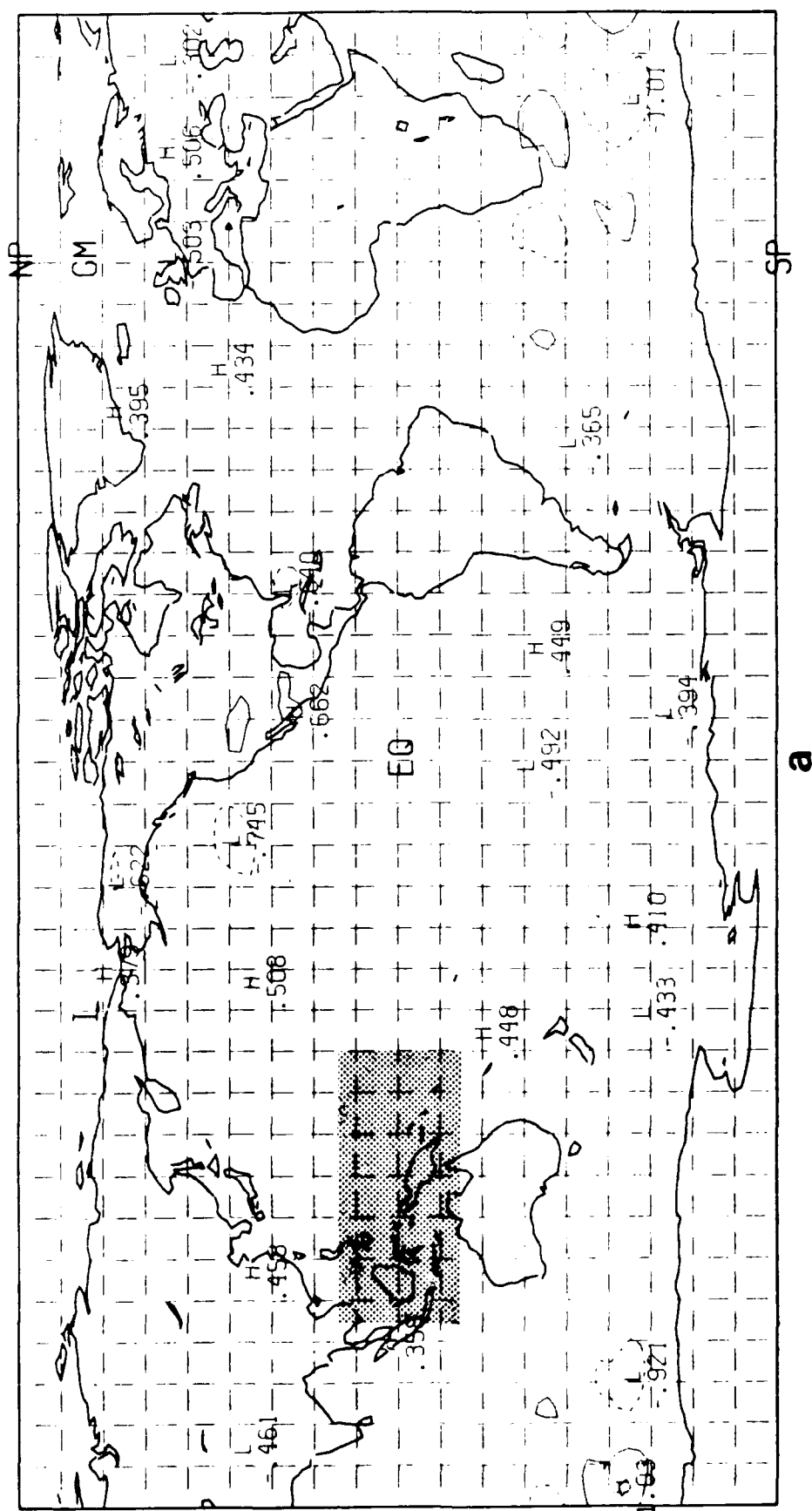
Figure 4.5 (continued)

Figure 4.5 (continued)

still found over the Atlantic and western Europe at this time, suggesting that the forcing for the anomalous synoptic-scale eddies in the Northern Hemisphere may occur somewhere over the eastern United States or western Atlantic Ocean. This is examined with greater temporal resolution below.

It is interesting to compare the results in Figure 4.5 with the growth curve for the anomalous energy in the midlatitude RT modes shown earlier in Figure 3.21a. Note that the three points labeled 1-5, 6-10 and 11-15 along the abscissa in Figure 3.21a correspond to the five-day mean periods shown in Figure 4.5. In Figure 3.21a, the rapid growth in the anomalous energy in the external mode and in vertical mode $\ell = 5$ during these periods is consistent with the dramatic change in the difference field observed in the sequence in Figure 4.5. In particular, the appearance of the closed anomalies in Figure 4.5b is consistent with the more than doubling of the anomalous energy in the $\ell = 5$ RT modes between days 1-5 and 6-10 in Figure 3.21a. The energy growth in these modes then slows somewhat between days 6-10 and 11-15, before leveling off by days 16-20. Recall that Figure 4.5c showed that the anomalies had nearly spread across the Pacific by days 11-15, and by days 16-20 (not shown in Figure 4.5) they completely encircled the Northern Hemisphere. These patterns are consistent with the evolution of the anomalous energy in the $\ell = 5$ RT modes. can be seen in Figure 3.21a that the energy in the external RT modes evolves in a similar manner, but grows much more rapidly in the early part of the simulation and continues to grow until days 21-25. Undoubtedly, some of the growth in the anomalous synoptic-scale eddies in Figure 4.5 is reflected in this curve as well, although their evolution appears to be more consistent with that of the $\ell = 5$ growth rate. Also, it should be noted that the growth curves in

Figure 3.21a show the midlatitude energy in both the Northern and Southern Hemispheres. However, it can be seen in Figure 4.5 that the relative magnitudes of the anomalies in the Southern Hemisphere evolve in roughly the same manner as those in the Northern Hemisphere, with some apparent differences in their geographical origin. This is examined in more detail below.

The localized development of the anomalous synoptic-scale eddies is more clearly revealed by examining the evolution of the difference field using finer temporal resolution than the five-day means in Figure 4.5. Accordingly, Figure 4.6 shows the daily evolution of zonal wave numbers 5–9 of the anomalous stream function at 300 mb between days 6 and 10 in the WSSTA simulation.   This is the period during which the closed anomalies first appeared in the five-day means shown in Figure 4.5. In the Northern Hemisphere, the difference field at day 6 in Figure 4.6a is relatively undisturbed except for some hint of the anomalies to the west and south of the United States. However, by day 7 (Figure 4.6b), a much more organized pattern has developed with closed anomalies clearly originating near the south-central and eastern parts of the United States. Note that in the Southern Hemisphere at this time there are midlatitude anomalies that appear to originate from two source points; one is located off the west coast of South America, and the other is located in the extreme southern Indian Ocean to the west of Australia. In the Northern Hemisphere, the strongest anomaly is located over the southeastern United States with two successively weaker closed centers downstream that extend into the middle of the North Atlantic Ocean. There also appears to be some upstream development at each location, such as over the southwestern United States in the Northern Hemisphere, and to the southeast of Africa in the

179

Figure 4.6   Daily anomalies for zonal wave numbers 5–9 of the stream function at 300 mb for days (a) 6, (b) 7, (c) 8, (d) 9 and (e) 10 of the WSSTA simulation. The format is the same as in Figure 4.1.
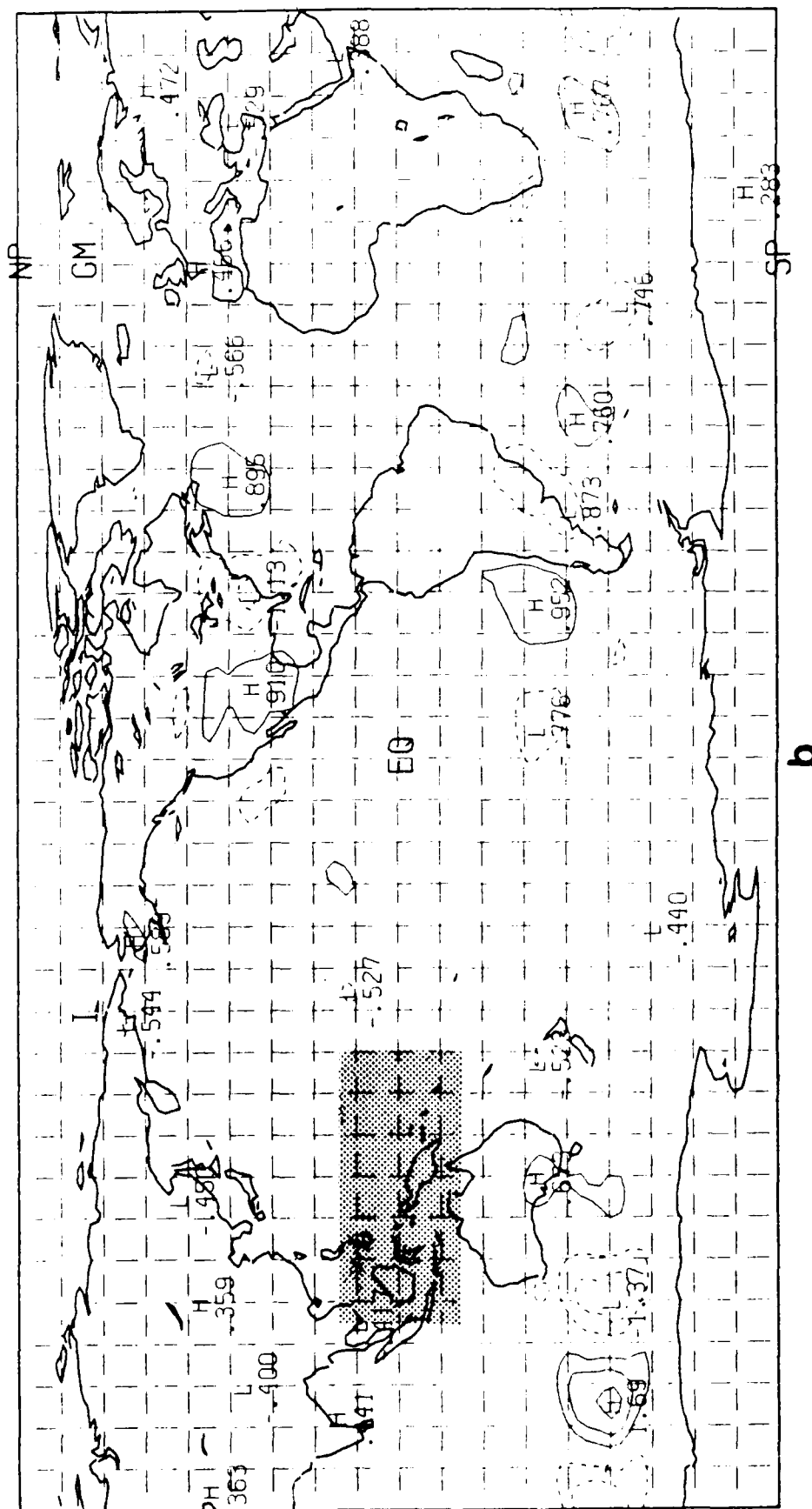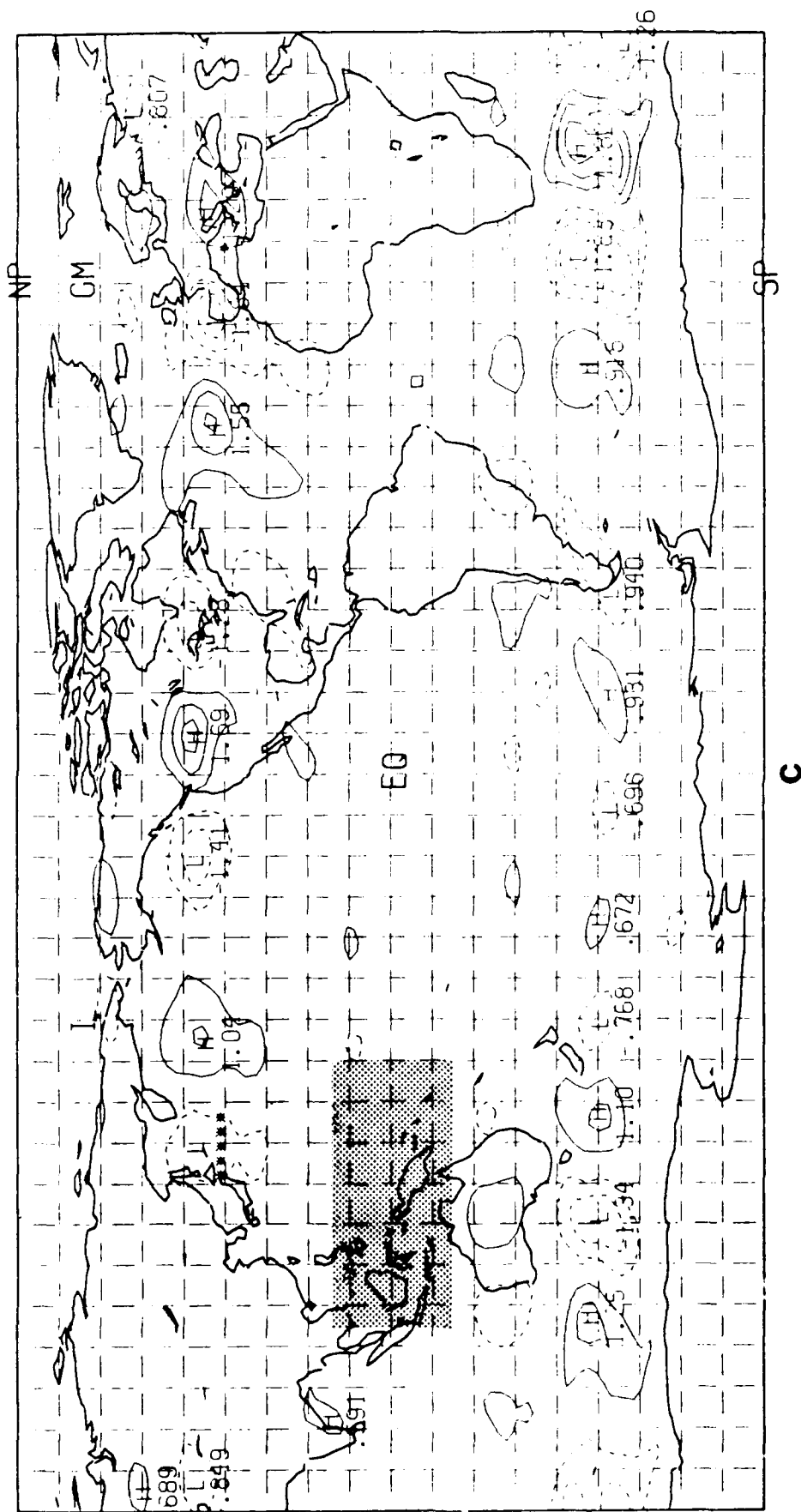
Figure 4.6 (continued)

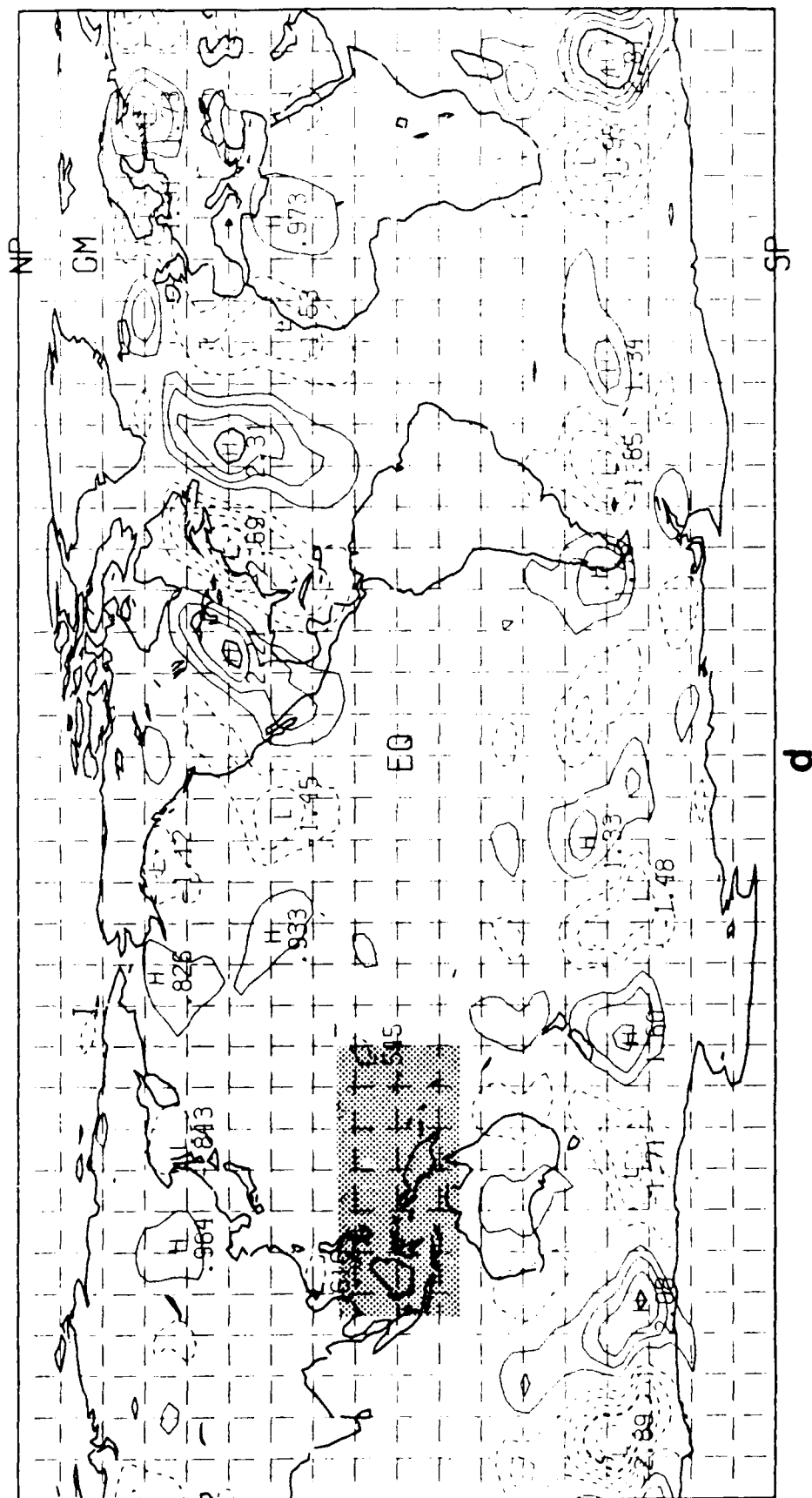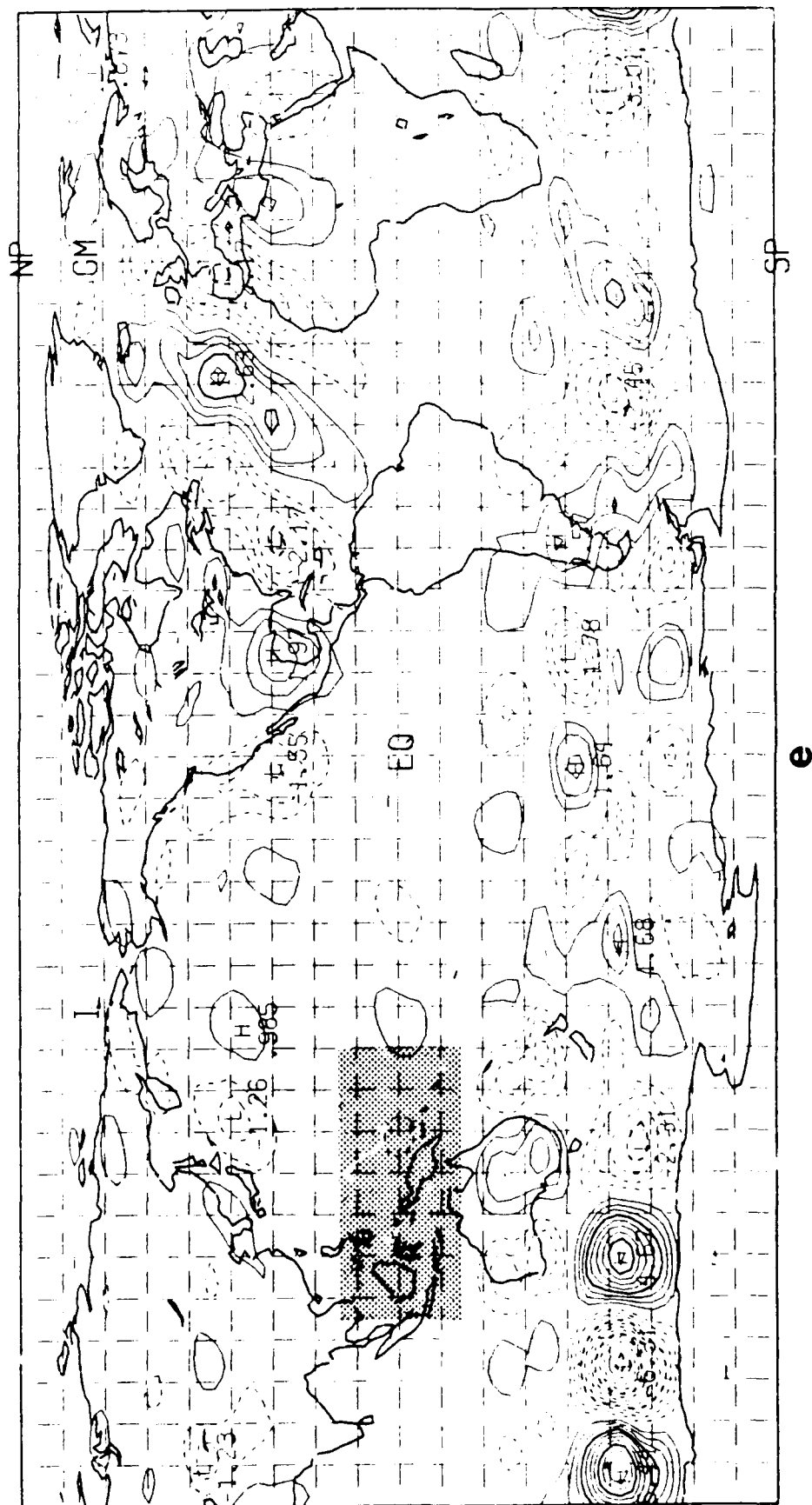Figure 4.6 (continued)

Figure 4.6 (continued)

Figure 4.6 (continued)

Southern Hemisphere. By day 8 (Figure 4.6c), the zonal propagation of the eddies is plainly evident as the closed anomalies extend as far downstream as the Mediterranean Sea in the Northern Hemisphere. A secondary source appears to have emerged off the coast of Japan at this time, although it will be seen in the remainder of the sequence that this is weak in comparison with the source in the Atlantic. In the Southern Hemisphere at this time, the anomalies appear to encircle the globe completely as a result of their originating from two widely separated source points. At days 9 and 10 (Figures 4.6d and 4.6e, respectively), the eastward progression of the pattern in the Northern Hemisphere continues with closed anomalies spreading across Asia. Based on the zonal asymmetry in the magnitudes of the anomalies in these figures, it is clear that the Atlantic sector remains the dominant source point in the Northern Hemisphere. It might be noted that the anomaly pattern in this sequence appears to be dominated by zonal wave number 6, while the 30-day mean pattern in Figure 4.1b is dominated by zonal wave number 5. The shift toward the larger-scale features in the latter is clearly a result of the fact that averaging over 30 days acts as a low-pass filter.

There are two important implications of the results in Figures 4.5 and 4.6. The first is that, under certain conditions, perturbations in the tropical diabatic forcing field may begin to have a substantial impact on the midlatitude synoptic-scale pattern on time-scales *less than two weeks*. With regard to numerical modeling applications, this would imply that the success of even medium-range (6–10 days) forecasts of midlatitude flow may depend critically on the accuracy of the model-predicted tropical diabatic forcing, especially in the winter hemisphere. It can be seen in Figures 4.5 and 4.6 that the forcing of

the anomalous synoptic-scale eddies is clearly stronger in the Northern Hemisphere since this simulation was conducted using December initial conditions. The second implication is that these changes in the synoptic-scale pattern may be forced at *specific geographical locations* in the midlatitudes. In the WSSTA simulation discussed here, the anomalous eddies in the Northern Hemisphere originate over the eastern United States and the western Atlantic Ocean. In the Southern Hemisphere, the anomalous eddies appear to originate from two widely separated locations, one off the west coast of South America and the other in the Indian Ocean.

Based on the longitudinal positions of the eddy source points in Figures 4.5 and 4.6, it seems unlikely that the anomalies develop simply as a result of an increase in the global or regional baroclinity of the atmosphere owing to the anomalous heating in low latitudes. For example, if this were the case, then it seems unlikely that little or no anomalous synoptic-scale development would occur in the vicinity of the East Asian jet. Accordingly, it seems more likely that some forcing mechanism may be operating locally to destabilize the flow in preferred locations. With this in mind, it is compelling to note that the apparent source points for the synoptic-scale anomalies in Figures 4.5 and 4.6 coincide well with the positions of the meridionally propagating wave trains in the long-wave response shown in Figure 4.1a. In addition, these source points occur just upstream from the maximum preferred 30-day mean locations of the anomalies shown in Figure 4.1b. In particular, it is interesting to compare the locations in which the closed anomalies first develop at day 7 of the simulation (Figure 4.6b), with the positions of the meridional wave trains in Figure 4.1a. In Figure 4.6b, three separate areas of synoptic-scale development—one in the

Northern Hemisphere and two in the Southern Hemisphere—are plainly visible in the general vicinities where each of the three meridional wave trains in Figure 4.1a intersects the midlatitude westerly jet (*cf.*, Figure 2.7a). In contrast, there is a conspicuous lack of synoptic-scale development in the vicinity of the East Asian jet that corresponds with the absence of a Northern Hemisphere branch of the Pacific wave train in Figure 4.1a. Although there are some hints of anomalous synoptic-scale development in the Pacific later in the simulation, they are insignificant compared with that in the Atlantic. As discussed in Section 4.1, the reason for the absence of the northern branch of the Pacific wave train has not been investigated in this study, but may be related to the horizontal shear in the subtropical winds in this region.

As the simulation progresses, the synoptic-scale anomalies that first appeared in the vicinities of the meridional wave trains begin to propagate downstream and develop greater amplitude. This can be seen at days 9 and 10 of the simulation (Figures 4.6d and 4.6e) as the anomalies strengthen over the Atlantic and propagate toward Europe. At the same time, it appears in these figures that the source point of the eddies remains fixed over the eastern United States. Similar behavior can be observed in the Southern Hemisphere at these times as the anomalies move off the east coast of South America and into the Atlantic. These results suggest that the forcing of the anomalous synoptic-scale eddies may result from an interaction between the midlatitude westerlies and the meridionally propagating modes associated with the classical teleconnection response. For example, one possibility is that the meridionally propagating energy perturbs the midlatitude westerly flow, and then the perturbations grow in an unstable environment. It is well-known that similar types of interactions

occur regularly in the midlatitudes, such as when eastward moving disturbances encounter an existing baroclinic zone and then develop rapidly. It is relevant to note that the southeastern United States is a major baroclinic zone during the Northern Hemisphere winter.

A final comment that should be made here is that some care must be taken when comparing Figures 4.1b and 4.6 since they are not concurrent. We may recall that the former represents a 30-day mean response during days 21–50 of the simulation, while the latter shows the daily evolution of the response between days 6 and 10 of the simulation. However, based on the prominence of the meridionally propagating wave trains in Figure 4.1b—especially in the Northern Hemisphere—and on the fact that their location depends strongly on the mean winds, it is reasonable to assume that the positions of the meridional paths along which energy escapes to the midlatitudes will remain fairly constant over time-scales relevant to these results. Therefore, because energy associated with rapidly propagating (i.e., external) RT modes reaches the extratropics long before a standing wave train is observed in the mean field, it is not surprising that any synoptic-scale forcing by these modes may begin relatively early in the simulation. This is in agreement with the evolution of the anomalous energy in the midlatitude RT modes in Figure 3.21a, which shows that the contribution from the external modes increases most rapidly during the first two weeks of the simulation. At the same time, the meridional wave trains appearing in Figure 4.1b are barely discernible during days 6–10 (not shown). Recently, Zhong and Nogues-Paegle (1989) has shown that anomalous tropical forcing in the NCAR GCM produces a statistically significant external mode response in the midlatitudes after only five days. Again, note that the growth of the
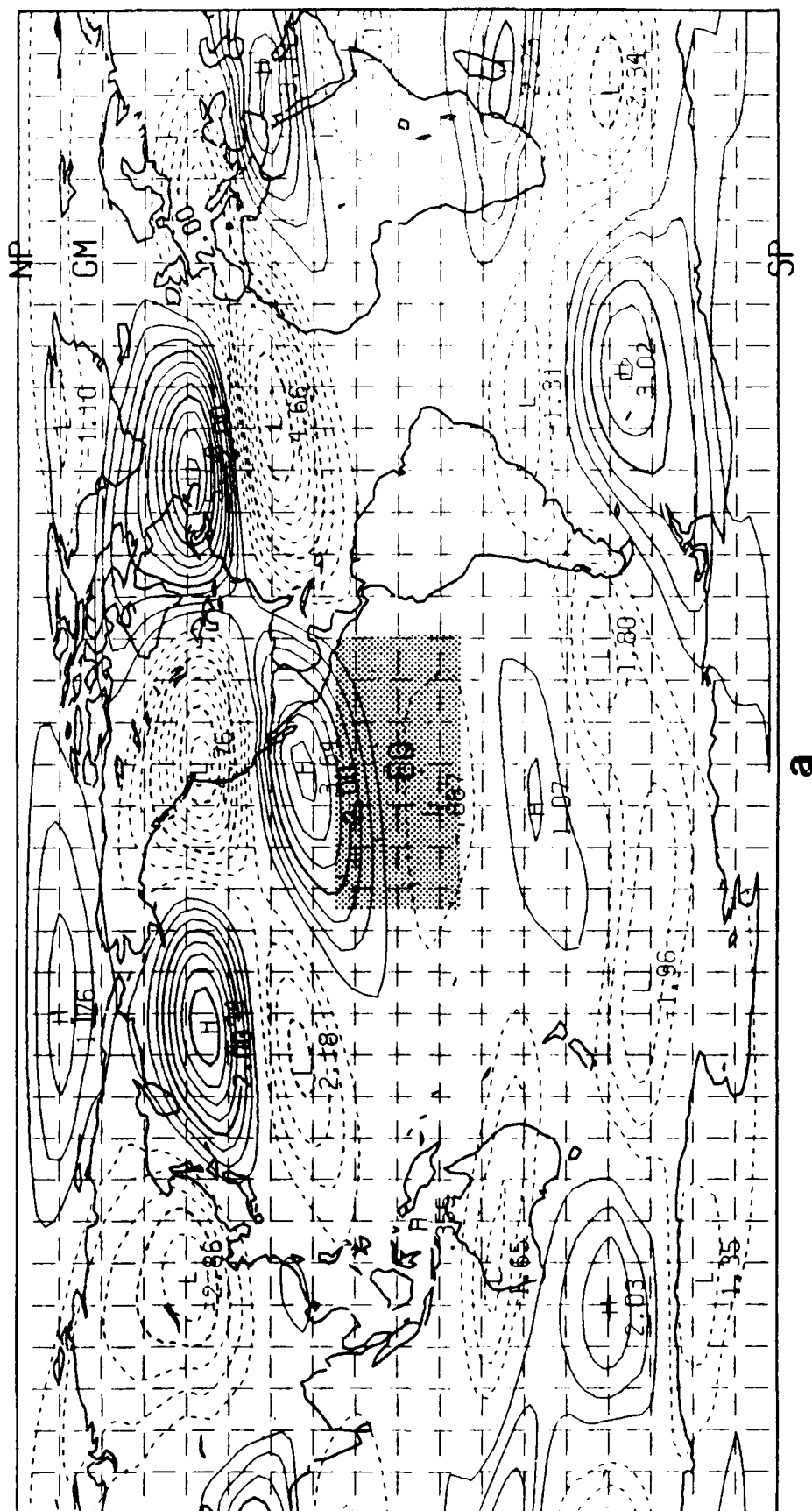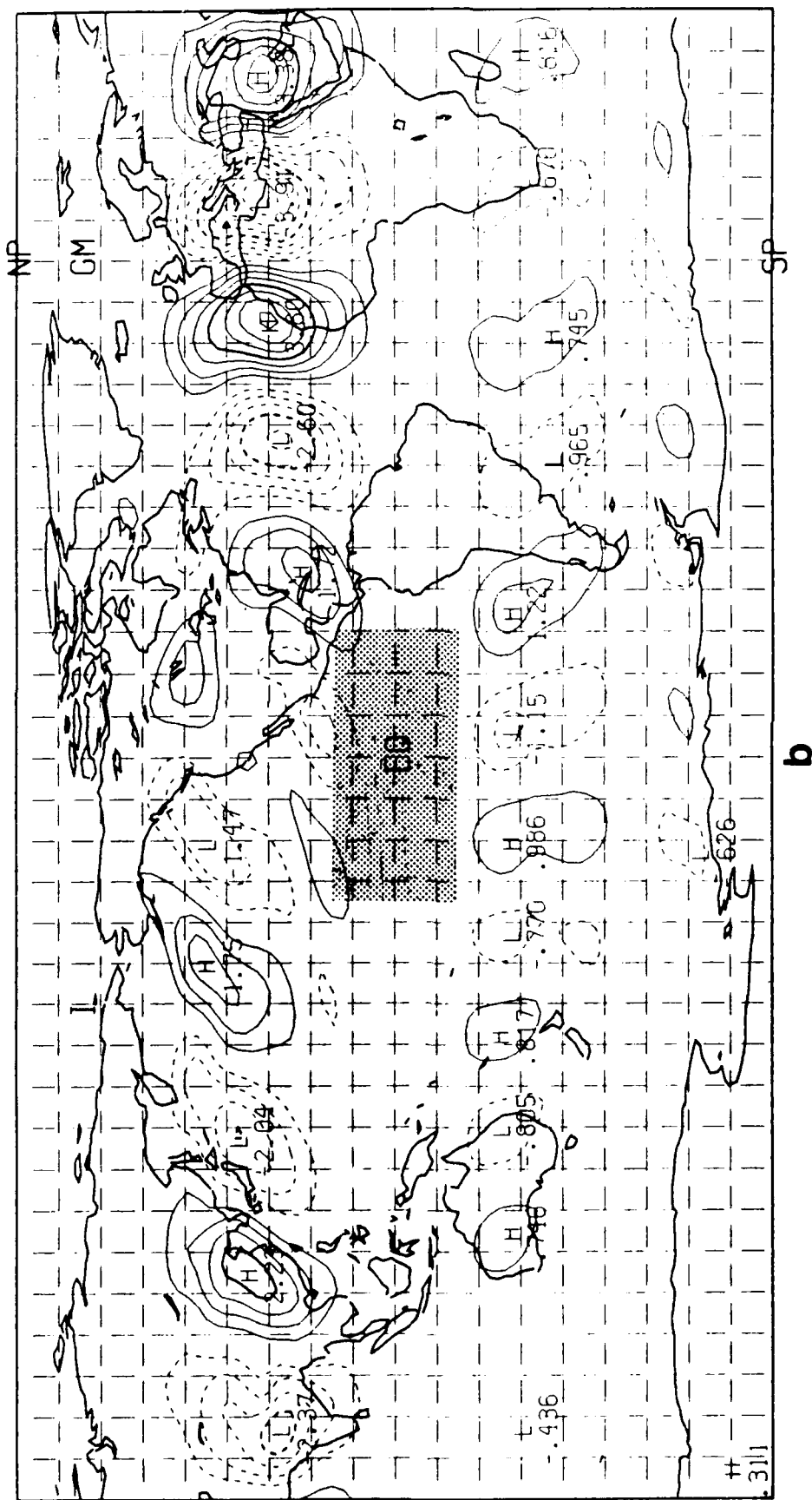
anomalous energy in the $\ell = 5$ RT modes in Figure 3.21a appears to follow that of the external modes, growing most rapidly during the first two weeks of the simulation when the anomalies first appear in Figure 4.6.

4.3 The Midlatitude Response in the ESSTA Simulation

Having established the above scenario for tropically forced wave motion in the midlatitudes based on the results of the WSSTA simulation, we will now examine some key aspects of the midlatitude response in the ESSTA simulation. As stated at the beginning of Section 4.1, the midlatitude response in the ESSTA simulation reveals a similar separation between the characteristics of the anomalous large-scale and synoptic-scale waves, except that in this case the long-wave pattern is somewhat more difficult to interpret.

Figures 4.7a and 4.7b show the contributions from those modes corresponding to zonal wave numbers 1–3 and 5–9, respectively, to the 30-day mean difference in the 300 mb stream function in this simulation. As in the WSSTA simulation, the main difference between these two scales of motion is that the long waves in Figure 4.7a are zonally elongated, while the synoptic-scale waves in Figure 4.7b are meridionally elongated. However, unlike in the WSSTA simulation, the long-wave response in this simulation has a stronger zonal component, making it more difficult to identify distinct meridional wave trains. However, there appears to be one discernible wave train in the east-central Pacific that emanates from the location of the SST anomaly. The northern branch of this wave train appears to be located along the west coast of the United States, although this may be questionable since the waves lack the characteristic eastward turning at high latitudes (*cf.* Figure 4.1a). In

Figure 4.7 The contributions from zonal wave numbers (a) 1–3 and (b) 5–9 to the 30-day mean difference in the stream function at 300 mb for the ESSTA simulation. The format is the same as in Figure 4.1.

(continued on next page)

190

Figure 4.7 (continued)

contrast, the southern hemisphere branch clearly exhibits this turning as it propagates southeastward toward the southern tip of South America. Note that, unlike in the WSSTA simulation, there is no discernible meridional wave train in the eastern Indian Ocean in this figure.

The meridional wave train in Figure 4.7a appears to correspond with the one over the Americas in the WSSTA simulation (Figure 4.1a), except that in the present case, it is clearly shifted westward in response to the location of the SST anomaly. This is verified by observing that the emanation point of this wave train is longitudinally collocated with the anomalous upper-level divergent forcing shown in Figure 2.4b. It should be noted that this aspect of the response is very different from that obtained in the WSSTA simulation, in which the anomalous upper-level divergence maximum is located over the maritime continent (Figure 2.4c), while the emanation point of the meridional wave train is located far to the east over the northwestern tip of South America (Figure 4.1a). As noted earlier, this is consistent with the theory of Webster and Chang (1988), who proposed that there may be preferred regions in the tropics from which energy escapes to the midlatitudes.

The general characteristics of the anomalous synoptic-scale waves in Figure 4.7b are similar to those obtained in the WSSTA simulation in Figure 4.1b, except that the time-mean response in the present case appears to be dominated by wave number 6 instead of by wave number 5. In addition, the latitudinal meandering in the path of the anomalies is considerably more pronounced in the present case; note the trough-like appearance of their path as they approach the west coast of the United States. As in the WSSTA simulation, these waves exhibit a marked zonal asymmetry in their magnitudes.

A key question then is whether there is a consistent link between this zonal asymmetry and the positions of the meridional wave trains, as proposed earlier. In the Northern Hemisphere, the anomalies in Figure 4.7b begin to strengthen after they have reached their southernmost position over Mexico, and then continue to grow in amplitude as they approach western Europe. They obtain their maximum amplitude over the Mediterranean Sea, and then decrease monotonically across Asia and the Pacific Ocean. We may recall that the Northern Hemisphere synoptic-scale anomalies in the WSSTA simulation in Figure 4.1b strengthened and weakened in roughly the same locations. This is somewhat disappointing since the northern branch of the meridional wave train in the present simulation appears to be located further to the west than in the WSSTA simulation, as discussed above. With this in mind, we might have expected the synoptic-scale anomalies in the ESSTA simulation to have reached their maximum amplitudes further upstream as well. Nonetheless, it is interesting to note that the location at which the synoptic-scale anomalies begin to strengthen in the ESSTA simulation (i.e., the position of the southward dip in the pattern over Mexico) agrees well with the apparent location of the northern branch of the meridional wave train in this simulation. Therefore, the results in Figure 4.7 may be a manifestation of the fact that, although the meridionally propagating energy may perturb the flow upstream, it is the position of the strong baroclinic zone along the eastern United States that ultimately determines where the perturbations reach their maximum amplitudes.

A more definitive conclusion can be drawn by comparing the midlatitude responses in the Southern Hemisphere in each simulation. This is due, in part, to the fact that there are no intense baroclinic zones in the midlatitudes during

this time (*cf.* Figure 2.7a) that might otherwise dominate the growth of the anomalies. In addition, the long-wave response in the Southern Hemisphere in the ESSTA simulation is somewhat easier to interpret than the response in the Northern Hemisphere, and thus can be contrasted more readily with that in the WSSTA simulation. In particular, the southern branch of the meridional wave train in the east-central Pacific in Figure 4.7a is easily discernible from the rest of the flow, and clearly lies further to the west than its counterpart in the WSSTA simulation (Figure 4.1a). Also, in contrast to the WSSTA simulation, there is no discernible secondary wave train to the west of Australia in the ESSTA simulation, although there are zonally elongated anomalies in this region.

Returning to the synoptic-scale anomalies in the ESSTA simulation shown in Figure 4.7b, we see that the anomalies in the Southern Hemisphere also exhibit a pronounced zonal asymmetry in their magnitudes. However, in this case, the characteristics of this zonal asymmetry clearly differ from those in the WSSTA simulation in Figure 4.1b in two important respects. The first is that the anomalies in Figure 4.7b obtain their maximum amplitudes off the west coast of South America, while in Figure 4.1b, they obtain a maximum further downstream near the southern tip of Africa. The westward shift of the maximum values in the ESSTA simulation is clearly consistent with the location of the meridional wave train in the east-central Pacific in Figure 4.7a. Note that there is the usual upstream development in the central Pacific. In contrast with the WSSTA simulation, the anomalies decrease in amplitude dramatically as they progress across South America and out over the Atlantic Ocean. Secondly, the magnitudes of the synoptic-scale anomalies in Figure 4.7b obtain a relative

maximum only in the one location described above, while those in Figure 4.1b obtain a second relative maximum near the southeastern tip of Australia. We may recall that the secondary maximum in Figure 4.1b corresponded with the meridional wave train to the west of Australia in Figure 4.1b. Significantly, this wave train is absent in the long-wave response in Figure 4.7a.

The above results are generally consistent with the scenario presented in this section whereby meridionally propagating energy from anomalous tropical forcing may perturb the midlatitude westerlies, and consequently, modify the synoptic-scale development in preferred locations. However, it seems clear that the ultimate response in the midlatitudes depends on the characteristics of the background flow upon which the response is superimposed. On the one hand, this clearly complicates the problem of anticipating the impact of the anomalous forcing since, in the atmosphere (and in models used for NWP), the anomalous response interacts with the background flow. For example, a developing baroclinic disturbance may transfer heat and momentum in such a way as to flatten the gradient, and hence, modify the background flow until the disturbance disappears. Thus, given the fact that the response itself is strongly dependent on the mean state of the atmosphere, there may be a feedback that acts continually to modify the response. On the other hand, it appears that the dependence of the response on certain climatological aspects of the general circulation, such as the positions of the midlatitude jets, or the existence of preferred regions of meridional energy propagation from the tropics, may in fact channel the anomalous energy into discrete scales of motion at specific geographical locations. As a result, anomalous tropical forcing undoubtedly influences the general circulation in a systematic, rather than random fashion.

5. SUMMARY AND CONCLUSIONS

The structure and dynamics of tropical-midlatitude interactions were investigated using a global numerical forecast model (the Navy's NOGAPS spectral model). The primary focus of this study was on improving our understanding of how changes in tropical diabatic forcing act to influence the general circulation, and in particular, the dynamics of midlatitude flow. The approach that was taken was to investigate the model response to imposed SST anomalies in the tropical Pacific Ocean. The analysis in the present study differed from those in previous studies of tropical-midlatitude interactions in two important respects.

The first, and most important difference, is that the dynamics of the problem were analyzed within the framework of the *complete* baroclinic numerical forecast model, instead of a simplified (*i.e.*, barotropic or linearized) version of the model. This was accomplished, in part, by analyzing the response in terms of the normal modes of the forecast model. Because the model response was interpreted in terms of fundamental structures such as Rossby modes, Kelvin modes and inertia-gravity modes, the results of this study represent a direct extension of the conceptual framework derived from theoretical and idealized modeling studies.

Secondly, rather than focusing on changes that occur on seasonal or nual time-scales such as those associated with the El Niño-Southern Oscillation phenomenon, emphasis was placed on investigating the near-term impact of tropical forcing anomalies on the evolution of the global flow. In the

present context, this refers to changes that occur on time-scales ranging from one week to one or two months. This approach was based on the philosophy that tropical-midlatitude interactions are intimately linked in the atmosphere and may have a substantial impact on the global circulation or time-scales well within the theoretical range of useful predictability in current atmospheric forecast models.

The data for this study were obtained from two separate simulations involving a total of four pairs of 50-day simulations with the NOGAPS spectral model. Each pair of simulations consisted of a control run and an anomaly run that differed only in that, in the latter, a localized SST anomaly was added to the initial climatological SST values. In the first simulation, the SST anomaly was located in the eastern Pacific Ocean, and in the second, the SST anomaly was located in the western Pacific Ocean. The results of each simulation were based on daily samples of the model forecast fields averaged from two Northern Hemisphere wintertime cases.

The conceptual framework that served as a background for this study is based on the results of theoretical and idealized modeling studies that have shown that perturbations in the tropical atmosphere caused by diabatic forcing are separable into two basic types of motions according to their vertical structures. The first type is characterized by cellular, or baroclinic motions in which the large-scale flow is of opposite sign at upper and lower levels. This type of response tends to be confined to low latitudes. The second type is characterized by large-scale flow that has the same sign at all levels. This type of response is not equatorially trapped and can propagate meridionally from the tropics to high latitudes. Accordingly, this type of response has been associated

with the well known standing wave patterns that characterize the midlatitude response to warm anomalies in the tropical oceans. Each of these response types can be described mathematically in terms of the vertical modes of well resolved, discrete systems. The horizontal structure of each response is described by a system of shallow-water equations that has the equivalent depth of the corresponding vertical mode as its scale height.

A key issue in this study was to determine the extent to which the conceptual framework discussed above for interpreting tropical-midlatitude interactions can be applied to more realistic models, and ultimately, to the atmosphere itself. To address this issue, a new technique was developed whereby the normal modes of the NOGAPS model were partitioned according to their latitudinal variances in order to define the tropical and extratropical contributions to the anomalous response energy. The basis for this partitioning derives from the fact that, when expressed in terms of a sum of the modes, the energy equations involve latitudinal integrals of the horizontal structure functions in the normal mode expansions. By judiciously selecting the limits of integration, we were able to obtain an estimate of the latitudinal variance of each mode within a given latitudinal band. These variance factors were used as criteria for determining whether a mode could be identified as being predominantly tropical or predominantly extratropical, and the modes were then grouped accordingly. Those modes that did not exhibit a predominant portion of their variance in either region were excluded. Thus, the tropical and midlatitude contributions to the anomalous response energy were defined in terms of sums involving only the subset of modes in each group.

The normal mode analysis revealed that, after several days, the anomalous

response in the tropics was dominated by external (vertical mode $\ell = 1$) rotational modes. The evolution of the energy in these modes peaked after two to three weeks, in agreement with the growth mechanism suggested by Lim and Chang (1986). These modes were later shown to be associated with equivalent barotropic waves that propagated to high latitudes. In addition, there was a strong baroclinic response in the $\ell = 4$ rotational modes after several days that appeared to be driven by the divergent flow associated with the diabatic forcing. This was consistent with the strong response of the $\ell = 4$ gravity modes early in the simulations. The projection of this response onto vertical mode $\ell = 4$ was explained by the fact that the vertical structures of these modes strongly resembled the divergence profile associated with the tropical diabatic heating anomaly. It is interesting to note that the dominant internal mode (baroclinic) response in the tropics reflects the vertical structure of the *divergence* induced by the diabatic heating (which resembles $\ell = 4$), rather than the vertical structure of the heating profile itself (which resembles $\ell = 5$).

In the midlatitudes, the response was dominated by the external rotational modes, in agreement with the conceptual framework described earlier in which deep barotropic modes may propagate to high latitudes. However, the most interesting result was that, in addition to the external mode response, the analysis revealed a strong *baroclinic* response in the $\ell = 5$ rotational modes that had roughly half the amplitude of the external (barotropic) response. The evolution of the baroclinic response roughly followed that of the barotropic response, with the former growing at a somewhat slower rate. The maximum period of growth for both responses occurred between days 5 and 15, and then reached a state of approximate equilibrium after 20 days.

Based on the relatively slow phase speeds of the $\ell = 5$ modes, and the fact that these modes were not dominant among the tropical internal modes, it was concluded that this response was strictly a midlatitude phenomenon possibly associated with baroclinic waves. This was strongly supported by a zonal wave number decomposition of the midlatitude standing wave pattern. The results of this decomposition showed that the standing wave pattern over North America (which, in one simulation, strongly resembled the classical PNA pattern) was actually a superpositioning of two distinct types of horizontal wave motion.

Zonal wave numbers 1-3 were associated with zonally elongated waves that formed several distinct meridional wave trains emanating from the tropics toward high latitudes. The equivalent barotropic structure of these waves was confirmed by the fact that they projected very strongly onto the external rotational modes. Remarkably, the emanation points for these wave trains were not necessarily collocated with the tropical SST anomalies. This is consistent with the existence of preferred regions of energy accumulation and subsequent meridional propagation in the tropics, as proposed by Webster and Chang (1988).

In contrast, the decomposition in terms of wave numbers 5-9 showed meridionally elongated anomalies that propagated more or less zonally between latitudes 30° and 45° in both hemispheres. These waves clearly exhibited the tilted trough structure associated with synoptic-scale baroclinic waves. Significantly, it was shown that these waves projected onto the $\ell = 5$ rotational modes, which was consistent with the strong response of these modes in the midlatitudes as revealed by the latitudinal partitioning.

One of the most interesting aspects of the anomalous synoptic-scale waves

was that, when averaged over 30 days, their amplitudes exhibited prominent zonal asymmetries. It was observed that the synoptic-scale anomalies obtained their maximum amplitudes downstream from where the meridionally propagating wave trains (associated with zonal wave numbers 1-3) intersected the midlatitude westerlies. This observation, combined with the similarity between the evolution of the $\ell = 1$ and $\ell = 5$ rotational modes in the midlatitudes, suggested the existence of a cause-and-effect relationship between the meridionally propagating long waves and the synoptic-scale baroclinic waves. This was supported by examining the evolution of the synoptic-scale anomalies, which showed that, in most cases, they appeared first in the vicinities of the time-mean positions of the meridional wave trains. Moreover, these anomalies appeared between days 5 and 10 of the simulation, suggesting that *anomalous tropical forcing may substantially influence the midlatitude synoptic-scale flow at preferred locations on time-scales less than two weeks.*

It should be noted that, at this point, there is only strong circumstantial evidence supporting some of the above conclusions. Thus, for example, the mechanism by which the meridionally propagating energy excites the synoptic-scale waves is unclear. One possibility is that the meridionally propagating energy perturbs the midlatitude westerly flow at some location(s), and then these perturbations grow in an unstable environment. This might explain why the largest synoptic-scale anomalies in the Northern Hemisphere were observed downstream from the intersection of a prominent meridional wave train and the strong baroclinic zone along the east coast of the United States. In contrast, it should be noted that little or no anomalous synoptic-scale development was observed in the vicinity of the East Asian jet, corresponding to

an absence of meridionally propagating waves in this region.

Combining the results of this study with those of other investigators, we might speculate that anomalous tropical forcing modifies the flow in the midlatitudes via the following sequence of events:

1. A perturbation of some sort in the tropics (say, an SST anomaly) produces a localized convective (*i.e.*, internal) forcing anomaly.

2. Almost immediately, the increased internal forcing produces an internal gravity mode response associated with increased divergent motion.

3. The increased divergent motion drives an internal rotational mode response through the divergence term in the large-scale vorticity equation. The internal mode response is manifested by equatorially trapped gravitational and rotational modes in the form of anomalous Hadley or Walker-type circulations (*e.g.*,Webster, 1972; Gill, 1980; Lim and Chang, 1983).

4. Over the next several days, an external rotational mode response develops in the tropics owing to vertical wind shear and viscous effects, which act to couple the internal and external modes (Lim and Chang, 1986), and owing to direct forcing from the SST anomaly itself.

5. The external rotational modes propagate from the tropics to the midlatitudes at preferred locations, as found for nondivergent Rossby waves propagating on a sphere (*e.g.*, Hoskins and Karoly, 1981; Horel and Wallace, 1981; Wallace and Gutzler, 1981; Webster and Chang, 1988).

6. The meridionally propagating external modes perturb the midlatitude

westerlies at specific locations producing an internal rotational mode response manifested by anomalous synoptic-scale baroclinic waves.

With regard to atmospheric modeling applications, the results of this study suggest that our ability to specify correctly the diabatic forcing in the tropics may be the dominant limiting factor on our ability to predict the general circulation for an extended length of time. A similar conclusion was reached by Tiedtke (1984) who assessed the impact of various cumulus parameterizations on the general circulation. This is of particular concern since it is well accepted that the parameterization of subgrid-scale diabatic processes is one of the least understood components of most numerical forecast models. In addition, it appears that baroclinic processes may play important roles in determining the extent to which tropical diabatic forcing errors diminish the skill of midlatitude forecasts. This seems logical given the fact that baroclinic instability is the dominant mechanism driving the so-called Rossby regime in the midlatitudes.

It is hoped that the results of this study can serve as a stepping stone for future research efforts. Clearly, the results reported here raise many questions that can not be answered satisfactorily without further investigation. For example, an obvious next step would be to repeat this analysis on a large number of cases in order to establish the statistical significance of certain results, and to establish their dependence on seasonal variations in the atmosphere. In a related issue, no attempt was made in this study to determine the dependence of the results on the mean winds in the tropics and subtropics. This is relevant since, under certain circumstances, internal modes may become untrapped, and presumably, could propagate to high latitudes.

Although the technique that was developed for partitioning the modes

yielded physically reasonable results, several questions remain regarding the growth rates of the different vertical modes in the tropics and midlatitudes. In particular, it seems that there should have been an observable lag between the growth of the external modes in the tropics and the midlatitudes, with the growth of the former preceding that of the latter. It is likely that this lag was not resolvable in the curves shown here for two reasons. The first is that the latitudinal ranges used to define the tropics and midlatitudes were contiguous. Given the rapid propagation speeds of these modes (being on the order of the speed of sound) it might have been preferable to have defined the equatorward boundary of the midlatitudes closer to, say 40° latitude, rather than at 19°. Secondly, greater temporal resolution than the five-day averaging periods used here undoubtedly is needed to distinguish any lag time between the responses in each region. At the same time, this, of course, would have increased the data storage and management problems involved.

There may undoubtedly be more rigorous ways of determining the latitudinal variances of the modes. One technique that is being examined currently is to project the horizontal structure functions back into physical space and then to partition the modes according to the latitudinal variances of the mass and momentum fields. This would eliminate the nonorthogonality problems that arise when the Legendre polynomials themselves are used to partition the modes.

Also, it should be noted that we excluded the zonally symmetric modes from most of the analysis. Although the results of this study clearly indicate that interactions between the eddy components of the flow may provide a key link between the tropical and midlatitude responses, there exists evidence from

other studies (*e.g.*, Higgins and Shirer, 1989) suggesting a more direct transition from the so-called Hadley regime to the Rossby regime. Direct feedbacks between the Hadley circulation and the midlatitude flow have also been examined by Chang and Lau (1980) who studied the effects of cold surges over Asia during the winter monsoon.

In addition to resolving issues related directly to the problems addressed in this study, it is hoped that some of these results may shed some light on other areas. For example, the variance factors used to partition the modes may provide insight into current problems in nonlinear normal mode initialization (NNMI), such as identifying the correct modes to balance in the tropics and midlatitudes. This is of particular interest in the tropics, where large-scale thermally forced gravity modes may be a crucial part of the circulation. At this point, these modes do not appear to be initialized properly in most NNMI schemes. Errico et al. (1988) point out that, in general, it stll is not well known which modes are most important in the tropics. It seems likely that the tropical variance factors developed in Chapter 3 could be used to provide some insight into this problem.

Finally, the fact that the anomalous responses in the tropics and midlatitudes were dominated by a limited number of modes corresponding to discrete horizontal and vertical scales suggests that the essential dynamics of this problem may be resolvable in a reduced model, *provided we retain the proper subset of modes.* At the same time, the continued development and application of new diagnostic tools, such as those based on the normal modes of a sophisticated model, will be essential for bridging the gap between the inherent

complexity of most atmospheric processes and our ability to interpret these processes within the context of a simple, yet dynamically consistent framework.

APPENDIX

THE NORMAL MODES OF THE NOGAPS MODEL

The NOGAPS forecast model is a global spectral model, as described by Hogan and Rosmond (1989). However, in order to determine the normal modes of the model, we need only consider the inviscid, adiabatic equations linearized about some basic state. The basic state that is chosen is a state at rest with a uniform pressure and temperature field given by $p_s = \bar{p}$ and $T(\sigma) = \bar{T}(\sigma)$, where p is the pressure at some height, p_s is the surface pressure, $T(\sigma)$ is the temperature defined on σ-surfaces and the overbar denotes a suitable horizontal average. As pointed out by Errico (1987), the mode structures are independent of $\bar{p}$, but depend significantly on $\bar{T}(\sigma)$, because $\bar{T}(\sigma)$ should correspond to a statically stable environment. In the NOGAPS model, $\bar{T}(\sigma)$ is taken to be the global mean values of $T(\sigma)$ derived from a specified data set. In order to get a limited eigenvalue problem, a separation of the equations into vertical and horizontal structures is sought (Andersen, 1977). The development outlined in this section closely follows that of Errico (1987).

As in most numerical forecast models, the dependent variables in the NOGAPS model are defined on discrete σ-surfaces as defined in Chapter 2. It turns out that it is simpler to describe the derivation of the vertical modes in terms of this discrete structure. Thus, we consider the dependent variables to be column vectors at discrete points whose elements are the dependent variables on

the L model σ-surfaces; *e.g.*,

$$\underline{\xi}(\lambda,\mu) = \{\xi(\mu,\lambda,\sigma_1), \xi(\mu,\lambda,\sigma_2),\ldots,\xi(\lambda,\mu,\sigma_L)\}^T\,, \qquad (A.1)$$

where an underline denotes a column vector with L data elements ξ. The symbols λ and μ are the longitude and sine of the latitude, respectively, and the superscript T denotes a transpose.

Using the notation in (A.1), we can write the inviscid, adiabatic, linearized vertically discrete model equations in the form

$$\frac{\partial \underline{\varsigma}}{\partial t} = -2\Omega\mu\underline{D} - 2\Omega\underline{V}\,, \qquad (A.2)$$

$$\frac{\partial \underline{D}}{\partial t} = 2\Omega\mu\underline{\varsigma} - 2\Omega\underline{U} - \nabla^2\underline{\varphi}\,, \qquad (A.3)$$

$$\frac{\partial \underline{\theta}}{\partial t} = -\mathbf{A}\,\underline{D}\,, \qquad (A.4)$$

$$\frac{\partial \pi}{\partial t} = -\mathbf{q}^T\underline{D}\,, \qquad (A.5)$$

where

$\underline{\varsigma} = \nabla^2\underline{\psi}$ is the vertical vorticity,

$\underline{D} = \nabla^2\underline{\chi}$ is the horizontal divergence,

$\underline{\theta} = \underline{T}(p_0/\bar{p})^{R/c_p}$ is the potential temperature,

$\pi = \bar{p} - p_{top}$,

$\underline{U} = \underline{u}\,(\cos\phi)/a$,

$\underline{V} = \underline{v}\,(\cos\phi)/a$,

$p_0 = 1000$ mb

$\underline{\psi}$ is the stream function,

χ is the velocity potential,

u, v are the horizontal velocity components,

Ω is the angular velocity of the earth,

p_{top} is the pressure at the top of the model,

ϕ is the latitude,

a is the radius of the earth,

∇^2 is the horizontal Laplacian defined in (3.2),

and the operators $\mathbf{A}$ and $\mathbf{q}$ are discussed below.

In the linearized form of the model, the tendencies of the velocity fields depend on the thermodynamic fields via the pseudo-geopotential

$$\varphi = \underline{\phi}_s + \mathbf{B}\underline{\theta} + \mathbf{c}\pi , \tag{A.6}$$

where $\underline{\phi}_s$ is a vector whose L components are all equal to the terrain geopotential ϕ_s.

Note that in the vertically discrete form, certain operators in (A.4)–(A.6) take the form of matrix or vector operators. For the purposes of this discussion, we need only note that

$\mathbf{B} = \mathbf{B}(\overline{T},\overline{p})$ is an $L \times L$ matrix related to the linearized hydrostatic relation,

$\mathbf{A} = \mathbf{A}(\dot{\sigma}\partial\theta/\partial\sigma)$ is an $L \times L$ matrix related to the linearized vertical advection of potential temperature,

$\mathbf{c} = \mathbf{c}(\overline{T},\overline{p})$ is an L-column vector related to the linearized hydrostatic relation and to the σ-coordinate representation of the pressure gradient force,

q is an L-column vector with elements $\Delta\sigma_k$, and is proportional to the discrete form of the integral operator $\int_0^1 d\sigma$.

We can differentiate (A.6) with respect to t in order to obtain

$$\frac{\partial\varphi}{\partial t} = \mathbf{B}\frac{\partial\theta}{\partial t} + \mathbf{c}\frac{\partial\pi}{\partial t}, \tag{A.7}$$

and then use (A.4) and (A.5) to write

$$\frac{\partial\varphi}{\partial t} = -\mathbf{S}D, \tag{A.8}$$

where

$$\mathbf{S} = (\mathbf{BA} + \mathbf{c}\,\mathbf{q}^T) \tag{A.9}$$

is an $L \times L$ matrix. It may be noted that $\mathbf{S}$ is the discrete form of the operator r in (3.1). The prognostic equations (A.2), (A.3) and (A.8) form the foundation for the separation into horizontal and vertical structures.

A.1 Vertical Structure

The only vertical coupling in (A.2), (A.3) and (A.8) occurs through the matrix operator $\mathbf{S}$ in (A.8). Thus, the separation of the horizontal and vertical structures is obtained by first computing the eigenvectors of $\mathbf{S}$. These eigenvectors represent the vertical structures of the normal mode solutions, while the corresponding eigenvalues play the roles of the equivalent depths in a series of shallow water equations. The vertical structures are determined by solving the eigenvalue problem

$$\mathbf{SZ} = g\mathbf{ZH}, \tag{A.10}$$

where g is gravity, $\mathbf{Z}$ is a matrix whose columns are the eigenvectors z_ℓ (i.e., the vertical modes), and $\mathbf{H}$ is a diagonal matrix whose elements are the eigenvalues

H_ℓ (*i.e.*, the equivalent depths). In the NOGAPS model, the vertical modes are normalized such that

$$\sum_{k=1}^{L} z_{k,\ell}\, z_{k,\ell}\, \Delta\sigma_k = 1, \tag{A.11}$$

for each vertical mode $\ell = 1, \ldots, L$, where $z_{k,\ell}$ represents the kth σ-level component of the ℓth vertical mode, and the values $\Delta\sigma_k$ are the discrete components of $d\sigma$ in the vertically continuous form $\int_0^1 z_\ell z_\ell d\sigma = 1$. It should be noted that, in the NOGAPS model, the vertical modes are not orthogonal in the sense that

$$\sum_{k=1}^{L} z_{k,j}\, z_{k,\ell}\, \Delta\sigma_k = 0, \quad \text{for } j \neq \ell, \tag{A.12}$$

is not true in general. The implications of this nonorthogonality are discussed in Section 3.1.

A typical set of values of $\overline{T}(\sigma)$ for the NOGAPS model is shown in Table A.1. The corresponding vertical modes z_ℓ are shown in Figure A.1. The values of $\overline{T}(\sigma)$ in Table A.1 are the global mean values at each σ-layer corresponding to the 30-day mean composite control run during days 21-50 of the simulations described in Section 2.2. The 18 equivalent depths H_ℓ are also shown in Table A.1, ordered from largest to smallest. Note that the values range from nearly 10 km for the external ($\ell = 1$) mode to only a few hundreths of a meter for the shallowest internal ($\ell = 18$) mode. Recall that the equivalent depths H_ℓ in Table A.1, and the vertical modes z_ℓ in Figure A.1, are the eigenvalues and eigenvectors, respectively, of the vertical structure equation (A.10).

The vertical modes of the NOGAPS model shown in Figure A.1 are typical of those in other models having similar vertical resolution (*cf.*, Wergen, 1987). In particular, we see that the external mode in Figure A.1a is equivalent

barotropic (*i.e.*, approximately independent of pressure) throughout the depth of the model atmosphere, while vertical modes $\ell = 2$ and $\ell = 3$ exhibit one and two sign changes with height, respectively. It can be seen in the remaining figures that the number of zero crossings for each mode increases by one for successively shallower equivalent depth. Note that, in general, the shallower modes have their greatest amplitude in the lower troposphere. However, because the modes have been normalized according to (A.11), no meaningful comparison can be made between the amplitudes of different modes at a given vertical level. Beginning in Section 1.2, a detailed discussion concerning the implications of these different types of vertical structures is given in the context of the analysis in this study.

Because the vertical eigenvectors form a complete set, a vector of σ-surface data values can be expanded in terms of these eigenvectors to obtain a vector of vertical mode coefficients. For example, the transform, or projection of the pseudo-geopotential $\underline{\varphi}$ onto the vertical modes is given by

$$\hat{\varphi} = \mathbf{Z}^{-1}\underline{\varphi}, \qquad (A.13)$$

where $\hat{\varphi}$ represents the transformed vector of vertical mode coefficients and the superscript -1 denotes an inverse. Conversely, the vector of σ-surface values can be determined from the vertical mode coefficients via

$$\underline{\varphi} = \mathbf{Z}\hat{\varphi}. \qquad (A.14)$$

Thus, by applying (A.14) to the prognostic equations (A.2), (A.3) and (A.8), we can transform this set into one describing the tendencies of the vertical mode coefficients. When this is done, (A.2) and (A.3) retain the same form, except that the dependent variables are replaced by the transformed ones. In contrast,

Table A.1   Values of $\overline{T}(\sigma)$ from the 30-day mean control run, and the set of equivalent depths H_ℓ, corresponding to the vertical modes in Figure A.1. Note that ℓ is a model index for σ and $\overline{T}$, but refers to the ordering of the vertical modes in the case of H.

| ℓ	σ	p	$\overline{T}$ (K)	H (m)
1	0.008	8.99	229.25	9669.53
2	0.028	28.97	209.14	3224.16
3	0.049	49.95	198.15	801.71
4	0.092	92.91	199.12	308.66
5	0.136	136.86	214.05	130.55
6	0.187	187.81	217.82	63.85
7	0.247	247.75	227.33	40.60
8	0.315	315.69	236.96	21.30
9	0.393	393.61	247.70	11.48
10	0.482	482.52	258.23	6.63
11	0.575	575.43	266.92	3.99
12	0.669	669.33	273.94	2.36
13	0.759	759.24	279.79	1.45
14	0.839	839.16	283.94	0.75
15	0.904	904.10	287.66	0.40
16	0.950	950.05	290.40	0.18
17	0.978	978.02	291.83	0.10
18	0.995	995.01	292.08	0.02
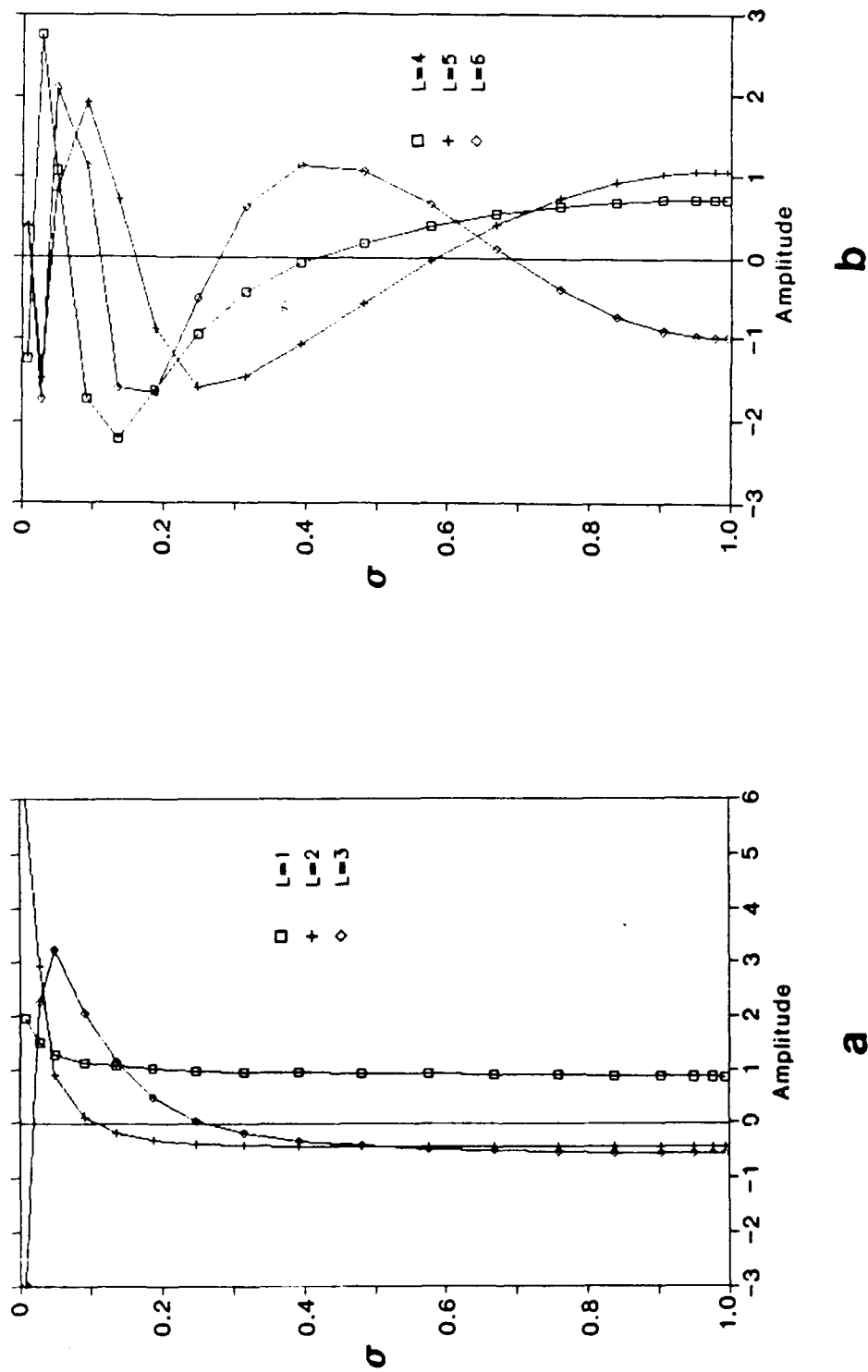
Figure A.1 The vertical modes of the 18-level NOGAPS model, based on the parameters values in Table A.1, for vertical modes (a) 1–3, (b) 4–6, (c) 7–9, (d) 10–12, (e) 13–15 and (f) 16–18.
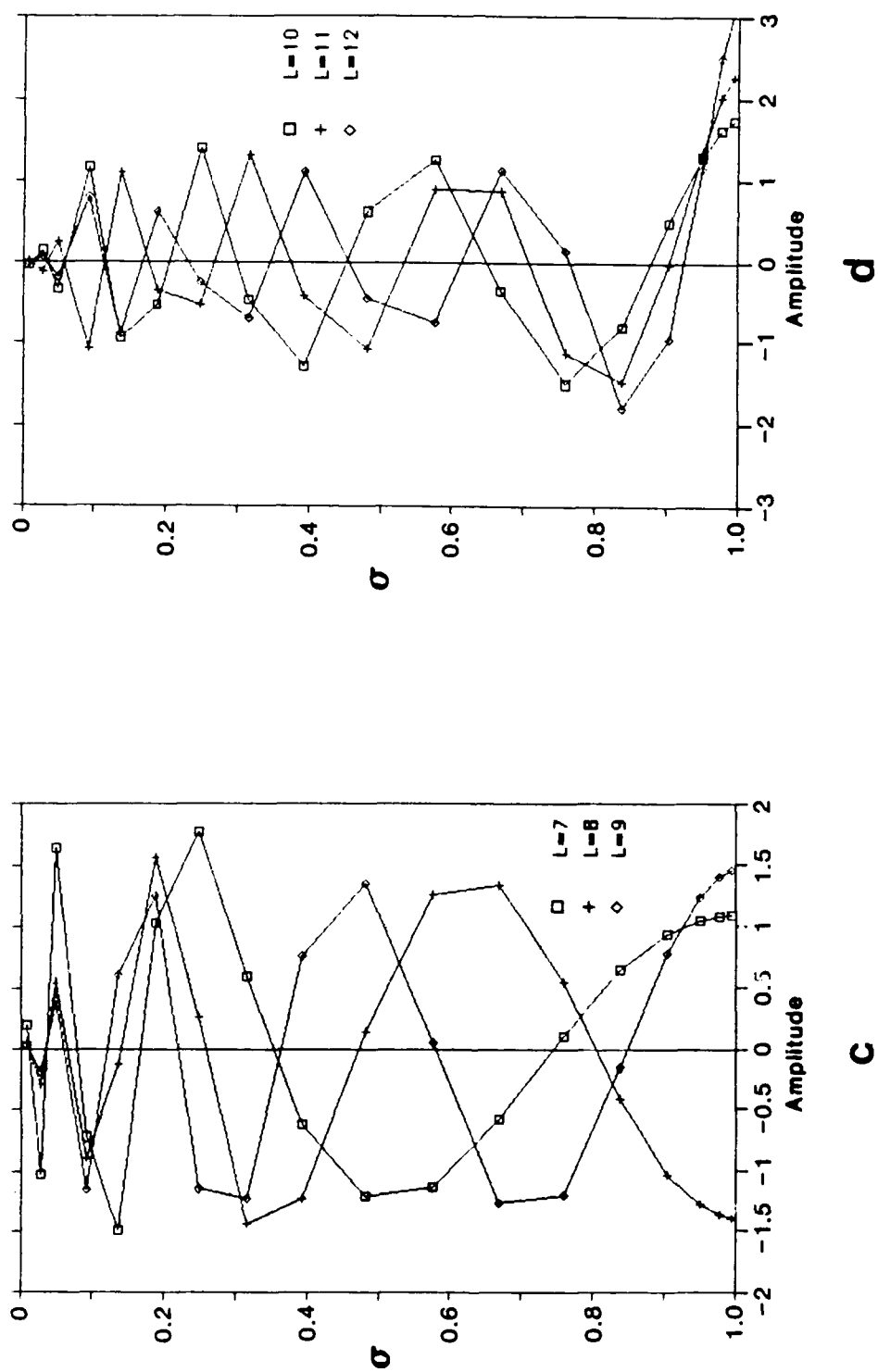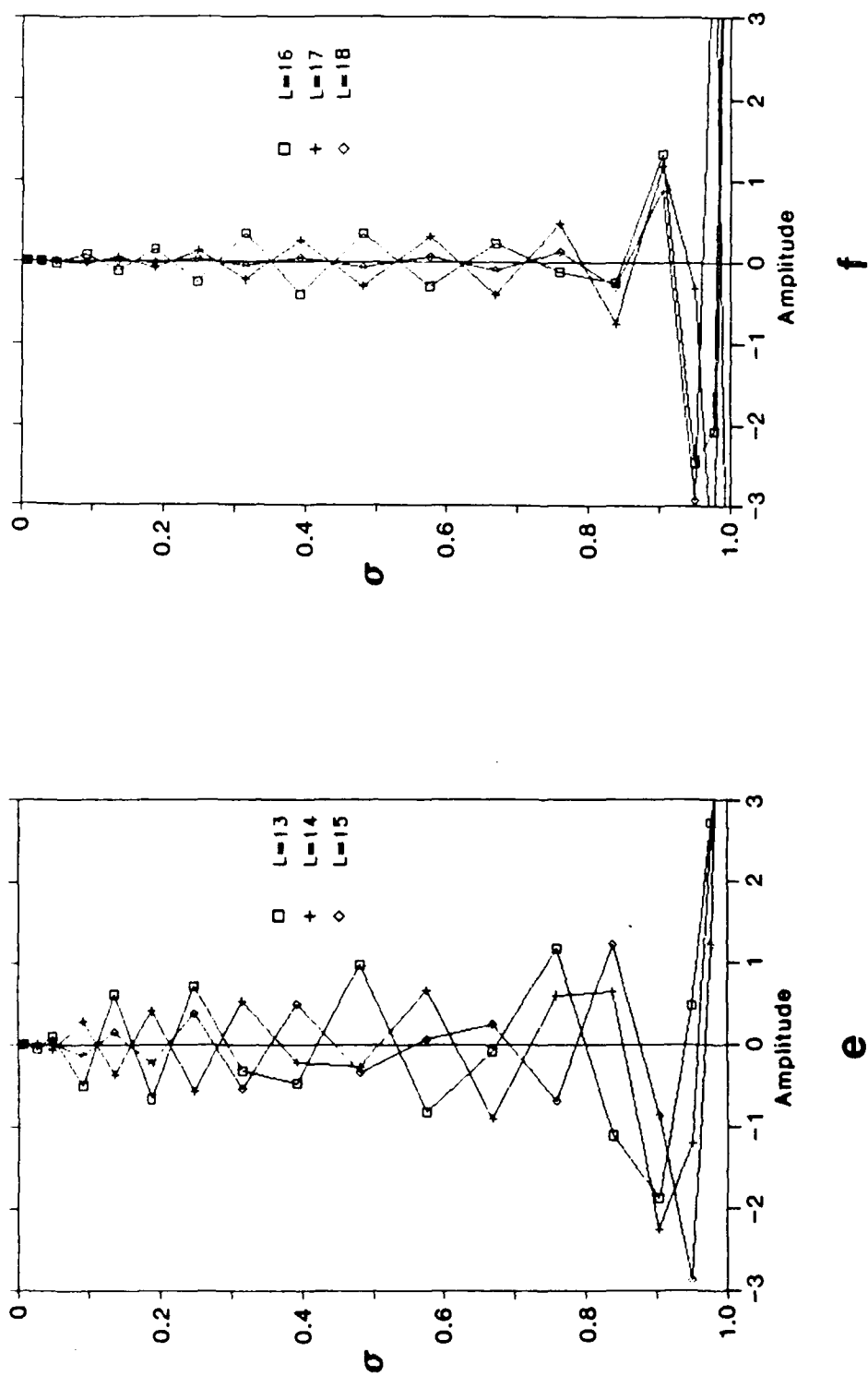
214

Figure A.1 (continued)

Figure A.1 (continued)

the form of (A.8) changes; the new relation is obtained by using (A.10) to yield

$$\frac{\partial \hat{\varphi}}{\partial t} = -g\mathbf{H}\hat{D}. \tag{A.15}$$

Thus, for each vertical mode ℓ, we have

$$\frac{\partial \hat{\varsigma}_\ell}{\partial t} = -2\Omega\mu\hat{D}_\ell - 2\Omega\hat{V}_\ell, \tag{A.16}$$

$$\frac{\partial \hat{D}_\ell}{\partial t} = 2\Omega\mu\hat{\varsigma}_\ell - 2\Omega\hat{U}_\ell - \nabla^2\hat{\varphi}_\ell, \tag{A.17}$$

$$\frac{\partial \hat{\varphi}_\ell}{\partial t} = -gH_\ell\hat{D}_\ell. \tag{A.18}$$

A.2   Horizontal Structure

For a given vertical mode ℓ, the system of prognostic equations (A.16)-(A.18) is decoupled from that for any other vertical mode. Each system represents a set of shallow-water equations on a sphere with the corresponding equivalent depth H_ℓ as its scale height.

We can transform (A.16)-(A.18) into a system of ordinary differential equations by expanding the vertical mode coefficients in terms of spherical harmonics analogous to (3.10), and then using the dimensionless forms (3.18)-(3.21) to obtain

$$\frac{d}{dt}\tilde{\varsigma}_{m,n} = i\left[c_{m,n}\tilde{\varsigma}_{m,n} + a_{m,n}\tilde{D}_{m,n-1} + a_{m,n+1}\tilde{D}_{m,n+1}\right], \tag{A.19}$$

$$\frac{d}{dt}\tilde{D}_{m,n} = i\left[b_{m,n}\tilde{\varphi}_{m,n} + c_{m,n}\tilde{D}_{m,n} + a_{m,n}\tilde{\varsigma}_{m,n-1} + a_{m,n+1}\tilde{\varsigma}_{m,n+1}\right], \tag{A.20}$$

$$\frac{d}{dt}\tilde{\varphi}_{m,n} = i\left[b_{m,n}\tilde{D}_{m,n}\right], \tag{A.21}$$

where

$$a_{0,0} = b_{0,0} = c_{0,0} = 0, \tag{A.22}$$

and

$$a_{m,n} = \frac{-2\epsilon_{m,n}}{n}\left[(n+1)(n-1)\right]^{1/2}, \tag{A.23}$$

$$b_{m,n} = \left[\frac{gH}{\Omega^2 a^2} n(n+1) \right]^{1/2} , \tag{A.24}$$

$$c_{m,n} = \frac{2m}{n(n+1)} , \tag{A.25}$$

$$\epsilon_{m,n} = \left[\frac{n^2 - m^2}{4n^2 - 1} \right]^{1/2} , \tag{A.26}$$

for $n > 0$. The subscript ℓ on $\tilde{\zeta}_{m,n}$, $\tilde{D}_{m,n}$, $\tilde{\varphi}_{m,n}$ and H is implied. In obtaining (A.19)–(A.21), we also have used the relations

$$U_{m,n} = \frac{-im}{n(n+1)} D_{m,n} - \frac{\epsilon_{m,n}}{n} \zeta_{m,n-1} + \frac{\epsilon_{m,n+1}}{n+1} \zeta_{m,n+1} , \tag{A.27}$$

and

$$V_{m,n} = \frac{-im}{n(n+1)} \zeta_{m,n} + \frac{\epsilon_{m,n}}{n} D_{m,n-1} - \frac{\epsilon_{m,n+1}}{n+1} D_{m,n+1} . \tag{A.28}$$

Equations (A.19)–(A.21) separate into independent sets for each zonal wave number m. Because the NOGAPS model is truncated *triangularly* at $m = M = 47$, we obtain 48 independent systems that have decreasing order n corresponding with increasing zonal wave number m, such that $n = 48$ for $m = 0$, $n = 47$ for $m = 1$, and so on, down to $n = 1$ for $m = 47$. Actually, it turns out that for each m, (A.19)–(A.21) separate further into two independent systems: one in which there are only even values of $(n - m)$ for $\tilde{D}_{m,n}$ and $\tilde{\varphi}_{m,n}$ and odd values for $\tilde{\zeta}_{m,n}$, and one in which the even and odd conditions are reversed. These two systems are called the symmetric and antisymmetric cases, respectively, in reference to the symmetries of the dependent variables about the equator.

At this point, it is thus convenient to adopt a slight change in notation whereby we use the subscript $q = n - m$ as an index on the dependent variables. Using this notation, we can write the symmetric and antisymmetric problems in the general matrix form

$$\frac{d\tilde{\mathbf{x}}_q}{dt} = i\mathbf{M}\tilde{\mathbf{x}}_q , \tag{A.29}$$

where $\check{\mathbf{x}}_q$ represents a vector whose elements are the appropriate values of $\check{\varsigma}_q$, $\check{D}_q$ and $\check{\rho}_q$, and the subscript m is implied. Then for each m (i.e., zonal wave number), the horizontal structures are given by the eigenvectors of $\mathbf{M}$, which we determine from the horizontal structure equation

$$\mathbf{MH} = \mathbf{HW}, \tag{A.30}$$

where $\mathbf{H}$ is a matrix whose columns are the horizontal eigenvectors $\mathbf{h}_j$ (i.e., the horizontal modes), $\mathbf{W}$ is a diagonal matrix whose elements are the eigenvalues ω_j (i.e., the frequencies of the modes), and the subscript j denotes a particular mode; i.e., there is a unique horizontal eigenvector $\mathbf{h}_j$ for each mode. Also, note that the size of the matrix $\mathbf{M}$ varies as a function of m.

Thus, the normal mode solutions to (A.19)–(A.21) take the form

$$\check{\mathbf{x}} = \alpha_j \mathbf{h}_j e^{i\omega_j t}, \tag{A.31}$$

where α_j is the time-dependent amplitude or normal mode coefficient. It should be noted that, here, the subscripts m and ℓ are implied for each mode. In practice, each mode is uniquely identified by the triplet of indices $J = (m, j, \ell)$, as discussed in Chapter 3.

Because the matrices $\mathbf{M}$ are real and symmetric (their forms are given in Errico, 1987), all α and $\mathbf{h}$ are real-valued. For a given equivalent depth, all the modes corresponding to $m > 0$ are orthonormal in the sense that

$$\langle \mathbf{h}_i \cdot \mathbf{h}_j \rangle = \begin{cases} 1 & \text{for } i = j, \\ 0 & \text{for } i \neq j, \end{cases} \tag{A.32}$$

where the operation on the left side denotes a vector inner-product. Those modes associated with $m = 0$ are not orthogonal in the sense of (A.32), and are discussed by Kasahara (1978).

For $m > 0$, the modes can be ordered from smallest to largest according to their frequencies ω_j, and then divided into three separate bands corresponding to the three types of modes. In the NOGAPS model, the smallest third in this sequence are negative-valued, and correspond to eastward propagating inertia-gravity modes (EG modes) in the linearized model. These include the Kelvin modes, which are low-frequency eastward propagating gravity modes; the Kelvin modes are discussed in some detail in Section 3.2. The middle third of the frequencies for each zonal wave number are positive-valued and correspond to rotational, or Rossby modes (RT modes), while the largest third in this ordering corresponds to the westward propagating inertia-gravity modes (WG modes). For increasing values of m in the NOGAPS model, the number of modes decreases by three from 144 (48 of each type) for $m = 0$ down to 3 (one of each type) for $m = 47$. This translates into 1176 modes of each type for each vertical mode, or a total of 1176 modes $\times$ 3 types $\times$ 18 vertical modes = 63504 degrees of freedom in the model. Finally, a vector of vertical mode coefficients can be expanded in terms of the horizontal modes, and vice versa, in a manner analogous to (A.13) and (A.14).

REFERENCES

Abramowitz, M., and I. A. Stegun, 1965: *Handbook of Mathematical Functions.* Dover, 1046 pp.

Andersen, J. H., 1977: A routine for normal mode initialization with nonlinear correction for a multi-level spectral model with triangular truncation. ECMWF Internal Report No. 15, 42 pp.

Arakawa, A., and W. Schubert, 1974: Interaction of a cumulus cloud ensemble with the large-scale environment: Part I. *J. Atmos. Sci.*, **31**, 674–701.

Baede, A. P. M., M. J. Jarraud and U. Cubasch, 1979: Adiabatic formulation ₋nd organization of the ECMWF's spectral model. ECMWF Techr⋅ ₋' Report No. 15, 1–40.

Bjerknes, J., 1969: Atmospheric teleconnections from the equatorial Pacific. *Mon. Wea. Rev.*, **97**, 163–172.

Blackmon, M. L., J. E. Geisler and E. J. Pitcher, 1983: A general circulation study of January climate anomaly patterns associated with interannual variation of equatorial Pacific sea surface temperatures. *J. Atmos. Sci.*, **40**, 1410–1425.

Branstator, G., 1985: Analysis of general circulation model sea surface temperature anomaly simulations using a linear model. Part I: Forced Solutions. *J. Atmos. Sci.*, **42**, 2225–2241.

Chang, C.-P., and K.-M. Lau, 1980: Northeasterly cold surges and near equatorial disturbances over the Winter MONEX area during December 1974. Part II: Planetary-scale aspects. *Mon. Wea. Rev.*, **108**, 298–312.

Charney J. G., R. Fjørtoft and J. von Neumann, 1950: Numerical integration of the barotropic vorticity equation. *Tellus*, **2**, 237–254.

Coakley, J. A., Jr., and P. Chylek, 1975: The two stream approximation in radiative transfer: Including the angle of incident radiation. *J. Atmos. Sci.*, **32**, 409–418.

Donner, L. J., H.-L. Kuo and E. J. Pitcher, 1982: The significance of thermodynamic forcing by cumulus convection in a general circulation model. *J. Atmos. Sci.*, **39**, 2159–2181.

Errico, R. M., 1984: The dynamical balance of a general circulation model. *Mon. Wea. Rev.*, **112**, 2439–2454.

———, 1987: A Description of software for determination of normal modes of the the NCAR community climate model. NCAR Technical Note TN-277+STR, 86 pp.

Errico, R. M., E. H. Barker and R. Gelaro, 1988: A determination of balanced normal modes for two models. *Mon. Wea. Rev.*, **116**, 2717–2724.

Errico, R. M., and P. J. Rasch, 1988: A comparison of various normal mode initialization schemes and the inclusion of diabatic processes. *Tellus*, **40A**, 1–25.

Fennessy, M.J., L. Marx and J. Shukla, 1985: General circulation model sensitivity to 1982–83 equatorial Pacific sea surface temperature anomalies. *Mon. Wea. Rev.*, **113**, 858–864.

Frank, W. M., 1983: The cumulus parameterization problem. *Mon. Wea. Rev.*, **111**, 1859–1871.

Geisler, J. E., M. L. Blackmon, G. T. Bates and S. Muñoz, 1985: Sensitivity of January climate response to the magnitude and position of equatorial Pacific sea surface temperature anomalies. *J. Atmos. Sci.*, **42**, 1037–1049.

Gelaro, R., and H. N. Shirer, 1986: A parameterization technique for nonlinear spectral models. *J. Atmos. Sci.*, **43**, 671–687.

Ghil, M., 1987: Dynamics, Statistics and Predictability of Planetary Flow Regimes. In *Irreversible Phenomena and Dynamical Systems Analyses in Geosciences*, C. Nicolis and G. Nicolis (eds.), D. Reidel Publ. Co., Dordrecht-Boston-Lancaster, pp. 241–283.

Gill, A. E., 1980: Some simple solutions for heat-induced tropical circulation. *Quart. J. Royal Meteor. Soc.*, **106**, 447–462.

Haltiner, G. J., and R. T. Williams, 1980: *Numerical Prediction and Dynamic Meteorology*, John Wiley and Sons, 477 pp.

Hamilton, K., 1988: A detailed examination of the extratropical response to tropical El Niño/Southern Oscillation events. *J. climatol.*, **8**, 67–86.

Harshvardahn, R. Davies, D. A. Randall and T. G. Corsetti, 1987: A fast radiation parameterization for atmospheric circulation models. *J. Geophys. Res.*, **92**, 1009–1016.

Held, I., 1987: Dynamics of low frequency phenomena in the atmosphere. Vol. 3: Nonlinear theory. Notes from an NCAR Summer Colloquium, 6–24 July 1987, 950 pp.

Higgins, R. W., and H. N. Shirer, 1989: Transitions from Hadley to Rossby flows in internally forced rotating spherical systems. (submitted to *J. Atmos. Sci.*)

Hogan, T. F., and T. Rosmond, 1989: The NOGAPS forecast model. NEPRF Technical Note. (in press)

Hollingsworth, A., K. Arpe, M. Tiedtke, M. Capaldo and H. Savijarvi, 1980: The performance of a medium-range forecast model in winter—Impact of physical parameterizations. *Mon. Wea. Rev.*, **108**, 1736–1773.

Holloway, G., 1986: Eddies, Waves, Circulation and Mixing: Statistical Geofluid Mechanics. In *Annual Reviews of Fluid Mechanics*, Vol. 18, Annual Reviews Inc., Palo Alto, California.

Horel, J. D., and J. M. Wallace, 1981: Planetary-scale atmospheric phenomena associated with the Southern Oscillation. *Mon. Wea. Rev.*, **109**, 813–829.

Hoskins, B. J., I. N. James and G. H. White, 1983: The shape, propagation and mean-flow interactions of large-scale weather systems. *J. Atmos. Sci.*, **40**, 1595–1612.

Hoskins, B. J., and D. J. Karoly, 1981: The steady linear response of a spherical atmosphere to thermal and orographic forcing. *J. Atmos. Sci.*, **38**, 1179–1196.

Hoskins, B.J., and A. J. Simmons, 1975: A multi-layer spectral model and the semi-implicit method. *Quart. J. Royal Meteor. Soc.*, **101**, 637–655.

Julian, P. R., and R. M. Chervin, 1978: A study of the Southern Oscillation and Walker Circulation phenomenon. *Mon. Wea. Rev.*, **106**, 1433–1451.

Kasahara, A., 1978: Further studies on a spectral model of the global barotropic primitive equations with Hough harmonic expansions. *J. Atmos. Sci.*, **35**, 2043-2051.

_____, 1984: The linear response of a stratified global atmosphere to tropical thermal forcing. *J. Atmos. Sci.*, **41**, 2217-2237.

Kasahara, A., and K. Puri, 1981: Spectral representation of three-dimensional global data by expansion in normal mode functions. *Mon. Wea. Rev.*, **109**, 37-51.

Keshavamurty, R. N., 1982: Response of the atmosphere to sea surface temperature anomalies over the equatorial Pacific and the teleconnections of the Southern Oscillation. *J. Atmos. Sci.*, **39**, 1241-1259.

Ko, S.-D., J. J. Tribbia and J. P. Boyd, 1989: Energetics of gravitational and rotational modes in a multilevel global spectral model. Part II: Kinetic energy, available potential energy and total energy. (to appear in *Mon. Wea. Rev.*)

Kok, C. J., and J. D. Opsteegh, 1985: Possible causes of anomalies in seasonal mean circulation patterns during the 1982-83 El Niño Event. *J. Atmos. Sci.*, **42**, 677-6___.

Krishnamurti, T. N., Y. Ramanathan, H.-L. Pan, R. J. Pasch and J. Molinari, 1980: Cumulus parameterization and rainfall rates I. *Mon. Wea. Rev.*, **108**, 465-472.

Kwizak, M., and A. J. Robert, 1971: A semi-implicit scheme for grid point atmospheric models of the primitive equations. *Mon. Wea. Rev.*, **99**, 32-36.

Lacis, A. A., and J. E. Hansen, 1974: A parameterization for the absorption of solar radiation in the earth's atmosphere. *J. Atmos. Sci.*, **31**, 118-133.

Lau, K.-M., and H. Lim, 1982: Thermally driven motions in an equatorial β-plane: Hadley and Walker circulations during the winter monsoon. *Mon. Wea. Rev.*, **110**, 336-353.

_____, and _____, 1984: On the dynamics of equatorial forcing of climate teleconnections. *J. Atmos. Sci.*, **41**, 161-176.

Lighthill, M. J., 1969: Dynamic response of the Indian Ocean to onset of the southwest monsoon. *Phil. Trans. Roy. Soc. London*, **256**, 45-92.

Lim, H., and C.-P. Chang, 1983: Dynamics of teleconnections and Walker circulations forced by equatorial heating. *J. Atmos. Sci.*, **40**, 1897–1915.

_____, and _____, 1986: Generation of internal- and external-mode motions from internal heating: Effects of vertical shear and damping. *J. Atmos. Sci.*, **43**, 948–957.

_____, and _____, 1987: On the dynamics of midlatitude-tropical interactions and the winter monsoon. In *Monsoon Meteorology*, C.-P. Chang and T.N. Krishnamurti (eds.), Oxford University Press, Inc., pp. 405–434.

Lord, S. J., 1982: Interaction of a cumulus cloud ensemble with the large-scale environment. Part III: Semi-prognostic test of the Arakawa-Schubert cumulus parameterization. *J. Atmos. Sci.*, **39**, 88–103.

Lord, S. J., W. C. Chao and A. Arakawa, 1982: Interaction of a cumulus cloud with the large-scale environment. Part IV: The discrete model. *J. Atmos. Sci.*, **39**, 104–113.

Louis, J.-F., 1979: A parametric model of vertical eddy fluxes in the atmosphere. *Boundary-Layer Meteorol.*, **17**, 187–202.

Matsuno, T., 1966: Quasi-geostrophic motions in the equatorial area. *J. Meteor. Soc. Japan*, **44**, 25–41.

Mechoso, C. R., A. Kitoh, S. Moorthi and A. Arakawa, 1987: Numerical simulations of the atmospheric response to a sea surface temperature anomaly over the equatorial eastern Pacific Ocean. *Mon. Wea. Rev.*, **115**, 2936–2956.

Opsteegh, J. D., and H. M. van den Dool, 1980: Seasonal differences in the stationary response of a linearized primitive equation model: Prospects for long range forecasting? *J. Atmos. Sci.*, **37**, 2169–2185.

Palmer, T. N., 1988: Medium and extended range predictability and stability of the Pacific/North American mode. *Quart. J. Royal Meteor. Soc.*, **114**, 691–713.

Palmer, T. N., and D. A. Mansfield, 1986: A study of wintertime circulation anomalies during past El Niño events using a high resolution general circulation model. II: Variability of the seasonal mean response. *Quart. J. Royal Meteor. Soc.*, **112**, 639–660.

Palmer, T. N., G. J. Shutts and R. Swinbank, 1986: Alleviation of a systematic westerly bias in general circulation and numerical weather prediction models through an orographic gravity wave drag parameterization. *Quart. J. Royal Meteor. Soc.*, **112**, 1001–1039.

Pedlosky, J., 1979: *Geophysical Fluid Dynamics.* Springer-Verlog, 624 pp.

Pitcher, E. J., M. L. Blackmon, G. T. Bates and S. Muñoz. 1988: The effect of North Pacific sea surface temperature anomalies on the January climate of a general circulation model. *J. At nos. Sci.*, **45**, 173–188.

Puri, K., 1983: The relationship between convective adjustment, Hadley circulation and normal modes of the ANMRC spectral model. *Mon. Wea. Rev.*, **111**, 23–33.

Rasmusson, E., and T. Carpenter, 1982: Variations in tropical sea surface temperature and surface wind fields associated with the Southern Oscillation/El Niño. *Mon. Wea. Rev.*, **110**, 354–384.

Robert, A. J., 1966: The integration of a low order spectral form of the primitive meteorological equations. *J. Meteor. Soc. Japan*, Ser. 2, **44**, 237–245.

Rowntree, P. R., 1972: The influence of tropical east Pacific Ocean temperature anomalies on the atmosphere. *Quart. J. Royal Meteor. Soc.*, **98**, 290–321.

Sagan, C., and J. B. Pollack, 1967: Anisotropic nonconservative scattering and the clouds of Venus. *J. Geophys. Res.*, **72**, 469–477.

Sardeshmukh, P. D., and B. J. Hoskins, 1985: Vorticity balances in the tropics during the 1982–83 El Niño-Southern Oscillation event. *Quart. J. Royal Meteor. Soc.*, **111**, 261–278.

_____, and _____, 1988: The generation of global rotational flow by steady idealized tropical divergence. *J. Atmos. Sci.*, **45**, 1228–1251.

Shirer, H. N., 1980: Bifurcation and stability in a model of moist convection in a shearing environment. *J. Atmos. Sci.*, **37**, 1586–1602.

_____, 1986: On cloud street development in three dimensions: Parallel and Rayleigh instabilities. *Contrib. Atmos. Phys.*, **59**, 126–149.

Shirer, H. N., and J. A. Dutton, 1979: The branching hierarchy of multiple solutions in a model of moist convection. *J. Atmos. Sci.*, **36**, 1705–1721.

Shirer, H. N., and R. J. Wells, 1983: Mathematical structure of the singularities at the transitions between steady states in hydrodynamic systems. *Lecture Notes in Physics*, **185**, Springer-Verlag, 276 pp.

Shukla, J., and J. M. Wallace, 1983: Numerical simulation of the atmospheric response to equatorial Pacific sea surface temperature anomalies. *J. Atmos. Sci.*, **40**, 1613–1630.

Silva Dias, P. L., W. H. Schubert and M. DeMaria, 1983: Large-scale response of the tropical atmosphere to transient convection. *J. Atmos. Sci.*, **40**, 2689–2707.

Simmons, A. J., 1982: The forcing of stationary wave motion by tropical diabatic heating. *Quart. J. Royal Meteor. Soc.*, **108**, 503–534.

Simmons, A. J., and B. J. Hoskins, 1978: The life cycles of some nonlinear baroclinic waves. *J. Atmos. Sci.*, **35**, 414–432.

Simmons, A. J., J. M. Wallace and G. W. Branstator, 1983: Barotropic wave propagation and instability, and atmospheric teleconnection patterns. *J. Atmos. Sci.*, **40**, 1363–1392.

Tiedtke, M., 1984: The effect of penetrative cumulus convection on the large-scale flow in a general circulation model. *Beitr. Phys. Atmosph.*, **57**, 216–239.

Vickroy, J. G., and J. A. Dutton, 1979: Bifurcation and catastrophe in a simple, forced, dissipative quasi-geostrophic flow. *J. Atmos. Sci.*, **36**, 42–52.

Wallace, J. M., and D. S. Gutzler, 1981: Teleconnections in the geopotential height field during the Northern Hemisphere winter. *Mon. Wea. Rev.*, **109**, 785–812.

Webster, P. J., 1972: Response of the tropical atmosphere to local steady forcing. *Mon. Wea. Rev.*, **100**, 518–541.

———, 1981: Mechanisms determining the atmospheric response to sea surface temperature anomalies. *J. Atmos. Sci.*, **38**, 554–571.

————, 1982: Seasonality in the local and remote atmospheric response to sea surface temperature anomalies. *J. Atmos. Sci.*, **39**, 41–52.

Webster, P. J., and H.-R. Chang, 1988: Energy accumulation and emanation regions at low latitudes: Impacts of a zonally varying basic state. *J. Atmos. Sci.*, **45**, 803–829.

Wergen, W., 1987: Diabatic nonlinear normal mode initialisation for a spectral model with a hybrid vertical coordinate. European Centre for Medium Range Weather Forecasts Technical Report No. 59, 83 pp.

Zhong, W., and J. Nogues-Paegle, 1989: Normal mode projections of GCM response to tropical forcing. (submitted to *Tellus*)

Distribution List

Applied Physics Laboratory
Johns Hopkins University
Johns Hopkins Road
Laurel MD 20707

Applied Physics Laboratory
University of Washington
1013 NE 40th St.
Seattle WA 98105

Applied Research Laboratory
Pennsylvania State University
P.O. Box 30
State College PA 16801

Applied Research Laboratory
University of Texas at Austin
P.O. Box 8029
Austin TX 78713-8029

Assistant Secretary of the Navy
Research, Development & Acquisition
Navy Department
Washington DC 20350-1000

Chief of Naval Operations
Navy Department
Washington DC 20350-2000
Attn: OP-02
      OP-71
      OP-987

Chief of Naval Operations
Oceanographer of the Navy
U.S. Naval Observatory
34th & Massachusetts Ave. NW
Washington DC 20392-1800
Attn: OP-096
      OP-0961B

David W. Taylor Naval Research Center
Bethesda MD 20084-5000
Attn: Commander

Defense Mapping Agency
Systems Center
12100 Sunset Hill Rd #200
Reston VA 22090-3207
Attn: Director
      Code SGWN

Director of Navy Laboratories
Department of the Navy
Crystal Plaza #5, Rm. 1062
Washington DC 20360

Fleet Antisub Warfare Tng Ctr-Atl
Naval Station
Norfolk VA 23511-6495
Attn: Commanding Officer

Fleet Numerical Oceanography Center
Monterey CA 93943-5005
Attn: Commanding Officer

National Ocean Data Center
1825 Connecticut Ave., NW
Universal Bldg. South, Rm. 206
Washington DC 20235

Naval Air Development Center
Warminster PA 18974-5000
Attn: Commander

Naval Air Systems Command HQ
Washington DC 20361-0001
Attn: Commander

Naval Civil Engineering Laboratory
Port Hueneme CA 93043
Attn: Commanding Officer

Naval Coastal Systems Center
Panama City FL 32407-5000
Attn: Commanding Officer

Naval Facilities Engineering
Command HQ
200 Stovall St.
Alexandria VA 22332-2300
Attn: Commander

Naval Oceanographic Office
Stennis Space Center MS 39522-5001
Attn: Commanding Officer

Naval Oceanography Command
Stennis Space Center MS 39529-5000
Attn: Commander

Naval Oceanographic & Atmospheric
Research Laboratory
Atmospheric Directorate
Monterey CA 93943-5006
Attn: Code 400

Naval Oceanographic & Atmospheric
Research Laboratory
Stennis Space Center MS 39529-5004
Attn: Code 100
      Code 105
      Code 115
      Code 125L (10)
      Code 125P
      Code 125EX
      Code 200
      Code 300

Naval Oceanographic & Atmospheric
Research Laboratory
Liaison Office
Crystal Plaza #5, Rm. 802
2211 Jefferson Davis Hwy.
Arlington VA 22202-5000
Attn: B. Farquhar

Naval Ocean Systems Center
San Diego CA 92152-5000
Attn: Commander

Naval Postgraduate School
Monterey CA 93943
Attn: Superintendent
      Meteorology Dept.
      Library
      Oceanography Dept.

Naval Research Laboratory
Washington DC 20375
Attn: Commanding Officer

Naval Sea Systems Command HQ
Washington DC 20362-5101
Attn: Commander

Naval Surface Weapons Center Det
Silver Spring
White Oak Laboratory
10901 New Hampshire Ave.
Silver Spring MD 20903-5000
Attn: Officer in Charge
      Library

Naval Surface Weapons Center
Dahlgren VA 22448-5000
Attn: Commander

Naval Underwater Systems Center
Newport RI 02841-5047
Attn: Commander

Naval Underwater Systems Center Det
New London Laboratory
New London CT 06320
Attn: Officer in Charge

Office of Naval Research
800 N. Quincy St.
Arlington VA 22217-5000
Attn: Code 10D/10P, Dr. E. Silva
      Code 112, Dr. E. Hartwig
      Code 12
      Code 10

Office of Naval Research
ONR European Office
Box 39
FPO New York 09510-0700
Attn: Commanding Officer

Office of Naval Technology
800 N. Quincy St.
Arlington VA 22217-5000
Attn: Code 20, Dr. P. Selwyn
      Code 228, Dr. M. Briscoe
      Code 234, Dr. C. Votaw

Scripps Institution of Oceanography
University of California
P.O. Box 6049
San Diego CA 92106

Space and Naval Warfare
Systems Command
Washington DC 20363-5100
Attn: Commander

U.S. Naval Academy
Director of Research
Annapolis MD 21402

Woods Hole Oceanographic Institution
P.O. Box 32
Woods Hole MA 02543
Attn: Director

REPORT DOCUMENTATION PAGE

Public reporting burden for this collection of information is estimated to average 1 hour per response, including the time for reviewing instructions, searching existing data sources, gathering and maintaining the data needed, and completing and reviewing the collection of information. Send comments regarding this burden estimate or any other aspect of this collection of information, including suggestions for reducing this burden, to Washington Headquarters Services, Directorate for Information Operations and Reports, 1215 Jefferson Davis Highway, Suite 1204, Arlington, VA 22202-4302, and to the Office of Management and Budget, Paperwork Reduction Project (0704-0188), Washington DC 20503.

1. Agency Use Only *(Leave blank)*.	2. Report Date. July 1990	3. Report Type and Dates Covered. Final

4. Title and Subtitle.

The Structure and Dynamics of Tropical-Midlatitude Interactions

5. Funding Numbers.

Program Element No 62435N

Project No RM35G81

Task No. 1

Accession No. DN656756

6. Author(s).

Dr. Ronald Gelaro

7. Performing Organization Name(s) and Address(es).

Naval Oceanographic and Atmospheric Research Laboratory
Atmospheric Directorate
Monterey, California 93943-5006

8. Performing Organization Report Number.

NOARL Report 7

9. Sponsoring/Monitoring Agency Name(s) and Address(es).

Office of Naval Technology, Arlington, VA 22217
Department of Meteorology, The Pennsylvania State University
University Park, PA 16802

10. Sponsoring/Monitoring Agency Report Number.

11. Supplementary Notes.

12a. Distribution/Availability Statement.

Approved for public release; distribution is unlimited. Naval Oceanographic and Atmospheric Research Laboratory, Stennis Space Center, Mississippi 39529-5004.

12b. Distribution Code.

13. Abstract *(Maximum 200 words)*.

The Navy is interested in many aspects of atmospheric and oceanic variability that can no longer be treated as mutually exclusive phenomena. For example, it has become clear that seasonal predictions of oceanic storm activity and cloudiness, as well as seasonal variations in most oceanic circulations, are evolving phenomena that are continually modified by feedbacks between the atmosphere and the ocean. At shorter time scales, the prospect for developing coupled whole-earth prediction systems to provide better real-time fleet support depends critically on our ability to identify and understand the processes that link the atmosphere and oceans.

An understanding of the interactions between the tropical oceans and the atmosphere, developed within the context of the Navy's environmental prediction systems, is therefore essential for achieving naval environmental research goals regarding coupled air-sea model development and increased understanding of the role of oceanic processes in the global environment. The objective of the study described in this report is to investigate the influence of tropical ocean thermal anomalies on the general circulation of the atmosphere, placing particular emphasis on the impact of these anomalies on the near-term variability of the midlatitude flow.

14. Subject Terms.

tropical-midlatitude, interaction, normal mode, tropical meteorology

15. Number of Pages. 234

16. Price Code.

17. Security Classification of Report.	18. Security Classification of This Page.	19. Security Classification of Abstract.	20. Limitation of Abstract.
Unclassified	Unclassified	Unclassified	Same as report

NSN 7540-01-280-5500